Technical Development Work on Design of Rigid Debris-resisting Barriers

GEO Report No. 358

L.A. Wong, H.W.K. Lam, C. Lam & J.S.H. Kwan

Geotechnical Engineering Office
Civil Engineering and Development Department
The Government of the Hong Kong
Special Administrative Region

[Blank Page]

Technical Development Work on Design of Rigid Debris-resisting Barriers

GEO Report No. 358

L.A. Wong, H.W.K. Lam, C. Lam & J.S.H. Kwan

© The Government of the Hong Kong Special Administrative Region

First published, December 2022

Prepared by:

Geotechnical Engineering Office,
Civil Engineering and Development Department,
Civil Engineering and Development Building,
101 Princess Margaret Road,
Homantin, Kowloon,
Hong Kong.

Preface

In keeping with our policy of releasing information which may be of general interest to the geotechnical profession and the public, we make available selected internal reports in a series of publications termed the GEO Report series. The GEO Reports can be downloaded from the website of the Civil Engineering and Development Department (http://www.cedd.gov.hk) on the Internet.

Raymond WM Cheung
Head, Geotechnical Engineering Office
December 2022

Foreword

Rigid debris-resisting barriers are commonly used to mitigate natural terrain landslide hazards. As part of the development of natural terrain landslide risk management strategy for Hong Kong, the technical guidance on the design of rigid debris-resisting barriers has been continuously reviewed and updated.

This GEO Report comprises nine Sections based on nine GEO Technical Notes that document the technical development work conducted by the GEO since 2015, with a view to enhancing and optimising the design of rigid debris-resisting barriers. With reference to the findings of the technical development work, GEO Technical Guidance Note (TGN) No. 52 was promulgated in 2020 which stipulates the technical recommendations pertaining to the enhancement of rigid debris-resisting barrier design, covering geotechnical stability, structural integrity and detailing for deflector.

The study was mainly carried out by Mr L.A. Wong and Mr H.W.K. Lam under my supervision. Pilot analytical study of displacement approach was undertaken by Dr C. Lam and Dr J.S.H. Kwan. Colleagues in the GEO and practitioners in the geotechnical industry provided constructive comments on the formulation of the enhanced technical guideline. Expert advice was provided by Dr Suzanne Lacasse, Professor David Petley and Professor Kenichi Soga of the 7th Slope Safety Technial Review Board. All contributions are gratefully acknowledged.

T.K.C. Wong
Chief Geotechnical Engineer/Standards & Testing

Abstract

In 2000, GEO Report No. 104 was published based on the state of the knowledge as of the late 1990s which sets out the geotechnical parameters and considerations for the design of rigid debris-resisting barriers. In 2012, GEO Report No. 270 was published to supplement and update the relevant design guidance provided by GEO Report No. 104, based on a review of state-of-the-art literature and international technical guidance documents in the early 2010s. The recommendations given in GEO Report No. 270 were promulgated in GEO Technical Guidance Note (TGN) No. 33.

Based on a desk study review and site inspection of selected barriers, technical recommendations on proper detailing of rigid debris-resisting barriers were promulgated in GEO TGN No. 35. Subsequently, the prevailing design guidelines were updated based on the technical advice given by Professor O. Hungr from the perspective of value engineering as promulgated in GEO TGN No. 47.

Since then, the GEO has conducted a series of technical development work, with a view to further optimising the design of rigid debris-resisting barriers. The work included large-scale experimental studies, numerical analyses as well as analytical studies, covering geotechnical stability, structural integrity and detailing for deflector.

This series of technical development work provides further evidence to supplement and update relevant technical design guidance given in GEO Report No. 104, GEO Report No. 270, GEO TGN No. 35 and GEO TGN No. 47. Subsequently, GEO TGN No. 52 was promulgated which stipulates the technical recommendations pertaining to the enhancement of rigid debris-resisting barrier design. This GEO report documents the technical development work pertinent to the development of GEO TGN No. 52.

[Blank Page]

Explanatory Note

This GEO Report comprises nine Sections based on nine GEO Technical Notes that document the technical development work conducted by the GEO since 2015, with a view to enhancing the design of rigid debris-resisting barriers. It is grouped under three main aspects, covering geotechnical stability, structural integrity and detailing for deflector, as follows:

		Title	Page No.
Part 1A:	***Geotechnical Stability: Assessment of Dynamic Soil Debris Impact Force***		
	Section 1	Study of Dynamic Soil Debris Impact Load on Rigid Debris-resisting Barriers (TN 5/2019)	11
Part 1B:	***Geotechnical Stability: Displacement Approach for Geotechnical Stability Assessment of Boulder Impact***		
	Section 2	Displacement-based Assessment of Boulder Impacts on Rigid Debris-resisting Barriers - A Pilot Study (TN 9/2016)	81
	Section 3	Verification of Displacement Approach for Rigid Debris-resisting Barriers Subject to Boulder Impacts (TN 4/2019)	147
Part 2:	***Structural Integrity***		
	Section 4	Study of Flexural Response of Rigid Barriers Subject to Boulder Impact (TN 3/2018)	185
	Section 5	Large-scale Experimental Study of Structural Response of Rigid Barriers Subject to Hard Impacts (TN 7/2018)	237
	Section 6	Supplementary Experimental Study of Structural Response of Rigid Barriers Subject to Hard Impacts (TN 3/2019)	273
	Section 7	Analytical Study of Cushioning Effect Provided by Rockfill Gabions in Reducing Flexural Response of Rigid Barriers Subject to Boulder Impacts (TN 6/2019)	293
Part 3:	***Detailing for Deflector***		
	Section 8	Spillage Mechanism of Landslide Debris Intercepted by Rigid Barriers and Deflectors to Prevent Spillage (TN 5/2018)	343
	Section 9	Supplementary Study of Spillage Mechanism of Landslide Debris Intercepted by Rigid Barriers and Deflectors to Prevent Spillage (TN 7/2019)	371

[Blank Page]

Part 1A

Geotechnical Stability: Assessment of Dynamic Soil Debris Impact Force

[Blank Page]

Section 1:
Study of Dynamic Soil Debris Impact Load on Rigid Debris-resisting Barriers

L.A. Wong & H.W.K. Lam

This section is largely based on GEO Technical Note No. TN 5/2019 produced in December 2019

Foreword

This Technical Note summarises findings of a study of dynamic soil debris impact load on rigid debris-resisting barriers. This study was carried out by Mr L.A. Wong under the supervision of Mr H.W.K. Lam, in collaboration with Dr. C.E. Choi from the Hong Kong University of Science and Technology. The Drafting Unit of the Standards and Testing Division assisted in formatting this Note.

Dr. C.E. Choi and various colleagues in the GEO provided constructive comments on the Note. All contributions are gratefully acknowledged.

T.K.C. Wong
Chief Geotechnical Engineer/Standards and Testing
December 2019

Abstract

Local design practice adopts hydrodynamic model to estimate dynamic soil debris impact load on rigid debris-resisting barriers. With a view to optimising the design of rigid debris-resisting barriers, GEO has initiated various studies including centrifuge modelling, advanced numerical modelling and large-scale physical tests to investigate dynamic soil debris impact on rigid barriers. In particular, a series of large-scale impact tests using realistic debris mix and a 1.8 m high L-shaped reinforced concrete model barrier were conducted in the newly established flume facility in the Kadoorie Centre in Hong Kong. This Note documents the key findings of these studies.

Contents

			Page No.
Title Page			11
Foreword			12
Abstract			13
Contents			14
List of Tables			16
List of Figures			17
1	Introduction		18
2	Large-scale Flume Tests in Kadoorie Centre, Hong Kong		18
	2.1	General	18
	2.2	Flume Facilities and Test Setup	18
	2.3	Model Barrier	19
	2.4	Instrumentation System	21
	2.5	Soil Debris Materials	21
	2.6	Test Programme	23
	2.7	Test Results	23
		2.7.1 Debris Impact Mechanism	23
		2.7.2 Interpretation of Dynamic Soil Debris Pressure Coefficient	26
3	Numerical Analyses		27
	3.1	General	27
	3.2	Results of Numerical Analysis	28
4	Comparison with Overseas Design Guidelines and Researches		28
5	Discussion on Dynamic Soil Debris Pressure Coefficient and Its Application		30
6	Summary		32
7	References		32

		Page No.
Section 1 Appendix A:	Specifications of Instrumentations for Large-scale Flume Tests Conducted in Kadoorie Centre, Hong Kong	35
Section 1 Appendix B:	Water Content of Debris Mix for Large-scale Flume Tests Conducted in Kadoorie Centre, Hong Kong	39
Section 1 Appendix C:	Results of Large-scale Flume Tests Conducted in Kadoorie Centre, Hong Kong	43
Section 1 Appendix D:	Sample Interpretation of Test Results for Large-scale Flume Test Nos. 1 & 2	55
Section 1 Appendix E:	Numerical Analysis of Debris Impact on Rigid Barrier	59
Section 1 Appendix F:	Various Studies on Debris Impact Load	68
Section 1 Appendix G:	Sample Calculation for the Review of Multiple-surge Load Model	73

List of Tables

Table No.		Page No.
2.1	Test Programme	23
2.2	Summary of Test Results	27
3.1	Summary of Results of Numerical Analysis	28
4.1	Summary of Dynamic Pressure Coefficient in Overseas Design Guidelines	29
4.2	Summary of Dynamic Pressure Coefficient in Literatures	29
5.1	Summary of Review of Multiple-surge Load Model	32

List of Figures

Figure No.		Page No.
2.1	Photograph of the Flume Facility (Left), Front View of Model Barrier (Upper Right) and Side View of Model Barrier (Lower Right)	19
2.2	Instrumentation Plan (Top: Overview of Flume; Bottom: Model Barrier)	20
2.3	Mixing of Debris Materials by a Concrete Truck Mixer (Left) and Debris Stored at the Storage Container (Right)	22
2.4	Ten Numbers of 200 mm Diameter Granitic Spheres for Simulation of Hard Inclusions in Test No. 2	22
2.5	Footages Taken from High Speed Camera during Test No. 1	24
2.6	Sketch of Observed Debris Impact Mechanism in Test No. 1	25
2.7	Footages Taken from High Speed Camera during Test Nos. 2, 4 and 5	25
3.1	Debris Impact Mechanism Simulated in Numerical Analysis	28
5.1	Multiple Surge Load Model for Geotechnical Stability and Structural Integrity Assessment under Soil Debris Impact	31

1 Introduction

In Hong Kong, rigid debris-resisting barriers are commonly adopted to resist debris flows. The current design practice generally adopts limit equilibrium method for the design of rigid barriers in both geotechnical stability and structural integrity, where the dynamic impact load for soil debris is estimated using the hydrodynamic equation as shown in Equation 1.1 below. Kwan (2012) recommended the dynamic pressure coefficient (α) as 2.5, which aims to account for debris containing boulders not larger than 0.5 m in diameter. Such dynamic pressure coefficient is largely empirical and was established with reference to the state-of-the-art literatures and international guidelines in early 2010s.

$$F = \alpha \rho v^2 h w \sin\theta \quad \text{..... (1.1)}$$

where
- F = Dynamic soil debris impact force (in N)
- α = Dynamic soil debris pressure coefficient, α (dimensionless)
- ρ = Density of debris (in kg/m^3)
- v = Impact velocity of debris (in m/s)
- h = Debris flow thickness (in m)
- w = Debris flow width (in m)
- θ = Inclination of dynamic soil debris impact force (in degree)

In recent years, GEO has initiated various studies to investigate dynamic soil debris impact on these barriers. These studies involve review of latest literature, advanced numerical analyses and large-scale physical tests. This Note documents the key findings of these studies, with particular focus on the large-scale physical tests using the newly established flume facility in the Kadoorie Centre in Hong Kong to study dynamic soil debris impact load on rigid barriers.

There are on-going studies pertaining to other design aspects of rigid barriers, such as geotechnical stability and structural integrity of rigid barriers subject to boulder impact, cushioning effect of gabion, detailing etc., which are separately covered.

2 Large-scale Flume Tests in Kadoorie Centre, Hong Kong

2.1 General

To further investigate the dynamic soil debris impact load, GEO has collaborated with the HKUST and carried out a series of large-scale physical impact tests using the newly established flume facilities in the Kadoorie Centre in Hong Kong (HKUST, 2019). The key objectives of these tests are to gain a better understanding on soil debris impact mechanism and to validate the α values obtained from the centrifuge tests. Details of the flume facilities, setup, model rigid barrier, debris mix and test programme are discussed in this Section.

2.2 Flume Facilities and Test Setup

The flume established in the Kadoorie Centre is about 28 m long, 2 m wide and 1 m deep (see Figure 2.1). It comprises three key components, including a storage tank at the upstream, a transportation channel, and a deposition zone.

The storage tank has a capacity of about 10 m^3, with a gradient of 30° at the base to facilitate initiation of debris flows. There is a mechanical opening gate at the outlet of the storage tank which has been designed to simulate landslide initiation in a repeatable manner.

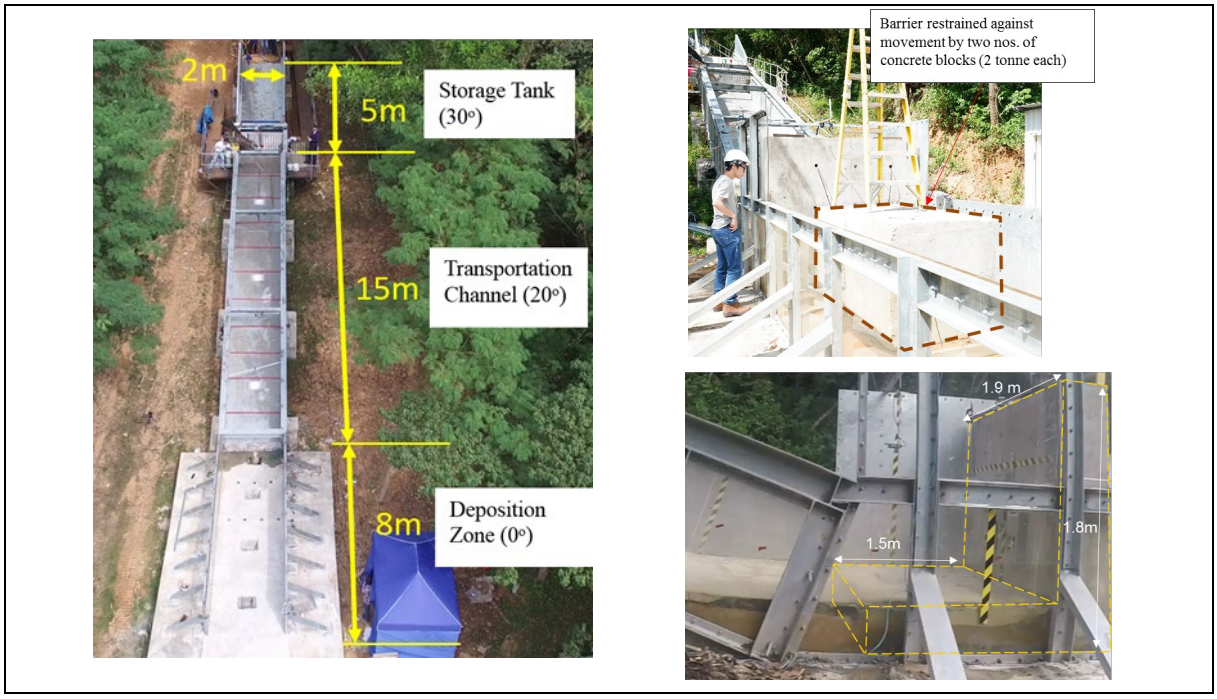

Figure 2.1 Photograph of the Flume Facility (Left), Front View of Model Barrier (Upper Right) and Side View of Model Barrier (Lower Right)

There is a 2 m wide transportation channel below the storage tank, which is formed by a steel frame structure with two sides of 1 m high side-walls. The side-walls are propped to each other with cross beams at the top at a spacing of about 5 m.

The transportation channel is inclined at 20°. One of the sidewalls is made of acrylic and is transparent, which enables observations of debris flow behaviour during the tests.

The deposition zone of 2 m wide and 8 m long, where two side-walls along this zone are supported by external raking struts, is located at the outlet of the transportation channel. It is founded on a 5 m wide and 8 m long levelled concrete pad.

The transition between the transportation channel and the deposition zone is made of mass concrete, which is smoothened to minimise energy loss of the debris flow during testing.

2.3 Model Barrier

To simulate a realistic debris-barrier interaction, a model barrier was constructed at the deposition zone to receive strikes from debris flow materials. The model barrier is an L-shaped reinforced concrete barrier (see Figure 2.1) where the wall stem is 1.8 m high

(including thickness of base slab), 1.9 m wide and 0.3 m thick, and the base slab is 1.5 m long (excluding thickness of wall stem), 1.9 m wide and 0.3 m thick. The characteristic strength of concrete used is 30 MPa. The reinforcement of the barrier involves two layers of A393 wire mesh (characteristic strength of 500 MPa) at the front side (i.e. tension side) of the wall stem, and one layer of such wire mesh at the other side of the stem and wall base.

There are box-outs at the wall stem and the base slab to accommodate instruments (see Figure 2.2). Details of the instrumentations of the model barrier are given in Section 2.4.

The model barrier is founded on a layer of compacted granitic fill materials placed at the deposition zone of the flume. To prevent energy loss due to barrier movement so as to ensure that maximum debris impact force can be captured, two additional concrete blocks (total weight of over 4 tonnes) were placed behind the model barrier as shown in Figure 2.1.

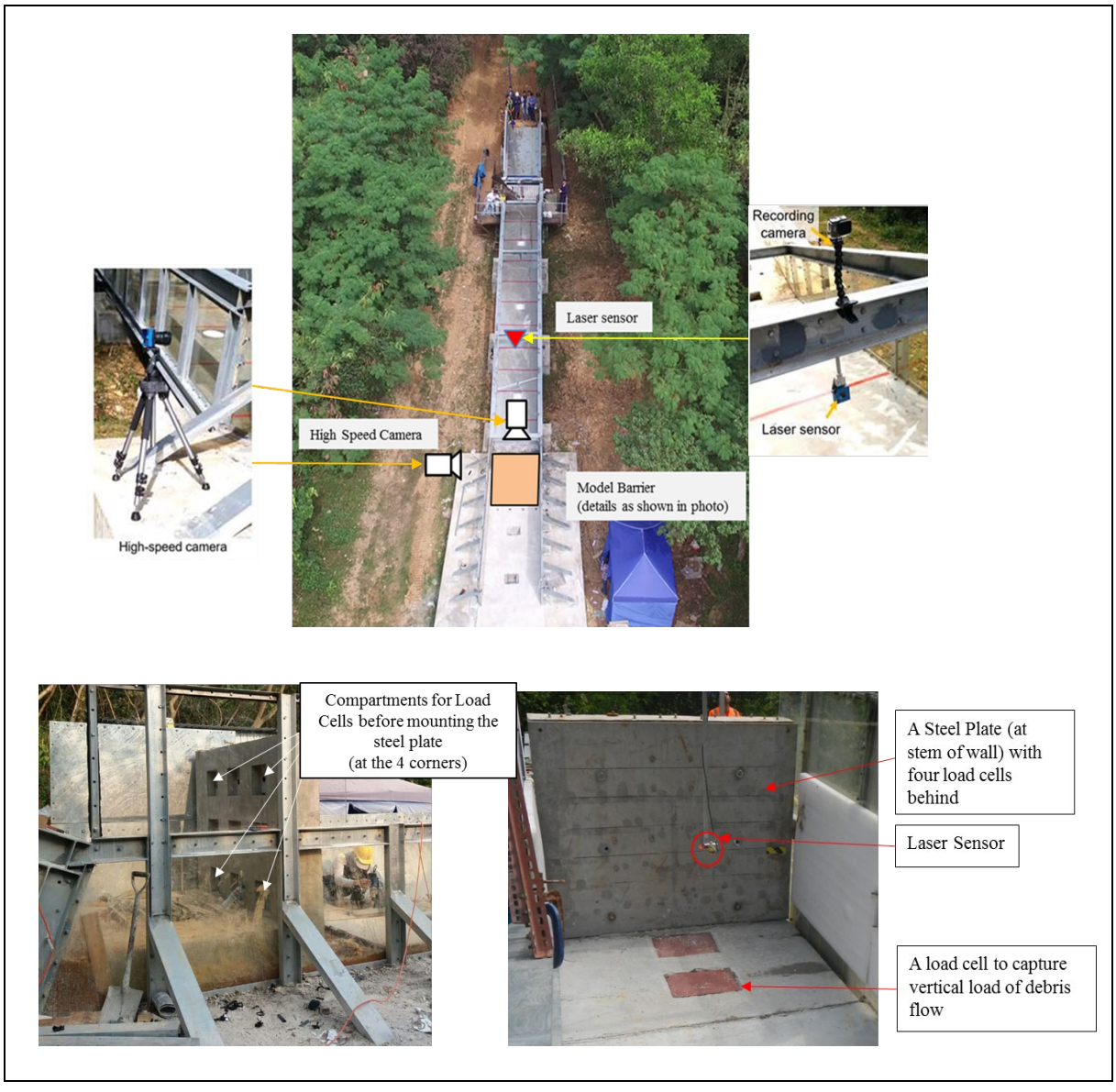

Figure 2.2 Instrumentation Plan (Top: Overview of Flume; Bottom: Model Barrier)

2.4 Instrumentation System

The instrumentations used in this study are summarised in Figure 2.2, which were calibrated by the HKUST. Two high-speed cameras, one at the side of deposition zone, and the other on a cross beam in the transportation zone (see the top photo in Figure 2.2), were installed to capture the impact process and the flow velocity of the debris flow. Two numbers of laser sensors (one at the transportation zone and the other at 0.9 m upstream of the barrier's stem at the deposition zone) were installed to measure the time histories of debris flow depth. Four load cells were installed at the model barrier for the measurement of time histories of debris impact force. These load cells were installed at the box-outs near the four corners of the wall stem of the model barrier (see the bottom left photo in Figure 2.2), and a steel force plate of about 1.5 m high, 1.9 m wide and 0.02 m thick was mounted in front of the wall stem and was used to transfer impact load to the load cells (see the bottom right photo in Figure 2.2). Upon debris impact on the model barrier, pressure would exert onto the steel plate which would transmit the force to the four load cells. Debris impact force is given by the summation of the load measurement taken at the four load cells. Specifications of the instruments are given in Section 1 Appendix A.

2.5 Soil Debris Materials

In this study, soil debris mix, including the water content, solid contents and its compositions were deliberated with reference to local and overseas literatures. Literatures indicate that granular flows or viscous debris flows typically involve a water content of 20% to 45% (Takahashi, 2007; Fei & Shu, 2004; Cui et al, 2005; Volkwein et al, 2011) as summarised in Section 1 Appendix B. As regards the solid content of the soil debris mix, reference was made to local data of granitic saprolite of different weathering grades and formations (Pun & Ho, 1996) and study reports of local debris flow events where ground investigation data of the solid composition of the deposited materials are available (the 1990 Tsing Shan Debris Flow and the 2005 Fei Ngo Shan Debris Flow).

Based on the above literature review together with the results of trial debris flows conducted at the flume, a soil debris mix with 40% of water and 60% of solid content (comprising 35% gravel, 60% sand, 5% silt and clay) was adopted in the tests. The Froude Number of the trial flows using such design debris mix was estimated to be 5 to 8, which is comparable to that of typical debris flow design events, i.e. around 5. To ensure consistency of the soil debris mix, the constituents of the debris materials were mechanically mixed by a concrete truck mixer (see Figure 2.3).

In some of the tests (i.e. Test Nos. 2, 4 and 5 in Table 2.1), different numbers of uniformly sized granitic spheres (200 mm in diameter) were placed behind the opening gate before loading the storage tank with soil debris mix (see Figure 2.4). These spheres were intended to simulate the presence of hard inclusions contained in a debris flow. Upon release of the opening gate, these spheres would flow along the transportation channel, together with soil debris mix.

Figure 2.3 Mixing of Debris Materials by a Concrete Truck Mixer (Left) and Debris Stored at the Storage Container (Right)

Figure 2.4 Ten Numbers of 200 mm Diameter Granitic Spheres for Simulation of Hard Inclusion in Test No. 2

2.6 Test Programme

The key objective of this series of large-scale flume tests is to study dynamic soil debris pressure coefficient (α). Five tests were carried out as summarised in Table 2.1 below. In each of these tests, the storage tank was first filled with a designated volume of soil debris mix (see Section 2.5 for details of soil debris mix), together with the hard inclusions in Test Nos. 2, 4 and 5. These materials were then released from the storage tank, through the opening gate, to simulate a debris flow initiation. The debris materials, including soil debris and hard inclusions (if any), would flow along the transportation channel and would eventually impact onto the instrumented model barrier at the deposition zone. The flow characteristics, such as flow depth, flow velocity, and impact load on the model barrier, were captured for the interpretation of dynamic soil debris pressure coefficient (α).

Table 2.1 Test Programme

Test No.	Debris Source Volume (m^3)	Debris Material	Hard Inclusions Adopted	Remark
1	~ 4	40% of water (by volume) and 60% solid components comprising 35% gravel, 60% sand, 5% silt and clay (see Section 2.5 for details)	No	-
2	~ 4		10 nos. of 200 mm diameter granitic boulders	-
3	~ 4		No	Repeat of Test 1
4	~ 4		30 nos. of 200 mm diameter granitic boulders	-
5	~ 4		30 nos. of 200 mm diameter granitic boulders	Repeat of Test 4

2.7 Test Results

2.7.1 Debris Impact Mechanism

Debris impact mechanisms are first analysed. Footages taken from high speed camera and a graphical representation showing the debris impact mechanism for Test No. 1 are given in Figures 2.5 and 2.6 respectively.

When the debris materials were released from the storage tank, the debris flowed along the transportation channel in a supercritical flow (Froude Number of 5 to 8). When the debris

hit the model barrier, debris run-up was observed. The frontal part of the flow deflected backwards after the debris reached its maximum run-up height (as shown in time T = 0.5 to 1.0 s in Figure 2.6). It then fell off and interacted with the incoming part of the debris flow, causing significant flow turbulence (at time T = 1.3 s to T = 2 s in Figures 2.5 and 2.6). Debris deposition could have occurred. When the impact process proceeded, the incoming debris mass continued to flux into the deposited mass. Towards the end of the impact process, the debris level subsided gradually with a backflow of the debris materials.

Similar debris impact mechanism was observed in Test Nos. 2 to 5.

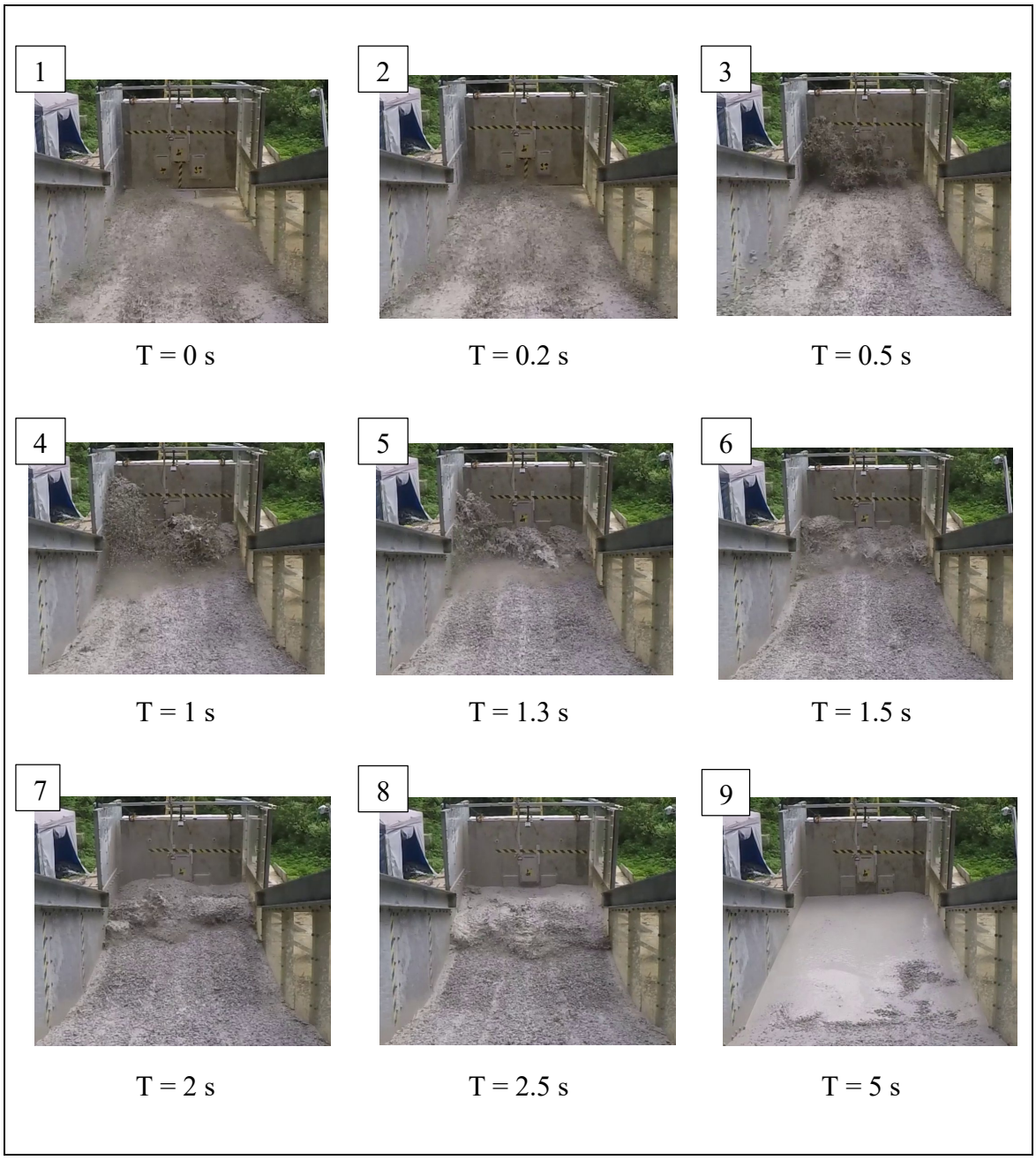

Figure 2.5 Footages Taken from High Speed Camera during Test No. 1

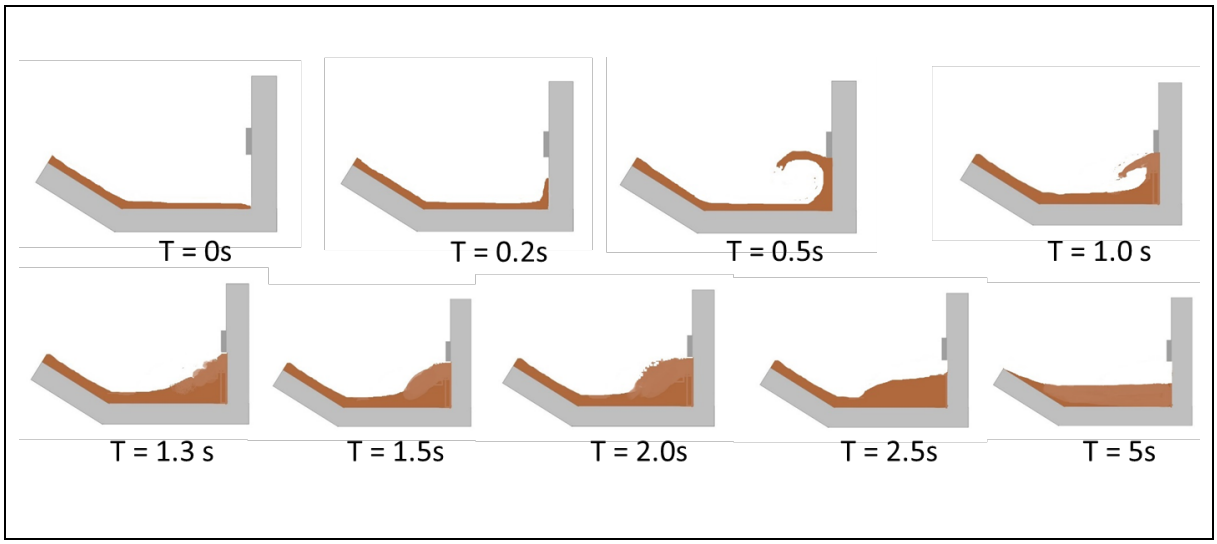

Figure 2.6 Sketch of Observed Debris Impact Mechanism in Test No. 1

Figure 2.7 shows the frontal part of the debris flow for Test Nos. 2, 4 and 5 when it reached the model barrier, where hard inclusions of 200 mm dia. granitic spheres were contained in the debris mix. Although ten (for Test No. 2) and thirty (for Test Nos. 4 and 5) numbers of boulders were placed immediately behind the opening gate together with the soil debris mix, only some of them flowed at the frontal part of the debris flow. The impact force data taken at the wall stem showed that the number of force spikes (due to the effect of direct impact of hard inclusions) is less than the number of spheres added in the soil debris (see Sections C.2, C.4 and C.5 in Section 1 Appendix C). This suggests that only part of the hard inclusions contained in the soil debris had given a direct impact on the model barrier (see also Figure 2.7).

Test No. 2 Test No. 4 Test No. 5

Figure 2.7 Footages Taken from High Speed Camera during Test Nos. 2, 4 and 5

More details including the time histories of impact force, debris flow velocity and debris flow thickness, as well as the videos taken for each test are reported in Section 1 Appendix C.

2.7.2 Interpretation of Dynamic Soil Debris Pressure Coefficient

According to the hydrodynamic model in Equation 1.1, the interpretation of dynamic soil debris pressure coefficient (α) requires various input parameters including impact force, flow depth, flow velocity, width of impact, debris density and impact angle as discussed below.

The impact force on the model barrier was taken as the summation of the loads measured from the four load cells, and is time-dependent. In Test Nos. 2, 4 and 5 where hard inclusions were added in the debris mix, distinct force spikes of very short duration (in the order of milli-second) and high magnitude were observed, which are deemed to the effect of impacts from the hard inclusions. These distinct force spikes were discounted in the interpretation of soil debris impact load (i.e. without the effect of hard inclusions) and the rationale is further discussed in Section 5.

Flow depth of the debris approaching the barrier is also time-dependent throughout the tests. The flow depth at about 0.9 m upstream of the model barrier was measured using the laser sensor. The flow depth measurement was cross-checked with the footages of the flow taken from high-speed camera located at the side view of the flume. For Test Nos. 2 and 4, due to instrumental errors of the laser sensor, the flow depth was taken based on an analysis of the footages taken by high speed camera at the side view of the flume.

The flow velocity was interpreted based on the observed time difference when the flow reached different parts of the flume. The flow velocity at different parts of the debris flow (including frontal and subsequent parts) was interpreted by tracing the footages taken by high-speed camera inside the flume. In addition, the frontal flow velocity was further cross-checked against the time difference for the flow front reaching different instruments (e.g. laser sensor at 0.9 m upstream of the force plate and load cells at the wall stem of the model barrier).

The width of debris impact was taken as the width of the barrier which is 1.9 m.

Debris density was taken as the initial debris density estimated based on the debris mix proportion and is approx. 2,000 kg/m^3.

The above input parameters (i.e. impact force, flow depth, flow velocity, width of impact, debris density and impact angle) can be used to interpret the dynamic soil debris pressure coefficient (α) using Equation 1.1. Some parameters, i.e. impact force, flow depth, and flow velocity, varied with time throughout the impact process. The interpretation of α values was based on synchronized sets of these input parameters. A sample interpretation for Test Nos. 1 and 2 is given in Section 1 Appendix D. The same approach was adopted for the interpretation of α values for the other three tests. The peak dynamic soil debris coefficient are shown in Table 2.2, which ranges from 0.76 to 1.01.

Table 2.2 Summary of Test Results

Test No.	Frontal Debris Flow Velocity (m/s)	Frontal Debris Flow Thickness (mm)	Froude Number [1]	Peak Soil Debris Impact Force [2] (kN)	Peak Dynamic Soil Debris Pressure Coefficient (See Section 1 Appendix D for Details)
1	6.1	50	5 - 8	4.9	0.76
2	6.3	50	4 - 9	6.2	0.98
3	6.3	35	4 - 11	4.5	0.81
4	5.7	35	5 - 10	4.3	0.99
5	6.3	40	4 - 10	4.2	1.01

Notes:
[1] Froude Number of typical debris impact scenarios for routine designs (e.g. 0.5 m thick debris travelling at 10 m/s) is approx. 5.
[2] For Test Nos. 2, 4 and 5, there is inherent difficulty in exercising judgement in discounting the force spikes due to impact of hard inclusions. Force spikes of relatively small magnitude have been taken as part of soil debris impact load and thus the dynamic soil debris pressure coefficient has been interpreted conservatively (i.e. on the high side).

3 Numerical Analysis

3.1 General

The scale of the simulated debris flows in the flume tests given in Section 2 was less than 5 m^3. To further analyse dynamic soil debris impact load for debris flow events of a larger scale, advanced numerical analysis using a three-dimensional finite-element computer package namely LS-DYNA was conducted. Drucker-Pager yield criterion was assumed to simulate the internal rheology of the landslide debris. Arbitrary Lagrangian-Eulerian technique was adopted to simulate debris materials.

The numerical model was first validated using the test results of Test No.1 (see Section 2.7.2). The input parameters adopted in the validation exercises were given in Section 1 Appendix E.

Based on the validated parameters, the numerical model was then used to analyse an impact scenario involving a debris source volume of 400 m^3, flowing along a 10 m wide channel, and impacting onto a 10 m wide, 5 m high and 1 m thick reinforced concrete model barrier. The characteristic concrete strength of 30 MPa was adopted for the model barrier. Steel reinforcement of 40 mm diameter was specified explicitly in both horizontal and vertical spacing of 200 mm.

3.2 Results of Numerical Analysis

Figure 3.1 shows the debris impact mechanism captured from the numerical analysis, which could generally resemble the field observations in the flume tests as discussed in Section 2.7.1. The flow characteristics (e.g. flow depth and flow velocity) and dynamic impact force were captured from the model for analyses. Table 3.1 shows the summary of the results of numerical analysis.

The peak dynamic soil debris coefficient was 0.97 for this numerical analysis. Details are given in Section 1 Appendix E and are summarised in Table 3.1.

Table 3.1 Summary of Results of Numerical Analysis

Frontal Debris Flow Velocity (m/s)	Frontal Debris Flow Thickness (m)	Peak Debris Impact Force (kN)	Peak Dynamic Soil Debris Pressure Coefficient
11.9	0.75	1450	0.97

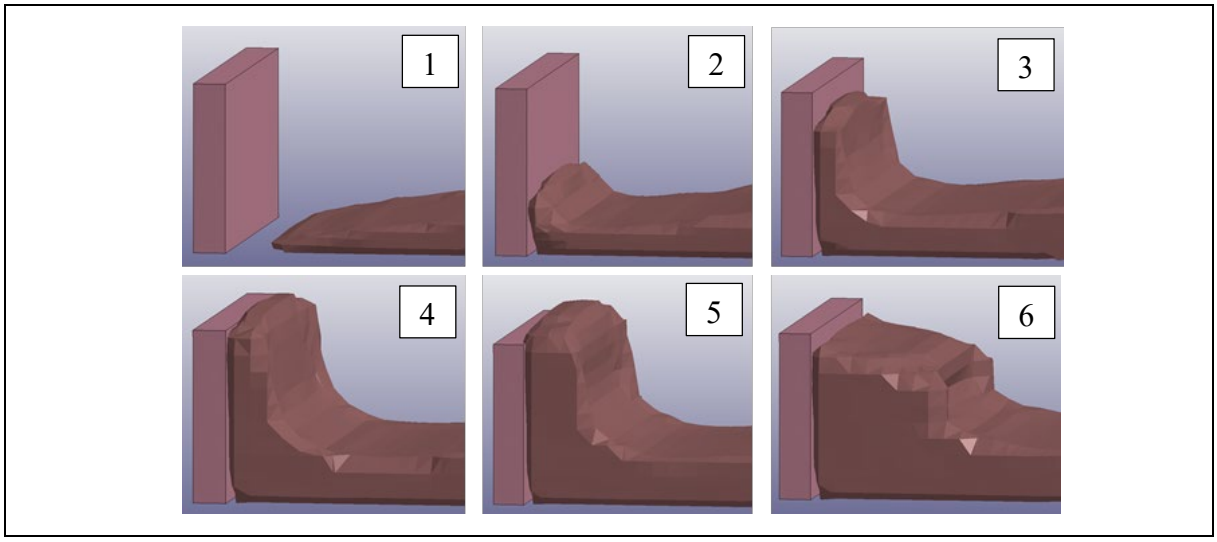

Figure 3.1 Debris Impact Mechanism Simulated in Numerical Analysis

4 Comparison with Overseas Design Guidelines and Researches

Kwan (2012) reviewed the literatures and international guidelines in early 2010s (Hungr et al, 1984; MLR, 2006; NILIM, 2007; SWCB, 2005). In this study, a review of the latest overseas design codes has been conducted, which covered several newly promulgated overseas design guidelines (ASI, 2011 & 2013; CAGHP, 2018). The α value promulgated in the overseas guidelines are summarised in Table 4.1.

Table 4.1 Summary of Dynamic Pressure Coefficient in Overseas Design Guidelines

Region	Dynamic Coefficient, α (for soil debris impact)	References
Canada	1	Hungr et al (1984)
Mainland	1 to 1.47	MLR (2006)
Mainland	1.33 (For rectangular barrier); or 1.47 (For square barrier)	CAGHP (2018)
Japan	1	NILIM (2007)
Austria	1	ASI (2013)
Taiwan	1	SWCB (2005)

Researches that have been conducted to study debris impact mechanism were reviewed. These researches involve small-scale debris impact tests, monitoring of field debris flow events and centrifuge tests. The dynamic pressure coefficients interpreted from these researches are summarised in Table 4.2 below. Information of these studies are discussed in Section 1 Appendix F.

Table 4.2 Summary of Dynamic Pressure Coefficient in Literatures

References	Dynamic coefficient, α (for soil debris impact)	Study Approach
Hu (2011)	1.01 (upper bound)	Monitoring of debris flow events in JiangJia Ravine, Yunnan Province, Mainland
Cui et al (2015)	0.47 to 1.02 (for Froude No. 3 to 5)	Laboratory flume tests (0.3 m^3)
Bugnion et al (2012)	0.4 to 2 (mean at 0.82)	Large-scale flume tests (50 m^3)
Proske et al (2011)	1	Laboratory flume tests (source volume not reported)
Canelli et al (2012)	< 1.8	Laboratory flume tests (0.4 m^3)

From Tables 4.1 and 4.2, α values are typically around 1 to 1.5.

5 Discussion on Dynamic Soil Debris Pressure Coefficient and Its Application

Having considered the overseas literatures and design codes, results of recent large-scale physical test and advanced numerical modelling, α value is typically below 1.5. If such value is adopted following the local design practice (based on the multiple-surge load model given in Figure 2.1 in Kwan (2012), partial load factor of 1.0 for dynamic load, debris velocity reduction in GEO (2015), observed frontal flow velocity and frontal flow thickness for the impact scenarios being considered, see Section 1 Appendix G for details), the predicted dynamic soil debris impact force for impact scenarios given in Test Nos. 1 to 5 in Section 2 and that for the numerical analysis in Section 3 was assessed as part of this study. Results of the assessment as shown in Table 5.1 indicates that if an α value of 1.5 is adopted, the predicted dynamic soil debris impact force following the local design practice is consistently about two times of the measured peak soil debris force (excluding force spike due to impact from hard inclusions) for Test Nos. 1 to 5 and the numerical outputs. This reflects the margin of conservatism in adopting this design framework (i.e. multiple surge model with an α value of 1.5) for predicting dynamic soil debris impact load.

As mentioned in Section 1, in the current design practice, α of 2.5 is recommended which takes into account debris containing boulders not larger than 0.5 m in diameter. To rationalise the use of hydrodynamic equation for rigid barrier designs, it is considered more appropriate to treat soil debris impact load and boulder impact load separately, since the physics behind and the barrier response under impact by these two distinct types of materials are very different. Boulder impact on rigid barriers typically involves small areal load in a very transient impact duration, i.e. very impulsive, and is generally not compatible with hydrodynamic equation, which is more appropriate for fluid-like materials such as soil debris flow. Besides, barrier response under boulder impact is sensitive to many factors such as mass ratio (or inertia) between impactor and barrier, stiffness of barriers, boundary condition of barrier, etc., which are not considered in the hydrodynamic model. (Note: In this regard, for boulder impact, more appropriate design approaches such as Displacement Approach (Lam & Kwan, 2016) and Enhanced Flexural Stiffness Method (Wong & Lam, 2018) were being developed.) It is also not a common practice to adopt an α value to cover boulder impact in overseas design guidelines.

In view of the above, the dynamic soil debris impact force should be used in the pseudo-static force equilibrium analyses for both geotechnical stability and structural integrity based on the multiple-surge load model shown in Figure 5.1. For design events involving both soil debris and boulders, the geotechnical stability of the barriers under boulder impacts should be assessed separately based on the Displacement Approach while for structural integrity check, the multiple-surge load model in Figure 2.1 of GEO Report No. 270 (Kwan, 2012) should still be followed as appropriate.

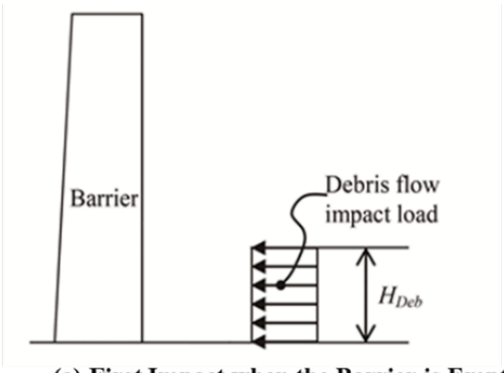

(a) First Impact when the Barrier is Empty

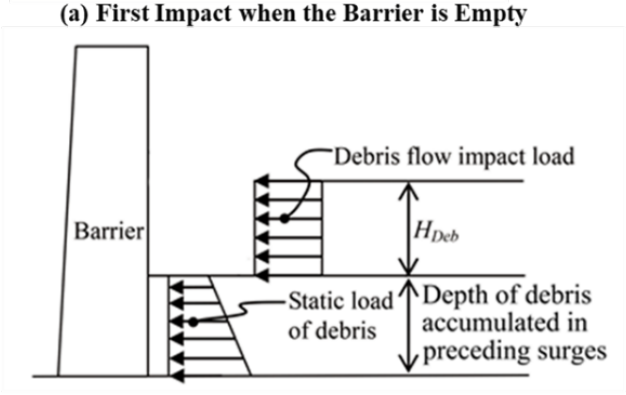

(b) Subsequent Surges Hitting the Barrier

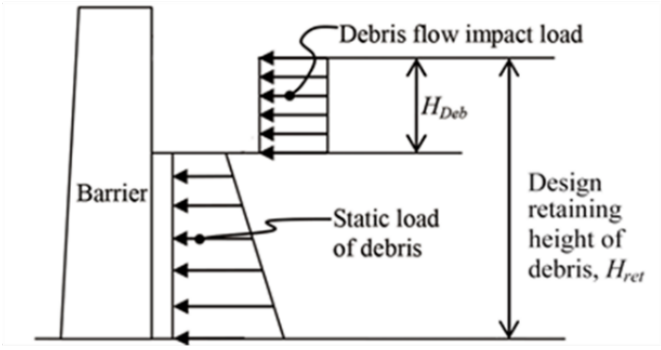

(c) Last Surge which Fills Up the Barrier to the Design Debris Retaining Height, H_{ret}

Notes:

(1) Design calculations for scenario (b) should be carried out for debris impacts at different levels corresponding to the depth of the debris accumulated in preceding surges.

(2) Debris retaining height, H_{ret}, shall be estimated using the retention capacity of the barrier. H_{ret} is not necessary the height of barrier wall. Normally, the height of the barrier wall could be greater than H_{ret} to provide freeboard and safety margin of debris retention volume.

(3) Reference should be made to GEO TGN No. 44 (GEO, 2015) for the assessment of debris impact velocity and impact load thickness (H_{Deb}).

Figure 5.1 Multiple Surge Load Model for Geotechnical Stability and Structural Integrity Assessment under Soil Debris Impact

Table 5.1 Summary of Review of Multiple-surge Load Model

Design Event	Predicted Soil Debris Force based on Multiple-surge Load Model (Assuming $\alpha = 1.5$) (kN)	Measured Peak Soil Debris Force from Flume Tests or Numerical Analyses (Extracted from Section 2 and 3) (kN)
Test No. 1	9.9 (See Section 1 Appendix G)	4.9
Test No. 2	11.5	6.2
Test No. 3	9.4	4.5
Test No. 4	7.3	4.3
Test No. 5	8.9	4.2
Numerical Analysis	2867	1450

6 Summary

GEO has recently carried out various studies to investigate dynamic soil debris impact on rigid barriers. In particular, the large-scale physical tests as discussed in Section 2 using the newly established flume facility in the Kadoorie Centre in Hong Kong provided quality experimental data to analyse dynamic pressure coefficient (α) for soil debris impact for designing rigid barriers in practice.

Other technical areas for rigid barrier designs including geotechnical stability and structural integrity of rigid barriers subject to boulder impacts, cushioning effect of gabion, detailing etc., would be separately covered.

7 References

ASI (2011). *ONR 24802 Protection Works for Torrent Control - Design of Structures.* Austrian Standard Institute, Austria, 96 p.

ASI (2013). *ONR 24801 Protection Works for Torrent Control - Static and Dynamic Actions on Structures*. Austrian Standard Institute, Austria.

Bugnion, L., McArdell, B.W., Bartelt, P. & Wendeler, C. (2012). Measurements of hillslope debris flow impact pressure on obstacles. *Landslides* 9(2): 179-187.

CAGHP (2018). *Specification of Design for Debris Flow Prevention* (T/CAGHP *021-2018)*. China Association of Geological Hazard Prevention, 55 p. (in Chinese)

Canelli, L., Ferrero, A.M., Migliazza, R. & Segalini, A. (2012). Debris flow risk mitigation by the means of rigid and flexible barriers - experimental tests and impact analysis. N*atural Hazard and Earth System Sciences*, 12, 1693-1699. doi:

10.5194/nhess-12-1693-2012.

Cui, P., Chen, X.Q., Wang, Y.Y., Hu, K.H., & Li, Y. (2005). Jiang-jia Ravine debris flows in south-western China. *In Debris-flow hazards and related phenomena*. Edited by M. Jakob and O. Hungr. Springer, Berlin. pp. 565–594.

Cui, P., Zeng, C. & Lei, Y. (2015). Experimental analysis on the impact force of viscous debris flow. *Earth Surface Processes and Landforms* 40(12): 1644-1655.

Fei, X.J. & Shu, A.P. (2004). *Movement Mechanism and Disaster Control for Debris Flow*. Tsinghua University Press, Beijing (in Chinese), 216 p.

GEO (2015). *Assessment of Landslide Debris Impact Velocity for Design of Debris-resisting Barriers (GEO TGN 44)*. Geotechnical Engineering Office, Hong Kong, 4p.

HKUST (2019). *Large-scale Debris Impact Tests on Rigid Barriers,* Final Testing Report (Phase 1 – Part B) prepared for Geotechnical Engineering Office, Hong Kong, 22 p.

Hungr, O., Morgan, G.C. & Kellerhals, R. (1984). Quantitative Analysis of Debris Torrent Hazards for Design of Remedial Measures. *Canadian Geotechnical Journal*, vol. 21, pp 663-677.

Hu, K., Wei, F. & Li., Y. (2011). Real-time measurement and preliminary analysis of debris-flow impact force at Jiangjia Ravine, China. *Earth Surface Processes and Landforms,* doi: 10.1002/esp. 2155.

Kwan, J.S.H. (2012). *Supplementary Technical Guidance on Design of Rigid Debris-resisting Barriers (GEO Report No. 270)*. Geotechnical Engineering Office, Hong Kong, 88 p.

Lam, C. & Kwan, J.S.H. (2016). *Displacement-based Assessment of Boulder Impacts on Rigid Debris-resisting Barriers - A Pilot Study (Technical Note No. TN 9/2016).* Geotechnical Engineering Office, Hong Kong, 66 p.

MLR (2006). *Specification of Geological Investigation for Debris Flow Stabilization.* DZ/T 0220-2006, National Land Resources Department, China, 32 p (in Chinese).

NILIM (2007). *Manual of Technical Standard for Designing Sabo Facilities against Debris Flow and Driftwood*. Technical Note of NILIM No. 365, Natural Institute for Land and Infrastructure Management, Ministry of Land, Infrastructure and Transport, Japan, pp 73 (in Japanese).

Proske, D., Suda, J. & Hübl, J. (2011). Debris flow impact estimation for breakers. *Georisk*, vol. 5, no. 2, June 2011, pp 143-155.

Pun, W.K. & Ho, K.K.S. (1996). *Analysis of triaxial tests on granitic saprolite performed at Public Works Central Laboratory (Discussion Note No. DN 4/1996).* Geotechnical Engineering Office, Hong Kong, 72 p.

SWCB (2005). *Manual of Soil and Water Conservation*. Soil and Water Conservation Bureau, Taiwan, 692 p (in Chinese).

Takahashi T. (2007). *Debris flow: Mechanics, Prediction and Countermeasures*. Taylor & Francis, Leiden, 448 p.

Volkwein, A., Wendeler, C. & Guasti, G. (2011). Design of flexible debris flow barriers. *Proceedings of the 5th International Conference on Debris-Flow Hazards. Mitigation, Mechanics, Prediction and Assessment*, Padua, Italy, 1093-1100.

Wong, L.A., & Lam, H.W.K. (2018). *Study of Flexural Response of Rigid Barriers Subject to Boulder Impact (Technical Note No. TN 3/2018).* Geotechnical Engineering Office, Hong Kong, 40 p.

Section 1
Appendix A

Specifications of Instrumentations for Large-scale Flume Tests Conducted in Kadoorie Centre, Hong Kong

Contents

	Page No.
Contents	36
List of Table	37

List of Table

Table No.		Page No.
A1	Details of Instruments	38

A description of the instrumentations used in this study is presented in Section 2.4. Details of the instruments adopted are summarised in Table A1 below.

Table A1 Details of Instruments

Instruments	Measurable Range	Frequency	Accuracy	Quantity and Installation Location	Key Purpose
Laser sensor	< 1 m	2 kHz	+/- 0.5%	1 sensor at lower part of the flume 1 sensor in front of the barrier wall	To capture flow depth
Basal load cell at wall base slab	< 1.1 kN	2 kHz	+/- 0.001 kN	1 load cell at the base slab of wall	To capture vertical pressure of debris flow
Load cells at wall stem	< 44 kN	2 kHz	+/- 0.045 kN	4 load cells at wall stem (covered by a steel plate)	To capture impact force of debris
High speed camera (2336 x 1728 pixel)	-	560 frames per second	-	1 camera installed at the side of flume (near deposition zone) and 1 camera installed near the top of barrier	To capture kinematics of flow-barrier interactions (e.g. debris flow velocity and flow depth).

Section 1
Appendix B

Water Content of Debris Mix for Large-scale Flume Tests Conducted in Kadoorie Centre, Hong Kong

Contents

	Page No.
Contents	40
List of Table	41
References	42

List of Table

Table No.		Page No.
B1	Classification of Debris Flows in Literature	42

A description of the soil debris mix used in this study is presented in Section 2.5. The water content of the soil debris materials and reported data of relevant literatures have been reviewed (Takahashi, 2007; Fei & Shu, 2004; Cui et al, 2005; Volkwein et al, 2011) and summarised in Table B1.

Table B1 Classification of Debris Flows in Literature

References	Flow Types	Water Content by Volume
Volkwein et al (2011)	Mud flow	40% - 64%
	Granular flow	21% - 45%
Fei & Shu (2004)	Water-stone flow	47% - 73%
	Mudflow	53% - 73%
	Dilute debris flow	50% - 73%
	Sub-viscous debris flow	41% - 50%
	Viscous debris flow	17% - 41%
Cui et al (2005)	Flood	90%
	Dilute debris flow	66%
	Sub-viscous debris flow	57%
	Viscous debris flow - low	39%
	Viscous debris flow - middle	34%
	Viscous debris flow - high	19%
Takahashi (2007)	Fluid debris flow	51% - 82%
	Quasi-viscous debris flow	40% - 51%
	Viscous debris flow	21% - 40%
	Highly viscous debris flow	< 21%

References

Cui, P., Chen, X.Q., Wang, Y.Y., Hu, K.H., & Li, Y. (2005). Jiang-jia Ravine debris flows in south-western China. *In Debris-flow hazards and related phenomena*. Edited by M. Jakob and O. Hungr. Springer, Berlin. pp. 565–594.

Fei, X.J. & Shu, A.P. (2004). *Movement Mechanism and Disaster Control for Debris Flow*. Tsinghua University Press, Beijing (in Chinese), 216 p.

Takahashi T. (2007). *Debris flow: Mechanics, Prediction and Countermeasures*. Taylor & Francis, Leiden, 448 p.

Volkwein, A., Wendeler, C. & Guasti, G. (2011). Design of flexible debris flow barriers. *Proceedings of the 5th International Conference on Debris-Flow Hazards. Mitigation, Mechanics, Prediction and Assessment*, Padua, Italy, 1093-1100.

Section 1
Appendix C

Results of Large-scale Flume Tests Conducted in Kadoorie Centre, Hong Kong

Contents

	Page No.
Contents	44
C.1 Test No. 1	45
C.2 Test No. 2	47
C.3 Test No. 3	49
C.4 Test No. 4	51
C.5 Test No. 5	53

C.1 Test No. 1

Video taken in Test No. 1

Flow Depth Time History for Test No. 1

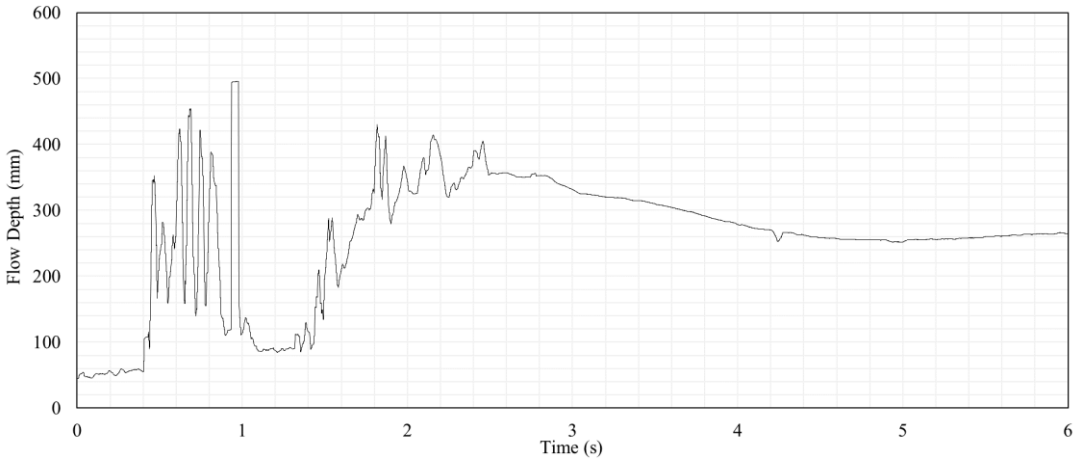

It was found that the above depth readings (from a laser sensor) fluctuate during 0.4 second to 1.1 second. It was due to the splashing of reflected wave of frontal debris flow and was not a true reflection of flow depth approaching debris. As such, during that period of time, the flow depth was assumed ranging from 50 mm to 85 mm (i.e. the measured flow depth immediately at 0.4 second and 1.1 second respectively) in the interpretation of α.

Flow Velocity Time History for Test No. 1

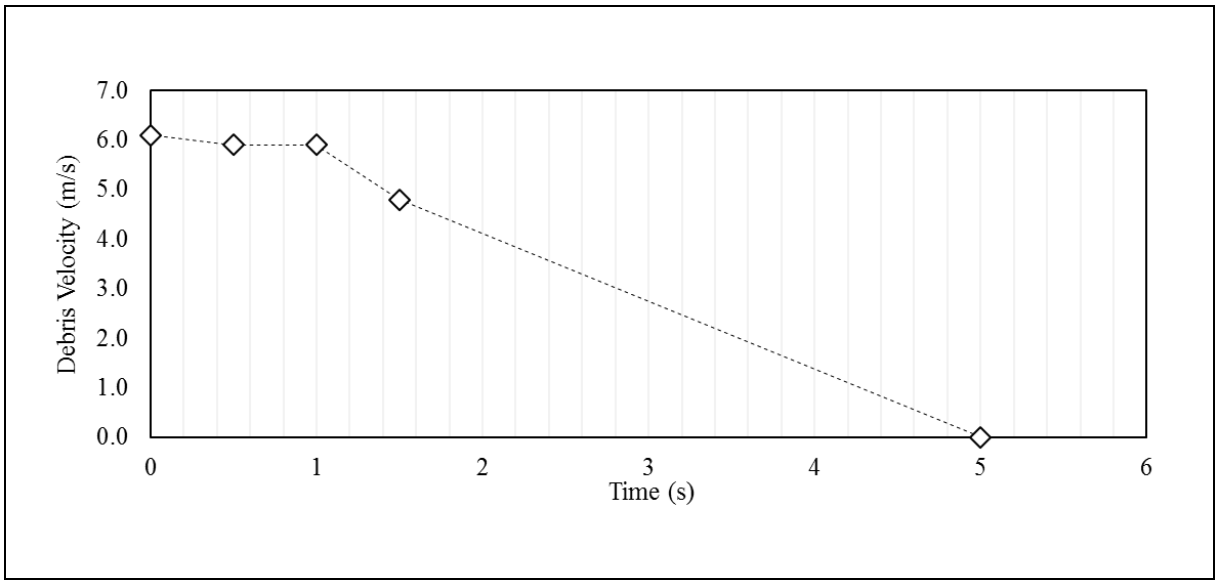

Force Time History for Test No. 1

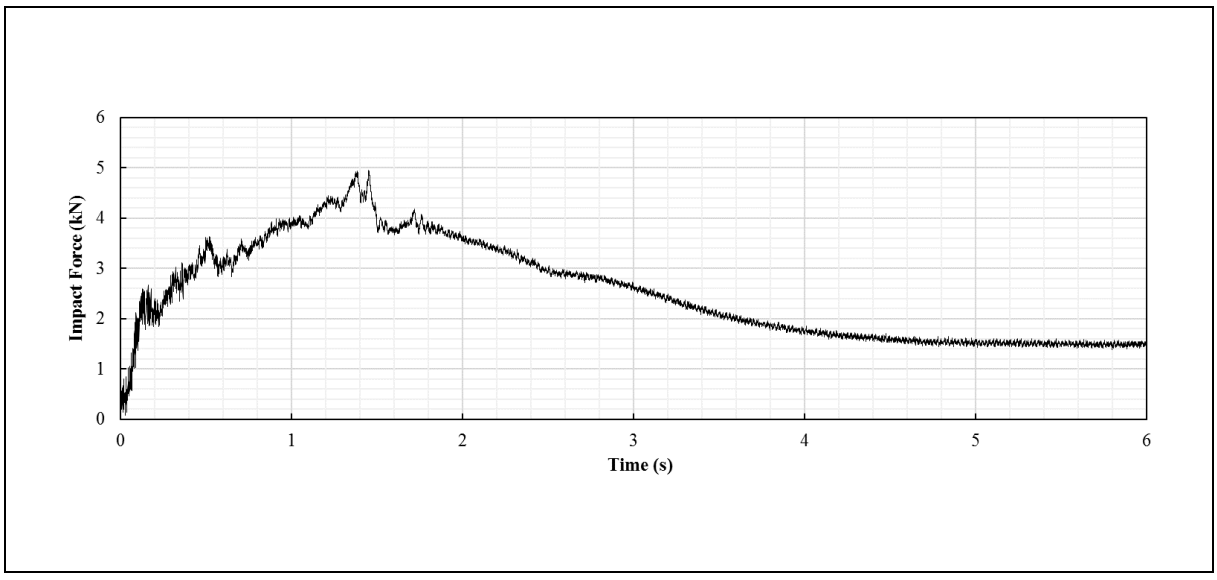

C.2 Test No. 2

Video taken in Test No. 2

Flow Depth Time History for Test No. 2

The laser sensor has shown anomalous data as a result of instrument errors during Test No. 2, and that flow depth could not be directly obtained. As such, debris flow depth was interpreted based on the footage taken by high speed camera located at the side view of the deposition zone.

Flow Velocity Time History for Test No. 2

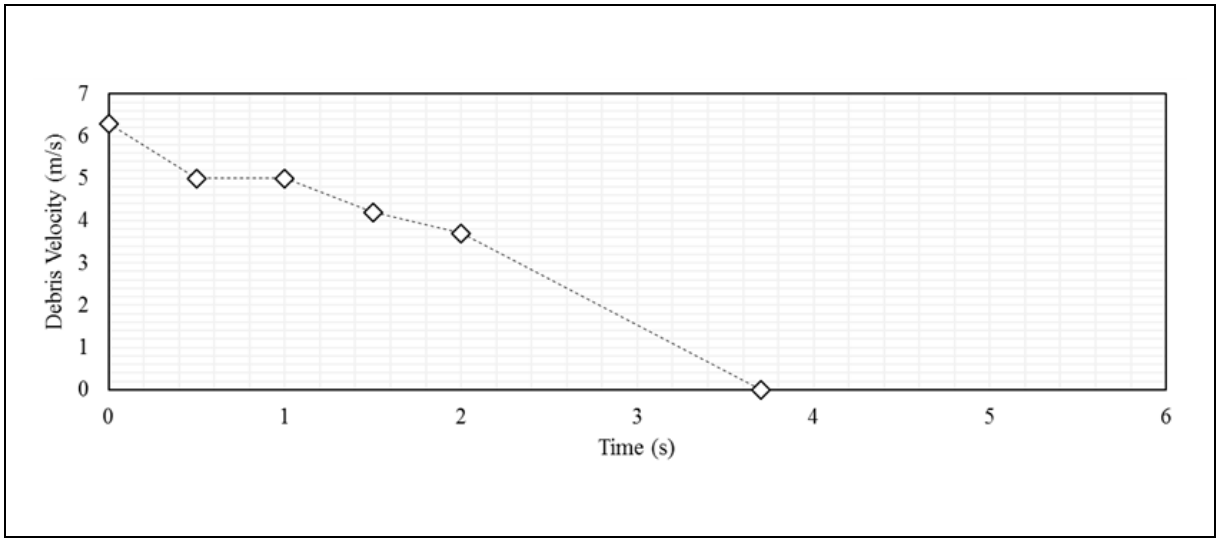

Force Time History for Test No. 2

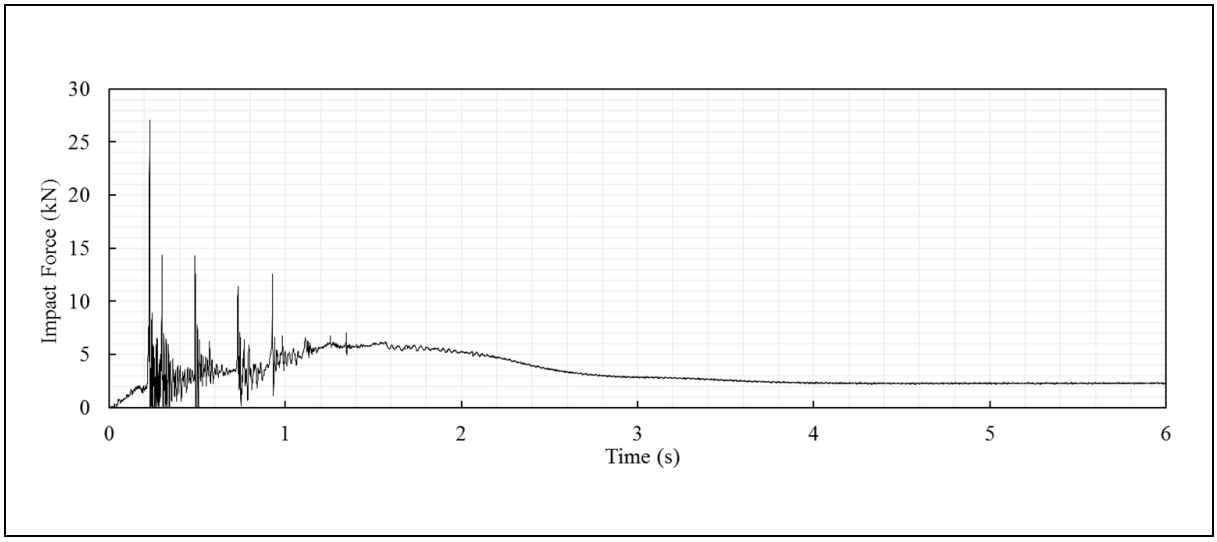

C.3 Test No. 3

Video taken in Test No. 3

Flow Depth Time History for Test No. 3

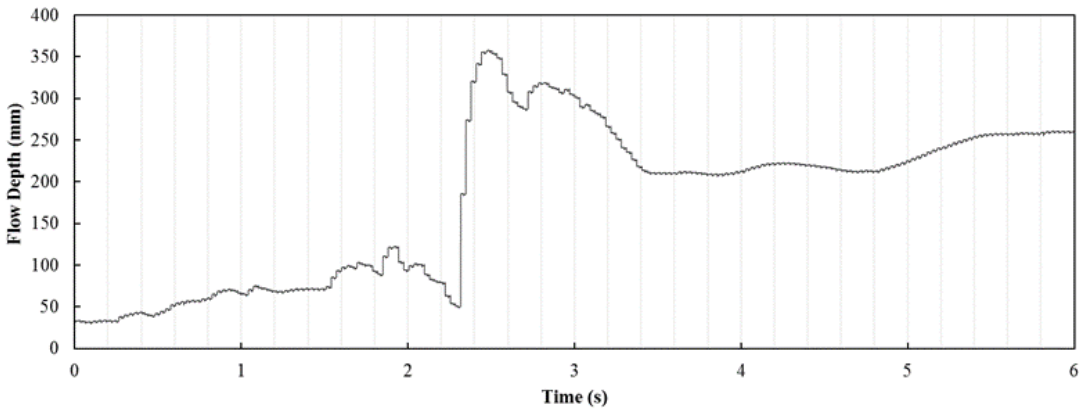

Flow Velocity Time History for Test No. 3

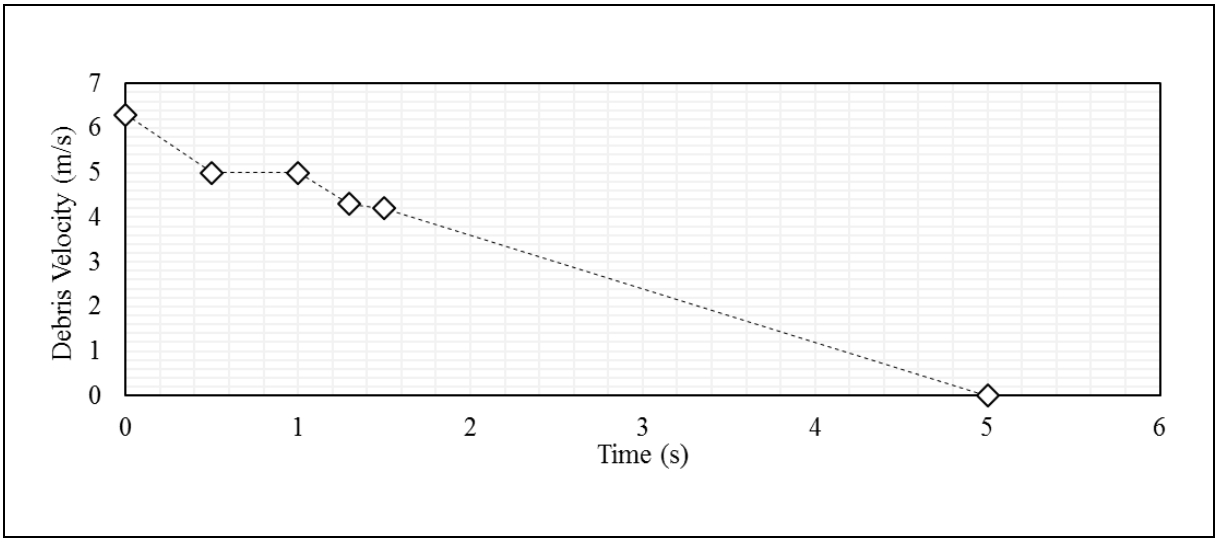

Force Time History for Test No. 3

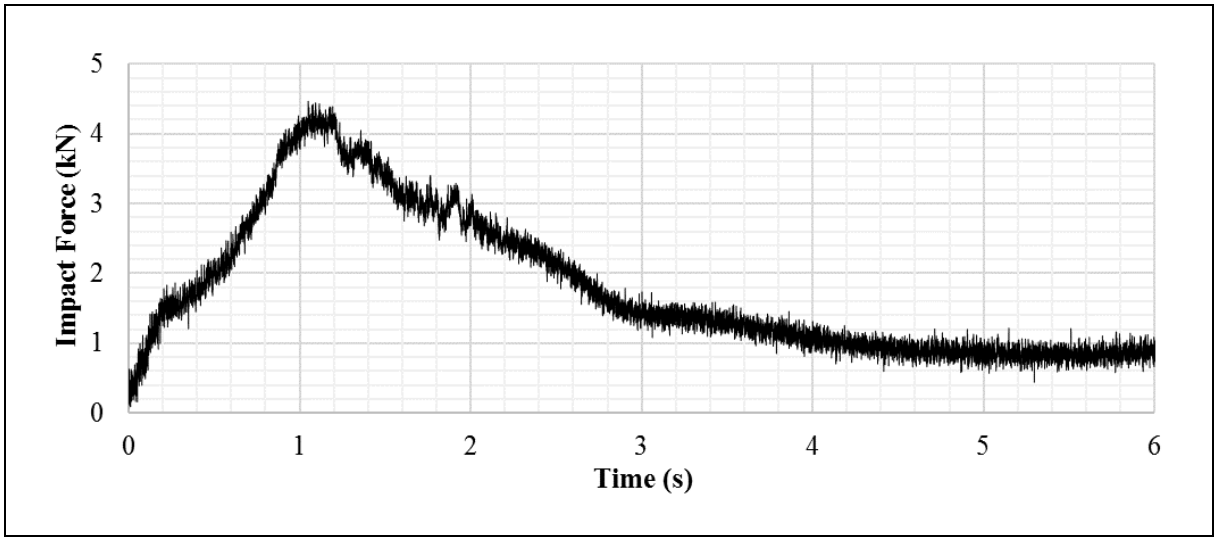

C.4 Test No. 4

Video taken in Test No. 4

Flow Depth Time History for Test No. 4

The laser sensor has shown anomalous data as a result of instrument errors during Test No. 4, and that flow depth could not be directly obtained. As such, debris flow depth was interpreted based on the footage taken by high speed camera located at the side view of the deposition zone.

Flow Velocity Time History for Test No. 4

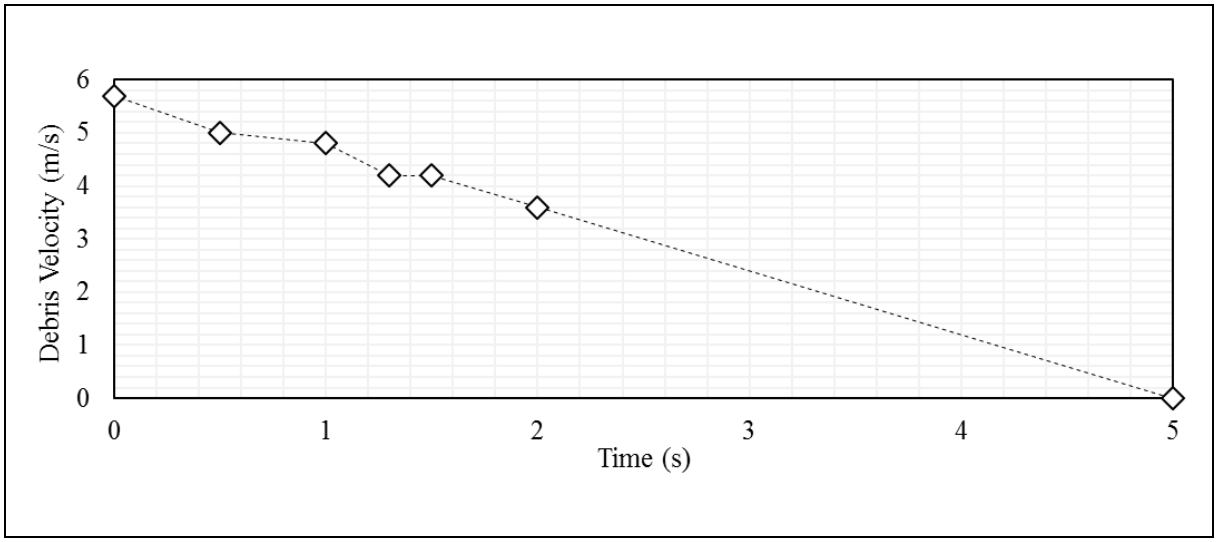

Force Time History for Test No. 4

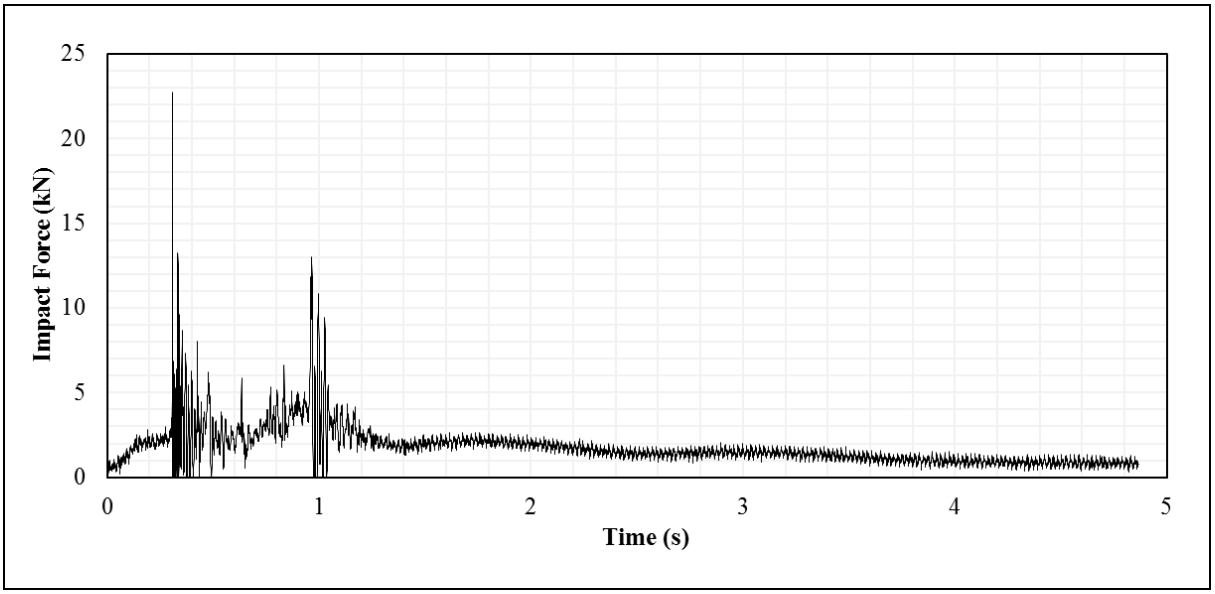

C.5 Test No. 5

Video taken in Test No. 5

Flow Depth Time History for Test No. 5

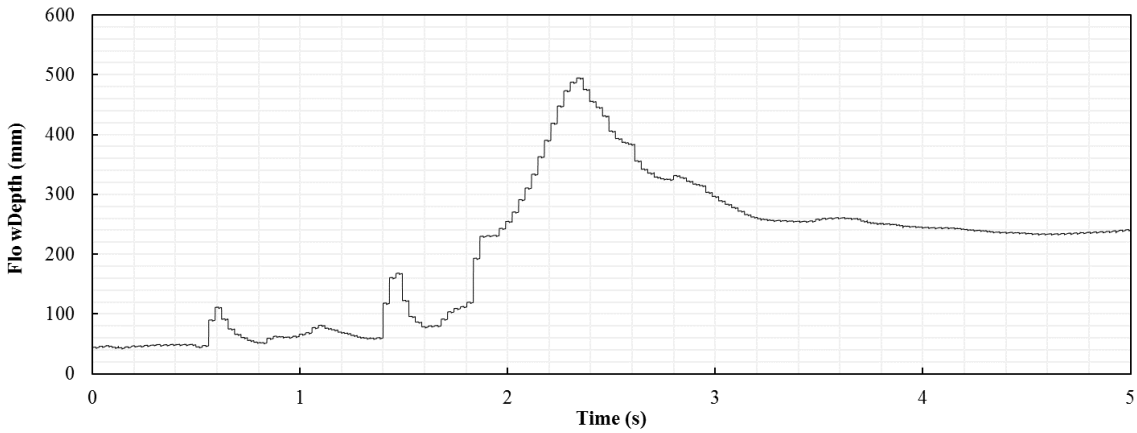

Flow Velocity Time History for Test No. 5

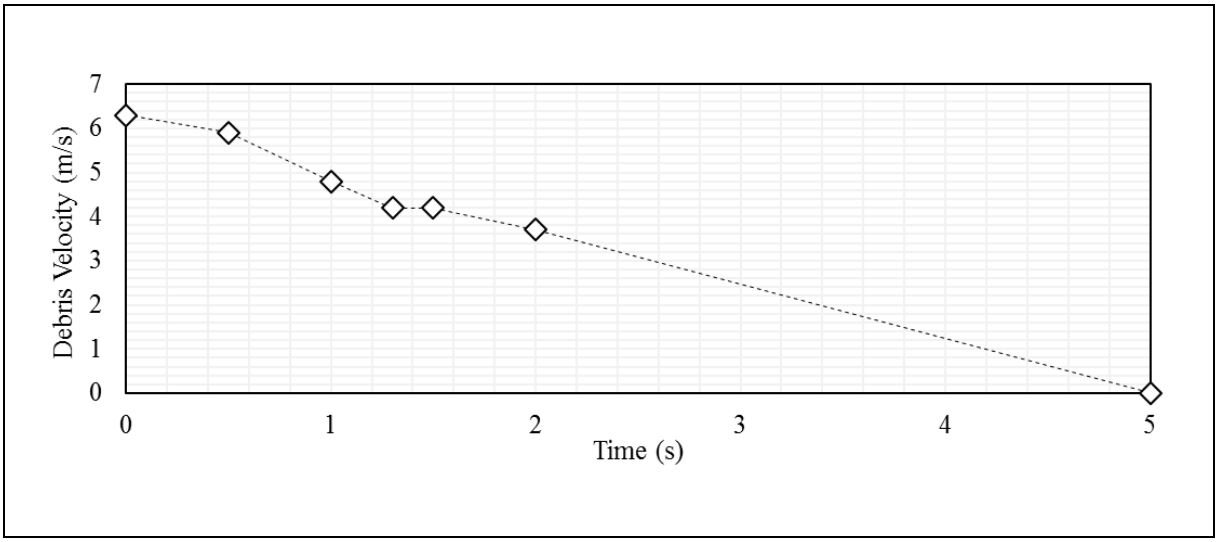

Force Time History for Test No. 5

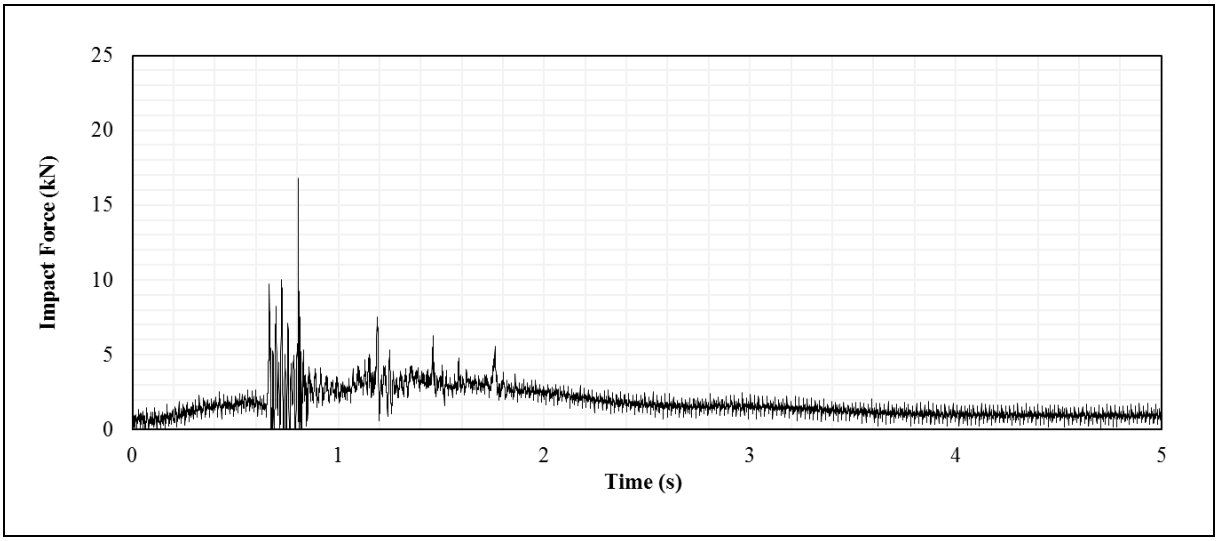

Section 1
Appendix D

Sample Interpretation of Test Results for Large-scale Flume Test Nos. 1 & 2

Contents

	Page No.
Contents	56
List of Tables	57

List of Tables

Table No.		Page No.
D1	Interpretation of Dynamic Pressure Coefficient for Test No. 1 (Without Hard Inclusions)	58
D2	Interpretation of Dynamic Pressure Coefficient for Test No. 2 (With Hard Inclusions)	58

The test results presented in Section 1 Appendix C have been used to analyse the dynamic soil debris impact pressure coefficient (α). The interpretation of α took into account the variation of flow kinematic and debris impact force at different time intervals. In the analysis, impact force, debris impact velocity and debris flow thickness under the same time interval are synchronised for data interpretation. A sample calculation for Test Nos. 1 and 2 is given below:-

Table D1 Interpretation of Dynamic Pressure Coefficient for Test No. 1 (Without Hard Inclusions)

Time	0.5 s	1.0 s	1.5 s	2.0 s
Debris Velocity (m/s)	5.9	~ 5.4	~ 5.0	~ 4.4
Debris Flow Depth (mm)	50	50 - 85	85	> 90
Soil Debris Impact Force (kN)	3.6	4.0	4.9 (Peak)	3.6
Interpreted α	0.58	0.45 - 0.76	0.66	< 0.58
Froude Number	8.3	5.9 - 8.3	5.4	4.6

Table D2 Interpretation of Dynamic Pressure Coefficient for Test No. 2 (With Hard Inclusions)

Time	0.5 s	1.0 s	1.5 s	2.0 s
Debris Velocity (m/s)	~ 5.4	~ 5.0	~ 4.6	~ 3.9
Debris Flow Depth (mm)	40 - 50	60 - 70	80 - 90	90 - 100
Soil Debris Impact Force [(1)] (kN)	3.2	5.2	6.2 (Peak)	4.8
Interpreted α	0.59 - 0.74	0.80-0.93	0.87-0.98	0.85-0.94
Froude Number	7.6 - 8.5	6.0 - 6.4	4.8 - 5.1	3.9 - 4.1

Note: [(1)] See Section 2.7.2 for the interpretation of soil debris impact force.

Section 1
Appendix E

Numerical Analysis of Debris Impact on Rigid Barrier

Contents

	Page No.
Contents	60
List of Tables	61
List of Figures	62
E.1 Background	63
E.2 Validation of LS-DYNA Model	63
E.3 Analysis of Large-scale Debris Impact Scenarios	65
E.3.1 Model Setup	65
E.3.2 Results of Simulation	66
References	67

List of Tables

Table No.		Page No.
E1	Key Parameters for Model Validation for Steel Reinforcement	64
E2	Key Parameters for Model Validation for Concrete	64
E3	Key Parameters for Model Validation for Debris Material	64
E4	Summary of Numerical Back-analysis	65
E5	Summary of Interpretation of Numerical Results	67

List of Figures

Figure No.		Page No.
E1	Printout of LS-DYNA Input Replicating the Flume Test No. 1	63
E2	Comparison of Force-time History	65
E3	Snapshot of Numerical Analysis of Debris Impact of 400 m^3	66
E4	Snapshot of Debris Impact Mechanism Simulated in Numerical Analyses	66

E.1 Background

Study of large-scale debris impact scenario has been carried out through numerical analysis based on the following steps:

(a) Validating LS-DYNA model using Flume Test No. 1 carried out in Kadoorie Centre (see Section 2.7); and

(b) Carrying out validated numerical simulations pertaining to a large-scale debris impact scenario on rigid barriers.

The details of both part (a) and (b) are discussed in this Appendix.

E.2 Validation of LS-DYNA Model

The validation has been first carried out against Flume Test No. 1 which was conducted in Kadoorie Centre as discussed in Section 2. In the validation exercise, geometry of the flume, model barrier and its location have been input in accordance with their actual values. The model barrier has been assumed as fully fixed to the ground in order to simulate the restraints given by the two concrete blocks behind. Concrete and reinforcements have been explicitly modelled and the material properties have been input in accordance with their actual values. A summary of the inputs is given in Table E1 and Table E2 below. These properties include the elastic modulus, Poisson's ratio and the dimensions of each member, the density, the uniaxial compressive strength of concrete, etc. A snapshot of the model is shown in Figure E1 below.

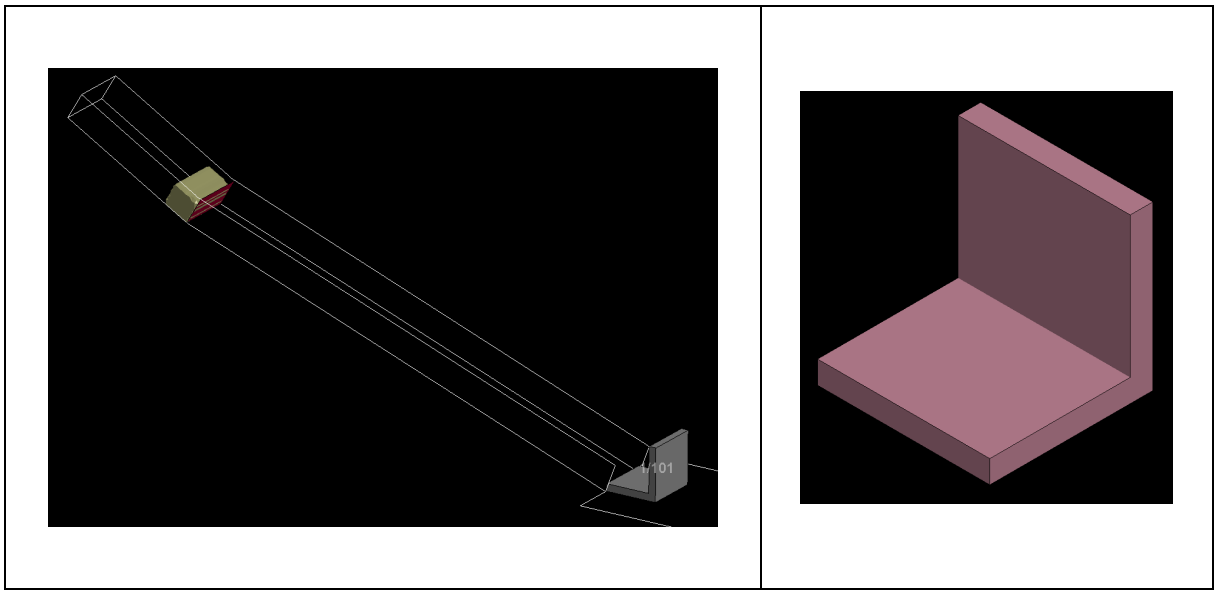

Figure E1 Printout of LS-DYNA Input Replicating the Flume Test No. 1

Table E1 Key Parameters for Model Validation for Steel Reinforcement

Part Name	Reinforcement
Constitutive Model	Plastic Kinematic
Density	7,800 kg/m^3
Young's Modulus	205 GPa
Poisson's Ratio	0.3
Yield Stress	460 MPa

Table E2 Key Parameters for Model Validation for Concrete

Part Name	Concrete
Constitutive Model	CSCM Concrete
Density	2,400 kg/m^3
Uniaxial Compressive Strength	30 MPa

In this study, debris materials have been modelled in LS-DYNA following a similar modelling technique reported in Koo (2017). Drucker-Pager yield criterion has been assumed to simulate the internal rheology of the landslide debris. Arbitrary Lagrangian-Eulerian technique has been used in the numerical simulations. The key parameters of model debris include Coulomb type basal friction angle, internal friction angle and turbulence coefficient. In the validation exercise, these parameters have been back-analysed such that frontal debris thickness, debris velocity and debris impact force obtained from LS-DYNA simulation and Kadoorie flume tests are similar. The following set of parameters have been obtained in the back-analysis:-

Table E3 Key Parameters for Model Validation for Debris Material

Debris Source Volume	~ 4 m^3
Internal Friction Angle	12°
Basal Friction Angle	10°

The above calibrated set of input parameters for soil debris was in line with the back-analysed values from several notable landslide events in Hong Kong (Koo, 2017). The outputs of numerical back-analysis, including impact force-time history, frontal debris thickness and debris velocity, have been examined. These data are then compared with the flume test results, which are shown in Table E4 and Figure E2.

Table E4 Summary of Numerical Back-analysis

	Flume Test No. 1	LS-DYNA
Debris Thickness (frontal)	50 mm	50 mm
Debris Velocity (frontal)	6.1 m/s	6.1 m/s
Peak Debris Impact Force	4.95 kN	4.95 kN

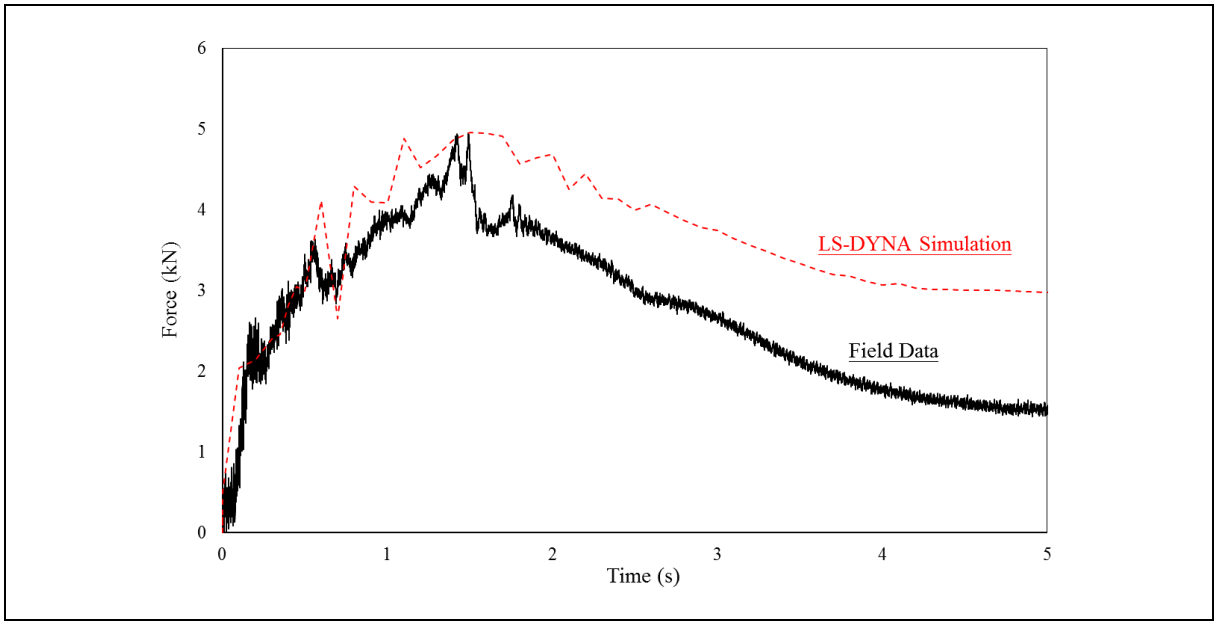

Figure E2 Comparison of Force-time History

E.3 Analysis of Large-scale Debris Impact Scenarios

E.3.1 Model Setup

Based on Section E.2 above, the ability to simulate debris-barrier interaction using LS-DYNA has been demonstrated. LS-DYNA is adopted in the next step of investigation. In this analysis, the same modelling parameters for model barrier and debris materials have been adopted. The numerical model has been scaled up with a larger rigid barrier and a greater debris source volume. A debris source volume of approx. 400 m^3 has been simulated along a 10 m wide flow channel. A reinforced concrete barrier of 10 m wide, 5 m high and 1 m thick has been simulated (see Figure E3 below).

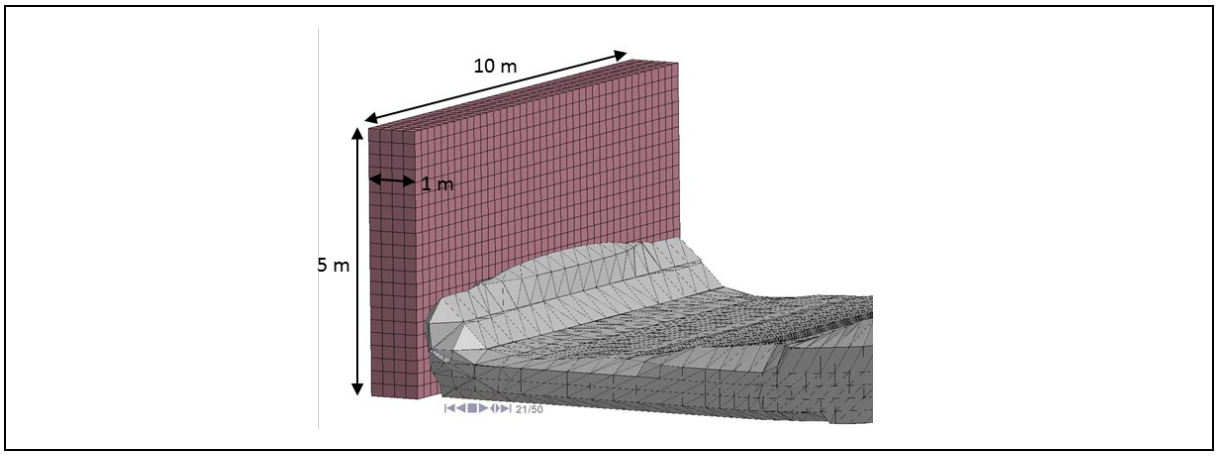

Figure E3 Snapshot of Numerical Analysis of Debris Impact of 400 m^3

E.3.2 Results of Simulation

Debris impact mechanism has been captured from the LS-DYNA simulation. A similar interaction mechanism as described in Section 2.7.1 has been observed.

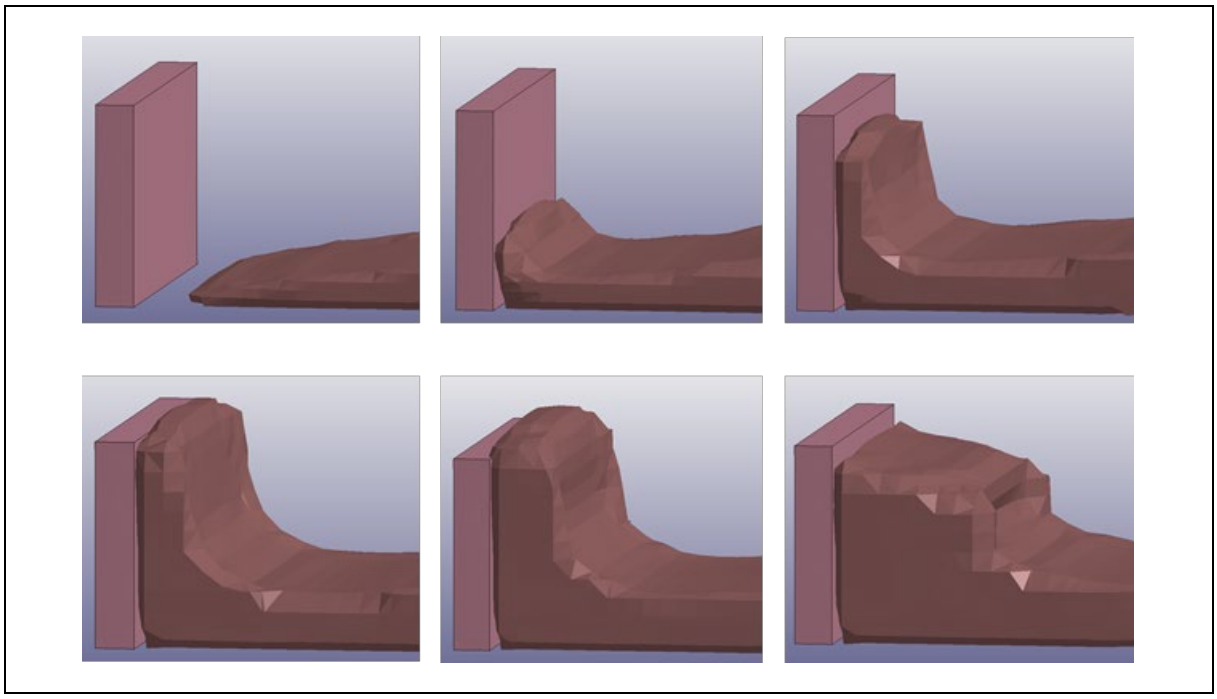

Figure E4 Snapshot of Debris Impact Mechanism Simulated in Numerical Analyses

The numerical results have been analysed using the same methodology adopted in Section 1 Appendix D. The interpreted dynamic pressure coefficient (α) is summarised in Table E5 below.

Table E5 Summary of Interpretation of Numerical Results

Time	0.5 s	1.0 s	1.5 s	2.0 s
Debris Velocity (m/s)	10.0	8.3	7	6.6
Debris Flow Depth (m)	1.25	1.5	1.5	1.5
Force (kN)	1090	1450 (Peak)	1280	1130
Interpreted α	0.48	0.78	0.97	0.96

References

Koo (2017). *3D Debris Mobility Assessment using LS-DYNA (GEO Report No. 325).* Geotechnical Engineering Office, Hong Kong, 90 p.

Section 1
Appendix F

Various Studies on Debris Impact Load

Contents

	Page No.
Contents	69
References	72

Studies of various scales have been carried out in different parts of the world to investigate debris impact mechanism. Key features of these studies are summarised in this Appendix.

Flume Test by Geobrugg at Veltheim, Switzerland (Bugnion et al, 2012)

Flume: 40 m x 8 m, 30°
Debris source volume: 50 m^3
Debris impact load was measured based on two small load cells (with an area of 120 x 120 mm and 200 x 200 mm respectively) installed at the flume.

Field Measurement by Institute of Mountain Hazards and Environment, Mainland (Hu et al, 2011)

Year of Debris Flow: 2004
Debris impact loads were based on measurement from three small load cells (150 mm dia.) installed at a 1.8 m high cantilever steel post placed at the JiangJia Ravine, Yunnan, Mainland.

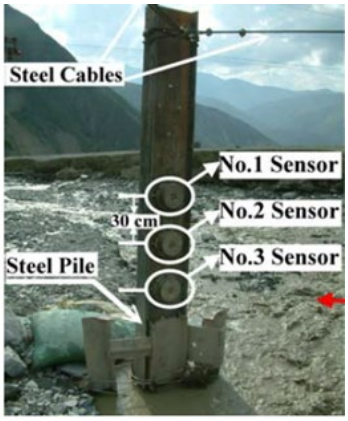

Flume Test by University of Parma, Italy (Canelli et al, 2012)

Flume: 4 m x 0.4 m, 30º
Debris source volume: 0.4 m^3
Debris impact loads were measured based on four small load cells installed at an approx. 400 mm high steel plate at the end of the flume.

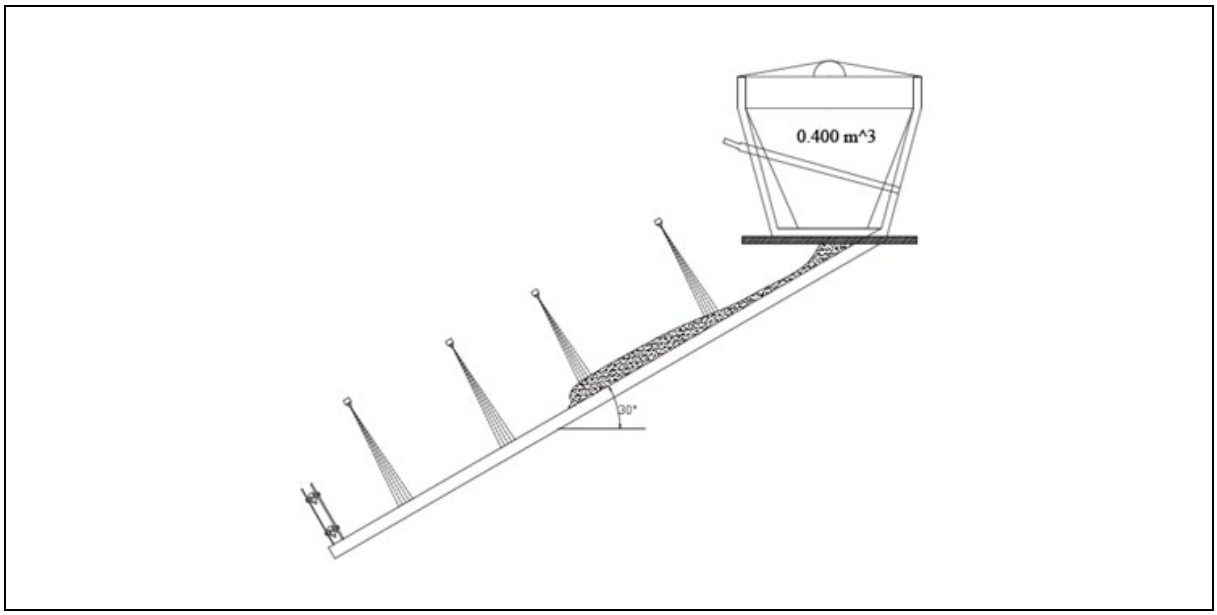

Flume Test by Institute of Mountain Hazards and Environment, Mainland (Cui et al, 2015)

Flume: 3 m x 0.4 m, 10º to 15º
Debris source volume: 0.3 m^3
Debris impact loads were measured based on five small load cells (20 mm dia.) installed at a 180 mm high cantilever steel post placed at the centre of the outlet of the flume.

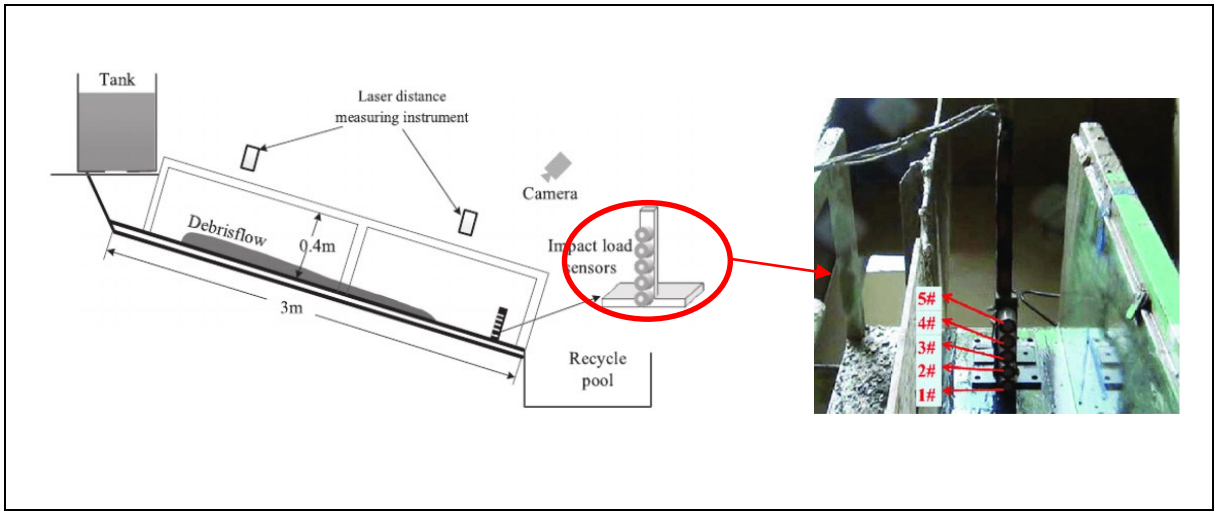

Flume Test by United States Geological Survey at Oregon, USA (Iverson et al, 2010)

Flume: 95 m x 2 m, 31°
Debris source volume: 10 m^3
Debris impact tests were carried out in 1996. A flimsy wooden board was used to receive strike from a debris flow. No measurement of debris impact load or displacement of the structure was taken.

References

Hu, K., Wei, F. & Li., Y. (2011). Real-time Measurement and Preliminary Analysis of Debris-flow Impact Force at Jiangjia Ravine, China. *Earth Surface Processes and Landforms,* doi: 10.1002/esp. 2155.

Bugnion, L., McArdell, B.W., Bartelt, P. & Wendeler, C. (2012). Measurements of hillslope debris flow impact pressure on obstacles. *Landslides* 9(2): 179-187.

Canelli, L., Ferrero, A.M., Migliazza, R. & Segalini, A. (2012). Debris flow risk mitigation by the means of rigid and flexible barriers - experimental tests and impact analysis. N*atural Hazard and Earth System Sciences*, 12, 1693-1699. doi: 10.5194/nhess-12-1693-2012.

Cui, P., Zeng, C. & Lei, Y. (2015). Experimental analysis on the impact force of viscous debris flow. *Earth Surface Processes and Landforms* 40(12): 1644-1655.

Iverson R.M., Logan, M., LaHusen, R.G. & Berti, M. (2010). The perfect debris flow? Aggregated results from 28 large-scale experiments. *Journal of Geophysical Research: Earth Surface* 115, F03005.

Section 1
Appendix G

Sample Calculation for the Review of Multiple-surge Load Model

Contents

	Page No.
Contents	74
List of Table	75
List of Figure	76

List of Table

Table No.		Page No.
G1	Sample Calculation for Design Impact Force for Test No. 1	78

List of Figure

Figure No.		Page No.
G1	Multiple-surge Load Model following Recommendation by Kwan (2012)	77

As discussed in Section 5, a review of the multiple-surge load model has been conducted. The following assumptions have been made in this review:-

(a) Debris flow is assumed to impact surge-by-surge (see Figure G1);

(b) Load from debris is considered as a combination of:-

(i) Dynamic soil debris impact load (using Equation 1.1);

(ii) Lateral earth pressure from deposited debris (earth pressure coefficient of unity);

(iii) Water pressure from deposited debris; &

(iv) Surcharge of dynamic debris surge;

(c) Partial load factor of dynamic soil debris impact load of unity;

(d) Debris impact velocity for each surge of debris based on velocity hydrograph (obtained from flume tests or numerical analysis) with an upper bound of 70% of the maximum debris velocity; &

(e) Debris flow thickness for each surge of debris taken as the frontal thickness.

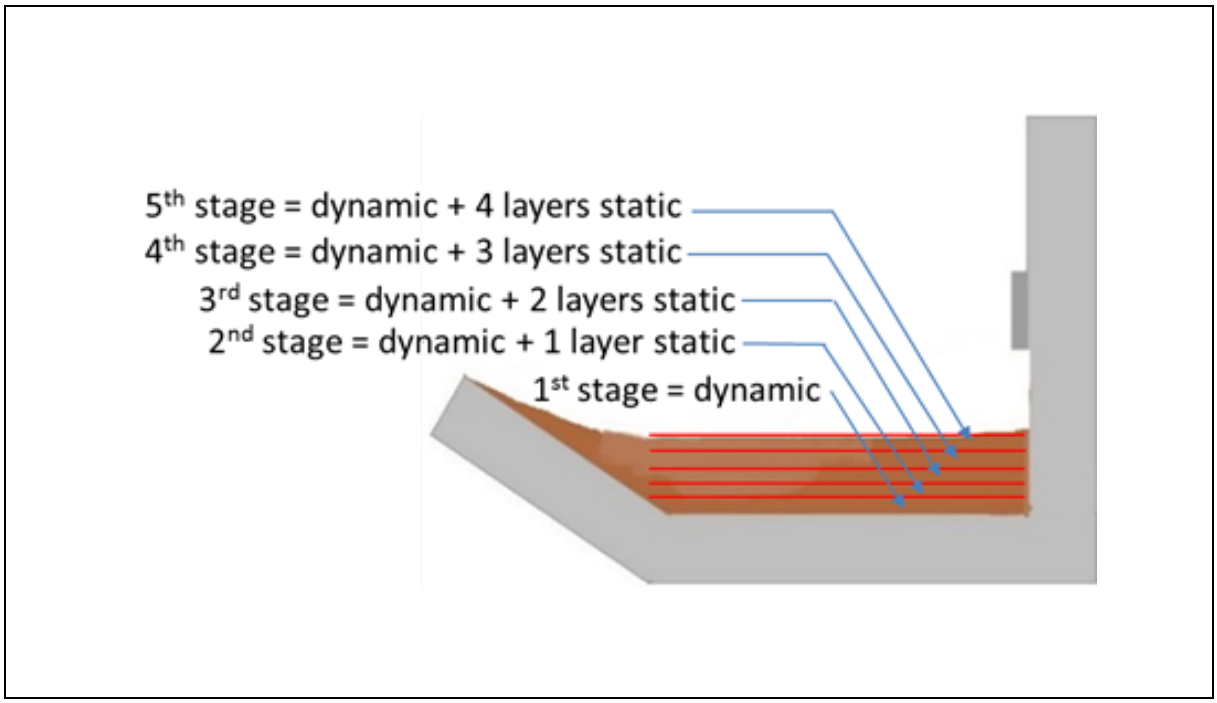

Figure G1 Multiple-surge Load Model following Recommendation by Kwan (2012)

The assumptions above reflect the current design practice. Yet, the dynamic soil debris pressure coefficient (α) is assumed as 1.5 in this review. A sample calculation for design impact force for Test No. 1 conducted in Kadoorie Centre is given in Table G1 below:-

Table G1 Sample Calculation for Design Impact Force for Test No. 1

	Design Debris Velocity (m/s)	Debris Flow Depth (mm)	Deposited Debris Thickness (mm)	Predicted Dynamic Soil Debris Impact Force (kN)	Static Force (kN)	Total Design Impact Force (kN)	Measured Peak Force in Test No. 1 (kN)
Stage 1 (Frontal)	6.1	50	0	9.8	0.0	9.8	4.9
Stage 2 (0.5 s)	5.9	50	50	9.5	0.1	9.6	
Stage 3 (1.0 s)	5.9	50	100	9.5	0.4	9.9	
Stage 4 (1.5 s)	4.8	50	150	6.3	0.7	7.0	
Stage 5 (2.0 s)	4.3	50	200	5.0	1.1	6.1	

Part 1B

Geotechnical Stability: Displacement Approach for Geotechnical Stability Assessment of Boulder Impact

[Blank Page]

Section 2: Displacement-based Assessment of Boulder Impacts on Rigid Debris-resisting Barriers - A Pilot Study

C. Lam & J.S.H. Kwan

This section is largely based on GEO Technical Note No. TN 9/2016 produced in October 2016

Foreword

This Technical Note presents a new approach for assessing the dynamic effect of boulder impacts on rigid debris-resisting barriers. The study was inspired by the work of Dr Nelson Lam of The University of Melbourne on dynamic impact analyses. Dr Carlos Lam of the S&T Division, under the supervision of Dr Julian S.H. Kwan, followed the principles of the dynamic impact analyses and derived formulae for assessing the effect of boulder impacts on rigid barriers. Dr Nelson Lam provided valuable technical support to and insightful comments on the study. Professor Oldrich Hungr of The University of British Columbia commented on the draft version of this Note. The Drafting Unit of the Standards and Testing Division assisted in preparing the figures and formatting this Note. All contributions are gratefully acknowledged.

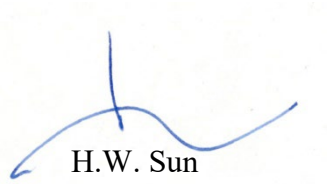

H.W. Sun
Chief Geotechnical Engineer/Standards and Testing
October 2016

Abstract

This Technical Note presents a new approach for assessing the dynamic effect of boulder impacts on rigid debris-resisting barriers. The approach adopts energy and momentum conservation principles with consideration given to the mass inertia effect of barriers to calculate displacements of barriers caused by boulder impacts. Both translational and rotational barrier movement are considered. Key assumptions of the new approach are stated. Parametric studies have been carried out using the new approach to assess the effect of simultaneous impacts by multiple boulders on barrier movement. Results show that the relationship between the mass of a barrier and its movement is highly nonlinear as a result of the inertia effect.

Contents

		Page No.
Title Page		81
Foreword		82
Abstract		83
Contents		84
List of Table		86
List of Figures		87
1	Introduction	88
2	Nature of Boulder Impact Load	88
3	Effects of Mass Inertia and Energy Loss on Energy Transfer	90
3.1	Theory	90
3.2	Effect of COR and Mass Ratio on Energy Transfer	91
4	Translational Movement	92
4.1	Theory	92
4.2	Effect of Simultaneous Impacts by Multiple Boulders	93
5	Rotational Movement	95
5.1	Theory	95
5.2	Effect of Simultaneous Impacts by Multiple Boulders	97
6	Further Analyses	99
6.1	Boulder Diameter for Pre-determined Barrier Movement	99
6.2	Effect of Successive Boulder Impacts	100
7	Discussion	101
8	Conclusions	102
9	References	102
Section 2 Appendix A:	Illustration of Effects of Inertia and Energy Loss	104

		Page No.
Section 2 Appendix B:	Translational Movement	111
Section 2 Appendix C:	Rotational Movement	118
Section 2 Appendix D:	Derivation of Miscellaneous Equations	132
Glossary of Symbols		143

List of Table

Table No.		Page No.
3.1	Summary of Energy-transfer Equations for Different Types of Collisions	90

List of Figures

Figure No.		Page No.
2.1	Measured Debris Impact Pressure on a Rigid Obstacle in Jiangjia Ravine, China (Hu et al, 2006)	89
2.2	Prototype Impact Load on a Rigid Barrier Model in a Centrifuge Test	89
3.1	Schematic Illustrations of Elastic, Partially Elastic and Inelastic Collisions	90
3.2	Effect of COR and Mass Ratio on Energy Transfer	92
4.1	Translational Movement of an L-shaped Rigid Barrier on Flat Ground	93
4.2	Effect of Simultaneous Impacts by Multiple Boulders on Translational Movement	94
5.1	Rotational Movement of an L-shaped Rigid Barrier	95
5.2	Rotational Movement of an L-shaped Rigid Barrier with Side Walls	96
5.3	Effect of Simultaneous Impacts by Multiple Boulders on Rotational Movement	98
6.1	Diameters of a Single Boulder Causing 5-mm Translational Barrier Movement	100
6.2	Cumulative Translational Movement of an L-shaped Rigid Barrier under Successive Boulder Impacts	101

1 Introduction

Rigid debris-resisting barriers are commonly adopted as mitigation measures of debris flow hazard. In the prevailing design practice, the geotechnical stability of rigid debris-resisting barriers is assessed based on limit equilibrium analyses (Kwan, 2012). The use of pseudo-static force in the limit equilibrium analyses may not correctly reflect the effect of transient load, in particular, momentary loading which lasts for some milliseconds e.g. boulder impact load.

Displacement-based assessment approaches, which have been widely adopted for the stability analyses of slopes and gravity retaining walls under seismic loading, could provide a potential means for evaluating the performance of rigid debris-resisting barriers subject to boulder impact. For example, Newmark (1965) developed the "sliding block" concept to evaluate seismic slope stability in terms of earthquake-induced slope displacement, as opposed to a factor of safety against yield under peak ground accelerations.

This Technical Note (TN) documents a pilot study of displacement-based assessment approach for boulder impacting on rigid debris-resisting barriers. The study followed the principles of dynamic analyses proposed by Dr Nelson Lam of the University of Melbourne (Yang et al, 2012; Ali et al, 2014; Lam, 2015). This TN will first present theories behind Dr Lam's dynamic analyses, which are pertinent to the effects of mass inertia and energy loss on energy transfer between two impact objects. It is then followed by parametric studies using displacement-based calculations to assess the effect of boulder impact load on rigid barriers with a focus on simultaneous impacts by a number of boulders on barriers. Assumptions and detailed formulation are presented.

2 Nature of Boulder Impact Load

Hu et al (2006) reported field measurement data of debris-flow impact load on a steel baffle installed in a natural drainage line in Jiangjia Ravine, China. The measurement was made using load cells. Figure 2.1 shows a typical time trace of the measured impact pressure. The load cell recorded a rather constant impact pressure with local spikes. The magnitude of the spikes was up to five times the constant pressure. Based on site observation, Hu et al (2006) commented that the spikes could be induced by large boulder impacts. Cui (2015) provided supplementary information to clarify that the diameters of the boulders can be up to 0.5 m in Jiangjia Ravine.

More recently, HKUST has carried out a centrifuge test to study the impact load of dry sand flow with hard inclusions on a model rigid barrier. In the prototype scale, the hard inclusions in the sand flow correspond to boulders of 0.9 m diameter. Figure 2.2 shows the preliminary result of the centrifuge test. There are several spikes in the measured load. According to the image records from the high-speed camera, the spikes were results of impacts by the hard inclusions.

As shown in Figures 2.1 and 2.2, boulder impact duration is short and the associated dynamic load is transient. For evaluating the performance of impact-resisting structures, displacements may therefore offer a more rational criterion than factors of safety calculated based on force and moment equilibrium analyses.

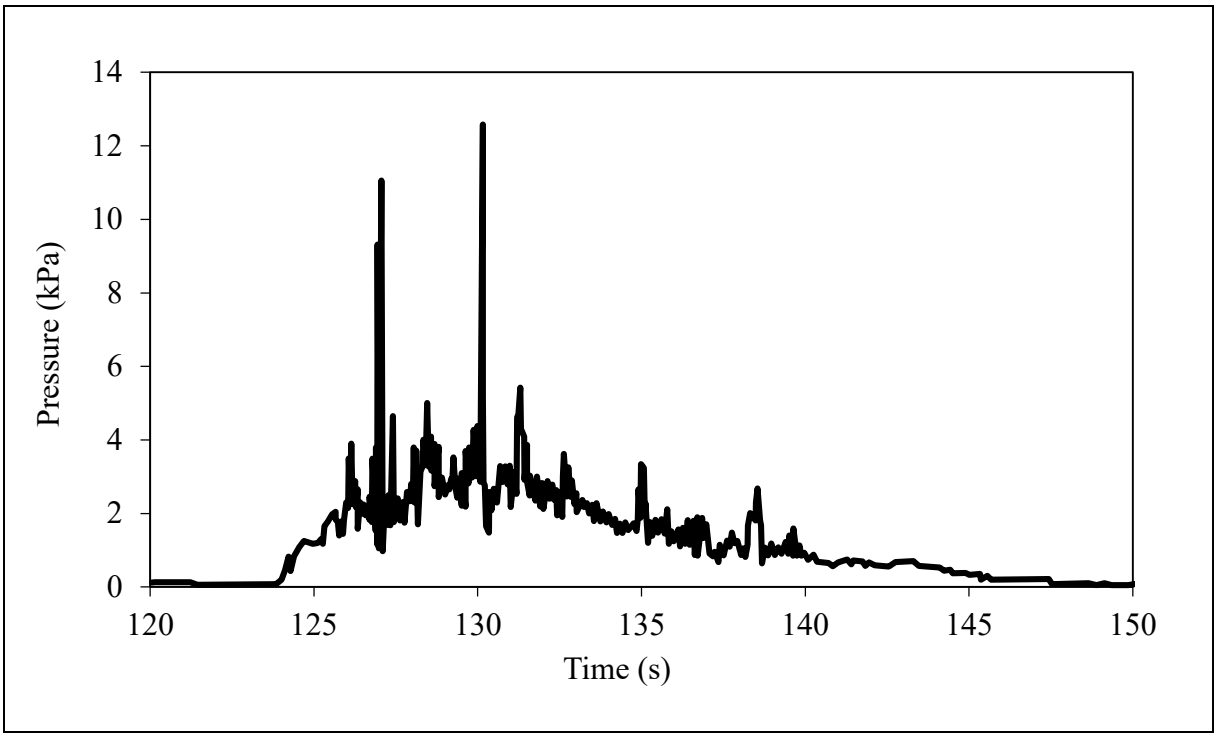

Figure 2.1 Measured Debris Impact Pressure on a Rigid Obstacle in Jiangjia Ravine, China (Hu et al, 2006)

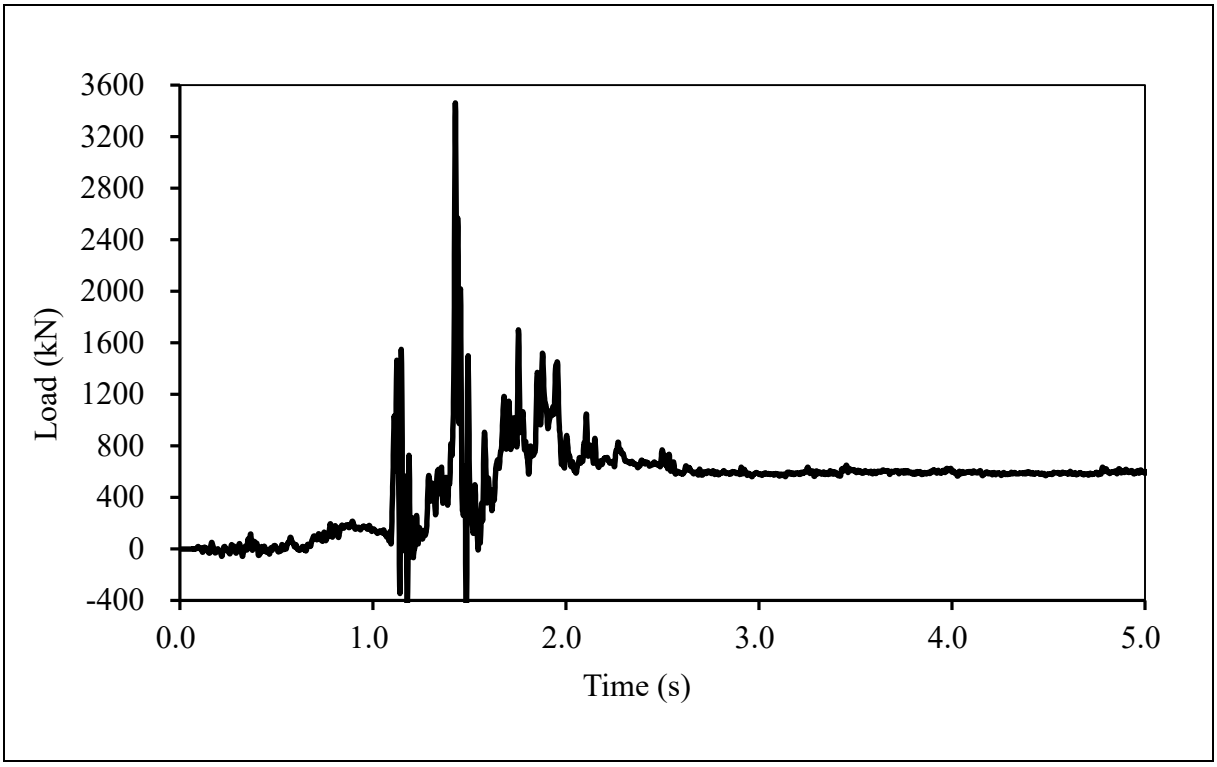

Figure 2.2 Prototype Impact Load on a Rigid Barrier Model in a Centrifuge Test

3 Effects of Mass Inertia and Energy Loss on Energy Transfer

3.1 Theory

During collision, momentum and kinetic energy transfer from one object to another. Figure 3.1 schematically illustrates three collision types, namely, elastic, inelastic, and partially inelastic. To illustrate the effects of mass inertia and energy loss on the amount of energy transferred from an impactor to an impact-resisting object, mathematical derivations of energy-transfer equations based on consideration of momentum and energy conservation have been performed. The derivations of the equations are given in Section 2 Appendix A. Table 3.1 summarises the energy-transfer equations for the three different types of collisions.

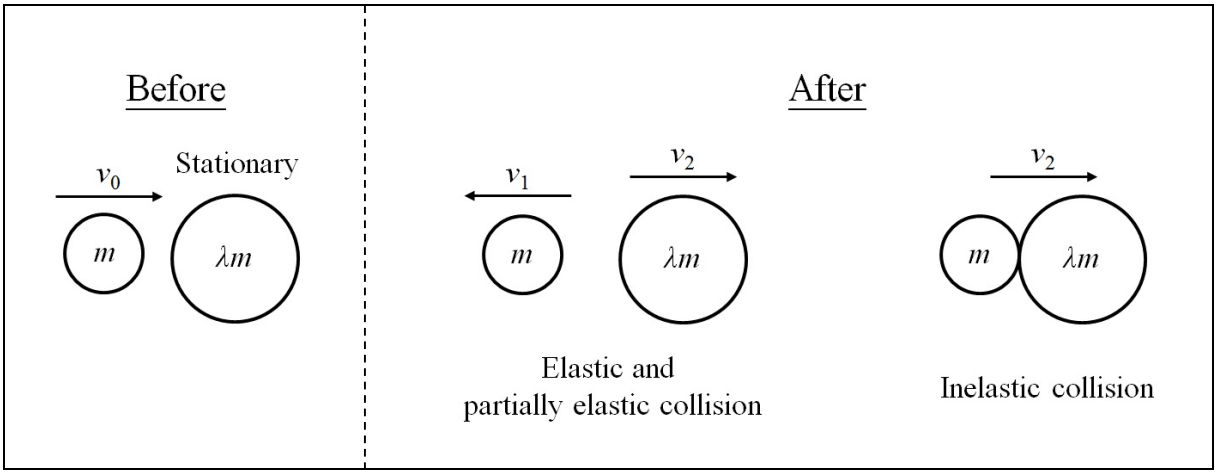

Figure 3.1 Schematic Illustrations of Elastic, Partially Elastic and Inelastic Collisions

Table 3.1 Summary of Energy-transfer Equations for Different Types of Collisions

Inelastic (COR = 0)	Elastic (COR = 1)	Partially Inelastic (0 < COR < 1)
$\frac{KE_2}{KE_0} = \frac{1}{(1+\lambda)}$	$\frac{KE_2}{KE_0} = \frac{4\lambda}{(1+\lambda)^2}$	$\frac{KE_2}{KE_0} = \lambda\left(\frac{1+COR}{1+\lambda}\right)^2$

The parameters used in the above equations are defined as follows:

where COR = coefficient of restitution, defined as the ratio of relative speeds after and before an impact (dimensionless);
KE_0 = initial kinetic energy of the impactor (in J);
KE_2 = kinetic energy gained by the impact-resisting object (in J);
λ = mass ratio between the impact-resisting object and the impactor (dimensionless, ≥ 1).

The coefficient of restitution (COR) is a global measure for kinetic energy loss during impact. The loss can be due to plastic deformation, visco-elastic material behaviour and wave propagation in the bodies (Seifried et al, 2010). This parameter is elaborated further as follows:

(a) When COR = 0, kinetic energy is not conserved and the collision is termed "inelastic". The two objects coalesce and travel together after the collision.

(b) When COR = 1, kinetic energy is conserved and the collision is termed "elastic". The objects rebound from each other with the same relative speed but in opposite directions.

(c) When $0 < \text{COR} < 1$, this is the most common form of collision in the real world. The objects do not coalesce and some kinetic energy is converted to other forms of energy such as heat, sound and work done deforming the objects. Kinetic energy is not conserved.

The value of COR is a property of a pair of objects in a collision and is function of the impact velocity (e.g. Perera et al, 2016; Ali et al, 2014). According to Wyllie (2015), Masuya et al (2001) conducted experiments to determine the value of COR between concrete and a single boulder. The tests involved dropping a boulder from a known initial height (h_i) onto a horizontal concrete slab and then measuring the rebound height (h_r). Using the relationship between potential and kinetic energy, the value of COR was calculated using the expression $\sqrt{h_r / h_i}$ and was found to be 0.18 for the chosen test conditions. Giani (1992) and Chau et al (1998) reported COR values in the normal direction of 0.5 for falling rocks impacting on bedrock surfaces.

3.2 Effect of COR and Mass Ratio on Energy Transfer

To illustrate the effects of COR and mass ratio on the kinetic energy gained by an impact-resisting object (e.g. a rigid barrier) in a collision, Figure 3.2 plots the energy ratio KE_2 / KE_0 against the mass ratio, λ, for COR ranging from 0.2 to 1.0 using the energy-transfer equation derived for the partially inelastic case (Table 3.1). Note that the value of λ must not be smaller than unity, and in this parametric study it varies from 1 to 1,000. The results are presented on a log-log plot to show the wide range of mass and energy ratios.

Two observations can be made from Figure 3.2. First, for a given COR, the energy ratio KE_2 / KE_0 decreases with increasing mass ratio, λ. This means that the heavier the impact-resisting object, the less kinetic energy it will gain from a collision and this is true regardless of the value of the COR. Second, the energy ratio decreases with COR. This is because the lower the COR is in a collision, the more kinetic energy is lost through conversion to other forms of energy.

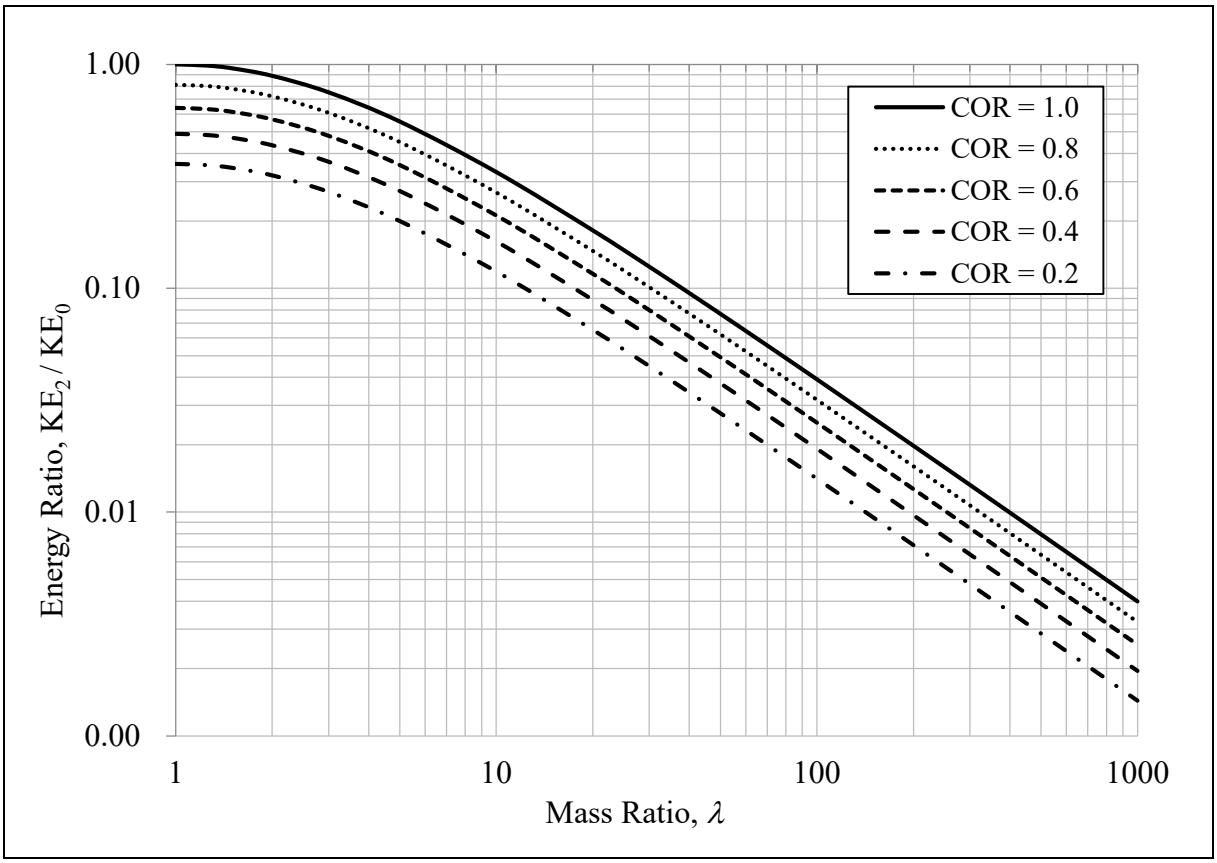

Figure 3.2 Effect of COR and Mass Ratio on Energy Transfer

4 Translational Movement

4.1 Theory

If a free-standing rigid barrier on flat ground is impacted by a boulder and is assumed to undergo pure translational movement as illustrated in Figure 4.1, the amount of movement can be calculated using the following equation:

$$\Delta = \frac{KE_2}{(Mg - uA)\tan\delta'} \quad \text{..... (4.1)}$$

where Δ = translational movement of barrier (in m)
KE_2 = kinetic energy gained by the rigid barrier (in J)
M = mass of barrier (in kg)
g = gravity (9.81 m/s^2)
u = water uplift pressure acting on barrier (in N/m^2)
A = contact area between barrier base and ground surface (in m^2)
δ' = effective interface friction angle between concrete and soil (in degrees).

Derivation of Equation 4.1, which is based on consideration of energy conservation, is given in Section 2 Appendix B. Worked examples of using Equation 4.1 for calculating barrier's translational movement are also given in Section 2 Appendix B.

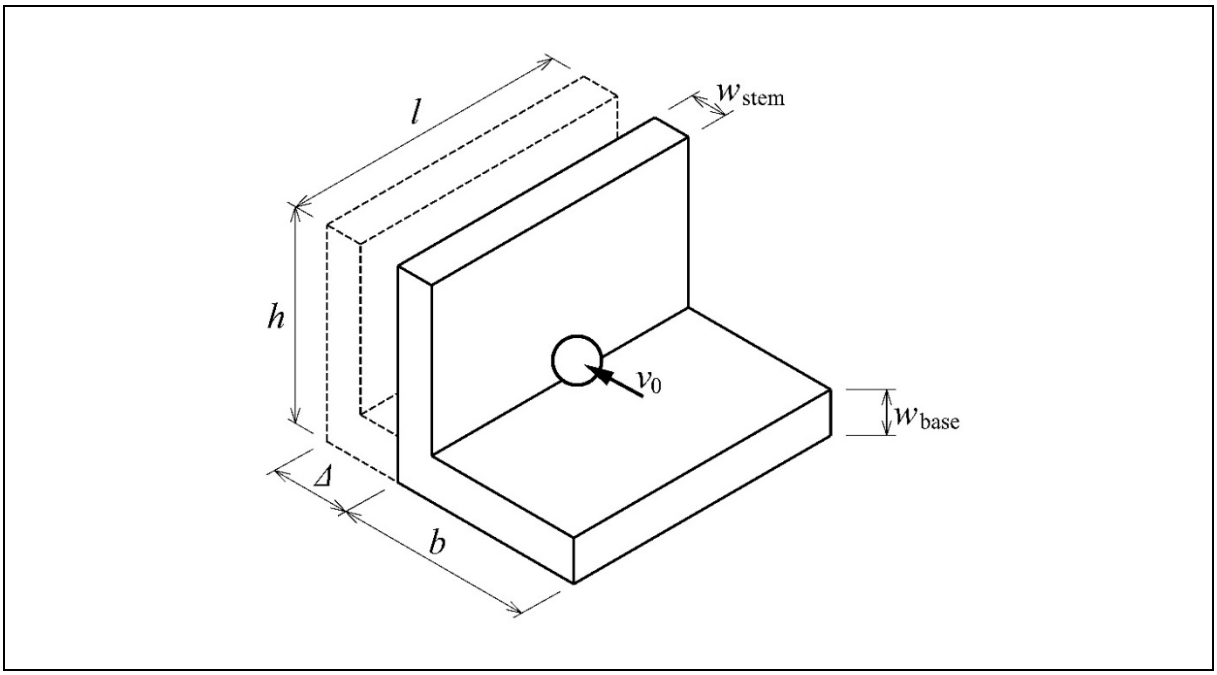

Figure 4.1 Translational Movement of an L-shaped Rigid Barrier on Flat Ground

4.2 Effect of Simultaneous Impacts by Multiple Boulders

To assess the effect of simultaneous impacts by multiple boulders on the translational movement of a rigid barrier, a parametric study has been carried out to calculate the amount of translational movement for a range of barrier sizes and impact scenarios. The barrier considered has an "L" shape as shown in Figure 4.1. For the parametric study, the wall (h) and the base slab (b) have the same dimension varying from 5 m to 10 m. The length (l) is 10 m. The width of the stem wall (w_{stem}) and the base slab (w_{base}) are both 0.8 m. If a reinforced concrete density (ρ_c) of 2,500 kg/m^3 is assumed, the barrier's mass considered thus ranges from about 185 × 10^3 kg to 385 × 10^3 kg. This range covers the weights of typical barriers in Hong Kong. Other assumptions and parameters adopted for this parametric study are:

(a) the barrier is assumed to be impacted by one, two and four boulders;

(b) the pore water pressure (u) at the base slab is assumed zero;

(c) boulder velocity (v_0) = 10 m/s;

(d) boulders diameter (ϕ) = 1.2 m;

(e) boulder density (ρ_b) = 2,650 kg/m^3;

(f) COR= 0.5; and

(g) concrete-soil interface friction angle (δ') = 34°.

The results of the parametric study are presented on a semi-log scale in Figure 4.2. Two observations can be made from this plot. First, as expected, for a given barrier mass, increasing the number of boulders leads to an increase in barrier movement. However, the amount of increase is not proportional to the number of boulders. For example, for a barrier mass of 300×10^3 kg, the amount of movement is merely 1 mm due to a single-boulder impact. However, if the same barrier is simultaneously impacted by four boulders, the movement is predicted to increase to 16 mm. This large difference is due to the nonlinear relationship between the energy-transfer ratio, KE_2 / KE_0, and the mass ratio, λ, as shown in Figure 3.2 - increasing the mass of the impactor(s) will lead to a lower mass ratio (λ) and thus a higher energy-transfer ratio (KE_2 / KE_0). Second, for a given boulder impact scenario, it can be seen that increasing the mass of a barrier would lead to a significant reduction in its movement. This is again due to the nonlinear relationship between KE_2 / KE_0 and λ.

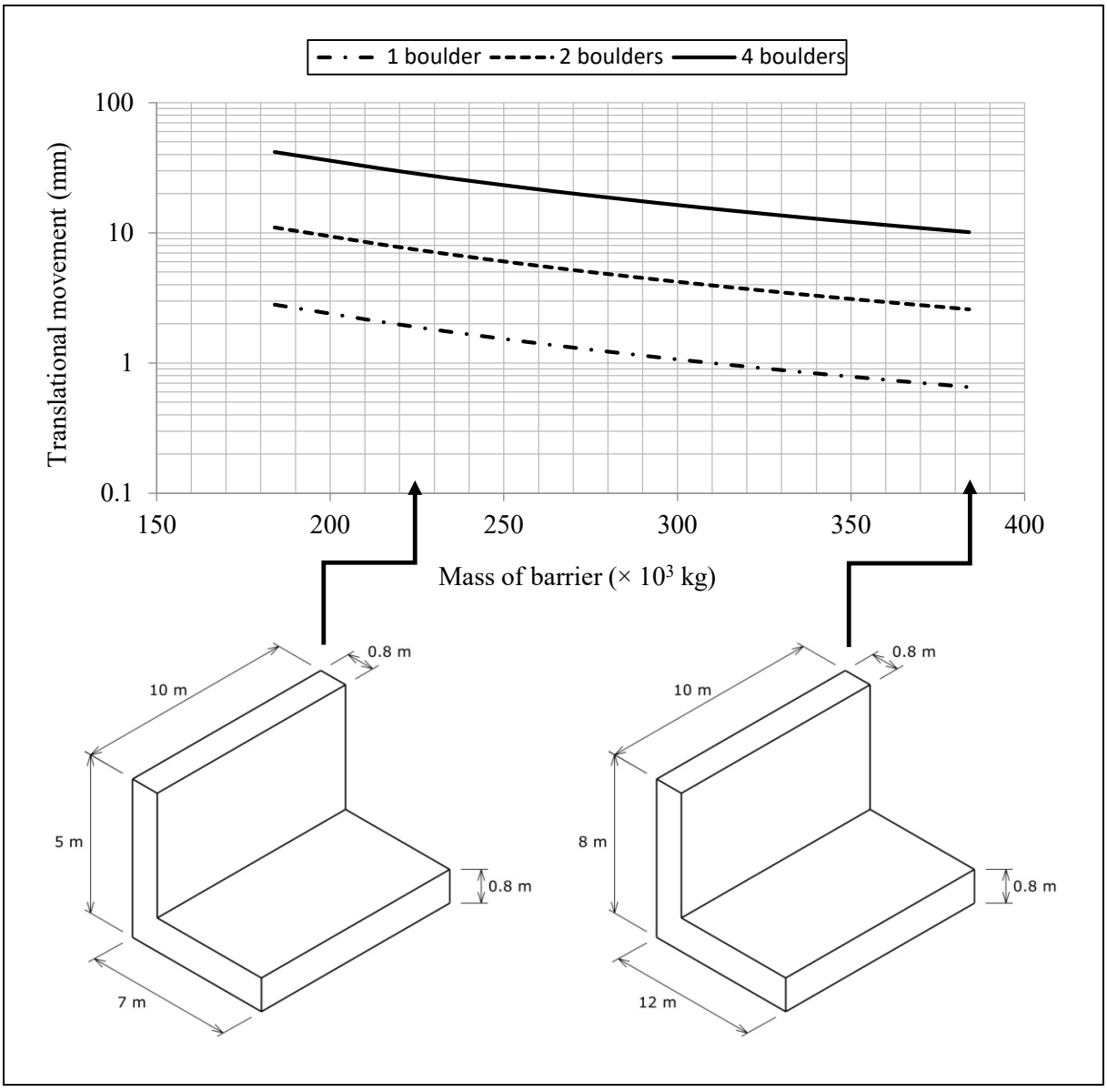

Figure 4.2 Effect of Simultaneous Impacts by Multiple Boulders on Translational Movement

5 Rotational Movement

5.1 Theory

If a free-standing rigid barrier on flat ground is impacted by a boulder at the crest and is assumed to undergo a rotational movement as illustrated in Figure 5.1, the amount of movement, which is expressed in terms of the rise of the centre of gravity, can be calculated using the following equation:

$$\Delta_{\text{C.G.}} = \frac{mv_0^2}{2Mg} \times \frac{\kappa h}{r}\left(\frac{1+\text{COR}}{1+\kappa}\right)^2 \quad \text{..... (5.1)}$$

where h = height of barrier (in m)
m = mass of boulder (in kg)
M = mass of barrier (in kg)
r = distance between the axis of rotation and the point of impact (in m)
v_0 = velocity of boulder (in m/s)
$\Delta_{\text{C.G.}}$ = rise of the barrier's centre of gravity (in m)
$\kappa = \frac{I_\theta}{mhr}$ (dimensionless; ≥ 1)
COR = coefficient of restitution (dimensionless).

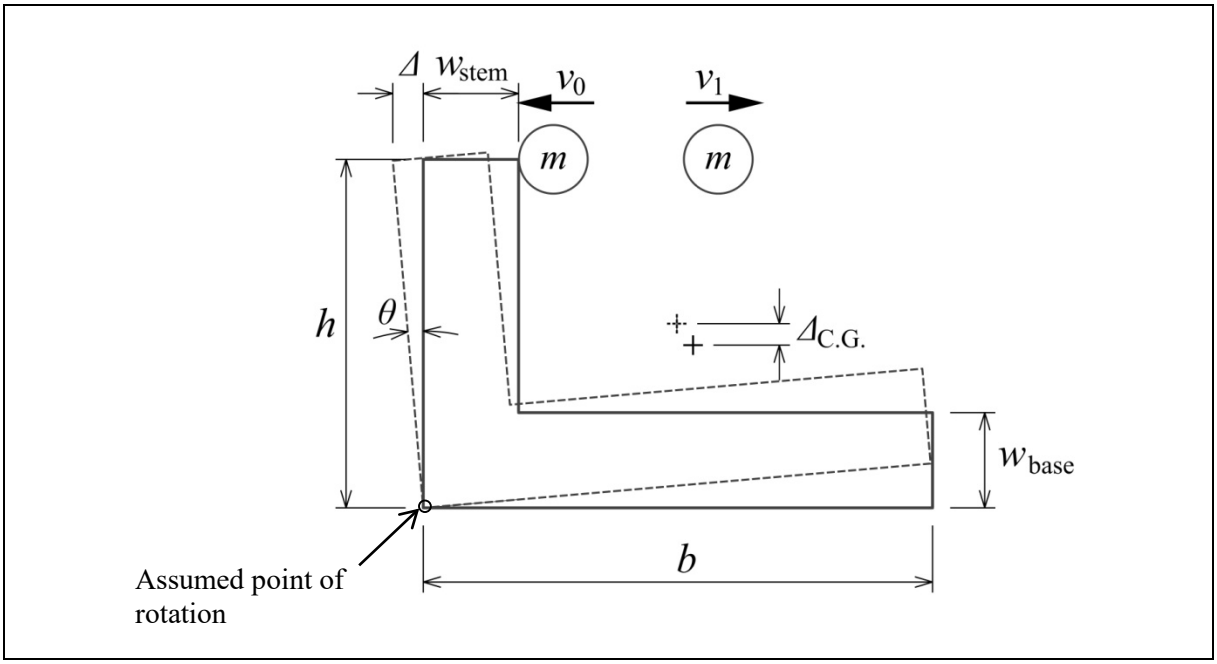

Figure 5.1 Rotational Movement of an L-shaped Rigid Barrier

Derivation of Equation 5.1 can be found in Section 2 Appendix C. Note that the value of κ must not be smaller than unity. For the calculation of the dimensionless number, κ, knowledge of the barrier's mass moment of inertia, I_θ, is required. For L-shaped barriers, I_θ can be calculated using the following approximate relationship:

$$I_\theta \approx \frac{M_{\text{stem}}}{3}\left(h^2 + hw_{\text{base}}\right) + \frac{M_{\text{base}}}{3}b^2 \quad \text{..... (5.2)}$$

where I_θ = mass moment of inertia of barrier (in kg m^2)
b = length of base slab (in m)
h = height of barrier (in m)
M_{stem} = mass of stem wall (in kg)
M_{base} = mass of base slab (in kg).

For an L-shaped barrier with rectangular side walls as illustrated in Figure 5.2, the contribution of the side walls to the barrier's overall mass moment of inertia also needs to be considered. The equation for I_θ thus becomes:

$$I_\theta \approx \frac{M_{\text{stem}}}{3}\left(h^2 + hw_{\text{base}}\right) + \frac{M_{\text{base}}}{3}b^2 + nM_{\text{side}}\left[\left(\frac{c^2+d^2}{12}\right) + \left(\frac{d}{2} + w_{\text{base}}\right)^2 + \left(\frac{c}{2} + w_{\text{stem}}\right)^2\right] \text{..... (5.3)}$$

where c = length of side wall (in m)
d = height of side wall (in m)
M_{side} = mass of a single side wall (in kg)
n = number of side walls (typ. 2).

The computed $\Delta_{\text{C.G.}}$ can be converted to the angle of rotation θ using the following equation:

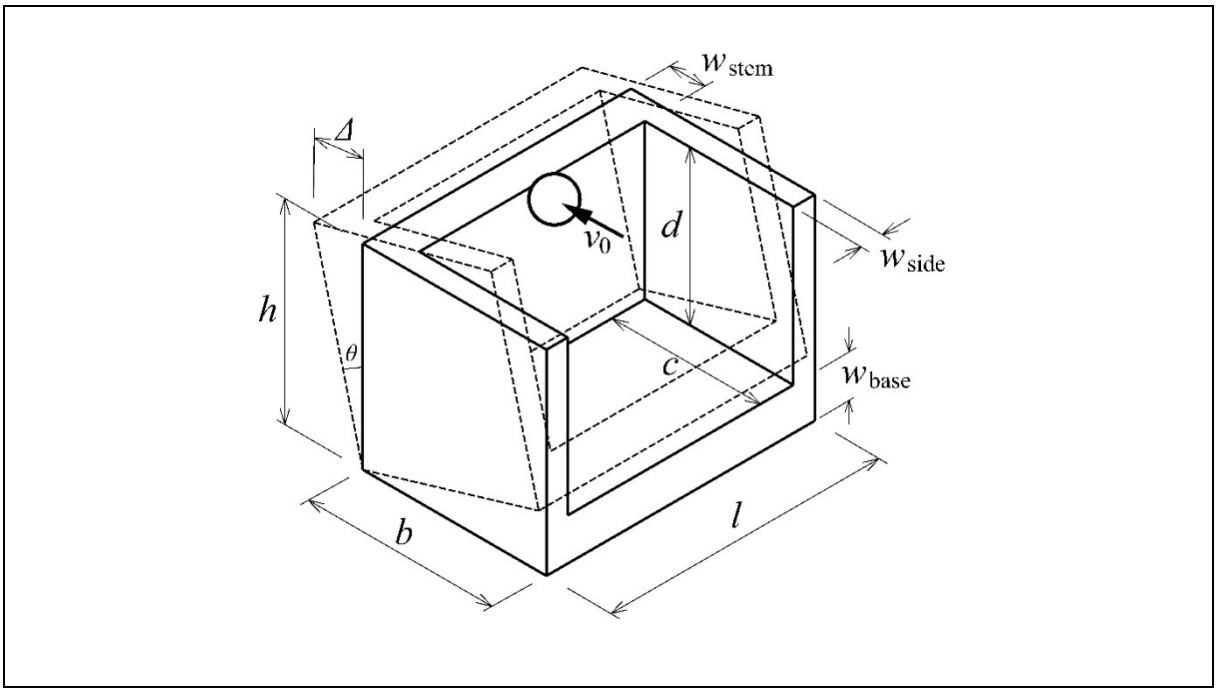

Figure 5.2 Rotational Movement of an L-shaped Rigid Barrier with Side Walls

$$\theta = \sin^{-1}\left[\frac{\bar{y} + \Delta_{\text{C.G.}}}{\sqrt{\bar{x}^2 + \bar{y}^2}}\right] - \tan^{-1}\left(\frac{\bar{y}}{\bar{x}}\right) \quad \text{..... (5.4)}$$

where $\bar{x}$ = horizontal distance to the barrier's centre of gravity from global vertical axis (in m)

$\bar{y}$ = vertical distance to the barrier's centre of gravity from global horizontal axis (in m).

It should be noted that Equation 5.4 is derived based on the assumption that the barrier does not overturn. The stability of the barrier against overturning can be assessed by comparing the computed $\Delta_{\text{C.G.}}$ with the critical value $\Delta_{\text{C.G.(crit)}}$. If $\Delta < \Delta_{\text{C.G.(crit)}}$, the barrier will not overturn. The value of $\Delta_{\text{C.G.(crit)}}$ can be computed as:

$$\Delta_{\text{C.G.(crit)}} = \sqrt{\bar{x}^2 + \bar{y}^2} - \bar{y} \quad \text{..... (5.5)}$$

The critical angle of rotation can be expressed as:

$$\theta_{\text{crit}} = 90° - \tan^{-1}\left(\frac{\bar{y}}{\bar{x}}\right) \quad \text{..... (5.6)}$$

Equations 5.5 and 5.6 were derived by considering the various geometrical relationships when the barrier's centre of gravity lies immediately above the point of rotation, i.e., the critical condition in terms of overturning stability.

Derivations of Equations 5.2 to 5.6 are given in Section 2 Appendix D.

Worked examples using Equations 5.1 to 5.6 are given in Section 2 Appendix C.

5.2 Effect of Simultaneous Impacts by Multiple Boulders

To assess the effect of simultaneous impacts by multiple boulders on the rotational movement of a barrier, a parametric study has been carried out to calculate the amount of movement for a range of barrier sizes and different impact scenarios. The barrier considered has an "L" shape as shown in Figure 4.1. As for the parametric study discussed in Section 3.2, the wall (h) and the base slab (b) have the same dimension varying from 3 m to 8 m. The length (l) is 10 m. The width of the stem wall (w_{stem}) and the base slab (w_{base}) are both 0.8 m. If a reinforced concrete density (ρ_c) of 2,500 kg/m^3 is assumed, the mass of the barrier thus ranges from around 185×10^3 to 385×10^3 kg. This range covers the weights of typical barriers in Hong Kong. Other assumptions and parameters adopted for this parametric study are:

(a) the barrier is assumed to be impacted by one, two and four boulders;

(b) boulder velocity (v_0) = 10 m/s;

(c) boulders diameter (ϕ) = 1.2 m;

(d) boulder density (ρ_b) = 2,650 kg/m^3; and

(e) COR= 0.5.

Figure 5.3 presents the result of the parametric study in terms of the barrier's angle of rotation. Since the stem wall and base slab are assumed to have the same dimension ($h = b$) in this study, the critical angle of rotation (θ_{crit}) is 45° for all cases and this is plotted as a horizontal line in the figure. The results show that increasing the number of boulders will have a considerable effect on the angle of rotation, although none of the cases considered will lead to the barrier overturning since the calculated θ values are always less than θ_{crit}. For example, for the barrier having a mass of 200 × 10^3 kg, the barrier will rotate less than 0.2° when impacted by a single boulder. This same barrier will however rotate 2° if simultaneously impacted by four boulders. This difference can be attributed to the reduced effect of mass inertia in the second case. In addition, the result shows that increasing the mass of the barrier will be an effective means to reducing the angle of rotation especially when the mass of the barrier is small.

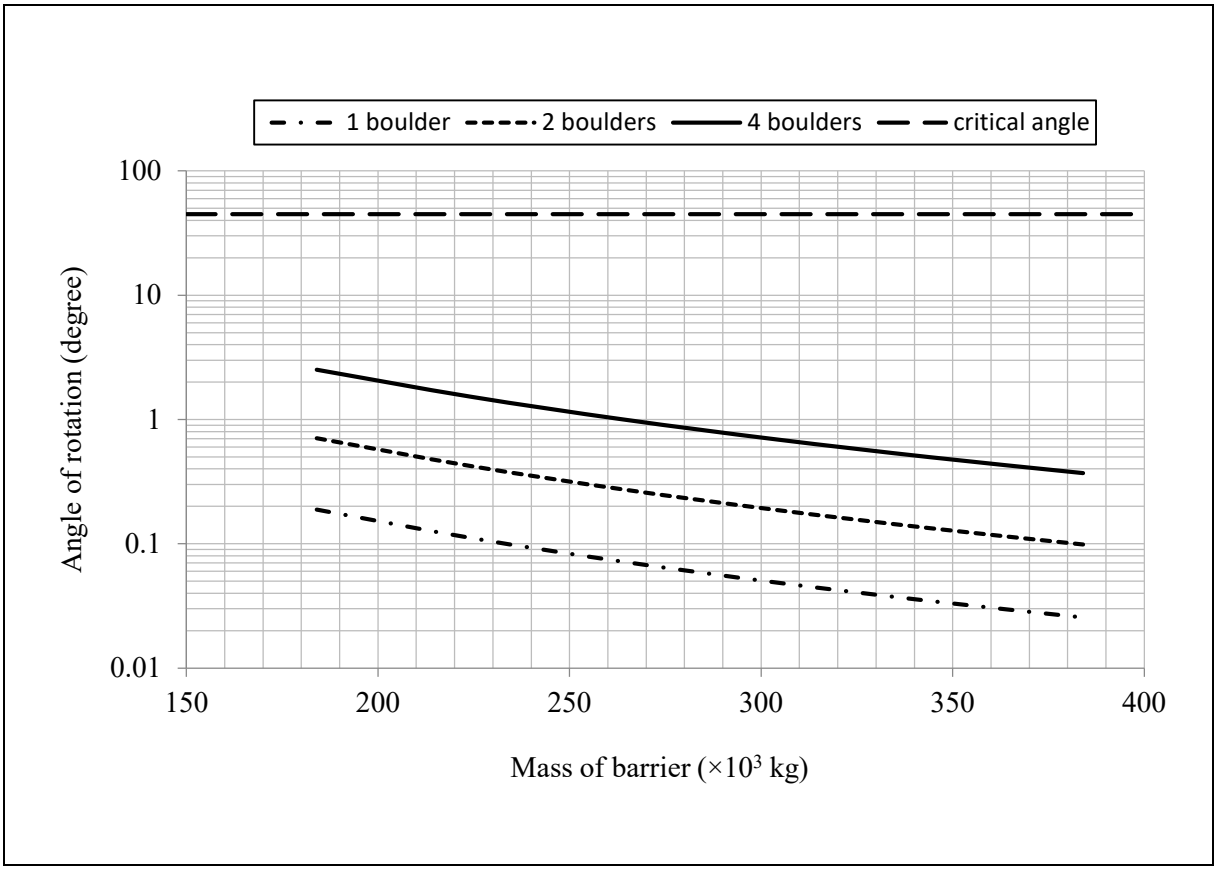

Figure 5.3 Effect of Simultaneous Impacts by Multiple Boulders on Rotational Movement

6 Further Analyses

6.1 Boulder Diameter for Pre-determined Barrier Movement

A parametric study has been performed using the analytical solutions developed for translational and rotational barrier movements and presented in Sections 4 and 5. In this study, the diameter of a single boulder that would cause an L-shaped barrier to slide a minimal distance, say 5 mm, or to rotate by a small amount, say 1°, is calculated for a range of barrier masses and impact velocities. The following assumptions are made for the calculations:

(a) equal stem height and base slab length (varies);

(b) stem and base slab thicknesses (w_{stem} and w_{base}) = 0.8 m;

(c) barrier length (l) = 10 m;

(d) boulder velocity (v_0) = 10 m/s;

(e) boulders diameter (ϕ) = 1.2 m;

(f) boulder density (ρ_b) = 2,650 kg/m^3;

(g) COR= 0.5;

(h) concrete-soil interface friction angle (δ') = 34°;

(i) triangular distribution of pore-water pressure (u) across the base slab, with a maximum value of 150 kPa; and

(j) barrier undergoes pure rotational or translational movement.

The result shows that translational movement is more critical than rotational movement in all cases analysed, as the angle of rotation is always found to be less than 0.5° when the 5-mm criterion is reached. Figure 6.1 plots the boulder diameter against a range of barrier masses for three impact velocities. As expected, for a fixed amount of barrier movement, the boulder diameter increases with the barrier mass but reduces with the impact velocity.

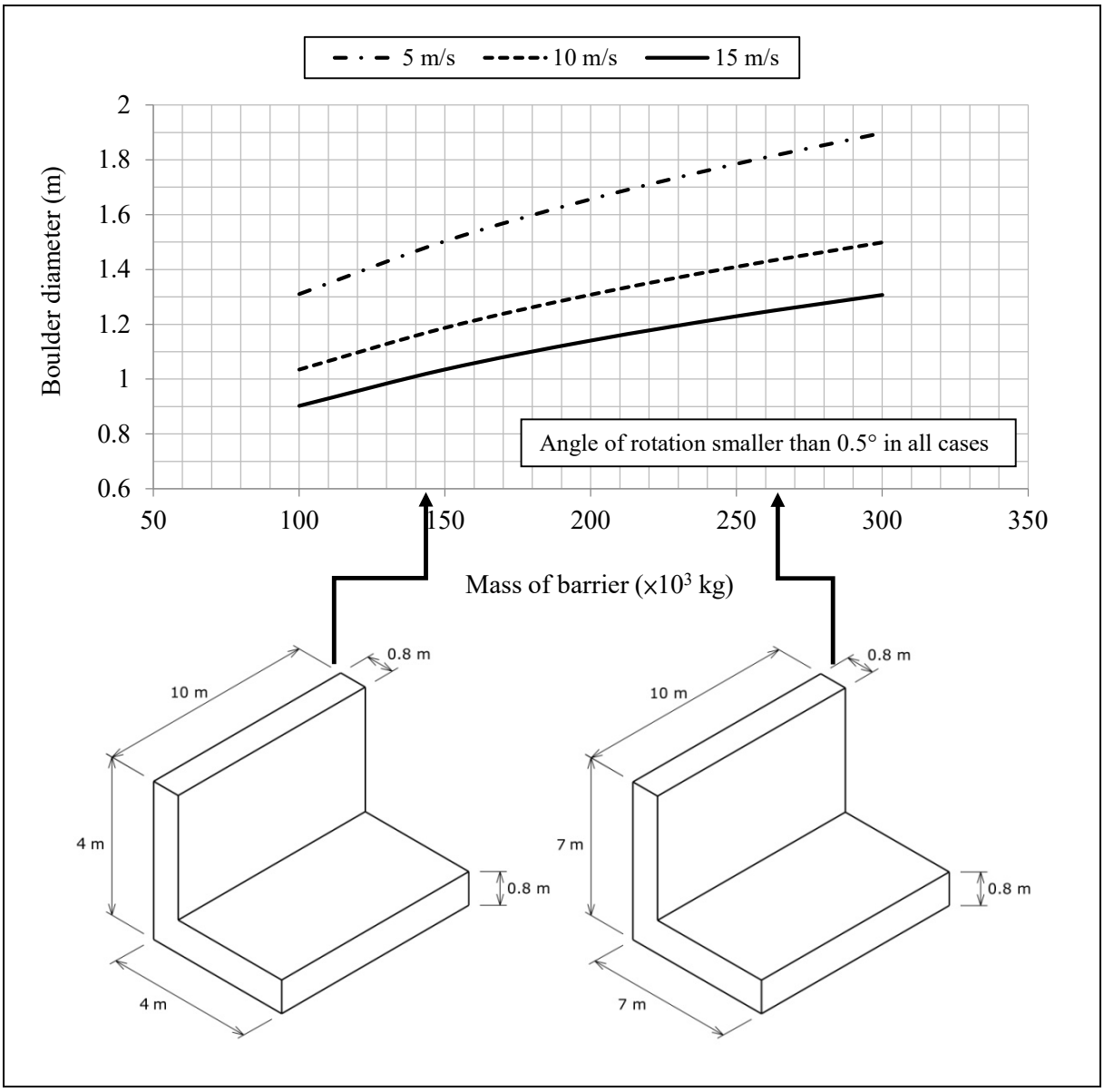

Figure 6.1 Diameters of a Single Boulder Causing 5-mm Translational Barrier Movement

6.2 Effect of Successive Boulder Impacts

The effect of successive boulder impacts on the cumulative movement of a rigid barrier is considered in this section. Only translational movement is considered as rotational movement is generally recoverable. The assumptions made for the calculations in Section 6.1 are adopted again. An L-shaped rigid barrier weighing 200×10^{10} kg is assumed to be successively hit by 1.3-m diameter boulders travelling at a velocity of 10 m/s - these values are chosen such that the barrier will be displaced by 5 mm after the 1st impact as indicated in Figure 6.1. The cumulative barrier movement is calculated with and without consideration of the increase in barrier mass due to the deposited boulders. Any possible cushioning effect due to the deposited boulders is ignored. Figure 6.2 plots the cumulative barrier movement against the number of deposited boulders up to 100. Figure 6.2 shows that if the increase in mass due

to the deposited boulders is not considered, the cumulative barrier movement will simply increase proportionally with the number of deposited boulders. In contrast, if the mass increase is considered, the cumulative barrier movement will approach a limiting value, which is about 200 mm in this case.

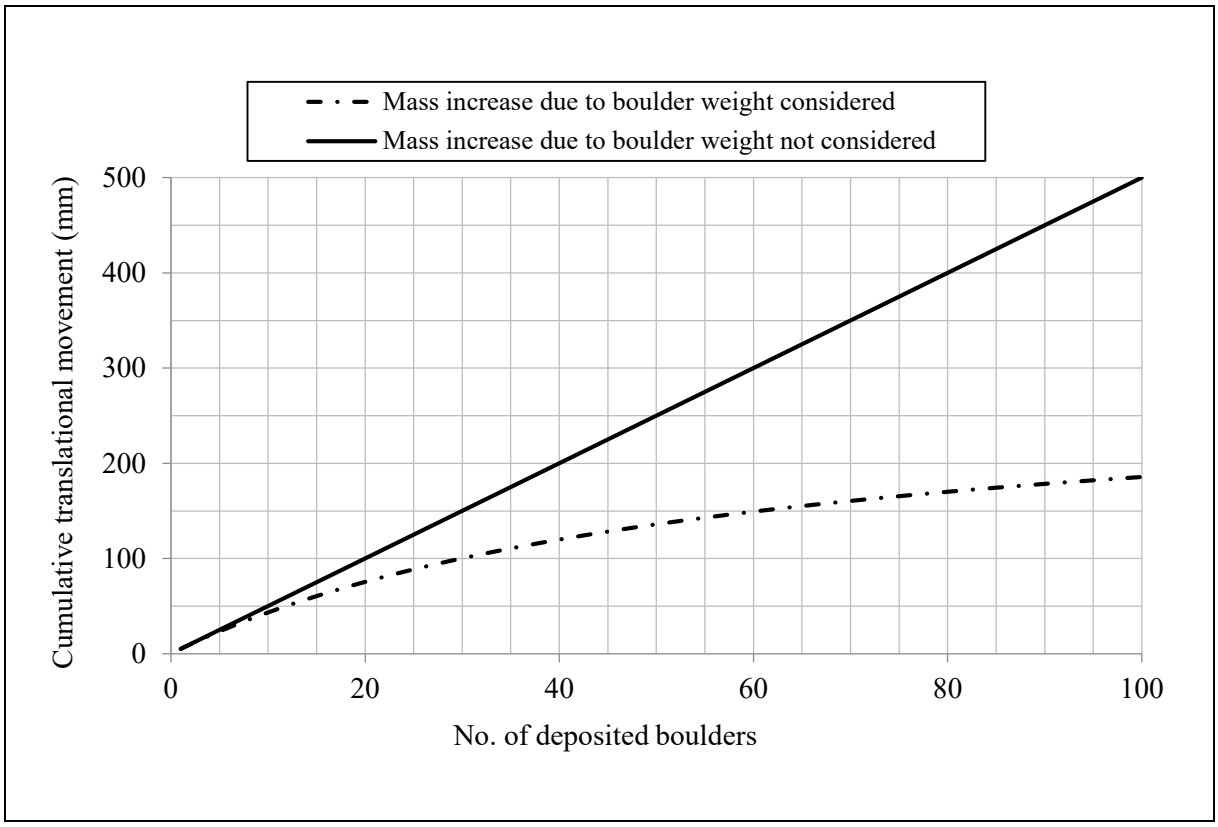

Figure 6.2 Cumulative Translational Movement of an L-shaped Rigid Barrier under Successive Boulder Impacts

7 Discussion

A key assumption of the displacement-based approach is that barriers are considered as perfectly rigid bodies. It is acknowledged that reinforced concrete structures may not behave as such under impact loading, and that the level of rigidity will depend on a number of factors such as barrier geometry and the amount of steel reinforcement. For displacement calculations, the energy loss due to elastic and plastic deformation of the barrier structure can be taken into account by adopting a reasonably conservative COR value such as 0.5 as used in this study.

The calculated translation and rotational displacements induced by boulder impacts on typical rigid barriers could be limited as demonstrated by this study. On this basis of the calculation results, the effects of boulder impacts on bearing stability are deemed insignificant. Nevertheless, the formulations reported in this TN are pertinent to barriers founded on levelled ground. As a good practice, barriers should be founded on a levelled and competent ground, and the ground in front of the barrier should be well protected against erosion as necessary.

For barriers sitting on sloping ground or in close proximity of slopes, other appropriate assessments should be carried out.

The present formulations have not considered the effect of cushioning materials. As properly designed cushioning materials can absorb some of the boulder impact energy through elasto-plastic deformation (Lam, 2016), it is probable that their use will also reduce barrier movement but the exact effect remains to be explored.

8 Conclusions

A displacement-based approach to the design of rigid barriers subject to boulder impacts has been presented in this Technical Note. To illustrate the underlying principles and the use of this alternative approach, mathematical derivations of the relevant equations and worked examples are presented. The results of parametric studies are also discussed to illustrate the effect of barrier size and different impact scenarios on barrier movement. Both translational and rotational movements are considered. The displacement-based approach could provide a more rational means for assessing the performance of rigid barriers subject to simultaneous impacts by multiple boulders.

9 References

Ali, M., Sun, J., Lam, N., Zhang, L. & Gad, E. (2014). Simple hand calculation method for estimating deflection generated by the low velocity impact of a solid object. *Australian Journal of Structural Engineering*, vol. 15, no. 3, pp 243-259.

Chau, K.T., Wong, R.H.C. & Lee, C.F. (1998). Rockfall problems in Hong Kong and some new experimental results for coefficients of restitution. *International Journal of Rock Mechanics and Mining Sciences*, vol. 35, no. 4-5, pp 662-663.

Cui, P. (2015). Personal communication.

Giani, G.P. (1992). *Rock Slope Stability Analysis*. Balkema, Rotterdam, 374 p.

Hu, K., Wei, F., Hong, Y. & Li, X. (2006). Field measurement of impact force of debris flow. *Chinese Journal of Rock Mechanics and Engineering*, vol. 25, suppl. 1, pp 2813-2819.

Kwan, J.S.H. (2012). *Supplementary Technical Guidance on Design of Rigid Debris-resisting Barriers (GEO Report No. 270).* Geotechnical Engineering Office, Hong Kong, 88 p.

Lam, C. (2016). *A Pilot Study of the Use of Cushioning Materials for Reducing Dynamic Impact Loads on Rigid Debris-resisting Barriers (Technical Note No. 5/2016)*. Geotechnical Engineering Office, Hong Kong, 70 p.

Lam, N.T.K. (2015). Personal communication.

Masuya, H., Ihara, T., Onda, S. & Kamijo, A. (2001). Experimental study on some parameters for simulation of rock fall on slope. *Proceedings of the Fourth Asia-Pacific Conference on Shock and Impact Loads on Structures*, Singapore, pp 63-69.

Newmark, N.M. (1965). Effects of earthquakes on dams and embankments. *Géotechnique*, vol. 14, no. 2, pp 139-160.

Perera, S., Lam, N., Pathirana, M., Zhang, L., Ruan, D. & Gad, E. (2016). Deterministic solutions for contact force generated by impact of windborne debris. *International Journal of Impact Engineering*, vol. 91, pp 126-141.

Seifried, R., Schiehlen, W. & Eberhard, P. (2010). The role of the coefficient of restitution on impact problems in multi-body dynamics. *Proceedings of the Institution of Mechanical Engineers, Part K: Journal of Multi-body Dynamics*, vol. 224, no. 3, pp 279-306.

Wyllie, D.C. (2015). *Rock Fall Engineering*. CRC Press, Boca Raton, 270 p.

Yang, Y., Lam, N.T.K. & Zhang, L. (2012). Evaluation of simplified methods of estimating beam responses to impact. *International Journal of Structural Stability and Dynamics*, vol. 12, no. 3, 1250016, 24 p.

Section 2
Appendix A

Illustration of Effects of Inertia and Energy Loss

Contents

	Page No.
Contents	105
List of Figures	106
A.1 Elastic Collision	107
A.2 Inelastic Collision	108
A.3 Partially Inelastic Collision	109

List of Figures

Figure No.		Page No.
A1	Collision between Two Objects with Rebounce	107
A2	Collision between Two Objects without Rebounce	109

A.1 Elastic Collision

Figure A1 shows the collision between two objects having masses m and λm, where $\lambda \geq 1$. Prior to the impact, the smaller object (impactor) travels at velocity v_0 and the heavier (impact-resisting) object is stationary. Immediately after the impact, the impactor rebounds with velocity v_1 and the impact-resisting object travels in the opposite direction at velocity v_2.

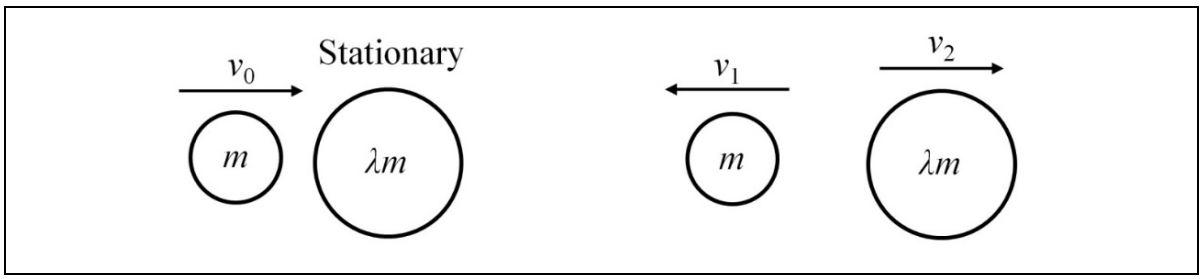

Figure A1 Collision between Two Objects with Rebounce

By conservation of momentum,

$$mv_0 = -mv_1 + (\lambda m)v_2 \quad \text{..... (A.1)}$$

If the collision is totally elastic, that is, no kinetic energy is loss, then by conversation of energy,

$$\frac{1}{2}mv_0^2 = \frac{1}{2}mv_1^2 + \frac{1}{2}(\lambda m)v_2^2 \quad \text{..... (A.2)}$$

Substituting Equation A.1 into Equation A.2, and rearranging gives:

$$\frac{v_2}{v_0} = \frac{2}{1+\lambda} \quad \text{..... (A.3)}$$

The ratio of the kinetic energy gained by the impact-resisting object (KE_2) to the initial energy of the impactor (KE_0) is:

$$\frac{KE_2}{KE_0} = \frac{\frac{1}{2}(\lambda m)v_2^2}{\frac{1}{2}mv_0^2} \quad \text{..... (A.4)}$$

Substituting Equation A.3 into Equation A.4 thus leads to:

$$\frac{KE_2}{KE_0} = \frac{4\lambda}{(1+\lambda)^2} \quad \text{..... (A.5)}$$

Equation A.5 can be used to calculate the energy taken up by an impact-resisting object if the collision is elastic. As can be seen, KE_2 equals KE_0 when λ is equal to 1. This means that all the kinetic energy of the impactor is transferred to the impact-resisting object. When λ is greater than 1, the energy ratio KE_2 / KE_0 will be smaller than 1 and the impactor will rebound with some kinetic energy (KE_1). This illustrates that the greater the mass of the impact-resisting object, the less kinetic energy it will gain from a collision.

At this point, it is useful to introduce the concept of the coefficient of restitution (COR), which is defined as the ratio of relative speeds after and before a collision. Thus,

$$\text{COR} = \frac{v_2 - (-v_1)}{v_0} = \frac{v_1 + v_2}{v_0} \quad \text{..... (A.6)}$$

In an elastic collision, COR has a value of 1. This can be proved by expressing v_1 and v_2 in terms of v_0 by using the momentum and kinetic energy equations (Equations A.1 and A.3) and then substituting them into Equation A.6.

A.2 Inelastic Collision

In an inelastic collision, some of the kinetic energy is converted to other forms of energy such as heat, sound and strain energy, so that kinetic energy is not conserved. Figure A2 shows the extreme case where the two objects coalesce and travel together at velocity v_2 upon impact. The value of COR is zero because the relative speed between the two objects is zero after the impact. This type of collision is termed perfectly inelastic.

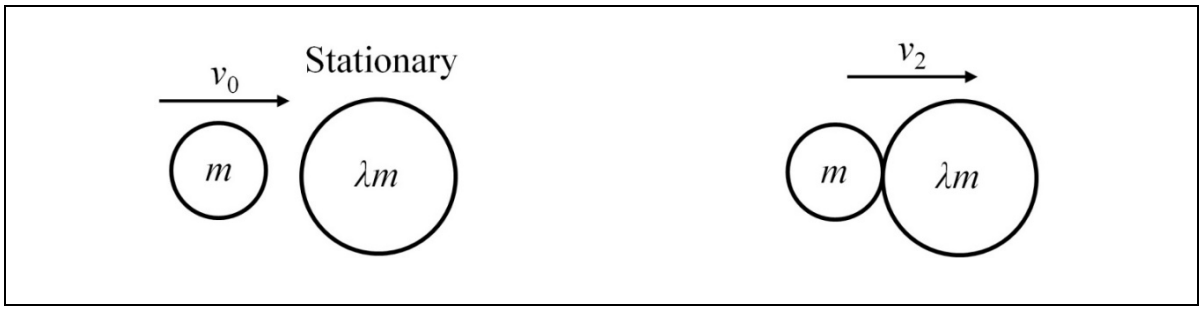

Figure A2 Collision between Two Objects without Rebounce

By conservation of momentum,

$$mv_0 = (m + \lambda m)v_2 \quad \text{..... (A.7)}$$

Rearranging this equation gives:

$$\frac{v_2}{v_0} = \frac{1}{1 + \lambda} \quad \text{..... (A.8)}$$

The ratio of the kinetic energy of the two objects after the impact (KE_2) to the initial energy of the impactor (KE_0) is:

$$\frac{KE_2}{KE_0} = \frac{\frac{1}{2}(m+\lambda m)v_2^2}{\frac{1}{2}mv_0^2} \quad \text{..... (A.9)}$$

Substituting Equation A.8 into Equation A.9 thus gives:

$$\frac{KE_2}{KE_0} = \frac{1}{(1+\lambda)} \quad \text{..... (A.10)}$$

A comparison between Equations A.5 and A.10 shows that significantly less kinetic energy is transferred to the impact-resisting object in an inelastic collision than in an elastic one.

A.3 Partially Inelastic Collision

In most inelastic collisions, the objects involved will not coalesce but will bounce off each other as illustrated in Figure A1. During the impact process, some of the kinetic energy is converted to heat, sound and strain energy. This type of collision is termed partially inelastic and is the intermediate case between elastic and perfectly inelastic collisions. As for the case of an elastic collision, the coefficient of restitution (COR) is expressed as:

$$COR = \frac{v_2 - (-v_1)}{v_0} = \frac{v_1 + v_2}{v_0} \quad \text{..... (A.11)}$$

By conservation of momentum,

$$mv_0 = -mv_1 + (\lambda m)v_2 \quad \text{..... (A.12)}$$

It can be seen that the mass of the impactor, m, can be cancelled out of Equation A.12. If v_2 is added to both sides and the whole equation divided by v_0, then

$$\frac{v_0 + v_1 + v_2}{v_0} = \frac{(1+\lambda)v_2}{v_0} \quad \text{..... (A.13)}$$

Substituting Equation A.11 into Equation A.13 and rearranging gives:

$$\frac{v_2}{v_0} = \frac{1+COR}{1+\lambda} \quad \text{..... (A.14)}$$

The ratio of the kinetic energy of the impact-resisting object (KE_2) to the initial energy of the impactor (KE_0) is:

$$\frac{\mathrm{KE}_2}{\mathrm{KE}_0} = \frac{\frac{1}{2}(\lambda m)v_2^2}{\frac{1}{2}mv_0^2} = \frac{\lambda m}{m}\left(\frac{v_2}{v_0}\right)^2 \quad \text{..... (A.15)}$$

Substituting Equation A.14 into Equation A.15 finally gives:

$$\frac{\mathrm{KE}_2}{\mathrm{KE}_0} = \lambda\left(\frac{1+\mathrm{COR}}{1+\lambda}\right)^2 \quad \text{..... (A.16)}$$

This equation can be used to estimate the kinetic energy of an impact-resisting object (KE_2) after a partially inelastic collision. When COR is unity, Equation A.16 will revert to Equation A.5, which was derived for the case of an elastic collision. Substituting a COR value of zero into Equation A.16 however will not yield Equation A.10, which was derived for the case of an inelastic collision. This is because of the different assumptions made for the two cases: in an inelastic collision the two objects coalesce after the collision, whilst in a partially inelastic collision the objects rebound from one another.

Section 2
Appendix B

Translational Movement

Contents

	Page No.
Contents	112
List of Figures	113
B.1 Theory	114
B.2 Worked Example – Single Boulder Impact	115
B.3 Worked Example – Multiple Boulder Impacts	116
B.4 Reference	117

List of Figures

Figure No.		Page No.
B1	Translational Movement of an L-shaped Rigid Barrier Impacted by a Boulder	114
B2	Translational Movement of a Rectangular Rigid Barrier Impacted by Two Boulders	116

B.1 Theory

In the case of a boulder impacting on a free-standing rigid barrier, the barrier will undergo translational and/or rotational movements to dissipate the kinetic energy gained from the collision. If the barrier is assumed to undergo only translation movement, the kinetic energy (KE_2) will be dissipated by the work done due to the frictional resistance between the base slab and the ground surface. Figure B1 shows a free-standing rigid barrier undergoing translational movement after an impact. An L-shaped barrier is assumed here but the following discussion is also applicable to other barrier shapes.

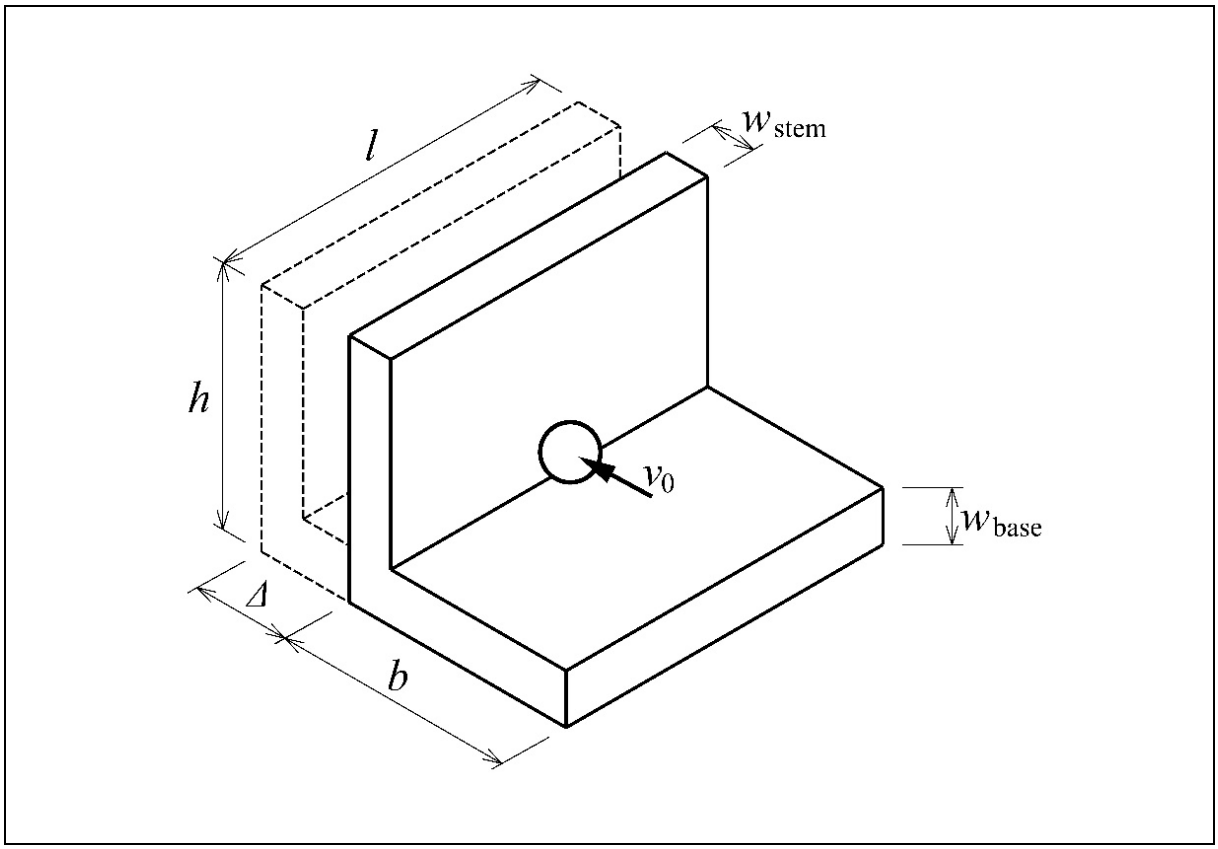

Figure B1 Translational Movement of an L-shaped Rigid Barrier Impacted by a Boulder

If the mass of the boulder is denoted as m and the mass of the barrier as M, the weight of the barrier is Mg, where g is gravity. The basal interface resistance (friction) between the barrier and the ground surface is thus $Mg\tan\delta'$, where δ' is the effective angle of interface friction between concrete and soil. For design purposes, the value of δ' may be taken as that corresponding to the critical state and may be estimated according to Geoguide 1 (GEO, 1993). If the barrier is subjected to a water uplift pressure u, the basal interface resistance then becomes $(Mg - uA) \times \tan\delta'$, where A is the contact area between the base slab and the soil.

Immediately after an impact by a single boulder, the barrier gains kinetic energy (KE_2). To take into account the effects of mass inertia and energy loss, KE_2 can be estimated using the

energy-transfer equation derived for the partially inelastic collision case (Table 2.1 and Equation A.16). A COR value of, say, 0.5 may be assumed in the calculation. The barrier-to-mass ratio, λ, is also required for the determination of KE_2 and can be computed as M / m.

Since the barrier is assumed to undergo only translational movement, by conservation of energy the barrier's kinetic energy must be dissipated through work done by the basal interface resistance. If the soil is assumed to behave as a rigid-perfectly plastic material, the amount of barrier movement, Δ, can be calculated as:

$$\Delta = \frac{\mathrm{KE}_2}{(Mg - uA)\tan\delta'} \quad \text{..... (B.1)}$$

B.2 Worked Example – Single Boulder Impact

To illustrate the use of Equation B.1, a free-standing L-shaped barrier, such as the one shown in Figure B1, is considered in this example. The barrier's stem wall is 5-m high (h) and the base slab is 5-m long (b). The widths of the stem wall (w_{stem}) and the base slab (w_{base}) are both 0.8 m, and the length of the barrier is 10 m (l). The barrier is made of reinforced concrete and its density (ρ_c) is assumed to be 2,500 kg/m^3. The ground water table is below the surface so there is no water pressure acting on the barrier. The effective interface friction angle (δ') between concrete and soil at the critical state is 34°. A boulder with a diameter (ϕ) of 1.2 m and a density (ρ_b) of 2,650 kg/m^3 hits the barrier at a horizontal velocity (v_0) of 10 m/s. The coefficient of restitution (COR) is taken as 0.5. The barrier is assumed to behave as a rigid body and to undergo translational movement after the impact.

Equation B.1 is used to calculate the translational movement of the barrier. The values of the required parameters are determined as follows.

Mass of boulder: $m = \rho_b \left[\frac{4}{3}\pi\left(\frac{\phi}{2}\right)^3\right] = 2{,}397.7$ kg

Mass of barrier: $M = \rho(h - w_{base})w_{stem}\, l + \rho b l w_{base} = 184{,}000$ kg

Barrier-to-boulder mass ratio: $\lambda = M / m = 76.7414$

Kinetic energy gained by barrier: $\mathrm{KE}_2 = \frac{1}{2} m v_0^2 \lambda \left(\frac{1+\mathrm{COR}}{1+\lambda}\right)^2 = 3{,}425$ J

Pore-water pressure: $u = 0$ Pa (N/m^2)

Substituting the above information into Equation B.1 thus gives:

$$\Delta = \frac{\mathrm{KE}_2}{(Mg - uA)\tan\delta'} = \frac{3{,}425}{(184{,}000 \times 9.81 - 0)\tan 34^\circ} = 0.0028 \text{ m (or 2.8 mm).}$$

B.3 Worked Example – Multiple Boulder Impacts

To illustrate the effect of multiple boulder impacts, the barrier considered in Section B.2 is assumed to be simultaneously impacted by two boulders as illustrated in Figure B2. All other conditions remain the same.

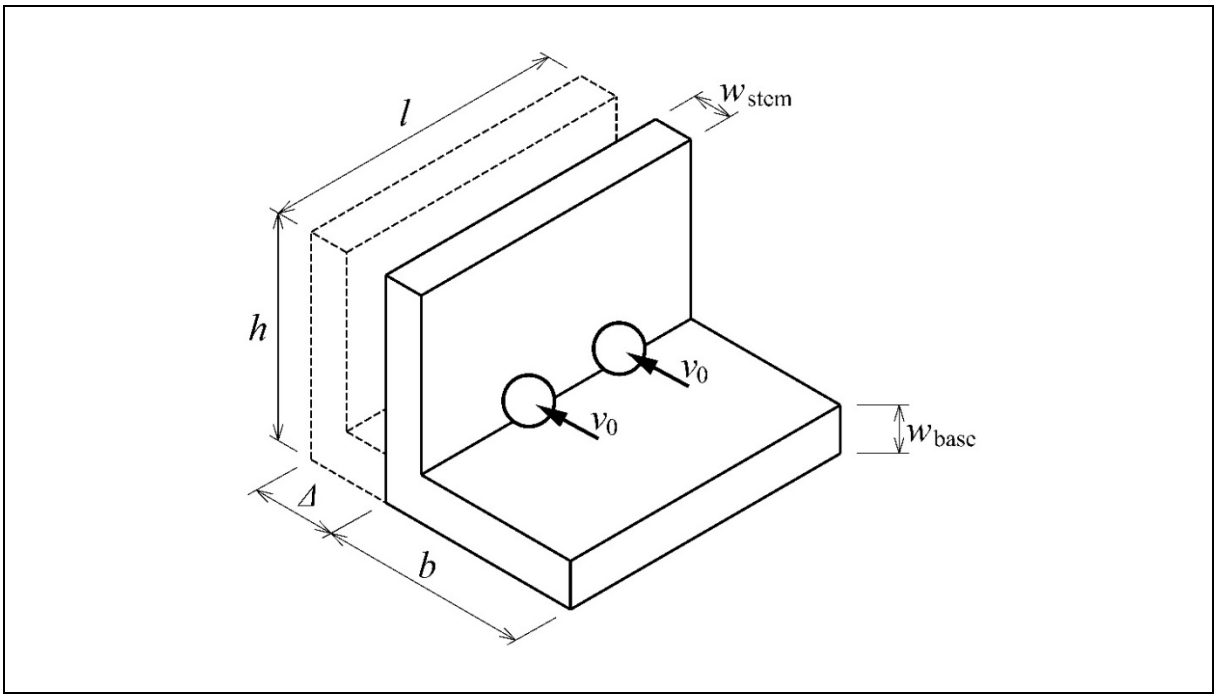

Figure B2 Translational Movement of a Rectangular Rigid Barrier Impacted by Two Boulders

The combined mass of the two boulders is used for the stability assessment. Therefore,

Total mass of boulders: $m = 2\rho_b\left[\frac{4}{3}\pi\left(\frac{\phi}{2}\right)^3\right] = 4{,}795.3$ kg

Barrier-to-boulder mass ratio: $\lambda = 184{,}000 / 4{,}795.3 = 38.3707$

Kinetic energy gained by barrier: $\mathrm{KE}_2 = \frac{1}{2}mv_0^2\lambda\left(\frac{1+\mathrm{COR}}{1+\lambda}\right)^2 = 13{,}354$ J

Pore-water pressure: $u = 0$ Pa (N/m^2)

Substituting these values into Equation B.1 gives:

$$\Delta = \frac{\mathrm{KE}_2}{(Mg - uA)\tan\delta'} = \frac{13{,}354}{(184{,}000 \times 9.81 - 0)\tan 34°} = 0.0110 \text{ m or } (11.0 \text{ mm}).$$

Comparing the results between this and the previous examples shows that the amount of kinetic energy gained by the barrier and thus its movement are not proportional to the number of boulders. In this example, nearly four times of movement (11.0 mm vs. 2.8 mm) is predicted when the barrier is impacted by two boulders instead of one. This can be attributed to the nonlinear relationship between the mass ratio (λ) and the energy-transfer ratio (KE_2 / KE_0) as shown in Figure 3.2.

The formulation presented in this study does not consider the effects of shear key which could be provided in practice. If the passive soil resistance provided by a shear key is also considered in the formulation, a smaller calculated translational movement will be obtained.

B.4 Reference

GEO (1993). *Guide to Retaining Wall Design, 2nd Edition (Geoguide 1)*. Geotechnical Engineering Office, Hong Kong, 258 p.

Section 2
Appendix C

Rotational Movement

Contents

		Page No.
Contents		119
List of Figures		120
C.1	Theory	121
C.2	Worked Example – Single Boulder Impact on an L-shaped Barrier	125
C.3	Worked Example – Multiple Boulder Impacts on an L-shaped Barrier	128
C.4	Worked Example – Single Boulder Impact on an L-shaped Barrier with Side Walls	129

List of Figures

Figure No.		Page No.
C1	A Rigid L-shaped Barrier Undergoing Rotational Movement after a Boulder Impact at the Top of the Stem Wall	121
C2	A Rigid L-shaped Barrier Undergoing Rotational Movement Following a Boulder Impact on the Stem Wall at Height h_b	125
C3	A Rigid L-shaped Barrier Impacted by a Single Boulder	126
C4	A Rigid L-shaped Barrier Impacted by Two Boulders	128
C5	A Rigid L-shaped Barrier with Side Walls Impacted by a Boulder	129

C.1 Theory

If a barrier is assumed to undergo rotational movement following a single-boulder impact, the amount of movement will not only depend on the weight but also the geometrical properties of the barrier. Figure C1 shows a rigid barrier with its height and slab length denoted as h and b respectively. The barrier is impacted at the top of its stem wall by a single boulder with mass m and travelling at velocity v_0. This impact position represents the worst-case scenario in terms of the overturning stability of the barrier. Immediately after the impact, the barrier gains kinetic energy (KE_2) and this is gradually converted to potential energy (PE) as the barrier rotates. The angle of rotation is θ and the top of the barrier displaces horizontally by Δ. The barrier's centre of gravity also changes by the vertical distance $\Delta_{C.G.}$.

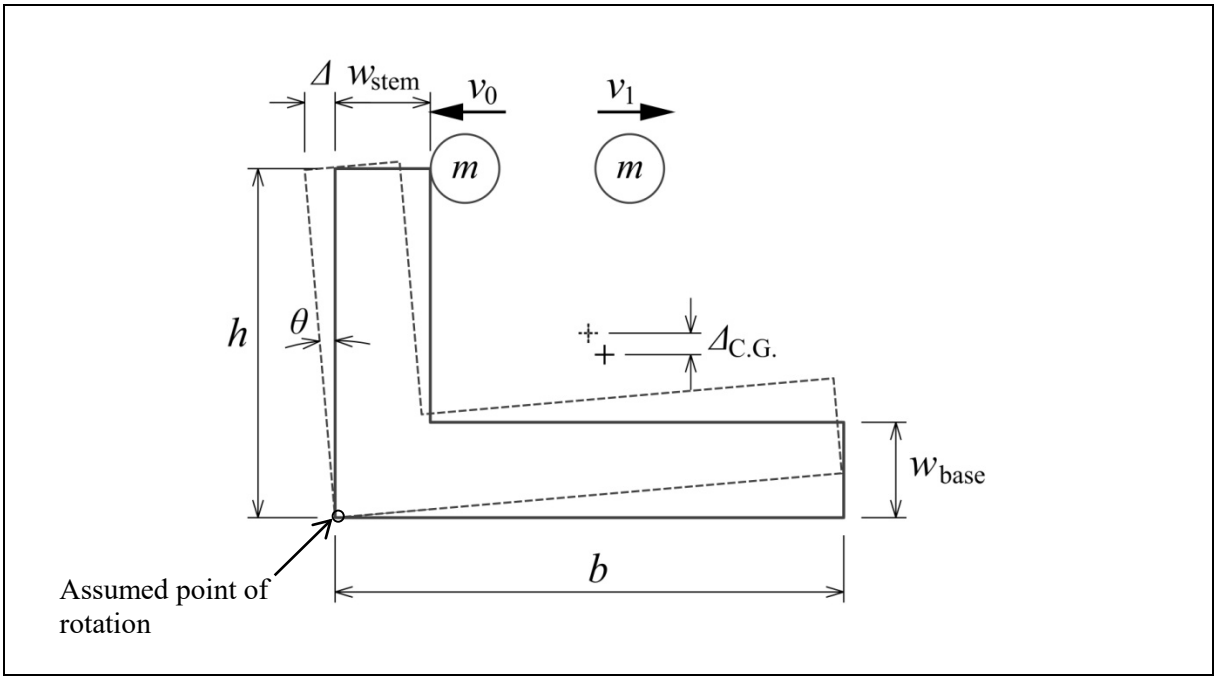

Figure C1 A Rigid L-shaped Barrier Undergoing Rotational Movement after a Boulder Impact at the Top of the Stem Wall

If the effects of barrier's inertia and energy loss are neglected, by conservation of energy the maximum value of $\Delta_{C.G.}$ can be obtained by simply equating the boulder's initial kinetic energy ($KE_0 = KE_2 = 0.5mv_0^2$) with the barrier's gain in potential energy ($PE = Mg\Delta_{C.G.}$) to obtain the following equation:

$$\Delta_{C.G.} = \frac{mv_0^2}{2Mg} \quad \text{..... (C.1)}$$

where M is the total mass of the barrier and g is gravity.

However, if effects of barrier's inertia and energy loss are considered, this problem will need to be solved by considering the conservation of angular momentum:

$$mv_0h = I_\theta\dot{\theta} - mv_1h \quad \text{..... (C.2)}$$

where v_0 and v_1 are the initial (impact) and rebound velocities of the boulder respectively, I_θ is the mass moment of inertia (rotational inertia) of the barrier, and $\dot{\theta}$ is the angular speed. The term $I_\theta\dot{\theta}$ represents the angular momentum of the barrier gained from the impact.

For L-shaped objects such as the one shown in Figure C1, I_θ can be approximated as:

$$I_\theta = \frac{M_{\text{stem}}}{3}\left(h^2 + hw_{\text{base}}\right) + \frac{M_{\text{base}}}{3} \times b^2 \quad \text{..... (C.3)}$$

where M_{stem} and M_{base} denote the masses of the stem wall and the base slab respectively.

For L-shaped barriers with rectangular side walls, Equation C.3 can be expanded to become:

$$I_\theta = \frac{M_{\text{stem}}}{3}\left(h^2 + hw_{\text{base}}\right) + \frac{M_{\text{base}}}{3} \times b + nM_{\text{side}}\left[\left(\frac{c^2 + d^2}{12}\right) + \left(\frac{d}{2} + w_{\text{stem}}\right)^2 + \left(\frac{c}{2} + w_{\text{stem}}\right)^2\right] \quad \text{..... (C.4)}$$

where n and M_{side} are the number and the mass of side walls respectively; c and d denote the length and height of the side walls respectively.

Derivation of Equations C.3 and C.4 are given in Section 2 Appendix D. From geometry, it can be shown that the angular speed $\dot{\theta}$ of the barrier has the following form:

$$\dot{\theta} = \frac{v_2}{r} \quad \text{..... (C.5)}$$

where v_2 is the velocity of the barrier at the point of impact, and r is the distance between the point of rotation and the impact location. For L-shaped barriers such as the one shown in Figure C1, r equals $\sqrt{h^2 + w_{\text{stem}}^2}$. Derivation of Equation C.5 is given in Section 2 Appendix D. Substituting Equation C.5 into Equation C.2 and rearranging thus gives:

$$v_0 + v_1 = \left(\frac{I_\theta}{mhr}\right)v_2 \quad \text{..... (C.6)}$$

Let $\kappa = \frac{I_\theta}{mhr}$ (dimensionless), Equation C.6 now becomes:

$$v_0 + v_1 = \kappa v_2 \quad \text{..... (C.7)}$$

Adding v_2 to both sides of the equation and then dividing by v_0 gives:

$$1 + \frac{v_1 + v_2}{v_0} = (1 + \kappa)\frac{v_2}{v_0} \quad \text{..... (C.8)}$$

Recalling COR = (v_1 + v_2)/v_0, Equation C.8 becomes:

$$\frac{v_2}{v_0} = \frac{1+\mathrm{COR}}{1+\kappa} \quad \text{..... (C.9)}$$

It can be seen that Equation C.9 has the same form as Equation A.14. Now consider the angular kinetic energy of the barrier:

$$\mathrm{KE}_2 = \frac{1}{2} I_\theta \dot{\theta}^2 \quad \text{..... (C.10)}$$

Substituting Equation C.5 into C.10 and letting $\kappa = \dfrac{I_\theta}{mhr}$ gives:

$$\mathrm{KE}_2 = \frac{1}{2} I_\theta \left(\frac{v_2}{r}\right)^2 = \frac{1}{2}\left(\frac{I_\theta}{mhr}\right)\frac{v_2^2 mh}{r} = \frac{1}{2} \times \frac{\kappa v_2^2 mh}{r} \quad \text{..... (C.11)}$$

Using Equations C.9 and C.11, the energy-transfer ratio can be expressed as:

$$\frac{\mathrm{KE}_2}{\mathrm{KE}_0} = \frac{\frac{1}{2} \times \frac{\kappa v_2^2 mh}{r}}{\frac{1}{2} m v_0^2} = \frac{\kappa h}{r}\left(\frac{v_2}{v_0}\right)^2 = \frac{\kappa h}{r}\left(\frac{1+\mathrm{COR}}{1+\kappa}\right)^2 \quad \text{..... (C.12)}$$

It is worth noting that Equation C.12 has a similar form to Equation A.16. The difference is due to the additional consideration of geometrical properties, which was not considered during the derivation of Equation A.16.

Rearranging Equation C.12 thus leads to:

$$\mathrm{KE}_2 = \frac{1}{2} m v_0^2 \frac{\kappa h}{r}\left(\frac{1+\mathrm{COR}}{1+\kappa}\right)^2 \quad \text{..... (C.13)}$$

By equating the barrier's change in potential energy (PE = $Mg\Delta_{\mathrm{C.G.}}$) to its gain in kinetic energy (KE_2), the rise of the barrier's centre of gravity ($\Delta_{\mathrm{C.G.}}$) can finally be expressed as:

$$\Delta_{\mathrm{C.G.}} = \frac{m v_0^2}{2Mg} \times \frac{\kappa h}{r}\left(\frac{1+\mathrm{COR}}{1+\kappa}\right)^2 \quad \text{..... (C.14)}$$

Comparing Equation C.1 with Equation C.14 shows that the effects of barrier's mass inertia and energy loss are considered by the additional term $\dfrac{\kappa h}{r}\left(\dfrac{1+\mathrm{COR}}{1+\kappa}\right)^2$.

From geometry, it can be shown that the angle of rotation θ is related to $\Delta_{C.G.}$ via the following equation:

$$\theta = \sin^{-1}\left[\frac{\bar{y} + \Delta_{C.G.}}{\sqrt{\bar{x}^2 + \bar{y}^2}}\right] - \tan^{-1}\left(\frac{\bar{y}}{\bar{x}}\right) \quad \text{..... (C.15)}$$

where $\bar{x}$ and $\bar{y}$ are the distances to the centre of gravity measured from the outer edge of the stem wall (global vertical axis) and the base (global horizontal axis) respectively. It should be noted that Equation C.15 is derived based on the assumption that the barrier does not overturn, so that the calculated $\Delta_{C.G.}$ from Equation C.14 is less than the critical value $\Delta_{C.G.(crit)}$, which may be computed using the following equation:

$$\Delta_{C.G.(crit)} = \sqrt{\bar{x}^2 + \bar{y}^2} - \bar{y} \quad \text{..... (C.16)}$$

The associated critical angle of rotation has the following form:

$$\theta_{crit} = 90° - \tan^{-1}\left(\frac{\bar{y}}{\bar{x}}\right) \quad \text{..... (C.17)}$$

The derivation of Equations C.15 to C.17 is given in Section 2 Appendix D.

Equations C.13 and C.14 are derived based on the assumption that the barrier is hit by a boulder at the top of its stem wall as shown in Figure C1. The process can be repeated to derive expressions for KE_2 and $\Delta_{C.G.}$ for cases where the boulder hits the stem wall at a lower position as shown in Figure C2. To this end, Equation C.2 is re-written as:

$$m v_0 h_b = I_\theta \dot{\theta} - m v_1 h_b \quad \text{..... (C.18)}$$

where h_b denotes the height of the boulder above the point of rotation. The distance between the point of rotation and the impact location (r) now equals to $\sqrt{h_b^2 + w_{stem}^2}$. Therefore, Equation C.6 is also re-written as:

$$v_0 + v_1 = \left(\frac{I_\theta}{m h_b r}\right) v_2 \quad \text{..... (C.19)}$$

Let $\kappa = \dfrac{I_\theta}{m h_b r}$ and Equation C.19 can be manipulated to provide the same expression for the velocity ratio v_2/v_0 as shown Equation C.9. Repeating the derivation process as before will lead to the expressions for the barrier's kinetic energy and the rise in its centre of gravity:

$$KE_2 = \frac{1}{2} m v_0^2 \frac{\kappa h_b}{r}\left(\frac{1 + COR}{1 + \kappa}\right)^2 \quad \text{..... (C.20)}$$

$$\Delta_{\text{C.G.}} = \frac{mv_0^2}{2Mg} \times \frac{\kappa h_\text{b}}{r} \left(\frac{1+\text{COR}}{1+\kappa} \right)^2 \quad \text{..... (C.21)}$$

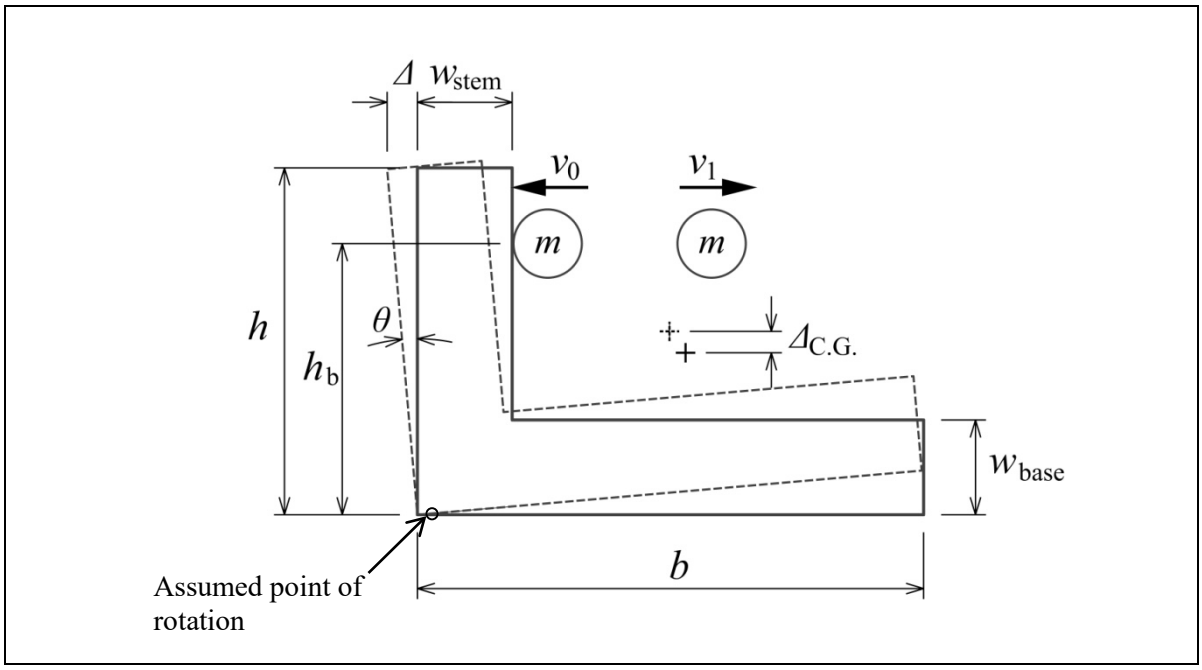

Figure C2 A Rigid L-shaped Barrier Undergoing Rotational Movement Following a Boulder Impact on the Stem Wall at Height h_b

C.2 Worked Example – Single Boulder Impact on an L-shaped Barrier

Figure C3 shows a free-standing rigid barrier. The barrier has an overall height (h) of 5 m and a length (l) of 10 m. The length of the base slab (b) is 5 m. The widths of the stem wall and the base slab (w_{stem} and w_{base}) are both 0.8 m. The density of reinforced concrete (ρ_c) is assumed to be 2,500 kg/m^3. A boulder with a diameter (ϕ) of 1.2 m and a density (ρ_b) of 2,650 kg/m^3 hits the top of the barrier at a horizontal velocity (v_0) of 10 m/s. The coefficient of restitution (COR) is taken as 0.5. The barrier is assumed to behave as a rigid body and to undergo rotational movement after the impact.

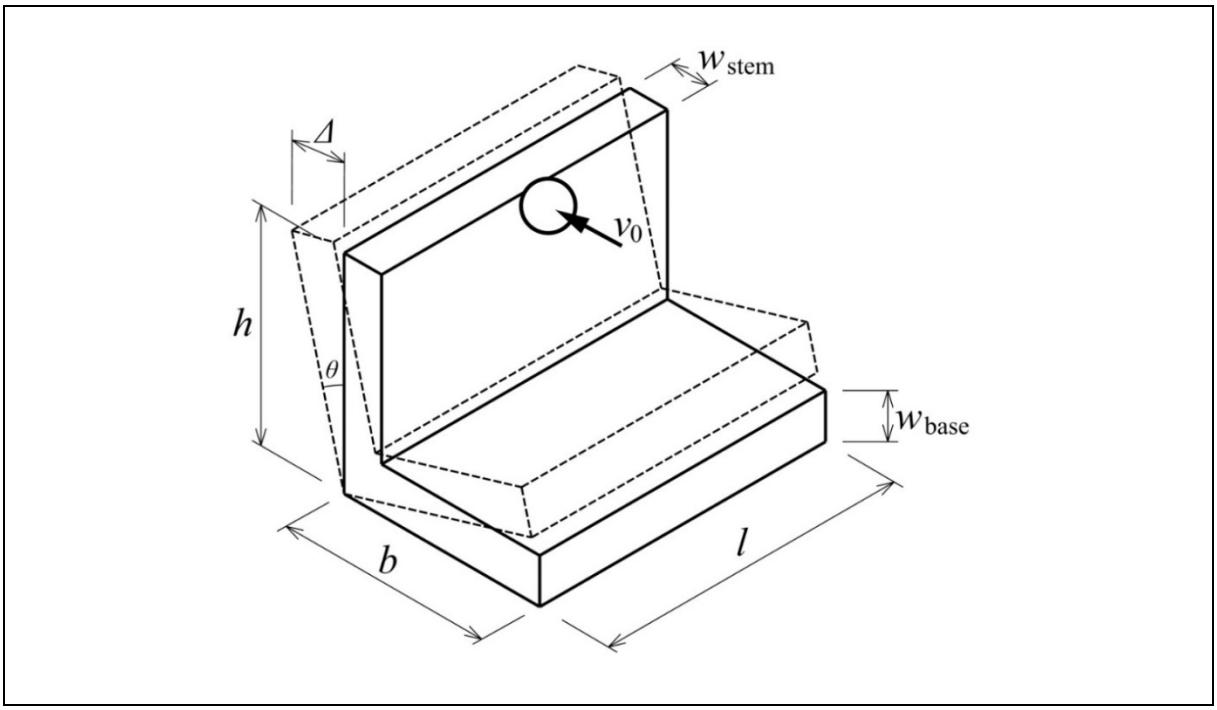

Figure C3 A Rigid L-shaped Barrier Impacted by a Single Boulder

Equation C.14 is used to calculate the rise of the barrier's centre of gravity, Δ_h, following the impact. The required parameters are computed first as follows:

Mass of boulder: $m = \rho_b \left[\frac{4}{3} \pi \left(\frac{\phi}{2} \right)^3 \right] = 2{,}397.8$ kg

Mass of stem wall: $M_{stem} = \rho_c \, l w_{base} (h - w_{base}) = 84{,}000$ kg

Mass of base slab: $M_{base} = \rho_c \, l b w_{base} = 100{,}000$ kg

Total mass of barrier: $M = M_{stem} + M_{base} = 184{,}000$ kg

Distance between axis of rotation and impact location:

$$r = \sqrt{h^2 + w_{stem}^2} = 5.0636 \text{ m}$$

Mass moment of inertia of barrier:

$$I_\theta = \frac{M_{stem}}{3} \left(h^2 + h w_{base} \right) + \frac{M_{base}}{3} \times b^2 = 1{,}645{,}333 \text{ kg·m}^2$$

Dimensionless number: $\kappa = \frac{I_\theta}{mhr} = 27.1042$

Substituting the required information into Equation C.14 leads to:

$$\Delta_{\text{C.G.}} = \frac{mv_0^2}{2Mg} \times \frac{\kappa h}{r}\left(\frac{1+\text{COR}}{1+\kappa}\right)^2 = \frac{2397.7\times10^2}{2\times184{,}000\times9.81} \times \frac{27.1042\times5}{5.0636} \times \left(\frac{1+0.5}{1+27.1042}\right)^2$$

$\Delta_{\text{C.G.}} = 0.0051$ m (or 5.1 mm).

The stability of the barrier against overturning can be assessed by comparing the calculated $\Delta_{\text{C.G.}}$ with the critical value $\Delta_{\text{C.G.(crit)}}$. For the calculation of $\Delta_{\text{C.G.(crit)}}$, the centre of gravity of the barrier first needs to be located with reference to a global origin, which can be conveniently set at the point of rotation. The computations are carried out as follows:

Horizontal distance from vertical global axis to centre of gravity:

$$\bar{x} = \frac{1}{A}\int x\,\mathrm{d}A = 1.5413 \text{ m}$$

Vertical distance from horizontal global axis to centre of gravity:

$$\bar{y} = \frac{1}{A}\int y\,\mathrm{d}A = 1.5413 \text{ m}.$$

Therefore, according to Equation C.16,

$$\Delta_{\text{C.G.(crit)}} = \sqrt{\bar{x}^2 + \bar{y}^2} - \bar{y} = 2.1797 - 1.5413 = 0.6384 \text{ m (or 638.4 mm)}.$$

Since $\Delta_{\text{C.G.}} < \Delta_{\text{C.G.(crit)}}$, the barrier will not overturn.

If required, the angle of rotation (θ) can also be computed using Equation C.15 as:

$$\theta = \sin^{-1}\left[\frac{\bar{y}+\Delta_{\text{C.G.}}}{\sqrt{\bar{x}^2+\bar{y}^2}}\right] - \tan^{-1}\left(\frac{\bar{y}}{\bar{x}}\right) = \sin^{-1}\left[\frac{1.5413+0.0051}{\sqrt{1.5413^2+1.5413^2}}\right] - \tan^{-1}\left(\frac{1.5413}{1.5413}\right)$$

$\theta = 0.19°$.

This calculated value of θ can be compared to the critical angle of rotation (θ_{crit}), which can be calculated according to Equation C.17:

$$\theta_{\text{crit}} = 90° - \tan^{-1}\left(\frac{\bar{y}}{\bar{x}}\right) = 90 - \tan^{-1}\left(\frac{1.5413}{1.5413}\right) = 45°$$

In addition, the horizontal displacement at the barrier top (Δ) is:

$$\Delta = h\sin\theta = 5\times\sin 0.19° = 0.0166 \text{ m (or 16.6 mm)}.$$

C.3 Worked Example – Multiple Boulder Impacts on an L-shaped Barrier

To illustrate the effect of multiple boulder impacts, the barrier considered in Section C.2 is assumed to be simultaneously impacted by two boulders as illustrated in Figure C4. All other conditions remain the same.

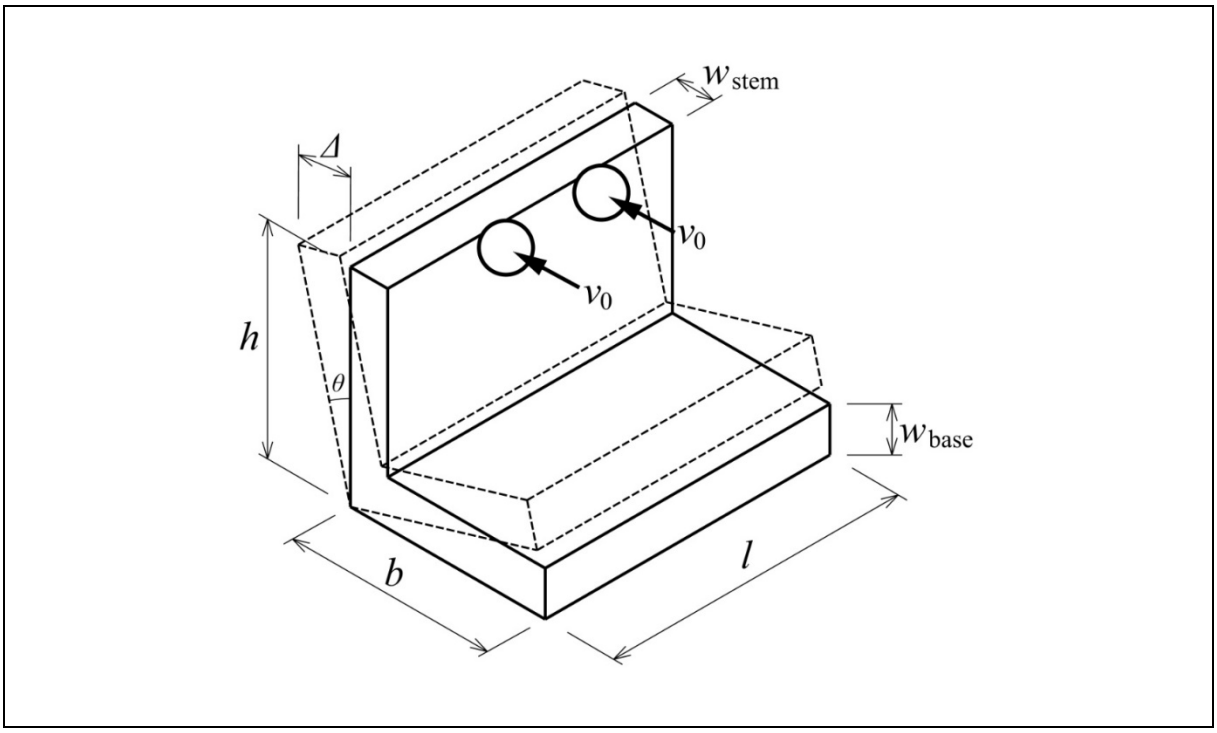

Figure C4 A Rigid L-shaped Barrier Impacted by Two Boulders

The combined mass of the two boulders is used for the assessment. Therefore,

Total mass of boulders: $$m = 2\rho_b\left[\frac{4}{3}\pi\left(\frac{\phi}{2}\right)^3\right] = 4{,}795.3 \text{ kg}$$

Dimensionless number: $$\kappa = \frac{I_\theta}{mhr} = 13.5521$$

Substituting the new information into Equation C.14 leads to:

$$\Delta_{C.G.} = \frac{mv_0^2}{2Mg} \times \frac{\kappa h}{r}\left(\frac{1+\text{COR}}{1+\kappa}\right)^2 = \frac{4795.3\times 10^2}{2\times 184{,}000\times 9.81} \times \frac{13.5521\times 5}{5.0636} \times \left(\frac{1+0.5}{1+13.5521}\right)^2$$

$\Delta_{C.G.} = 0.0189$ m (or 18.9 mm) $< \Delta_{C.G.(crit)}$ from Section C.2.

Since $\Delta_{C.G.} < \Delta_{C.G.(crit)}$, the barrier will not overturn.

The angle of rotation (θ) can be computed using Equation C.15 as:

$$\theta = \sin^{-1}\left[\frac{\bar{y} + \Delta_{C.G.}}{\sqrt{\bar{x}^2 + \bar{y}^2}}\right] - \tan^{-1}\left(\frac{\bar{y}}{\bar{x}}\right) = \sin^{-1}\left[\frac{1.5413 + 0.0189}{\sqrt{1.5413^2 + 1.5413^2}}\right] - \tan^{-1}\left(\frac{1.5413}{1.5413}\right)$$

$\theta = 0.71°$.

C.4 Worked Example – Single Boulder Impact on an L-shaped Barrier with Side Walls

Figure C5 shows an L-shaped barrier with two rectangular side walls. The barrier has an overall height (h) of 5 m and a length (l) of 10 m. The length of the base slab (b) is 5 m. The widths of the stem wall, side walls, and the base slab (w_{stem}, w_{side} and w_{base} respectively) are 0.8 m. The length (c) and height (d) of the side walls are both 4.2 m in this example ($= h - w_{base} = b - h_{stem}$). The density of reinforced concrete (ρ_c) is assumed to be 2,500 kg/m^3. A boulder with a diameter (ϕ) of 1.2 m and a density (ρ_b) of 2,650 kg/m^3 hits the top of the barrier at a horizontal velocity (v_0) of 10 m/s. The coefficient of restitution (COR) is taken as 0.5. The barrier is assumed to behave as a rigid body and undergo pure rotational movement after the impact.

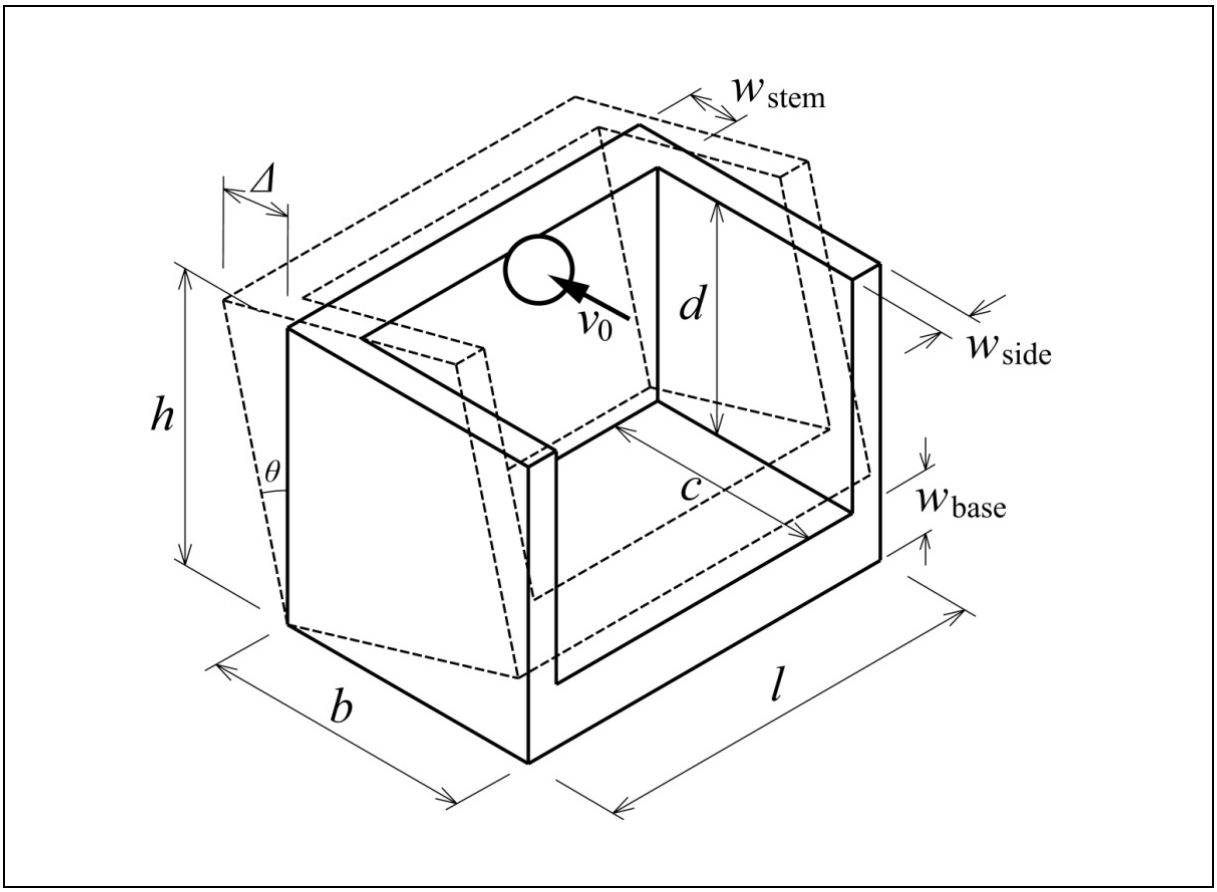

Figure C5 A Rigid L-shaped Barrier with Side Walls Impacted by a Boulder

Equation C.14 is used to calculate the rise of the barrier's centre of gravity, $\Delta_{C.G.}$, following the impact. The required parameters are computed first as follows:

Mass of boulder: $m = \rho_b \left[\frac{4}{3} \pi \left(\frac{\phi}{2} \right)^3 \right] = 2{,}397.8 \text{ kg}$

Mass of stem wall: $M_{stem} = \rho_c \, l \, w_{base} (h - w_{base}) = 84{,}000 \text{ kg}$

Mass of base slab: $M_{base} = \rho_c \, l \, b \, w_{base} = 100{,}000 \text{ kg}$

Mass of a single stem wall: $M_{side} = \rho_c \, d \, c \, w_{side} = 35{,}280 \text{ kg}$

Number of side walls: $n = 2$

Total mass of barrier: $M = M_{stem} + M_{base} + nM_{side} = 254{,}560 \text{ kg}$

Distance between axis of rotation and impact location:

$$r = \sqrt{h^2 + w_{stem}^2} = 5.0636 \text{ m}$$

Mass moment of inertia of barrier:

$$I_\theta = \frac{M_{stem}}{3}\left(h^2 + h w_{base}\right) + \frac{M_{base}}{3} \times b^2 + nM_{side}\left[\left(\frac{c^2 + d^2}{12}\right) + \left(\frac{d}{2} + w_{base}\right)^2 + \left(\frac{c}{2} + w_{stem}\right)^2\right]$$

$$I_\theta = 3{,}039{,}599 \text{ kg·m}^2$$

Dimensionless number: $\kappa = \frac{I_\theta}{mhr} = 50.0725$

Substituting the required information into Equation C.14 leads to:

$$\Delta_{C.G.} = \frac{mv_0^2}{2Mg} \times \frac{\kappa h}{r}\left(\frac{1 + \text{COR}}{1 + \kappa}\right)^2 = \frac{2397.7 \times 10^2}{2 \times 254{,}560 \times 9.81} \times \frac{50.0725 \times 5}{5.0636} \times \left(\frac{1 + 0.5}{1 + 50.0725}\right)^2$$

$\Delta_{C.G.} = 0.0020$ m (or 2.0 mm).

The stability of the barrier against overturning can be assessed by comparing the calculated $\Delta_{C.G.}$ with the critical value $\Delta_{C.G.(crit)}$. For the calculation of $\Delta_{C.G.(crit)}$, the centre of gravity of the barrier in the *x*- and *y*-directions first needs to be located with reference to a global origin, which can be conveniently set at the point of rotation. The computations can be carried out as follows:

Horizontal distance to the barrier's centre of gravity from global vertical axis:

$$\bar{x} = \frac{x_{\text{stem}} M_{\text{stem}} + x_{\text{base}} M_{\text{base}} + n\left(x_{\text{side}} M_{\text{side}}\right)}{M_{\text{stem}} + M_{\text{base}} + n M_{\text{side}}} = 1.9179 \text{ m}$$

Vertical distance to the barrier's centre of gravity from global horizontal axis:

$$\bar{y} = \frac{y_{\text{stem}} M_{\text{stem}} + y_{\text{base}} M_{\text{base}} + n\left(y_{\text{side}} M_{\text{side}}\right)}{M_{\text{stem}} + M_{\text{base}} + n M_{\text{side}}} = 1.9179 \text{ m}$$

Therefore, according to Equations C.16,

$$\Delta_{\text{C.G.(crit)}} = \bar{y}\left(\frac{1}{\cos\theta_{\text{crit}}} - 1\right) = 1.9179\left(\frac{1}{\cos 45^{\circ}} - 1\right) = 0.7944 \text{ m (or 794.4 mm)}$$

Since $\Delta_{\text{C.G.}} < \Delta_{\text{C.G.(crit)}}$, the barrier will not overturn.

The angle of rotation (θ) can also be computed using Equation C.14 as:

$$\theta = \sin^{-1}\left[\frac{\bar{y} + \Delta_{\text{h}}}{\sqrt{\bar{x}^2 + \bar{y}^2}}\right] - \tan^{-1}\left(\frac{\bar{y}}{\bar{x}}\right) = \sin^{-1}\left[\frac{1.9179 + 0.0020}{\sqrt{1.9179^2 + 1.9179^2}}\right] - \tan^{-1}\left(\frac{1.9179}{1.9179}\right) = 0.06^{\circ}$$

Section 2
Appendix D

Derivation of Miscellaneous Equations

Contents

		Page No.
Contents		133
List of Figures		134
D.1	Mass Moment of Inertia	135
D.1.1	Rectangular Shape	135
D.1.2	“L” Shape	136
D.1.3	“L” Shape with Rectangular Side Walls	138
D.2	Angular Velocity	139
D.3	Angle of Rotation	140
D.4	Critical Angle of Rotation	141

List of Figures

Figure No.		Page No.
D1	A Rectangular Barrier and Coordinate Systems	135
D2	An L-shaped Barrier and Coordinate Systems	136
D3	An L-shaped Barrier with Side Walls and Coordinate Systems	138
D4	Angular Velocity of a Rigid Barrier Undergoing Rotational Movement	140
D5	A Rigid Barrier Undergoing Rotational Movement	141
D6	A Rigid Barrier at Critical Overturning Condition	142

D.1 Mass Moment of Inertia

D.1.1 Rectangular Shape

Figure D1 shows a rectangular object with length l, width w, and height h. The mass moments of inertia about the two centroidal axes, x_c and y_c, are:

$$I_{x_c x_c} = \rho l\left(\frac{wh^3}{12}\right) = \frac{1}{12}Mh^2 \quad \text{..... (D.1)}$$

$$I_{y_c y_c} = \rho l\left(\frac{hw^3}{12}\right) = \frac{1}{12}Mw^2 \quad \text{..... (D.2)}$$

where ρ is density so that $M = \rho wlh$.

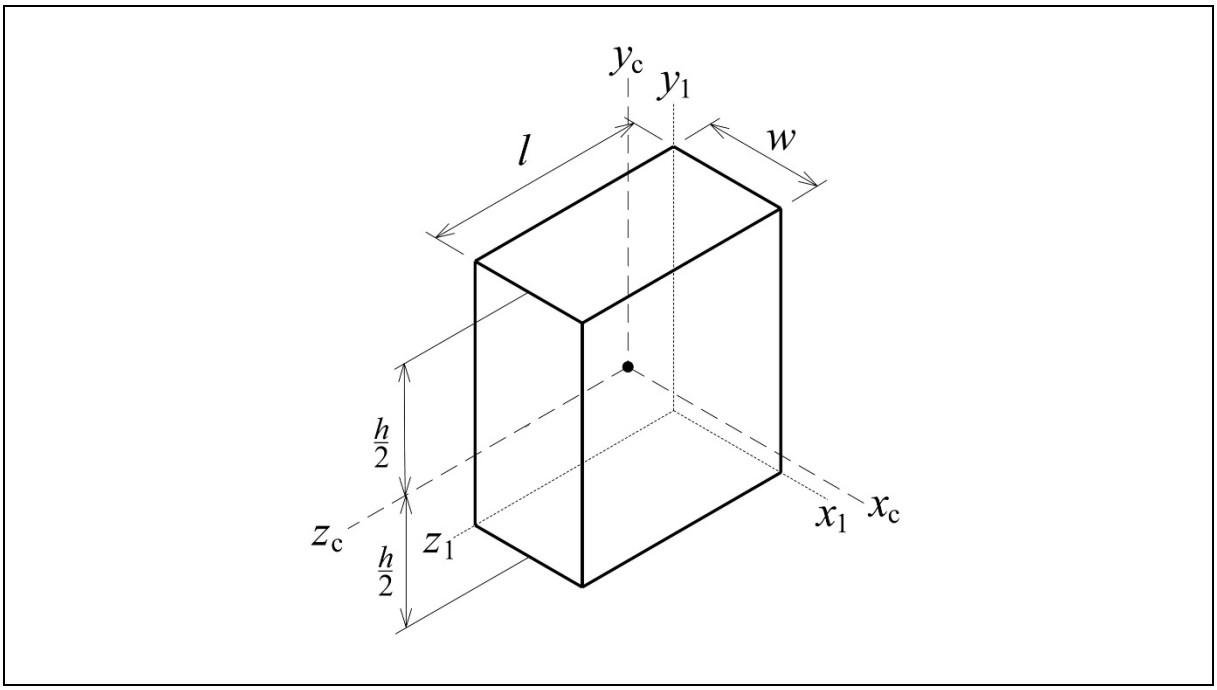

Figure D1 A Rectangular Barrier and Coordinate Systems

By the perpendicular axis theorem, the mass moment of inertia about the centroidal axis z_c is:

$$I_{z_c z_c} = I_{x_c x_c} + I_{y_c y_c} = M\left(\frac{h^2 + w^2}{12}\right) \quad \text{..... (D.3)}$$

By the parallel axis theorem, the mass moment of inertia about the axis z_1 is:

$$I_{z_1 z_1} = I_{z_c z_c} + M r^2 \quad \text{..... (D.4)}$$

where r is the distance between axes z_c and z_1, and can be expressed as:

$$r^2 = \left(\frac{h}{2}\right)^2 + \left(\frac{w}{2}\right)^2 = \frac{h^2 + w^2}{4} \quad \text{..... (D.5)}$$

Substituting Equations D.3 and D.5 into Equation D.4 gives:

$$I_{z_1 z_1} = M\left(\frac{h^2 + w^2}{12}\right) + M\left(\frac{h^2 + w^2}{4}\right) = M\left(\frac{h^2 + w^2}{3}\right) \quad \text{..... (D.6)}$$

D.1.2 "L" Shape

Equation D.6 is only valid for rectangular objects. For an L-shaped barrier consisting of a stem wall and a base slab and rotating about axis z_1 as shown in Figure D2, the total moment of inertia is the sum of the moments of inertia of these components, that is, $I_{z_1 z_1(\text{stem})}$ and $I_{z_1 z_1(\text{base})}$. As shown in Figure D2, the height and length of the base slab are denoted as h and b respectively, and the widths of the stem wall and the base slab are denoted as w_{stem} and w_{base} respectively. The distances between the axis of rotation and the centroidal axis of the stem wall and that of the base slab are respectively denoted as r_{stem} and r_{base}.

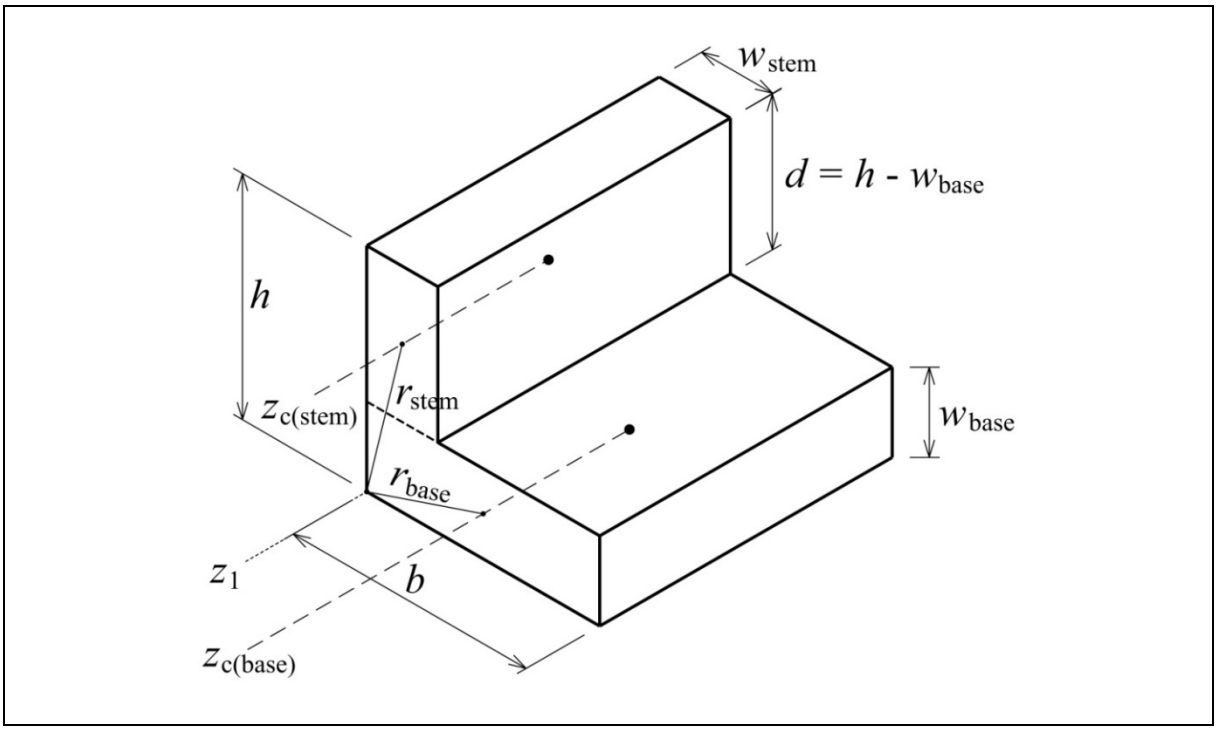

Figure D2 An L-shaped Barrier and Coordinate Systems

By the parallel axis theorem, the mass moment of inertia of the stem wall about axis z_1 can be written as:

$$I_{z_1z_1(\text{stem})} = I_{z_cz_c(\text{stem})} + M_{\text{stem}} r_{\text{stem}}^2 \quad \text{..... (D.7)}$$

which can be expanded as:

$$I_{z_1z_1(\text{stem})} = M_{\text{stem}}\left(\frac{d^2 + w_{\text{stem}}^2}{12}\right) + M_{\text{stem}}\left[\left(\frac{d^2}{4} + dw_{\text{base}} + w_{\text{base}}^2\right) + \left(\frac{w_{\text{stem}}}{2}\right)^2\right] \quad \text{..... (D.8)}$$

Since w_{stem} and w_{base} are much smaller than d, ignoring the contribution of their higher-order terms leads to:

$$I_{z_1z_1(\text{stem})} = M_{\text{stem}}\left(\frac{d^2}{12}\right) + M_{\text{stem}}\left(\frac{d^2}{4} + dw_{\text{base}}\right) \quad \text{..... (D.9)}$$

Substituting $d = h - w_{\text{base}}$ into Equation D.9 and rearranging thus gives:

$$I_{z_1z_1(\text{stem})} = \frac{M_{\text{stem}}}{3}\left(h - w_{\text{base}}\right)\left(h + 2w_{\text{base}}\right) \quad \text{..... (D.10)}$$

According to Equation D.6, the mass moment of inertia of the base slab about axis z_1 can be written as:

$$I_{z_1z_1(\text{base})} = \frac{M_{\text{base}}}{3}\left(b^2 + w_{\text{base}}^2\right) \quad \text{..... (D.11)}$$

Therefore, the mass moment of the L-shaped barrier is:

$$I_{z_1z_1} = \frac{M_{\text{stem}}}{3}\left(h - w_{\text{base}}\right)\left(h + 2w_{\text{base}}\right) + \frac{M_{\text{base}}}{3}\left(b^2 + w_{\text{base}}^2\right) \quad \text{..... (D.12)}$$

Expanding and ignoring the contribution of w_{base}^2 finally leads to:

$$I_{z_1z_1} = \frac{M_{\text{stem}}}{3}\left(h^2 + hw_{\text{base}}\right) + \frac{M_{\text{base}}}{3} \times b^2 \quad \text{..... (D.13)}$$

This approximate equation can be used to calculate the moment of inertia of an L-shaped barrier. It is worth noting that the calculated value of $I_{z_1z_1}$ will be slightly less than the true value since the higher-order terms of w_{stem} and w_{base} are ignored during the derivation of Equation D.13. For example, for an L-shaped barrier with h and b equal to 5 m and w_{stem} and w_{base} equal to 0.8 m, the value of $I_{z_1z_1}$ is underestimated by 6% if calculated using Equation D.13. This is deemed acceptable for the purpose of barrier design since the error is on the safe

side. In the main text, $I_{z_1 z_1}$ is referred to as I_θ to denote that it is the mass moment of inertia about the barrier's axis of rotation.

D.1.3 "L" Shape with Rectangular Side Walls

Figure D3 shows an L-shaped barrier with two rectangular side walls. The side walls have height d and length c. The mass of a single side wall is denoted as M_{side}.

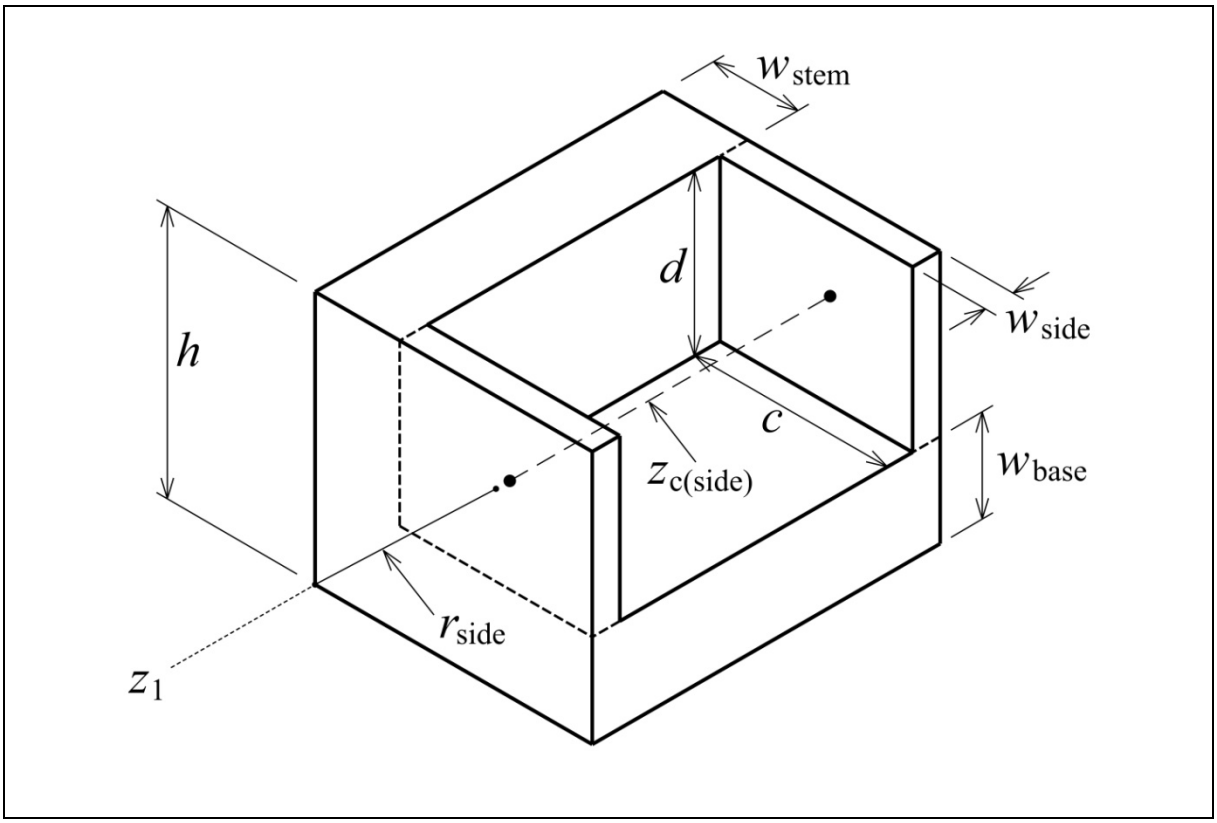

Figure D3 An L-shaped Barrier with Side Walls and Coordinate Systems

The mass moment of inertia of a single side wall about its centroidal axis z_c is:

$$I_{z_c z_c(\text{side})} = M_{\text{side}} \left(\frac{c^2 + d^2}{12} \right) \quad \text{..... (D.14)}$$

where $d = h - w_{\text{base}}$ and $c = b - w_{\text{stem}}$.

By the parallel axis theorem, the side wall's mass moment of inertia about the axis z_1 is:

$$I_{z_1 z_1(\text{side})} = I_{z_c z_c(\text{side})} + M_{\text{side}} r_{\text{side}}^2 \quad \text{..... (D.15)}$$

where r is the distance between axes z_c and z_1, and can be expressed as:

$$r_{\text{side}}^2 = \left(\frac{d}{2} + w_{\text{base}}\right)^2 + \left(\frac{c}{2} + w_{\text{stem}}\right)^2 \quad \text{..... (D.16)}$$

Substituting Equations D.14 and D.16 into Equation D.15 gives:

$$I_{z_1 z_1(\text{side})} = M_{\text{side}}\left(\frac{c^2 + d^2}{12}\right) + M_{\text{side}}\left[\left(\frac{d}{2} + w_{\text{base}}\right)^2 + \left(\frac{c}{2} + w_{\text{stem}}\right)^2\right] \quad \text{..... (D.17)}$$

or

$$I_{z_1 z_1(\text{side})} = M_{\text{side}}\left[\left(\frac{c^2 + d^2}{12}\right) + \left(\frac{d}{2} + w_{\text{base}}\right)^2 + \left(\frac{c}{2} + w_{\text{stem}}\right)^2\right] \quad \text{..... (D.18)}$$

Note that only a single side wall is considered above. For barriers with two identical side walls (or more), the combined mass moment of inertia is:

$$I_{z_1 z_1(\text{side})} = nM_{\text{side}}\left[\left(\frac{c^2 + d^2}{12}\right) + \left(\frac{d}{2} + w_{\text{base}}\right)^2 + \left(\frac{c}{2} + w_{\text{stem}}\right)^2\right] \quad \text{..... (D.19)}$$

where n is the number of side walls. Summing Equations D.13 and D.19 finally gives the mass moment of inertia of the whole barrier:

$$I_{z_1 z_1} = \frac{M_{\text{stem}}}{3}\left(h^2 + hw_{\text{base}}\right) + \frac{M_{\text{base}}}{3} \times b^2 + nM_{\text{side}}\left[\left(\frac{c^2 + d^2}{12}\right) + \left(\frac{d}{2} + w_{\text{base}}\right)^2 + \left(\frac{c}{2} + w_{\text{stem}}\right)^2\right] \quad \text{.....(D.20)}$$

Equation D.20 can be used to calculate the mass moment of inertia of an L-shaped barrier with any number of side walls about axis z_1, which is assumed to be the axis of rotation. Note that since Equation D.13 is an approximate equation, Equation D.20 is also approximate but the error is on the safe side as previously discussed. In the main text, $I_{z_1 z_1}$ is denoted as I_θ to denote that it is the mass moment of inertia about the axis of rotation.

D.2 Angular Velocity

Figure D4 shows a rectangular block rotating at velocity v_2. A rectangular shape is assumed here but the result is also valid for barriers of other shapes. The angle of rotation is denoted as θ. The arc length s as shown in Figure D4 can be expressed as:

$$s = v_2 t = r\theta \quad \text{..... (D.21)}$$

where t is time and r is the distance between the point of rotation and the point of boulder impact. Rearranging Equation D.21 and differentiating it with respect of t gives:

$$\dot{\theta} = \frac{\mathrm{d}\theta}{\mathrm{d}t} = \frac{v_2}{r} \quad \text{..... (D.22)}$$

where $\dot{\theta}$ is the angular speed.

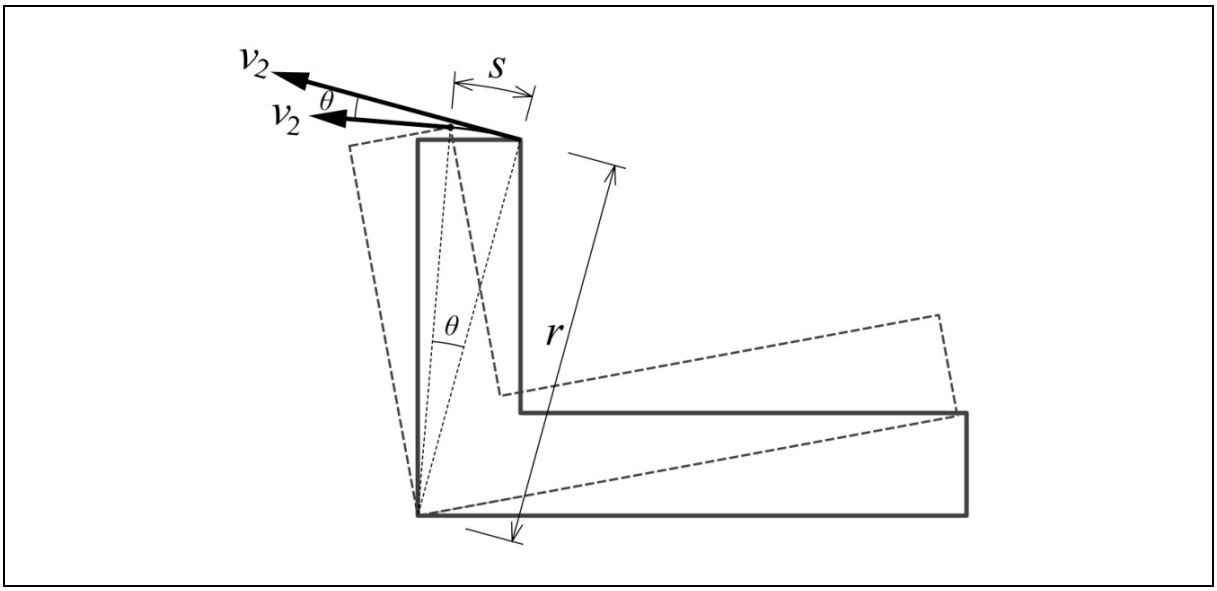

Figure D4 Angular Velocity of a Rigid Barrier Undergoing Rotational Movement

D.3 Angle of Rotation

Figure D5 shows a rigid barrier undergoing rotational movement after impact by a boulder. The angle of rotation is θ. The centre of gravity of the barrier is located at point $(\bar{x},\bar{y})$. For an object which has a uniform material density (or mass per unit area in two dimensions), its centroid is also its centre of gravity. The distance between the point of rotation and the centre of gravity is $\sqrt{\bar{x}^2+\bar{y}^2}$. This line is inclined to the horizontal at angle β and is equal to $\tan^{-1}\left(\frac{\bar{y}}{\bar{x}}\right)$. From geometry, it can be shown that:

$$\sin(\beta+\theta)=\frac{(\bar{y}+\Delta_{\text{C.G.}})}{\sqrt{\bar{x}^2+\bar{y}^2}} \quad \text{..... (D.23)}$$

Substituting $\beta=\tan^{-1}\left(\frac{\bar{y}}{\bar{x}}\right)$ and rearranging thus gives:

$$\theta=\sin^{-1}\left[\frac{\bar{y}+\Delta_{\text{C.G.}}}{\sqrt{\bar{x}^2+\bar{y}^2}}\right]-\tan^{-1}\left(\frac{\bar{y}}{\bar{x}}\right) \quad \text{..... (D.24)}$$

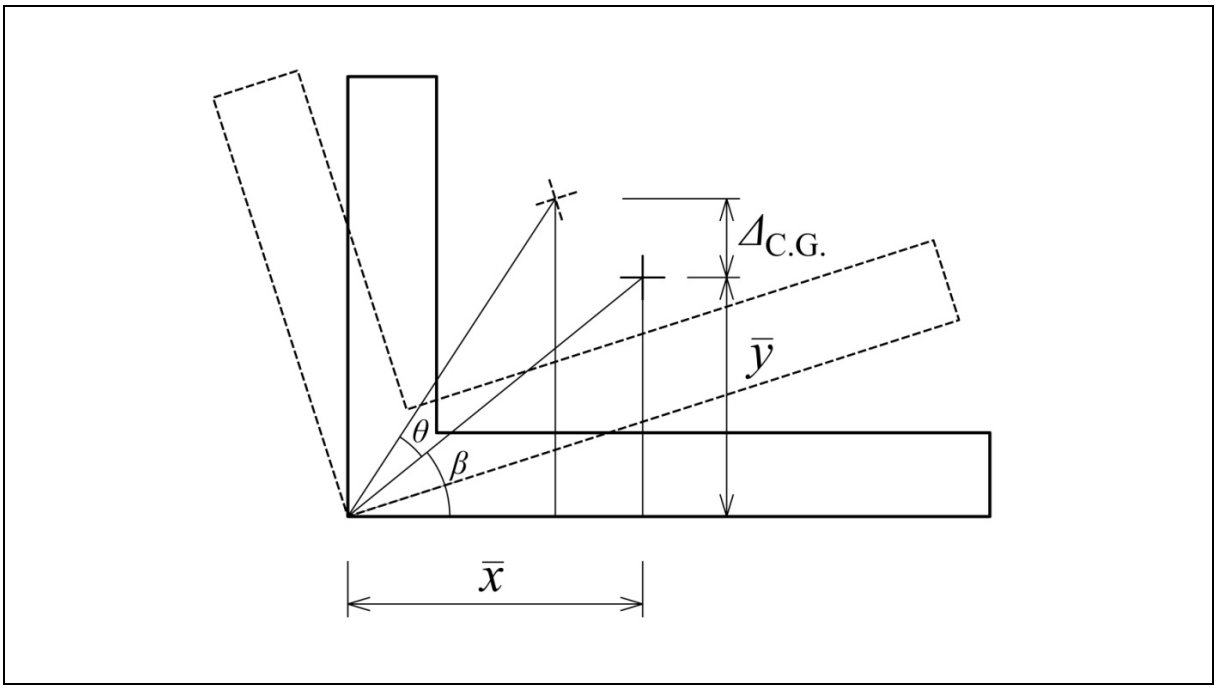

Figure D5 A Rigid Barrier Undergoing Rotational Movement

D.4 Critical Angle of Rotation

Figure D6 shows a rigid barrier at the critical condition in terms of overturning stability, that is, when the barrier's centre of gravity lies immediately above the point of rotation. It is assumed here that the barrier is situated on a horizontal ground surface. An L-shaped barrier is also assumed here but the following derivation is also applicable to other shapes provided that the barrier's centre of gravity is known. As shown in Figure D6, the centre of gravity is located at the perpendicular distance $\bar{x}$ measured from the outer edge of the stem wall and the perpendicular distance $\bar{y}$ measured from the bottom of the base slab. The distance between the point of rotation and the centre of gravity is thus $\sqrt{\bar{x}^2 + \bar{y}^2}$. At this critical condition, the barrier's angle of rotation and the rise of the centre of gravity are denoted as θ_{crit} and $\Delta_{C.G.(crit)}$ respectively. From geometry, it can be shown that:

$$90° = \theta_{crit} + \beta \quad \text{..... (D.25)}$$

Substituting $\beta = \tan^{-1}\left(\frac{\bar{y}}{\bar{x}}\right)$ and rearranging thus gives:

$$\theta_{crit} = 90° - \tan^{-1}\left(\frac{\bar{y}}{\bar{x}}\right) \quad \text{..... (D.26)}$$

The rise of the centre of gravity, $\Delta_{C.G.(crit)}$, can be expressed as:

$$\Delta_{C.G.(crit)} = \sqrt{\bar{x}^2 + \bar{y}^2} - \bar{y} \quad \text{..... (D.27)}$$

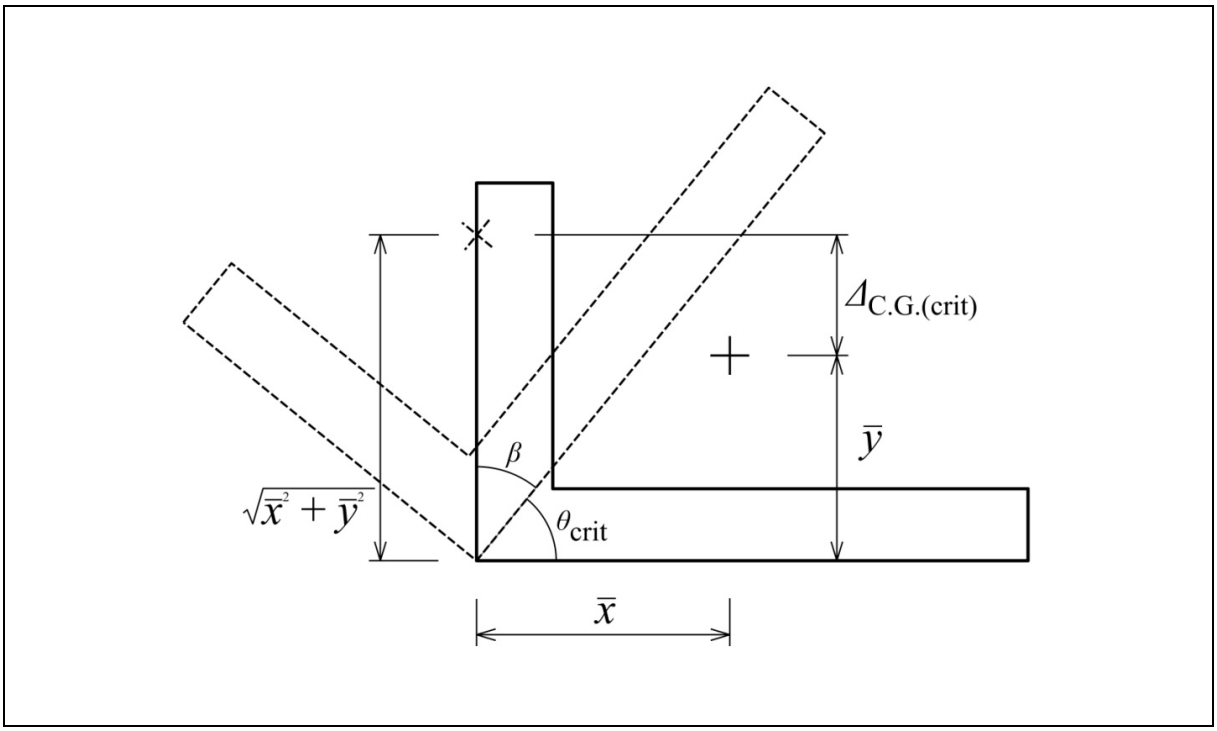

Figure D6 A Rigid Barrier at Critical Overturning Condition

Glossary of Symbols

Glossary of Symbols

A	contact area between barrier base and ground surface
b	base slab
c	length of side wall
COR	coefficient of restitution, defined as the ratio of relative speeds after and before an impact
d	height of side wall
g	gravity
h	height of wall
h_b	vertical height of boulder from the barrier's point of rotation
h_i	initial height of boulder for measurement of COR
h_r	rebound height of boulder for measurement of COR
KE_0	initial kinetic energy of the impactor
KE_1	rebound kinetic energy of the impactor
KE_2	kinetic energy gained by the impact-resisting object
l	length of wall
M	total mass of barrier
M_{base}	mass of base slab
M_{side}	mass of a single side wall
M_{stem}	mass of stem wall
m	mass of boulder
n	number of side walls
PE	barrier's gain in potential energy
r	distance between the axis of rotation and the point of impact

r_{base}	distance between the axis of rotation and the centroidal axis of the base slab
r_{side}	distance between the axis of rotation and the centroidal axis of the side wall
r_{stem}	distance between the axis of rotation and the centroidal axis of the stem wall
s	arc length
t	time
u	water uplift pressure acting on base slab
v_0	initial velocity of boulder
v_1	rebound velocity of boulder
v_2	velocity of barrier
w_{base}	width of base slab
w_{side}	width of side wall
w_{stem}	width of stem wall
x_1	global axis in the x-direction
x_c	centroidal axis in the x-direction (for a rectangular block)
$\bar{x}$	horizontal distance to the barrier's centre of gravity from global vertical axis
y_1	global axis in the y-direction
y_c	centroidal axis in the y-direction (for a rectangular block)
$\bar{y}$	vertical distance to the barrier's centre of gravity from global horizontal axis
z_1	global axis in the z-direction
z_c	centroidal axis in the z-direction (for a rectangular block)
$z_{c(base)}$	centroidal axis of base slab in the z-direction
$z_{c(stem)}$	centroidal axis of stem wall in the z-direction
Δ	horizontal displacement at barrier top on the downstream face
Δ_{crit}	critical horizontal displacement at barrier top on the downstream face
$\Delta_{C.G.}$	rise of the barrier's centre of gravity

$\Delta_{C.G.(crit)}$	rise of the barrier's centre of gravity at the critical overturning condition
θ	angle of rotation
θ_{crit}	critical angle of rotation
$\dot{\theta}$	angular speed
λ	mass ratio between the impact-resisting object and the impactor
β	angle to the horizontal of a straight line connecting the barrier's centre of gravity to the point of rotation
δ'	effective interface friction angle between concrete and soil
ρ_b	density of boulder
ρ_c	density of concrete
ϕ	diameter of boulder
κ	a dimensionless number considering mass and geometrical effects of barrier
I_θ	barrier's mass moment of inertia about the axis of rotation (= I_{z1z1})
I_{z1z1}	barrier's mass moment of inertia about the axis z_1

Section 3: Verification of Displacement Approach for Rigid Debris-resisting Barriers Subject to Boulder Impacts

L.A. Wong & H.W.K. Lam

This section is largely based on GEO Technical Note No. TN 4/2019 produced in December 2019

Foreword

This Technical Note summarises a series of studies on verification of Displacement Approach for assessing geotechnical stability of rigid debris-resisting barriers subject to boulder impact. This study was carried out by Mr L.A. Wong under the supervision of Mr H.W.K. Lam. The verification is largely based on physical tests and advanced numerical modelling. In particular, a series of physical tests were carried out in collaboration with the University of Melbourne and the Hong Kong University of Science and Technology. The Drafting Unit of the Standards and Testing Division assisted in formatting this Note.

Various colleagues in the GEO provided constructive comments on the Note. All contributions are gratefully acknowledged.

T.K.C. Wong
Chief Geotechnical Engineer/Standards and Testing
December 2019

Abstract

Boulder impact loads on rigid barriers are known to be highly transient and of high magnitude. Local design practice which adopts force and moment equilibrium analyses based on Hertz Load model for the assessment of geotechnical stability could often yield an overly conservative design solution. With a view to optimising the design of rigid barriers, GEO in the past few years has initiated various studies to establish an alternative design approach for assessing geotechnical stability of rigid barriers subject to boulder impacts. In particular, analytical solutions to predict sliding and overturning displacement have been developed which consider the inertia effect of the barrier wall and energy loss during an impact process. To verify the reliability of the analytical solutions, physical tests and numerical modelling have been carried out. In particular, a series of large-scale experiments have been conducted.

Contents

			Page No.
Title Page			147
Foreword			148
Abstract			149
Contents			150
List of Tables			152
List of Figures			153
1	Introduction		154
2	Small-scale Experiments to Verify Displacement Approach		156
3	Large-scale Impact Tests to Verify Displacement Approach		158
	3.1	General	158
	3.2	Flume Facilities and Test Setup	159
	3.3	Model Barrier	159
	3.4	Instrumentation System	160
	3.5	Test Program	161
	3.6	Test Results	162
		3.6.1 Boulder Impact Mechanism	162
		3.6.2 Prediction of Barrier Movement and Verification of Displacement Approach	165
4	Numerical Analysis		166
	4.1	Numerical Analysis for Prediction of Sliding of Barrier	166
	4.2	Numerical Analysis for Prediction of Rotation of Barrier	167
5	Effect of Multiple Impacts		169
6	Effect of Size of Boulder on Geotechnical Stability of Rigid Barrier		171
7	Conclusion		172
8	References		172

		Page No.
Section 3 Appendix A:	Results of Large-scale Flume Tests Conducted in Kadoorie Centre, Hong Kong	174

List of Tables

Table No.		Page No.
2.1	Comparison of Experimental Results and Predictions of Rotational Movement Based on Displacement Approach	157
2.2	Comparison of Experimental Results and Prediction Based on Displacement Approach for Sliding Movement	158
3.1	Details of Instruments	160
3.2	Test Program	161
3.3	Comparison of Prediction of Movements with Experimental Results	165
4.1	Comparison of Sliding Movement Predicted in Numerical Simulation and That Predicted Based on Displacement Approach	167
4.2	Comparison of Rotational Movement Predicted in Numerical Simulation and That Predicted Based on Displacement Approach	168
5.1	Results of Sensitivity Study of Rigid Barrier Subject to Multiple Boulder Impacts using Displacement Approach	171
6.1	Mass of Rigid Barrier Where Estimated Displacements Are Generally Insignificant	172

List of Figures

Figure No.		Page No.
1.1	Analytical Solutions for Prediction of Rotational (Upper) and Sliding (Lower) Movement of Rigid Barriers (Lam & Kwan, 2016)	155
2.1	Setup of Small-scale Experiments for the Verification of Displacement Approach for the Prediction of Rotational Movement	156
2.2	Setup of Small-scale Experiments for the Verification of Displacement Approach for the Prediction of Sliding Movement	158
3.1	Photograph of Flume (Left), Front View of Model Barrier (Upper Right) and Side View of Model Barrier (Lower Right)	160
3.2	Granitic Spheres Adopted in Large-scale Impact Tests	161
3.3	Snapshots of Test No. K5 Taken from High Speed Camera inside the Flume	162
3.4	Snapshots of Test No. K2 Taken from Normal Camera Installed in a Drone	163
3.5	Snapshots of Test No. K2 Taken from High Speed Camera Installed inside the Flume	164
3.6	Snapshots of Test No. K4 Taken from High Speed Camera Installed inside the Flume	164
4.1	Model Setup for Numerical Analysis for Prediction of Sliding Movement of Barrier	167
4.2	Model Setup for Numerical Analysis for Prediction of Rotational Movement of Barrier	168
5.1	Boulders Contained in Debris Flows in Hong Kong	169
5.2	Sensitivity Study of Rigid Barrier Subject to Multiple Boulder Impacts	170

1 Introduction

Boulder impact loads on rigid barriers are known to be highly transient and of high magnitude. Local design practice adopts force and moment equilibrium analyses for the assessment of geotechnical stability of rigid barriers subject to impacts from hard inclusions (i.e. boulders) contained in a debris flow. The boulder impact load is assumed to be pseudo-static and evaluated based on Hertz's Equation, with a load reduction factor of 0.1 (Kwan, 2012). Local design experience indicates that such approach may still require extensive foundations and/or tie-backs in order to achieve the geotechnical stability. Apparently, there is room for design optimisation in this respect.

In 2015, the GEO partnered with the University of Melbourne (UoM) and started to develop an alternative approach for assessing geotechnical stability of rigid barriers subject to boulder impacts (see Figure 1.1). Findings of this study have been documented in Lam & Kwan (2016).

Under the study by Lam & Kwan (2016), a novel approach, known as "Displacement Approach" in this report, has been proposed which considers energy transferred in the impact process to calculate the sliding and rotational movement of rigid barriers. Two sets of analytical solutions for Displacement Approach were derived, one for sliding movement and the other for rotational movement, and both of them take into account the contributions of the self-weight and, thus, the inertial resistance of the barrier in resisting an impact (Figure 1.1). The amount of energy transferred from boulders to the barrier is considered as a function of the mass ratio and the coefficient of restitution between the two objects. The prediction of sliding movement under the Displacement Approach is based on the energy dissipation by the barrier due to work done against basal friction, whereas the prediction of rotational movement is based on work done of the barrier against gravitational force (i.e. uplift of centre of gravity of barrier). Details of Displacement Approach, including its assumptions, derivation of the formulations and some worked examples, have been reported in Lam & Kwan (2016). This approach had not been verified at that time.

Experimental verification of Displacement Approach was recently carried out, in collaboration with local and overseas academics, which includes small-scale pendulum impact tests conducted by the UoM and large-scale impact tests conducted by the Hong Kong University of Science and Technology (HKUST). This Technical Note documents the key findings of these experimental studies, with particular focus on the large-scale physical tests using the newly established flume facility in the Kadoorie Centre in Hong Kong.

Rotational Movement (in terms of Rise of Barrier's Centre of gravity)

$$\Delta_{C.G.} = \frac{KE_0}{Mg} \times \frac{kh_b}{r}\left(\frac{1+\mathrm{COR}}{1+k}\right)^2$$

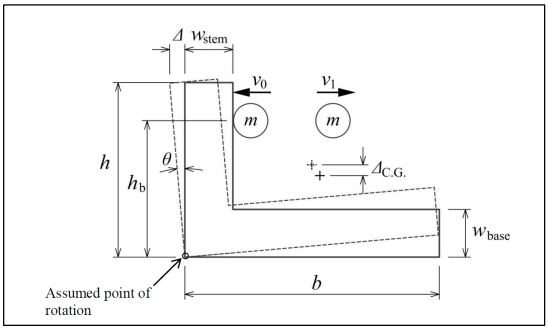

Note:

Angle of rotation of barrier,

$$\theta = \sin^{-1}\left(\frac{\bar{y}+\Delta_{C.G.}}{\sqrt{\bar{x}^2+\bar{y}^2}}\right) - \tan^{-1}\left(\frac{\bar{y}}{\bar{x}}\right),$$

where $\bar{x}$ and $\bar{y}$ are the distances to the barrier's centre of gravity measured from the outer edge of wall stem and the base respectively.

Sliding Movement

$$\Delta = \lambda\left(\frac{1+\mathrm{COR}}{1+\lambda}\right)^2 \frac{KE_0}{(Mg\text{-}uA)\tan\delta}$$

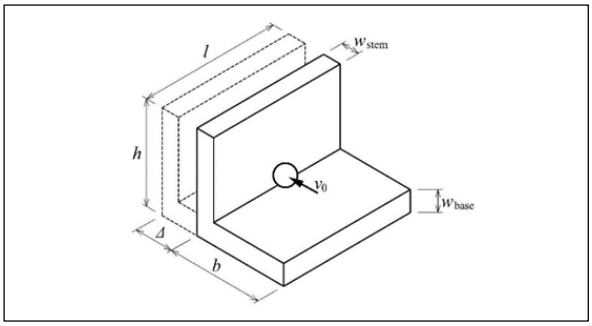

where $\Delta_{C.G.}$ = rise of the barrier's centre of gravity (in m)
Δ = sliding movement of barrier (in m)
KE_0 = kinetic energy of boulder before impact (in J)
M = mass of barrier (in kg)
g = gravitational acceleration (9.81 m/s^2)
k = $\frac{I_\theta}{mhr}$ (dimensionless; ≥ 1), where I_θ is the mass moment of inertia of barrier, and h is the height of barrier
h_b = distance between the point of impact to the point of rotation (in m)
r = distance between the axis of rotation and the point of impact (in m)
COR = coefficient of restitution (dimensionless), being (boulder rebound velocity + barrier's velocity after impact)/velocity of boulder before impact
λ = mass ratio between barrier and boulder (dimensionless)
u = water uplift pressure acting on barrier (in N/m^2)
A = contact area between barrier base and ground surface (in m^2)
δ = effective interface friction angle between concrete and its founding materials (in m^2)

Figure 1.1 Analytical Solutions for Prediction of Rotational (Upper) and Sliding (Lower) Movement of Rigid Barriers (Lam & Kwan, 2016)

2 Small-scale Experiments to Verify Displacement Approach

Since 2017, GEO has collaborated with the UoM to carry out two series of small-scale pendulum impact tests to verify the Displacement Approach with respect to the prediction of rotational and sliding movements for rigid barriers.

For the verification of prediction of rotational movement, a small-scale L-shaped rigid barrier was used which was 0.8 m high, 0.4 m wide and 0.2 m thick, with a 0.4 m long base slab (see Figure 2.1). The model barrier weighed approx. 230 kg. The impactor adopted for the tests was a cast iron sphere with a mass of 5 kg. In the impact tests, the impactor was lifted (using a pendulum setup) to 0.5 m, 1.0 m and 1.5 m high, which corresponds to a potential energy of 25 to 75 J, and then released to strike the crest of the centre of the wall stem at an impact velocity up to 5.4 m/s. The barrier directly seated on a concrete slab and was free from any restraints for sliding or rotation.

During the tests, a laser sensor was used to measure the time history of movement of the barrier at its crest. The experimental setup is shown in Figure 2.1 below. Table 2.1 shows the experimental results of rotational movements and the corresponding predicted rotational movements based on Displacement Approach. It was found that the two sets of values matched well. Further details of the tests and data interpretation are given in Lam et al (2018).

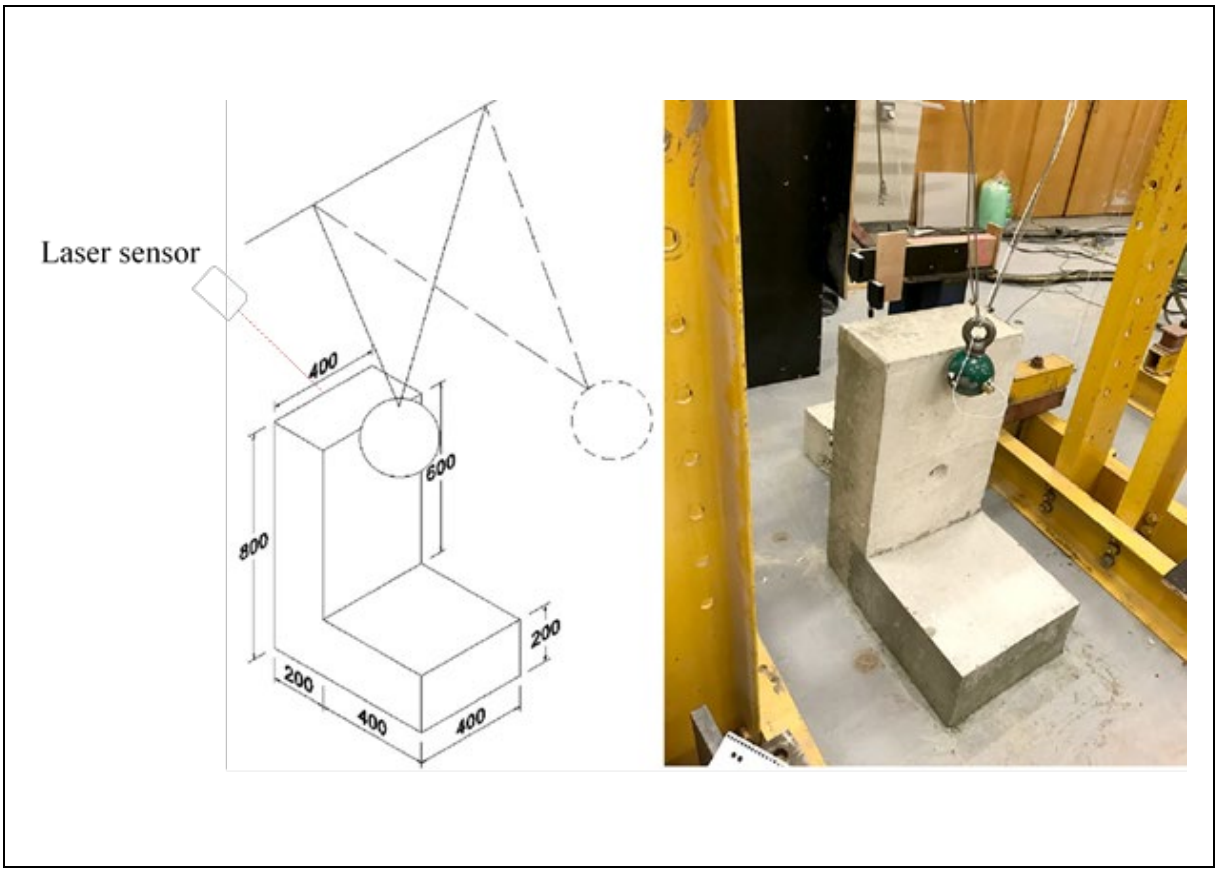

Figure 2.1 Setup of Small-scale Experiments for the Verification of Displacement Approach for the Prediction of Rotational Movement

Table 2.1 Comparison of Experimental Results and Predictions of Rotational Movement Based on Displacement Approach

Test No.	Measured Peak Horizontal Movement at Crest of Wall Stem (mm)	Predicted Horizontal Movement at Crest of Wall Stem Based on Displacement Approach (mm)
R1	6.7	6.2
R2	11.7	11.6
R3	15.5	15.3

Notes:
(1) The angle of rotation (θ) of the model barrier is a function of the horizontal movement at the crest of the wall stem (Δ) (i.e. $\sin \theta = \Delta/h$, where h = the height of the wall stem) assuming that the wall stem is rigid.
(2) COR used in the prediction of barrier's movement was estimated using the actual velocity of impactor before and after impact as interpreted from high speed camera footages, and the calculated velocity of model barrier after impact based on conservation of momentum.

To verify Displacement Approach for prediction of sliding movement of rigid barriers subject to boulder impacts, another series of small-scale physical tests were carried out at the UoM. The tests involved a free-standing L-shaped rigid barrier which was 0.5 m high, 0.6 m wide and 0.1 m thick, with a 0.4 m long base slab. The model barrier weighed approx. 130 kg and was placed on a concrete slab. The impactor was a cast iron sphere with a mass of 5 kg.

In this series of tests, the impactor was lifted to different heights, from 0.3 m to 1.8 m (corresponding to a potential energy ranging from 15 to 90 J), with an impact velocity up to 6.0 m/s. The impactor was then released to strike the base slab of the model barrier using a pendulum setup. Such impact location was adopted so as to ensure that the barrier would predominantly slide, but not move in other modes such as rotation, for the sake of verifying prediction of sliding movement based on the Displacement Approach. A steel plate weighing about 1.8 kg was placed at the impact location on the model barrier to prevent localised damage of concrete. The barrier seated on a concrete slab and was free from any restraints for sliding or rotation.

During the tests, two laser sensors were used to measure the time history of movements of the barrier at its crest and base respectively. The experimental setup is shown in Figure 2.2. Yong et al (2019) presented the prediction of barrier's movement based on Displacement Approach and the experimental results as extracted in Table 2.2, and found that the two sets of values matched well. In addition, numerical analyses were conducted. Further details of the tests, data interpretation and numerical analyses are given in Yong et al (2019).

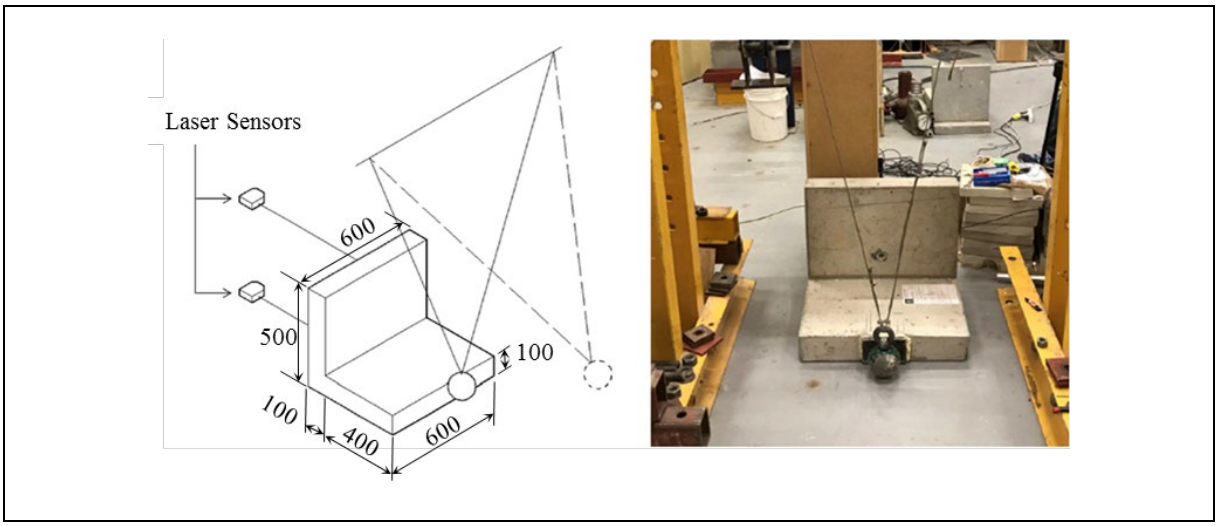

Figure 2.2 Setup of Small-scale Experiments for the Verification of Displacement Approach for the Prediction of Sliding Movement

Table 2.2 Comparison of Experimental Results and Prediction Based on Displacement Approach for Sliding Movement

Test No.	Measured Sliding Movement Using Laser Sensor (mm)	Predicted Sliding Movement Based on Displacement Approach (mm)
T1	1.8	1.5
T2	3.7	3.7
T3	5.0	4.9
T4	7.6	7.5
T5	8.8	8.7

Note: COR used in the prediction of barrier's movement was estimated using the actual velocity of impactor before and after impact as interpreted from high speed camera footages, and the calculated velocity of model barrier after impact based on conservation of momentum.

3 Large-scale Impact Tests to Verify Displacement Approach

3.1 General

To further verify Displacement Approach for boulder impact at a higher impact energy level, GEO collaborated with the HKUST to carry out a series of large-scale physical impact tests in the Kadoorie Centre in Hong Kong (HKUST, 2019). Details of the flume facilities, setup, model rigid barrier, debris mix and test programme are discussed in this Section.

3.2 Flume Facilities and Test Setup

The tests were carried out using the newly established flume facility at Kadoorie Centre in Hong Kong. The flume is in total 28 m long, 2 m wide and 1 m deep (see Figure 3.1). It comprises three key parts, including a storage tank at the upstream, a transportation channel, and a deposition zone.

The storage tank has a gradient of 30° at the base. There is a mechanical opening gate at the outlet of the storage tank which was designed to facilitate release of boulders in a repeatable manner.

There is a 2 m wide transportation channel below the storage tank, which is formed by a steel frame structure with two sides of 1 m high side-walls. The side-walls are propped to each other at the top with cross beams at a spacing of about 5 m.

The transportation channel is inclined at 20°. To avoid damage of the transparent side wall, polyethylene foam boards were installed along the transportation channel.

The deposition zone is 2 m wide and 8 m long, formed by two side-walls supported by external raking struts, and located at the outlet of the transportation channel. It is founded on a 5 m wide and 8 m long levelled concrete pad.

The transition between the transportation channel and the deposition zone is made of mass concrete and was smoothened to minimise energy loss to the boulder motion during testing.

3.3 Model Barrier

To simulate a realistic boulder-barrier interaction, a model barrier was constructed at the deposition zone to receive strikes for different impact scenarios. The model barrier was an L-shaped reinforced concrete barrier (see Figure 3.1), where the wall stem was 1.8 m high (including thickness of base slab), 1.9 m wide and 0.3 m thick, and the base slab was 1.5 m long (excluding thickness of wall stem), 1.9 m wide and 0.3 m thick. The characteristic strength of the concrete used was 30 MPa. The reinforcement of the barrier involved two layers of A393 wire mesh (characteristic strength of 500 MPa) at the front side (i.e. tension side) of the wall stem, and one layer of such wire mesh at the other side of the stem and wall base.

To prevent structural damage of the wall stem during the impact tests, a steel plate which is 1.5 m high, 1.9 m wide and 0.02 m thick was mounted onto the wall stem, with some stud connections. The weight of the model barrier, together with the protective steel plate, was about 5 tonnes.

The model barrier was founded on a layer of compacted granitic fill materials placed at the deposition zone. The model rigid barrier was set free to slide and rotate during the impact process. A small gap of approx. 50 mm is allowed between the side of the barrier wall and the sidewalls of the flume, to get rid of the effect of side frictions (see upper right photo in Figure 3.1).

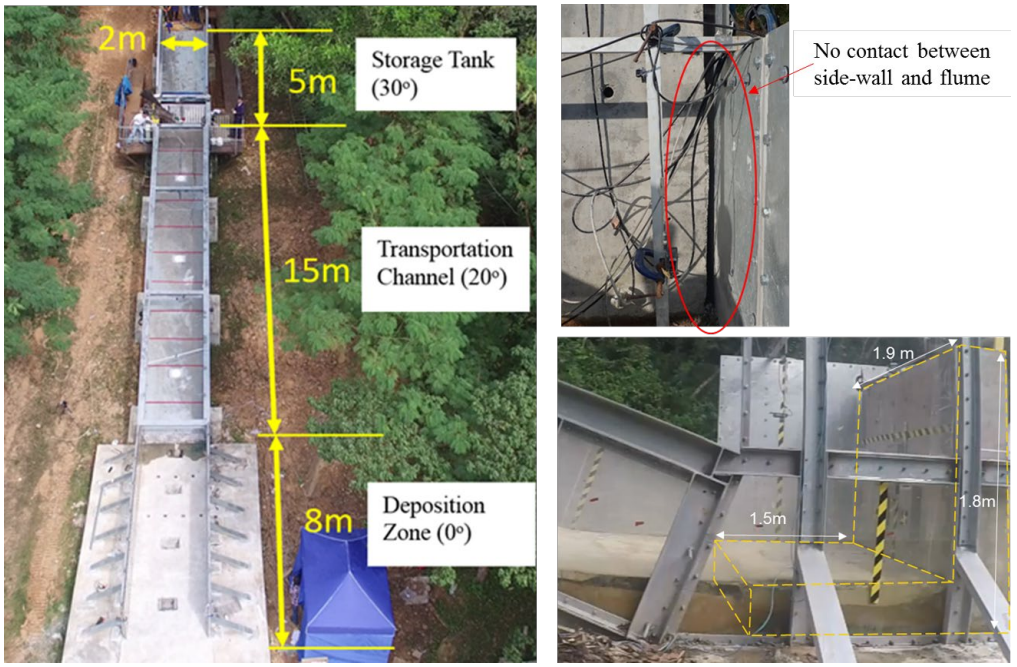

Note: Four laser sensors were installed at the four corners at the back of wall stem.

Figure 3.1 Photograph of Flume (Left), Front View of Model Barrier (Upper Right) and Side View of Model Barrier (Lower Right)

3.4 Instrumentation System

The instrumentations used in this study are summarised in Table 3.1 below. Two high speed cameras were adopted (one inside the flume and the other at the side of the barrier) to capture the impact process and impact velocity of the boulders. The movement of the model barrier was measured by the laser sensors installed at the back of its wall stem. Four laser sensors were adopted in Test Nos. K1 to K3 whereas two were adopted in Test Nos. K4 and K5 (see Section 3.5 for the test program).

Table 3.1 Details of Instruments

Instruments	Measurable Range	Frequency	Accuracy	Quantity and Installation Location	Key Purpose
Laser sensor	< 1 m	2 kHz	+/- 0.5%	4 sensors (for Test Nos. K1 to K3) or 2 sensors (for Test Nos. K4 and K5) at the back of the barrier wall	To capture movement of the barrier
High speed camera (2336 x 1728 pixel)	-	operating at 560 frames per second	-	1 camera installed in the middle of the flume	To capture impact process and boulder impact velocity

3.5 Test Program

Five impact tests involving different impact scenarios (i.e. different number and size of boulders) were carried out as summarised in Table 3.2. In general, according to the Displacement Approach, the kinetic energy gained by the barrier upon a boulder impact is sensitive to the mass ratio between barrier and impactor (i.e. λ as shown in Figure 1.1). In Test Nos. 4 and 5, a boulder up to 0.6 m in diameter was adopted, which is about 300 kg in weight and corresponds to a mass ratio of barrier to boulder of 17. Such a mass ratio is comparable to that for an impact scenario that may be encountered in routine designs (i.e. involving a sizeable boulder of 2 m in diameter of about 11 tonnes and a 200 tonnes rigid barrier).

For each test, a boulder or a cluster of boulders were first placed in the storage tank, just behind the opening gate as shown in Figure 3.2. Upon release of the opening gate, the boulder(s) would travel along the transportation channel and then strike onto the wall stem of the barrier at the deposition zone. The impact velocity of the boulders when approaching the model barrier and the displacement of the barrier (both transient and permanent) were measured based on the instrumentation plan given in Section 3.4.

Table 3.2 Test Program

Test No.	No. of Boulders	Boulder Diameter	Mass of Each Boulder	Mass Ratio between Model Barrier to Each Boulder
K1	1	200 mm	11 kg	449
K2	10	200 mm	11 kg	449
K3	10	400 mm	90 kg	55
K4	1	600 mm	300 kg	17
K5 (repeat of K4)	1	600 mm	300 kg	17

Ten 200 mm Diameter Granitic Spheres | Ten 400 mm Diameter Granitic Spheres (5 nos. in a row) | 600 mm dia. Granitic Sphere

Figure 3.2 Granitic Spheres Adopted in Large-scale Impact Tests

3.6 Test Results

3.6.1 Boulder Impact Mechanism

Boulder impact mechanisms were first analysed based on the footages taken from cameras placed in different locations of the flume. In Test Nos. K1, K4 and K5 which involved a single boulder impact, upon release of the boulder during these tests, the boulder predominantly rolled along the transportation channel of the flume with slight bouncing (see Figure 3.3 for snapshot of Test No. K5). When approaching the model barrier, the boulder hit the lower part of the wall stem, at about 0.3 m (i.e. the radius of the sphere) above base slab for Test Nos. K4 and K5 (see Figure 3.3 for Test No. K5) and 0.1 m (i.e. the radius of the sphere) above base slab for Test No. K1. In these three tests, upon impacting onto the wall stem, the barrier exhibited some forms of movements in different extents for different tests, as captured from the lasers sensors installed behind the barrier. The boulder then rebounded from the barrier and eventually deposited behind the barrier.

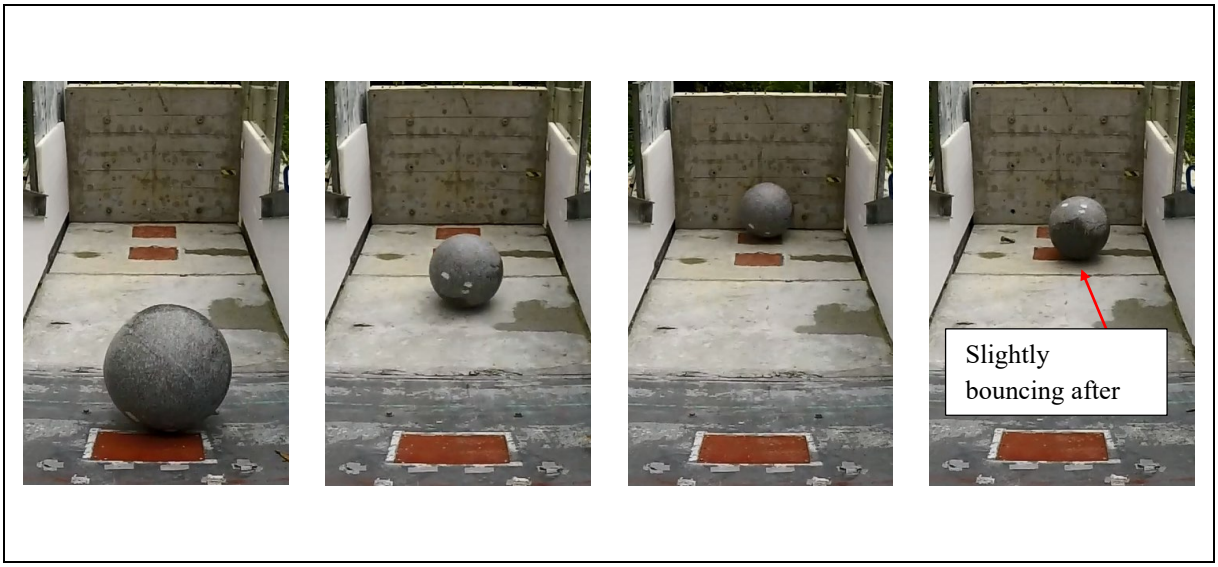

Figure 3.3 Snapshots of Test No. K5 Taken from High Speed Camera inside the Flume

In Test No. K2, ten numbers of 200 mm dia. boulders were released from the storage tank. Because the doors of the opening gate were designed to flip to the two sides of the flume, the boulders placed at the centre would roll out slightly earlier than those placed near the side walls. The ten boulders were found reaching the deposition zone of the flume at a slightly different time (see Figure 3.4).

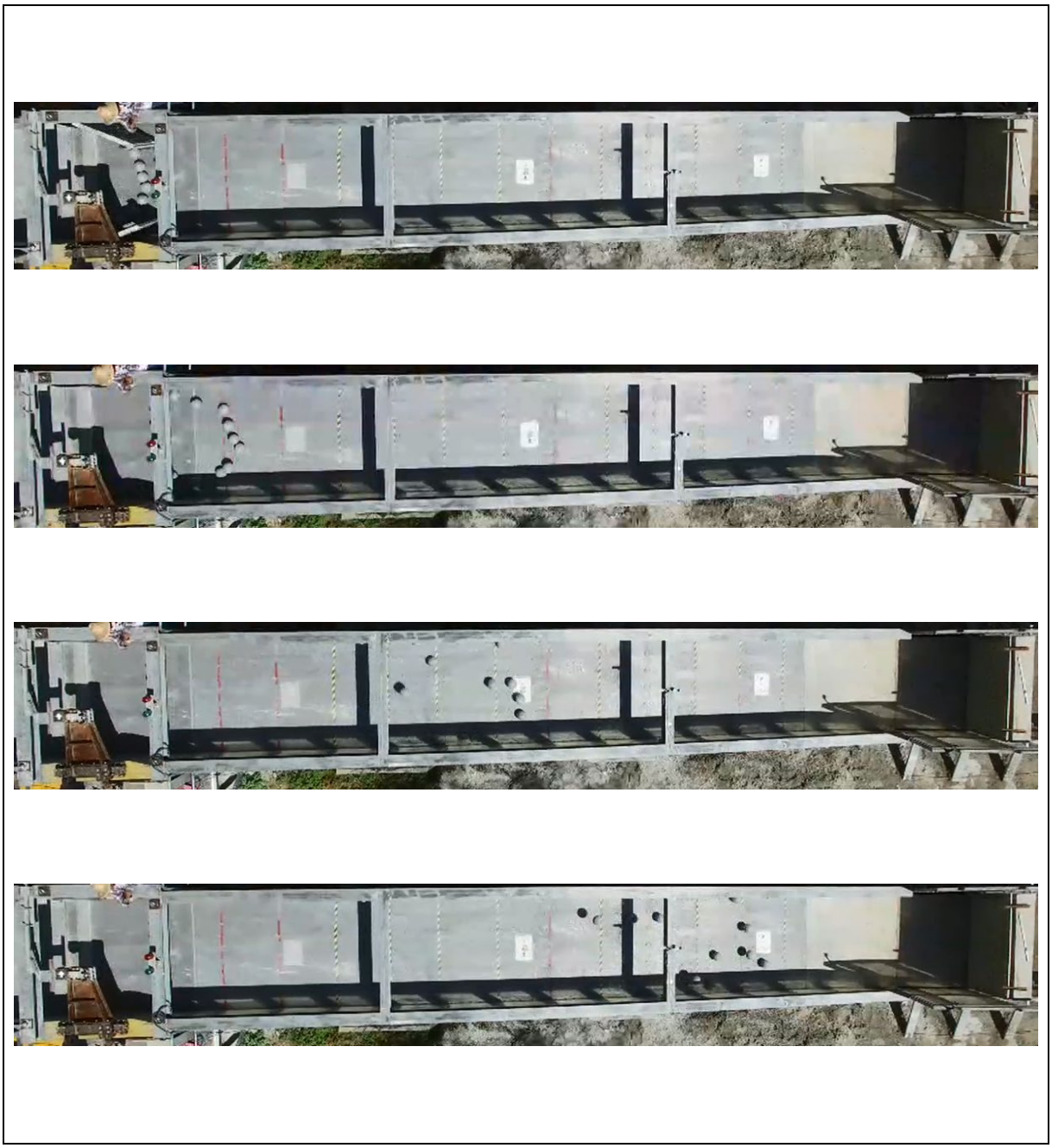

Figure 3.4 Snapshots of Test No. K2 Taken from Normal Camera Installed in a Drone

Based on footages taken from the high speed camera installed inside the flume, it was observed that those five (out of ten) boulders which travelled at the frontal part of the boulder cluster directly hit the model barrier (i.e. an "Effective Impact No." of 5 shown in Table 3.3) at an impact velocity of about 7 m/s. These five boulders then rebounded, colliding with some other boulders that travelled at the rear part of the boulder cluster. That subsequently triggered a series of random boulder-boulder collisions and boulder-sidewall collisions, resulting in energy dissipation within the boulder cluster (see Figure 3.5 and video in Section 3 Appendix A). Eventually, all ten boulders deposited on the base slab of the model barrier after the test.

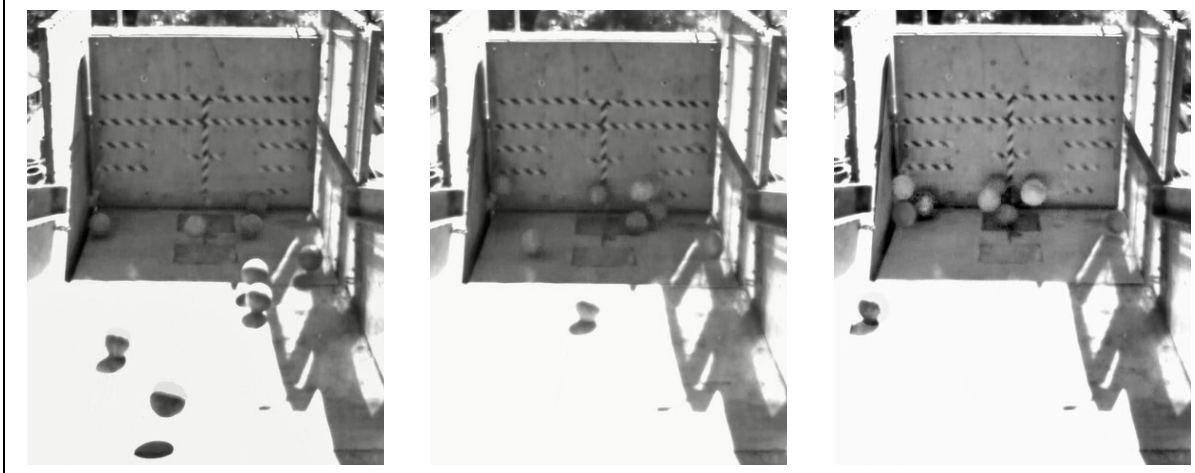

Figure 3.5 Snapshots of Test No. K2 Taken from High Speed Camera Installed inside the Flume

In Test No. K3 which involved 10 nos. of 400 mm diameter boulders, the boulders were placed behind the opening gate in two rows (i.e. 5 boulders in each row as shown in Figure 3.2). Upon release of the opening gate, the ten boulders travelled along the flume and reached the deposition zone of the flume at a slightly different time. Based on footages taken from the high speed camera, it was observed that only two (out of ten) boulders which travelled at the frontal part of the boulder cluster directly hit the model barrier (i.e. an "Effective Impact" of 2 as shown in Table 3.3) at an impact velocity of about 8 m/s. These two boulders then rebounded, collided with some other boulders that travelled at the rear part of the boulder cluster, and then triggered a series of random boulder-boulder collision and boulder-sidewall collisions, resulting in energy dissipation within the boulder cluster (see Figure 3.6 and video in Section 3 Appendix A). One piece of acrylic side-wall was found broken after the test. After a series of collisions, all ten boulders deposited on the base slab of the model barrier.

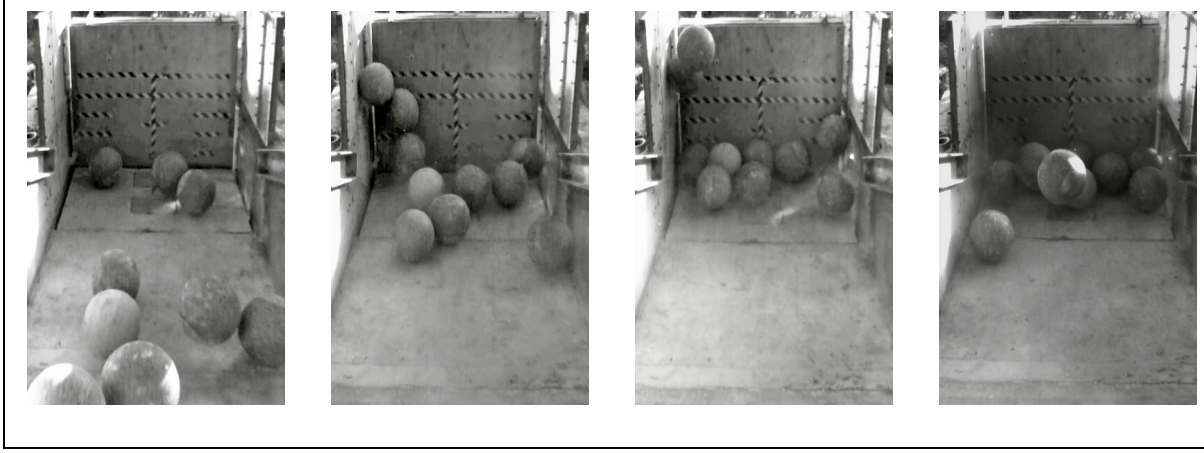

Figure 3.6 Snapshots of Test No. K4 Taken from High Speed Camera Installed inside the Flume

3.6.2 Prediction of Barrier Movement and Verification of Displacement Approach

The prediction of barrier movement for Displacement Approach requires various input parameters, including mass and impact velocity of boulder, mass of model barrier, coefficient of restitution (COR), interface friction angle between founding soil and model barrier, distance between the axis of rotation and the location of boulder impact, and mass moment of inertia of the model barrier.

The impact velocity of boulders was based on the observed time elapsed for the boulders to travel a known distance just before hitting the barrier (i.e. across the 1.5 m upstream of the wall stem of the model barrier), by tracing the footages taken by high-speed camera inside the flume.

Movement of the barrier was measured by four laser sensors in Test Nos. K1 to K3. In Test Nos. K4 and K5, two laser sensors were installed, and the time history of movement of the model barrier was cross-checked against the footage taken from the high speed camera at the side view of the model barrier. The measured movement of the model barrier was compared with that predicted using the analytical equations of the Displacement Approach, and the comparison is summarised in Table 3.3.

Table 3.3 Comparison of Prediction of Movements with Experimental Results

Test No.	Observed Impact Velocity (m/s)	Observed No. of "Effective Impact" (1)	Measured Sliding Movement (2)	Measured Rotation Movement (2)	Predicted Sliding Movement (3) (4)	Predicted Rotation Movement (3) (4)
K1	7.0	1	Not observable (< 0.5 mm)	Not observable	Negligible (< 0.5 mm)	Negligible
K2	7.0	5	Not observable (< 0.5 mm)	Not observable	Negligible (< 0.5 mm)	Negligible
K3	8.0	2	2.0 - 2.9 mm	0.2° - 0.3°	4.0 - 6.3 mm	0.4° - 0.6°
K4	6.5	1	0.7 mm	0.5°	13.9 - 21.8 mm	0.8° - 1.3°
K5	6.3	1	Not observable (< 0.5 mm)	0.5°	13.1 - 20.5 mm	0.8° - 1.3°

Notes:
(1) For Test Nos. K2 and K3 involving multiple boulder impact, "effective impact" refers to observed number of boulders directly hitting onto rigid barrier from the footage of high-speed cameras (see Section 3.6.1).
(2) The accuracy of laser sensor was ± 1 mm.
(3) The prediction by Displacement Approach assumes either sliding or rotation of barrier, but not both.
(4) The predictions shown above are based on a range of COR from 0.2 to 0.5 (Lam & Kwan, 2016) and a basal frictional angle of 36° is assumed. Estimated COR values for these five tests are around 0.3 to 0.4.

The results shown in Table 3.3 demonstrated that the extent of sliding and rotational movements of barrier predicted by the Displacement Approach are greater than that observed in the experiments. It is probably due to the fact that the predictions by means of the Displacement Approach are based on an assumption that the kinetic energy gained by the barrier after impact was dissipated through a specific mode of movement, i.e. either sliding or rotation. In reality, upon an impact, energy dissipation in different modes, e.g. sliding, rotation, structural deformation (e.g. bending, local indentation, internal fracturing), etc. would co-exist. In particular, for Test Nos. K4 and K5, two stud connections at the protective steel plate were found damaged and detached upon boulder impact, and the steel plate was swayed, and all these contributed to a certain amount of energy dissipation.

It is also worth-noting that for Test Nos. K2 and K3, as mentioned in Section 3.6.1, although ten boulders were released from the top of the flume, only some boulders gave rise to a direct impact on the model barrier. These direct impacts happened with some time delay. The rest of the boulders interacted and collided with other boulders, resulting in substantial dissipation of kinetic energy, without directly hitting the barrier. This observation echoes with Professor O. Hungr's view that simultaneous impact by several boulders need not be assumed in order to avoid undue conservatism (GEO, 2016). Notwithstanding this, the field observation indicates the complexity in dynamic impact involving a cluster of boulders and engineering judgement should be exercised when designing rigid barriers for such multiple impact scenarios. Impact involving cluster of boulders will be further discussed in Section 5.

4 Numerical Analysis

4.1 Numerical Analysis for Prediction of Sliding of Barrier

Yong et al (2019) presents the validation of three-dimensional finite-element computer package namely LS-DYNA for the analysis of geotechnical stability of concrete barrier using the test results of the small-scale impact tests as shown in Section 2. Adopting similar numerical approach, GEO recently conducted two numerical analyses to simulate impact scenarios involving boulder impact on rigid barriers for real-scale impact scenarios.

In the first numerical analysis, a 5.6 m high and 10 m wide L-shape rigid barrier (with a 1 m thick wall stem and 0.4 m thick and 5 m long base slab) was adopted to study its response under different impact scenarios. The weight of the barrier is about 120 tonnes. The barrier was founded on a rigid plane with a prescribed constant basal friction angle of 40° (see Figure 4.1).

The impact scenario under study involved a 1 m diameter boulder travelling at 10 m/s (i.e, kinetic energy of 70 kJ) and striking at 1 m above the centreline of the base slab (see Figure 4.1). The boulder was assumed perfectly rigid, and thus, in other words, any energy dissipation due to possible deformation and/or fracture of the boulder was conservatively ignored.

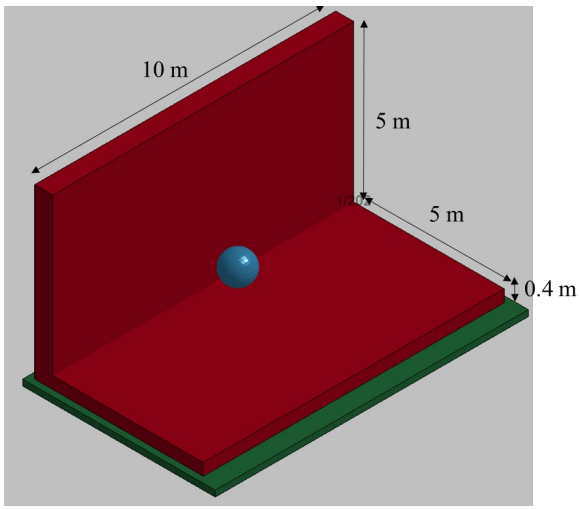

Figure 4.1 Model Setup for Numerical Analysis for Prediction of Sliding Movement of Barrier

The sliding movement of the model barrier has been obtained from LS-DYNA simulation and compared with that predicted using Displacement Approach. The comparison is shown in Table 4.1 below:

Table 4.1 Comparison of Sliding Movement Predicted in Numerical Simulation and That Predicted Based on Displacement Approach

Model No.	Sliding Movement from LS-DYNA Simulation (mm)	Predicted Sliding Movement from Displacement Approach (mm)
LS1	1.3	1.4
Note:	COR used in the prediction of barrier's movement was estimated using the actual velocity of impactor before and after impact, and the calculated velocity of model barrier after impact based on conservation of momentum.	

In general, the sliding movements based on LS-DYNA simulation and that predicted based on Displacement Approach are similar. A negligible amount of rotational movement (about 0.0007°) and insignificant energy loss by means flexural and localised fracture of barrier were observed in the numerical simulation.

4.2 Numerical Analysis for Prediction of Rotation of Barrier

Another impact scenario involving the same boulder (i.e. 1 m in diameter impacting at a

velocity of 10 m/s) hitting the crest of a rigid barrier was simulated to further validate Displacement Approach for the prediction of rotation of barrier. In the numerical analysis, a rigid barrier comprises a wall stem of 5.6 m high (including the thickness of the base slab), 10 m wide and 1 m thick, and a base slab of 5 m long (excluding the thickness of the wall stem), 10 m wide and 0.6 m thick was constructed. The weight of the barrier is about 144 tonnes. The barrier was founded on a rigid plane (see Figure 4.2).

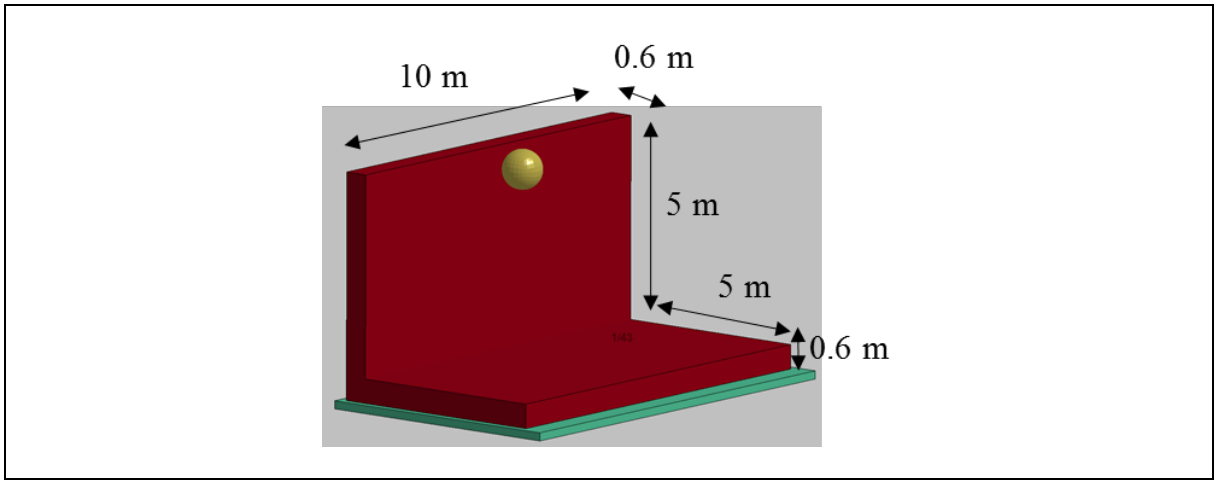

Figure 4.2 Model Setup for Numerical Analysis for Prediction of Rotational Movement of Barrier

The angle of rotation of the model barrier has been obtained from LS-DYNA simulation and compared with that predicted using Displacement approach. The comparison is shown in Table 4.2 below. The prediction by Displacement approach is higher than the numerical outputs obtained from the LS-DYNA simulation. In addition to the rotational mode of movement of the barrier, a sliding movement of 0.2 mm was observed in the numerical simulation. Other signs of energy dissipation by means of structural response of barrier including flexural and localised fracture were also observed.

Table 4.2 Comparison of Rotational Movement Predicted in Numerical Simulation and That Predicted Based on Displacement Approach

Model No.	Angle of Rotational from LS-DYNA Simulation	Predicted Angle of Rotational Based on Displacement Approach
LS2	0.018°	0.088°
Note:	COR used in the prediction of barrier's movement was estimated using the actual velocity of impactor before and after impact, and the calculated velocity of model barrier after impact based on conservation of momentum.	

5 Effect of Multiple Impacts

Field evidence of previous landslides suggests that debris flows in Hong Kong may contain cluster of boulders (see Figure 5.1 below). These boulders are typically 0.5 m diameter and occasionally 1 m or even larger.

2008 Yu Tung Road

2008 Yi O Village

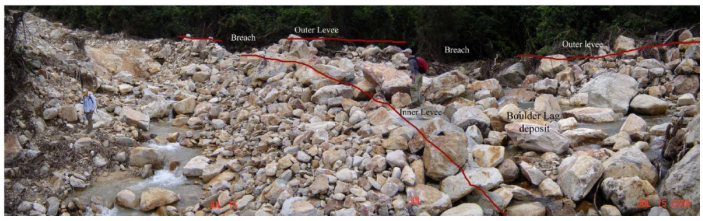

2008 Shek Pik

2016 Sai Wan Road

Figure 5.1 Boulders Contained in Debris Flows in Hong Kong

A sensitivity study of impact scenarios involving a cluster of boulders has been conducted using Displacement Approach. A typical rigid barrier with a wall stem of 5.8 m high (including the thickness of base slab), 10 m wide and 0.8 m thick, and a base slab of 6 m long (excluding the thickness of wall stem), 10 m wide and 0.8 m thick was considered in this study (Figure 5.2). This barrier weighs 230 tonnes.

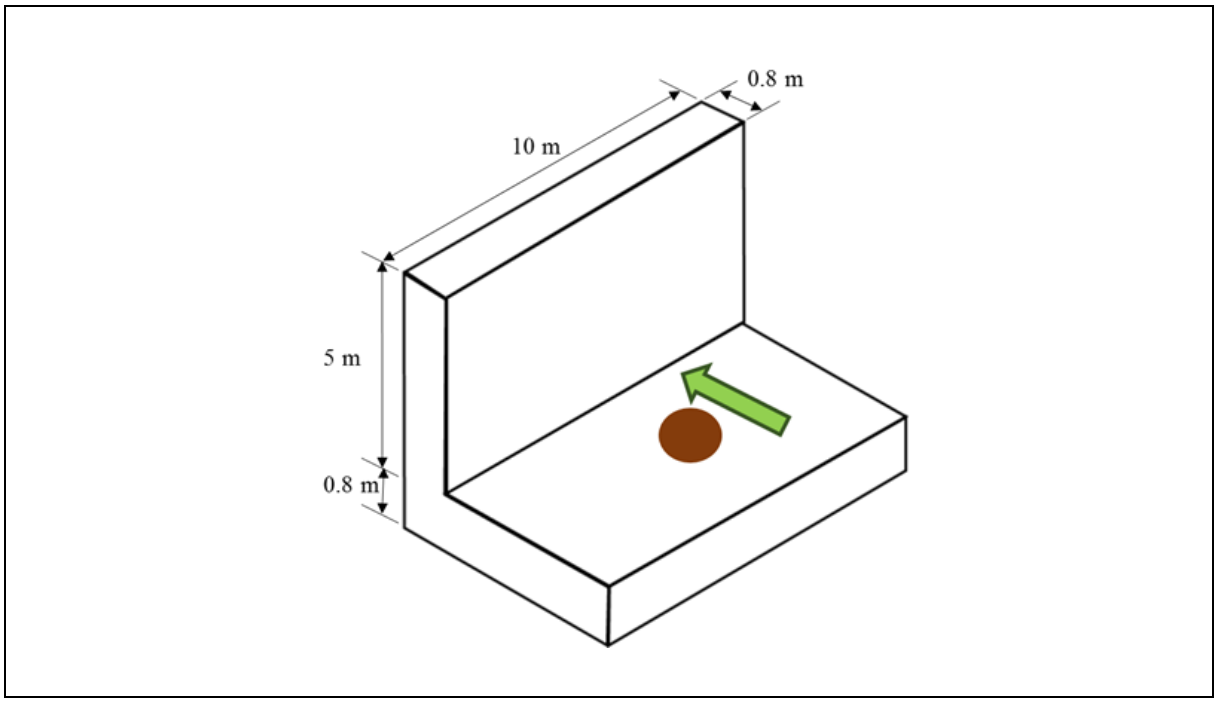

Figure 5.2 Sensitivity Study of Rigid Barrier Subject to Multiple Boulder Impacts

Impact scenarios involving a cluster of 20 and 200 numbers of 0.5 m diameter boulders, and individual large boulders (1.2 m and 2.0 m in diameter), have been considered. Both "successive impacts" and "simultaneous impacts" have been considered for impacts from boulder cluster (see Table 5.1). (Note: "Successive impacts" means that there is a time lag between each and every boulder impact and the predicted displacement is the cumulative effect of displacements due to each individual boulder impact. "Simultaneous impacts" means that there is no time lag between every boulder impact and the displacement is predicted as if there is one single impact with a lumped mass of all boulders.).

The predicted sliding and rotational movements of the rigid barrier are given in Table 5.1. For the impact scenarios considered, the amount of sliding and rotation of barrier predicted by Displacement Approach are generally insignificant. Further discussion on multiple impact scenarios is given in Section 3.6.2.

In both local and overseas design guidelines, there is no definite rules to determine an allowable displacement for rigid barriers. In this regard, engineering judgement should be exercised in determining an acceptable amount of displacement for routine designs, taking into account the proximity of barriers to downstream facilities to be protected, serviceability of barriers (e.g. any connection with adjacent services including utilities, drainage, planter walls, etc.), and so on.

When deciding the appropriate design boulder impact scenarios for displacement prediction, judgement should be exercised based on various factors including abundancy and size of boulders that could be entrained by a debris flow, likelihood of development of bouldery debris front, and probable chance of direct boulder-barrier interaction, etc.

Table 5.1 Results of Sensitivity Study of Rigid Barrier Subject to Multiple Boulder Impacts using Displacement Approach

Impact Scenarios	Predicted Sliding Movement	Predicted Rotational Movement
1 x 0.5 m diameter boulder	0.009 mm	0.0004°
200 x 0.5 m dia. Boulder (successive impact) 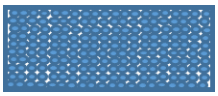	1.8 mm	0.0004° (see Note)
20 x 0.5 m dia. Boulder (simultaneous impact)	3.5 mm	< 0.2°
200 x 0.5 m dia. Boulder (10 successive series of simultaneous impacts) 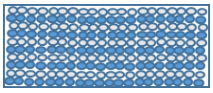	35 mm	< 0.2° (see Note)
1 x 1.2 m diameter boulder	2 mm	< 0.1°
1 x 2 m diameter boulder	38 mm	< 1.2°

Note: Coefficient of Restitution was taken as 0.5 (Lam & Kwan, 2016) and basal friction angle of 34° was assumed. Impact velocity of 10 m/s was adopted. The assessment of maximum transient rotational displacement of the barrier by multiple impacts may not be necessary as the barrier would move back by gravitational force to its original location after the impact.

6 Effect of Size of Boulder on Geotechnical Stability of Rigid Barrier

A sensitivity study has been conducted to analyse the effect of size of the impacting boulder on the geotechnical stability. This study considers impact scenarios involving a range of typical geometries of rigid barriers, all 10 m wide but with a range of wall height from 3 m to 6 m. These walls are subjected to boulder impacts at a velocity of 8, 10 and 12 m/s, with a varying sizes of boulder (resulting in barrier/boulder mass ratio of 1 to 100). The sliding and rotational movements of the barriers in each impact scenario have been predicted using Displacement Approach. Both sliding and rotational movements of the barriers increase non-linearly with the size of boulder. Based on the results of these analyses, it was found that for the impact scenarios as shown in Table 6.1, the resulting translational and rotational movements of the barrier are generally insignificant.

Table 6.1 Mass of Rigid Barrier Where Estimated Displacements Are Generally Insignificant

Boulder Impact Velocity (v)	$v \leq 8$ m/s	8 m/s < $v \leq 10$ m/s	10 m/s < $v \leq 12$ m/s
Mass of Rigid Barrier	> 20 times of mass of boulder	> 25 times of mass of boulder	> 30 times of mass of boulder

7 Conclusion

Boulder impact loads on rigid debris-resisting barriers are known to be highly transient and of high magnitude. Under the Displacement Approach, analytical solutions to predict sliding and overturning displacement have been developed, which consider the inertia effect of the barrier wall and energy loss during an impact process. The Displacement Approach has been verified by means of a series of physical impact tests and numerical analyses. As such, for appraising geotechnical stability of barrier subject to boulder impact, the barrier's global response in terms of sliding and overturning can be estimated, following the verified Displacement Approach. A series of sensitivity analyses has been conducted which showed that for a barrier with a mass exceeding the mass of a boulder by ratios stipulated in Table No. 6.1, sliding and overturning movements of the barrier due to the boulder impact are generally insignificant and further checking of geotechnical stability (i.e. estimation of translational and rotational movements) due to boulder impact is not required.

As a good practice, rigid debris-resisting barriers should be founded on a levelled and competent ground, and the ground in front of the barrier should be well protected against erosion as necessary.

As an alternative to the displacement check, designers may consider adopting measures such as baffles, boulder straining structures, cushioning materials, etc. to deal with the boulder impact, taking into account cost-effectiveness, constructability and maintenance requirement, etc.

8 References

GEO (2016). *Updates of Design Guidance of Rigid Debris-resisting Barriers (GEO TGN 47)*. Geotechnical Engineering Office, Hong Kong, 4 p.

HKUST (2019). *Large-scale Debris Impact Tests on Rigid Barriers*, Draft Testing Report (Phase 2) prepared for Geotechnical Engineering Office, Hong Kong, 19 p.

Kwan, J.S.H. (2012). *Supplementary Technical Guidance on Design of Rigid Debris-resisting Barriers (GEO Report No. 270)*. Geotechnical Engineering Office, Hong Kong, 88 p.

Lam, C. & Kwan, J.S.H. (2016). *Displacement-based Assessment of Boulder Impacts on Rigid Debris-resisting Barriers - A Pilot Study (Technical Note No. TN 9/2016).* Geotechnical Engineering Office, Hong Kong, 66 p.

Lam, C., Yong, A.C.Y., Kwan, J.S.H. & Lam, N.T.K. (2018). Overturning stability of L-shaped rigid barriers subjected to rockfall impacts. *Landslides*, 15(7): 1347-1357.

Yong, A.C.Y., Lam, C., Lam, N.T.K. & Perera, J.S. (2019). Analytical solution for estimating sliding displacement of rigid barriers subjected to boulder impact. *Journal of Engineering Mechanics, 2019*, 145(3): 04019006

Section 3
Appendix A

Results of Large-scale Flume Tests Conducted in Kadoorie Centre, Hong Kong

Contents

	Page No.
Contents	175
A.1 Test No. K1	176
A.2 Test No. K2	177
A.3 Test No. K3	178
A.4 Test No. K4	179
A.5 Test No. K5	181

A.1 Test No. K1

Video taken in Test No. K1

Time History of Barrier Movement for Test No. K1

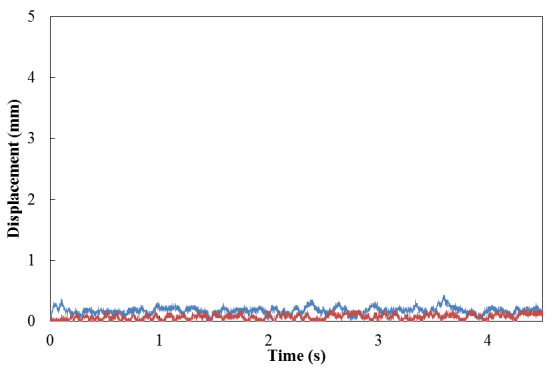

Lower Part of the Barrier

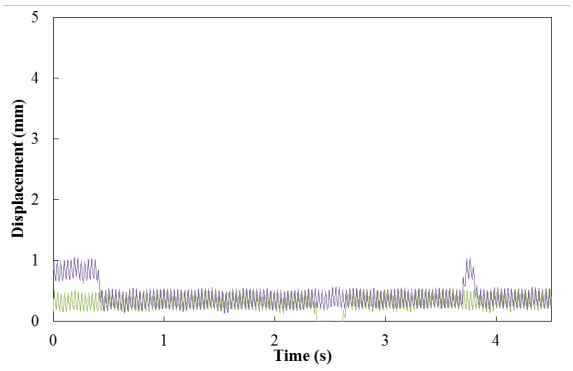

Upper Part of the Barrier

A.2 Test No. K2

Video taken in Test No. K2

Time History of Barrier Movement for Test No. K2

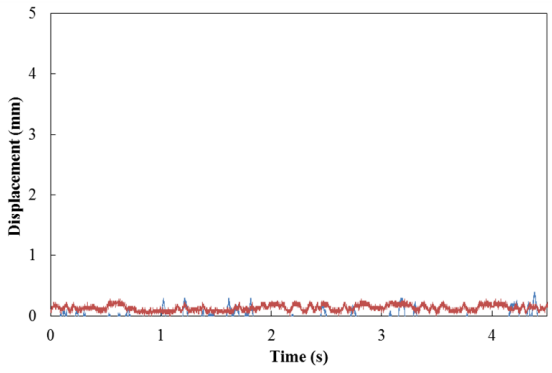

Lower Part of the Barrier

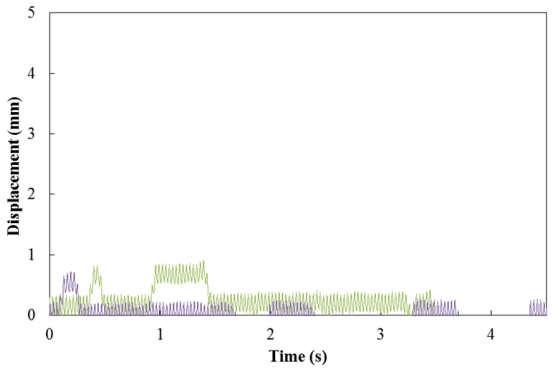

Upper Part of the Barrier

A.3 Test No. K3

Video taken in Test No. K3

Time History of Barrier Movement for Test No. K3

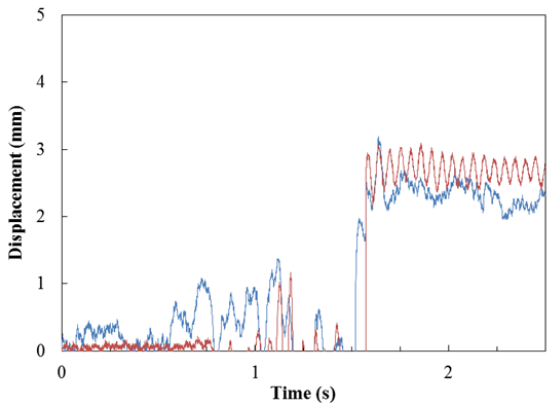

Lower Part of the Barrier

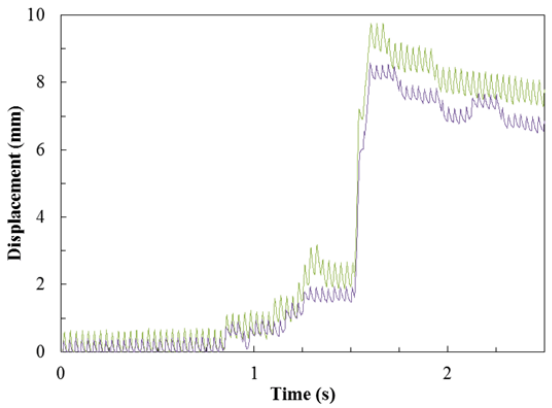

Upper Part of the Barrier

A.4 Test No. K4

Video taken in Test No. K4

Time History of Barrier Movement for Test No. K4

In Test Nos. K4 and K5, a pair of laser sensors was adopted (one at the top and the other at the bottom). Yet, the laser sensor at the upper part of the model barrier captured anomalous data. In this regard, the movement of the upper part of the model barrier was checked by interpretation of the footage taken from the high speed camera at the side view of the model barrier, in order to estimate the angle of rotation of barrier for the analysis in Section No. 3.6.2.

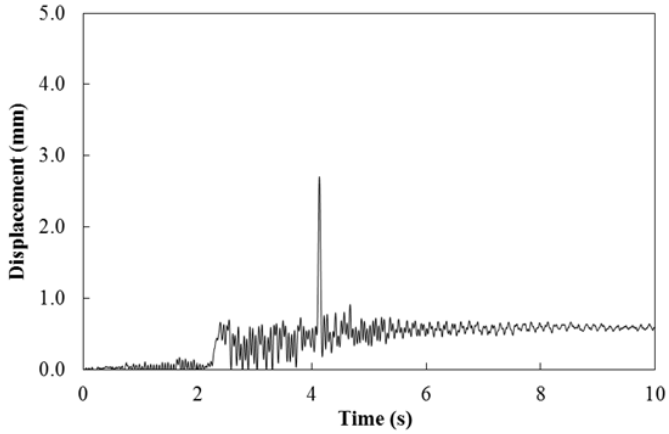

Lower Part of the Barrier

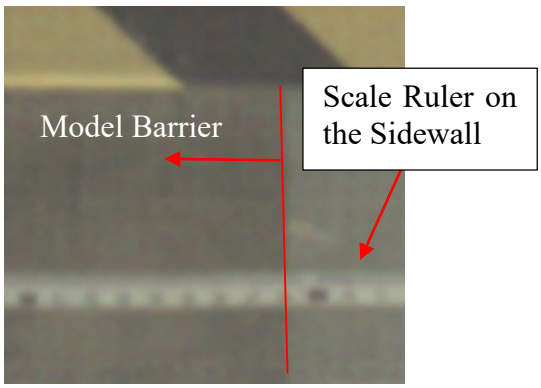

Before Impact

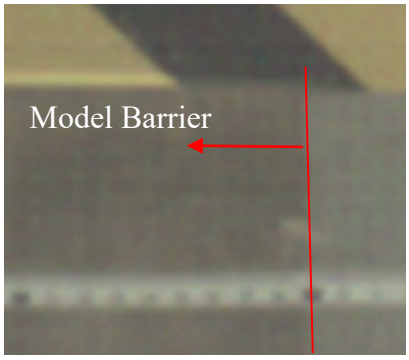

Instantaneously during Impact

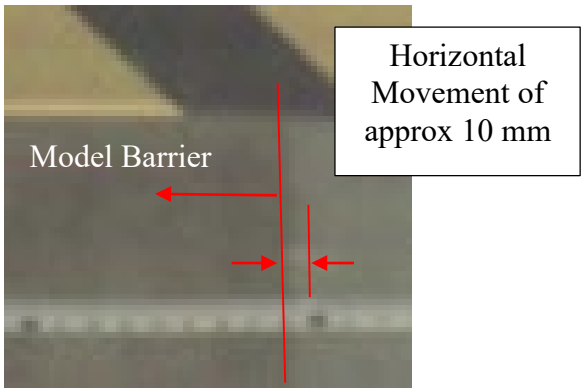

After Impact

Note: Time lag between each frame is about 2 milli-seconds.

Horizontal Movement of Model Barrier at 1.1 m above its Base Slab

A.5 Test No. K5

Video taken in Test No. K5

Time History of Barrier Movement for Test No. K5

In Test Nos. K4 and K5, a pair of laser sensors was adopted (one at the top and the other at the bottom). Yet, the laser sensor at the upper part of the model barrier captured anomalous data. In this regard, the movement of the upper part of the model barrier was checked by interpretation of the footage taken from the high speed camera at the side view of the model barrier, in order to estimate the angle of rotation of barrier for the analysis in Section No. 3.6.2.

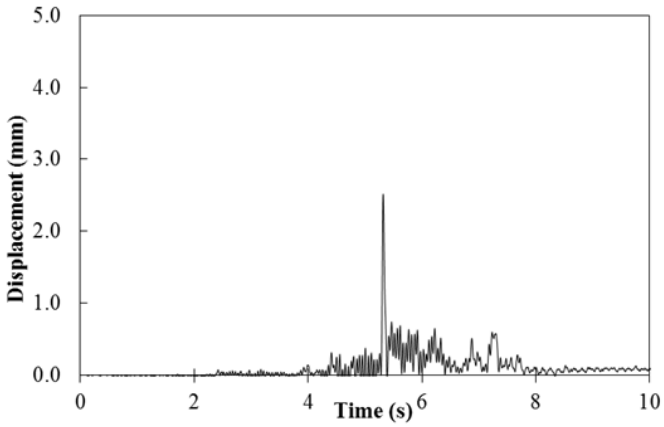

Lower Part of the Barrier

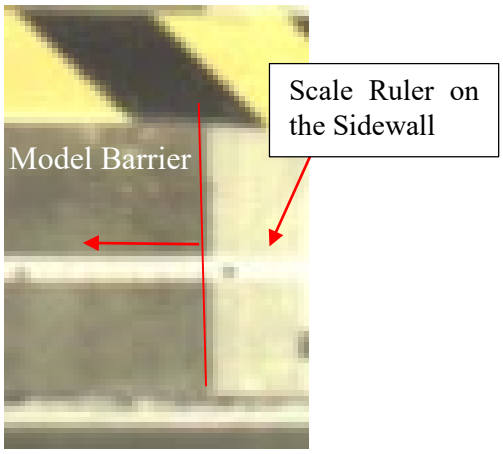

Before Impact

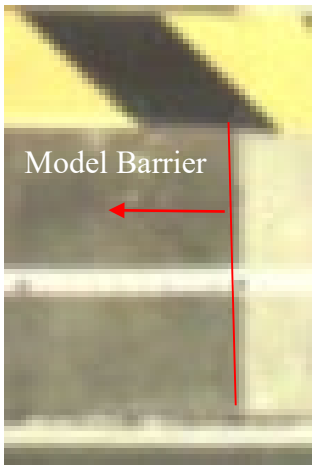

Instantaneously during Impact

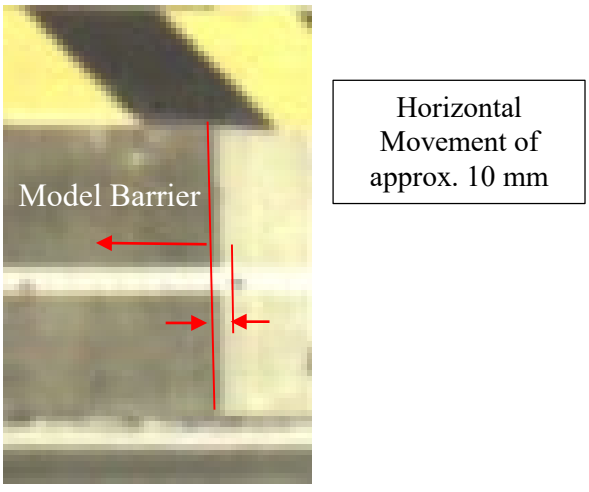

After Impact

Note: Time lag between each frame is about 2 milli-seconds.

Horizontal Movement of Model Barrier at 1.1 m above its Base Slab

Part 2

Structural Integrity

[Blank Page]

Section 4:
Study of Flexural Response of Rigid Barriers Subject to Boulder Impact

L.A. Wong & H.W.K. Lam

This section was originally produced in September 2018
as GEO Technical Note No. TN 3/2018

Foreword

This Technical Note summarises findings of a study of flexural response of rigid barriers subject to boulder impact. The study comprises a literature review, physical impact tests and numerical analyses. An analytical solution to estimate the boulder impact force on rigid barrier is proposed. Parametric studies were carried out to examine the proposed analytical solution under various impact scenarios.

This study was carried out by Mr. L.A. Wong under the supervision of Mr. H.W.K. Lam in collaboration with Professor N.T.K. Lam of the University of Melbourne and his assistant, Mr. A.C.Y. YONG. Ms. C.C.Y. CHEUNG assisted in preparing the numerical simulations. The Drafting Unit of the Standards and Testing Division assisted in formatting this Note.

The contents in the report were reviewed by Prof N.T.K. Lam. Many other colleagues in the GEO and practitioners in the geotechnical industry provided constructive comments on the Note. All contributions are gratefully acknowledged.

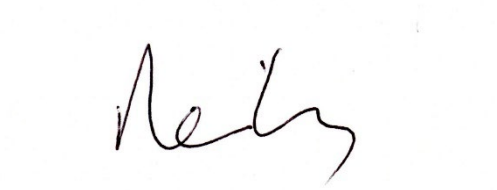

J.S.H. Kwan
Chief Geotechnical Engineer/Standards and Testing
September 2018

Contents

		Page No.
Title Page		185
Foreword		186
Contents		187
List of Tables		189
List of Figures		190
1	Background	191
2	Design Guidelines and Current Practice in Hong Kong	191
3	Enhanced Flexural Stiffness Method (EFSM)	192
3.1	General	192
3.2	Preliminary Experimental Verification of EFSM	193
4	Numerical Analyses	194
4.1	Effect of Boulder Impact Velocity (Translational)	195
4.2	Effect of Mass of Boulder	196
5	Further Discussion on Enhanced Flexural Stiffness Method	197
5.1	Effect of Coefficient of Restitution (COR)	197
5.2	Young's Modulus of Rigid Barrier	198
5.3	Effect of Rotational Velocity of Boulder	198
5.4	Effect of Young's Modulus of Boulder	199
5.5	Effect of Shape of Boulder	199
5.6	Effect of Location of Boulder Impact	200
6	Further Work	201
7	Conclusion	201
8	References	201
Section 4	Derivation of Enhanced Flexural Stiffness Method (EFSM)	205
Appendix A:		

		Page No.
Section 4 Appendix B:	Derivation of Flexural Stiffness of Wall (k) and Mass Ratio (λ)	208
Section 4 Appendix C:	Dynamic Effect on the Young's Modulus of Rigid Barrier	217
Section 4 Appendix D:	Prediction of Impact Force and Flexural Displacement for Small-scale Impact Test Using EFSM	222
Section 4 Appendix E:	Numerical Analyses - Model Validation	228

List of Tables

Table No.		Page No.
3.1	Comparison of FSM, EFSM and Results of Small-scale Impact Test	194
4.1	Input Details of the Parametric Study on the Effect of Boulder Impact Velocity	196
5.1	Sensitivity Study on the Rotational Velocity of the Boulder	198
5.2	Results of Sensitivity Study on the Young's Modulus of the Boulder	199
5.3	Results of Sensitivity Study on the Shape of the Boulder	200
5.4	Results of Sensitivity Study on the Location of Boulder Impact	201

List of Figures

Figure No.		Page No.
3.1	Set-up of Small-scale Impact Test for Verification of EFSM	193
4.1	Validated Numerical Simulations for Parametric Study on the Effect of Boulder Impact Velocity	195
4.2	Comparison of FSM, EFSM, Hertz Load and Numerical Analysis for the Study of Boulder Impact Velocity	196
4.3	Validated Numerical Simulations for Parametric Study on the Inertial Effect	197
4.4	Comparison of FSM, EFSM, Hertz Load and Numerical Analysis for the Study of Inertial Effect	197
5.1	Numerical Simulations with Impact Objects in Different Shapes: (a) Sphere, (b) Cylinder and (c) Cone	199
5.2	Numerical Simulations (i.e. Case Nos. 5.6.1, 5.6.2 & 5.6.3) with Boulder Impact on Three Different Model Rigid Barriers	200

1 Background

Reinforced concrete rigid barriers are commonly adopted in Hong Kong as structural counter-measures to mitigate natural terrain landslide hazards. GEO has initiated various research and development work on rigid barriers in recent years. Kwan et al (2018) highlighted some recent studies on the effect of boulder impact on rigid barriers. Ng et al (2016) and Song et al (2017) conducted a series of centrifuge tests of debris flows impacting on a rigid barrier, where very transient load due to the impact of large particles was observed. Lam (2016) carried out a pilot study on the use of cushioning materials for reducing boulder load on rigid barriers. Lam & Kwan (2016) and Lam et al (2017) presented a displacement-based methodology, with a view of providing an alternative to the conventional limit equilibrium analysis, for assessing geotechnical stability of rigid barriers under boulder impact.

While previous technical development work undertaken by GEO focused on the assessment of the geotechnical stability of rigid barriers, GEO has recently initiated a review of the structural design of rigid barriers as part of a holistic revamp of the rigid barrier design framework. This Technical Note (TN) summarizes the findings of this review, focusing on the flexural response of rigid barriers subject to boulder impact. The study comprises a review of local and overseas literatures, small-scale physical impact tests and numerical analyses using a finite element program. An analytical solution to estimate boulder impact force on rigid barriers is proposed.

2 Design Guidelines and Current Practice in Hong Kong

In the prevailing design guidelines in Hong Kong, design impact load of rigid barrier is taken as the superimposition of the debris flow impact load and the impact load of boulders contained in the debris flow.

Kwan (2012) recommended the use of a simplified Hertz Equation to establish the boulder impact load. This equation considers the impact of two perfectly elastic bodies (Timoshenko & Goodier, 1970; Zhang et al, 1996) and was found to produce conservative estimates of the impact force at the point of contact. Kwan (2012) reviewed several case histories and recommended an empirical reduction factor of 0.1 to the simplified Hertz load to avoid undue conservatism.

Instead of adopting the factored Hertz load, other design codes and literatures, e.g. CAGHP (2018), CGS (2004), Hungr et al (1984), Lo (2000) and Zhang et al (1996), suggest the use of Flexural Stiffness Method (FSM) to calculate the design boulder impact load. FSM considers the flexural stiffness of a structure subject to a dynamic boulder impact and calculates an equivalent static boulder load (F) using the following equation (derivation of the equation is given in Section 4 Appendix A):

$$F = v_0\sqrt{mk} \quad \text{..... (2.1)}$$

where F = boulder impact force (in N)
v_0 = the impact velocity of the boulder (in m/s)
m = the mass of the boulder (in kg)

k = the flexural stiffness of the barrier (in N/m, which is equal to $3EI/h^3$ for a cantilever structure with an impact at tip, where EI = Effective flexural rigidity of the cross section of barrier and h = the height of the barrier)

The key assumption of FSM is that the kinetic energy of an impact is completely transferred to the receiver, without considering any energy loss during an impact. As such, the impact force predicted by FSM could be very conservative (as demonstrated in Section 3.1).

3 Enhanced Flexural Stiffness Method (EFSM)

3.1 General

Professor N.T.K. Lam of the University of Melbourne has recently developed an Enhanced Flexural Stiffness Method (EFSM) by modifying FSM (Ali et al, 2014; Lam & Gad, 2016; UoM, 2017; Yang et al, 2012). EFSM considers the energy loss during an impact. Lam & Gad (2016) showed that the boulder impact load could be calculated using Equation 3.3 below (derivation of the equation is given in Section 4 Appendix A):

$$\Delta = \beta v_0 \sqrt{\frac{m}{k^*}} \quad \text{..... (3.1)}$$

$$F = k\Delta \quad \text{..... (3.2)}$$

For an impact on the crest of the barrier, $k^* = k$, and:

$$F = \beta v_0 \sqrt{mk} \quad \text{..... (3.3)}$$

where Δ = the flexural deflection of the barrier (in m)

β = $\sqrt{\lambda\left(\frac{1+COR}{1+\lambda}\right)^2}$ which is less than unity and is a function of Coefficient of Restitution (COR) between granitic rock impacting on concrete surface, which is typically around 0.2 to 0.3 according to Chau et al (1998) and Masuya et al (2001)

λ = the ratio between the participating mass of the barrier and the mass of the boulder

v_0 = the impact velocity of the boulder (in m/s)

m = the mass of the boulder (in kg)

k^* = the generalised stiffness of the barrier, which is a dynamic property (in N/m)

k = the flexural stiffness of the barrier (in N/m, which is equal to $3EI/h^3$ for a cantilever structure with an impact at the crest of the barrier, where EI = Effective flexural rigidity of the cross section of barrier and h = the height of the barrier)

The derivation of k^* and λ for boulder impact at the crest of the barrier is given in Section 4 Appendix B. Discussion on the input parameters to the expressions listed in this section will be given in Section 5.

3.2 Preliminary Experimental Verification of EFSM

An experimental investigation has been carried out at the University of Melbourne to verify the performance of EFSM (Lam et al, 2017). The test involved a 1 m high steel pole impacted by a 5 kg cast iron sphere. A high-speed camera and a laser sensor were used to capture the velocity of cast iron ball and steel pole, as well as the displacement of the tip of the steel pole. A schematic sketch and the setup of the impact test are given in Figure 3.1 below. Detailed information of the test is given in Section 4 Appendix D.

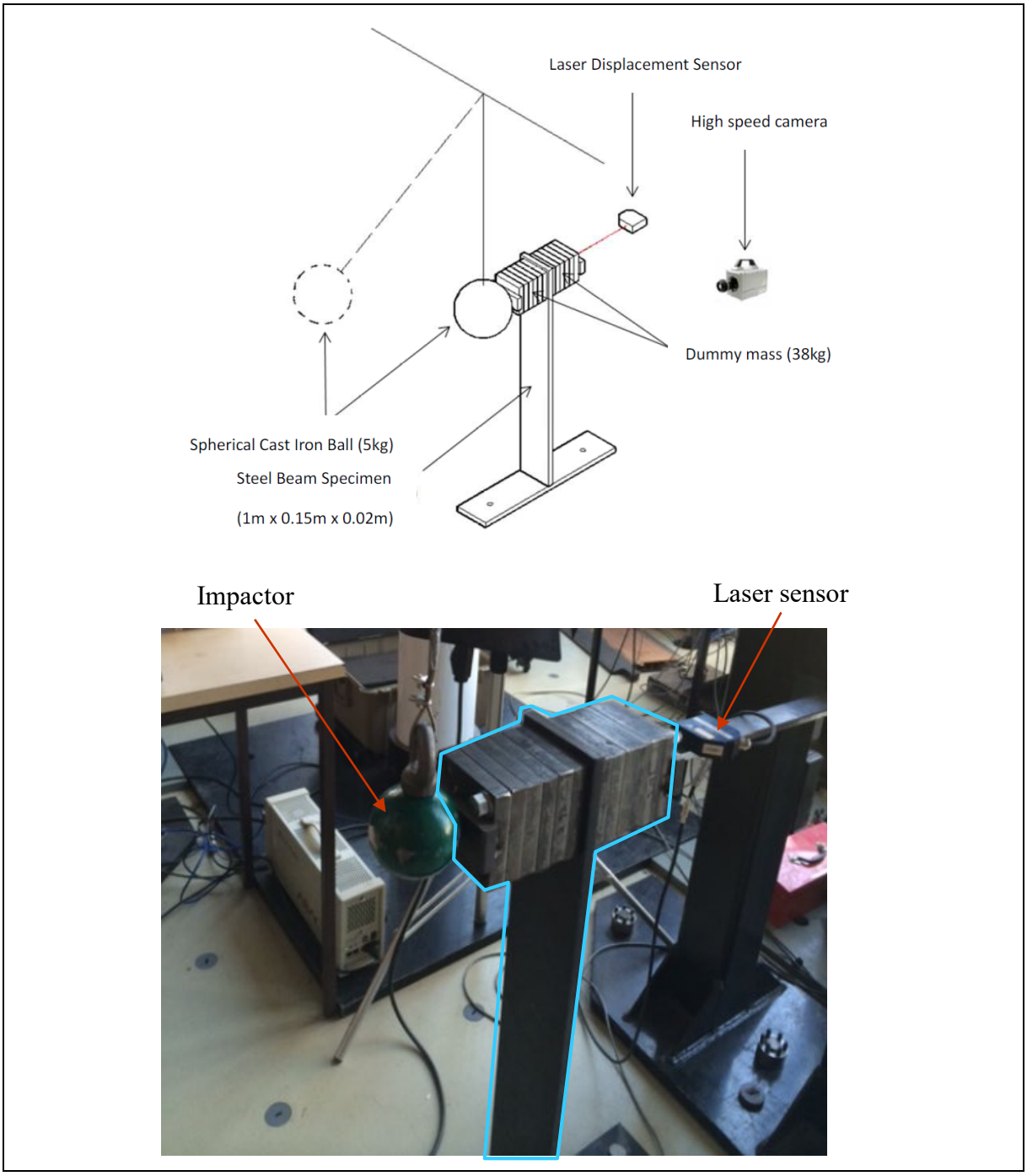

Figure 3.1 Set-up of Small-scale Impact Test for Verification of EFSM

The flexural response of the steel pole and the impact force estimated by means of FSM and EFSM, as well as the experimental results are summarised in Table 3.1. The prediction of the tip deflection of the pole and the impact force using EFSM are given in Section 4 Appendix D for reference. The impact force for the experimental test as given in Table 3.1 was calculated based on the flexural stiffness of the pole multiplied by the maximum tip deflection during impact. From Table 3.1, the flexural response (in terms of the tip deflection of the pole) as well as the impact force predicted by EFSM match well with those obtained from the experiment. In comparison, the flexural response (in terms of the tip deflection of the pole) as well as the impact force predicted by FSM are found to be about 2.5 times higher than the experimental results.

Table 3.1 Comparison of FSM, EFSM and Results of Small-scale Impact Test

Method	Deflection at the Crest of the Barrier (mm)	Estimated Boulder Impact Load (N)
Experimental result	16.9 (measured)	1,014
EFSM (Lam & Gad, 2016)	16.4 (predicted)	984
FSM (Hungr et al, 1984)	40.0 (predicted)	2,426

4 Numerical Analyses

A parametric study was carried out in order to investigate the flexural response of a rigid barrier when subject to the boulder impact scenarios that would be commonly encountered in routine design. A three-dimensional finite-element computer package namely "Livermore Software - Dial-a-yield Nonlinear Analysis" (LS-DYNA) was used in this study. The numerical model was first validated using results recorded from two documented full-scale impact tests pertaining to high-energy impact on reinforced concrete structures as reported by Fujikake et al (2009) and Kishi & Bhatti (2010). The validated model was then used to produce data relevant to the boulder impact on rigid barriers in order to further evaluate EFSM. Information on the full scale impact tests for model validation and the details of the validation exercise are given in Section 4 Appendix E.

Two key parameters as listed below were studied:

(a) impact velocity of the impactor, and

(b) mass of the impactor.

Output from the numerical simulations was then compared with the predicted response using the proposed EFSM (i.e. Equation 3.3).

4.1 Effect of Boulder Impact Velocity (Translational)

A systematic review on the effect of the boulder impact velocity on the flexural response of rigid barriers was conducted. The model boulder, which was spherical and was 1.5 m in diameter, was to impact onto a 5.2 m high, 0.8 m thick reinforced concrete model barrier. The model barrier was restrained in rotational and translational movement at the base, and thus behaved as a cantilevered wall. Seven boulder impact tests were modelled numerically, and the boulder impact velocity (translational) varied from 5 m/s to 11 m/s (see Figure 4.1 and Table 4.1).

The flexural response of the model barriers simulated using program LS-DYNA is shown in Figure 4.2, together with those predicted by FSM, EFSM and Hertz Equation with a reduction factor of 0.1. It was found that the boulder impact force predicted by EFSM matches well with the LS-DYNA simulation, whereas the other two methods, i.e. FSM and Hertz load with a reduction factor of 0.1, predicted a higher impact force than that from EFSM. Figure 4.2 also indicates that the boulder impact force increases with the boulder impact velocity.

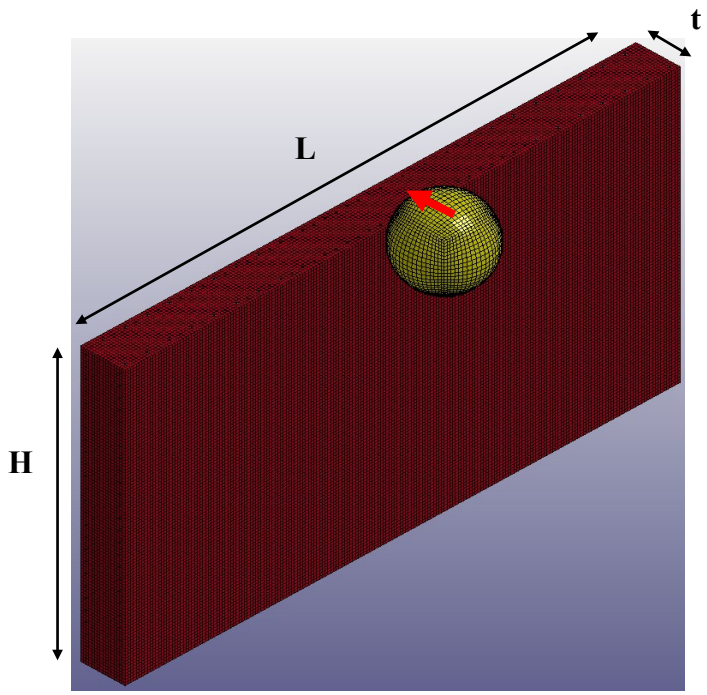

Note: Refer to Table 4.1 for the input details of each case.

Figure 4.1 Validated Numerical Simulations for Parametric Study on the Effect of Boulder Impact Velocity

Table 4.1 Input Details of the Parametric Study on the Effect of Boulder Impact Velocity

Barrier length, L (m)	10
Barrier height, H (m)	5.2
Barrier thickness, t (m)	0.8
Diameter of boulder, D (m)	1.5
Mass of boulder (kg)	4,683
Translational velocity of boulder, v_0 (m/s)	Varies in each model, from 5 m/s to 11 m/s
Reinforcement layout	T40 – 200 (for both vertical and horizontal reinforcement on tension and compression side)
Compressive strength of concrete (MPa)	30
Yield strength of reinforcements (MPa)	500

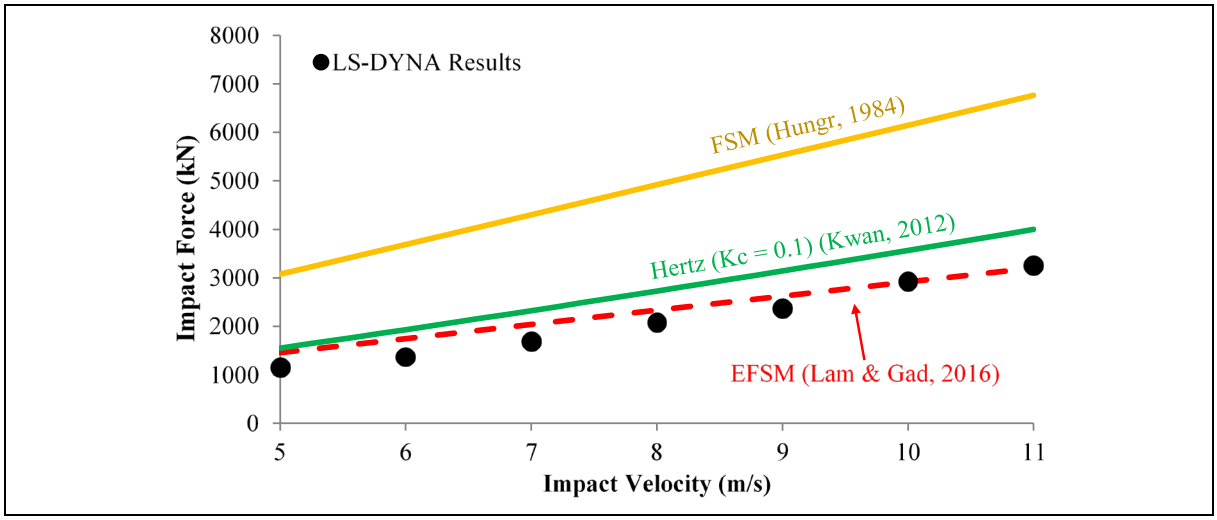

Figure 4.2 Comparison of FSM, EFSM, Hertz Load and Numerical Analysis for the Study of Boulder Impact Velocity

4.2 Effect of Mass of Boulder

Another series of numerical simulations were conducted. In this investigation, the same model barrier as that described in Section 4.1 was used, except that the boulder impact velocity was fixed at 10 m/s and the boulder diameter varied from 0.5 m to 1.5 m. Five numerical analyses were conducted (see Figure 4.3). The numerical results were shown in Figure 4.4, together with the analytical results obtained using FSM, EFSM and Hertz Equation with a reduction factor of 0.1. It was found that the prediction using EFSM matches well with the result of LS-DYNA simulation, whereas the other two methods, i.e. FSM and Hertz Load

with a reduction factor of 0.1, predicted a higher impact force than that from EFSM.

Figure 4.4 also indicates that boulder impact force is sensitive to the mass ratio (λ), where the boulder impact force increases with the boulder diameter non-linearly.

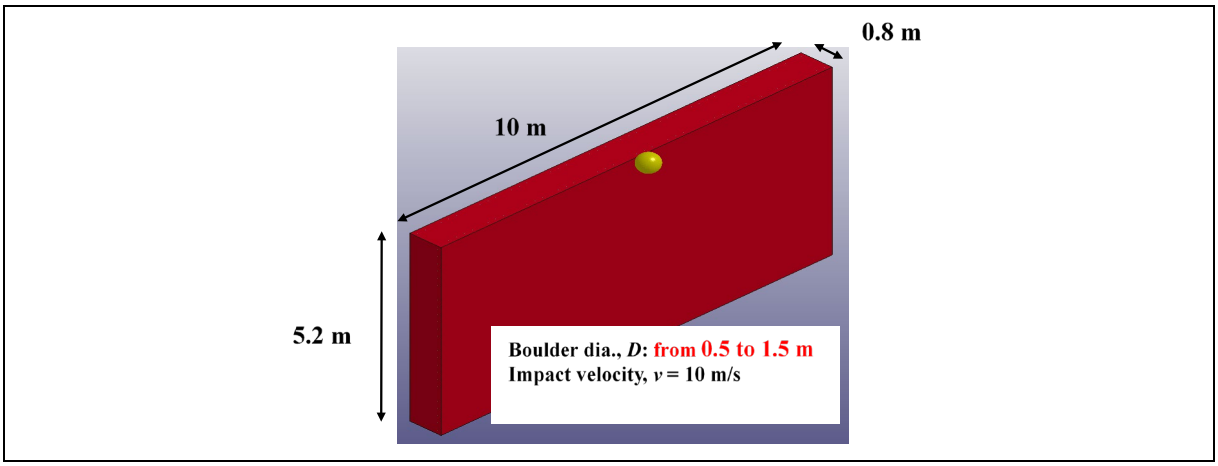

Figure 4.3 Validated Numerical Simulations for Parametric Study on the Inertial Effect

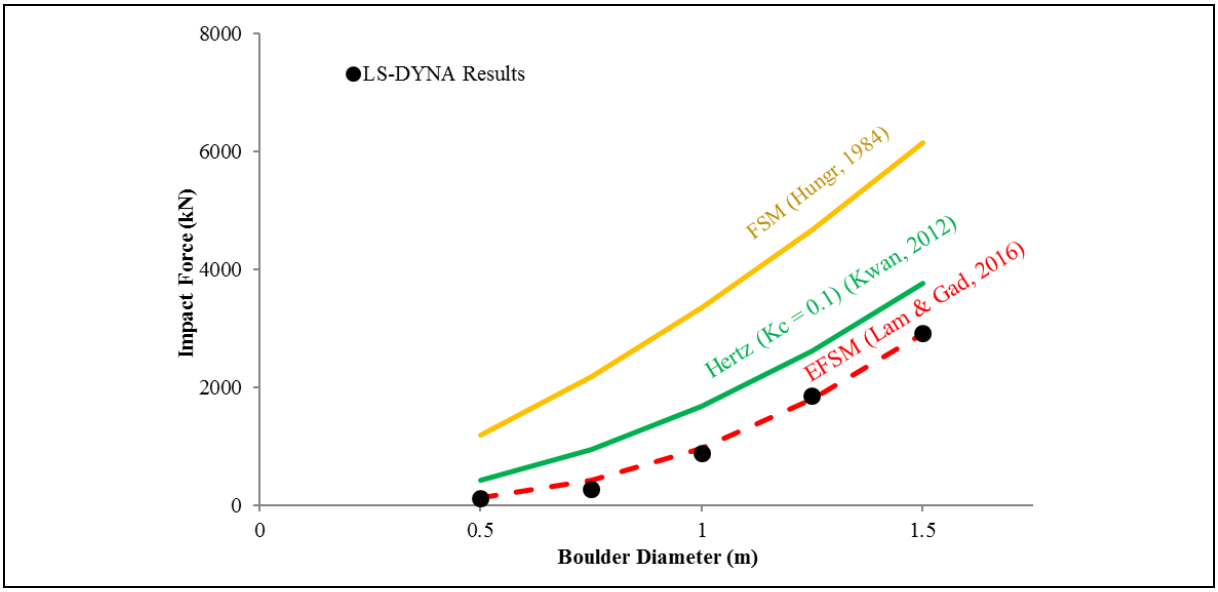

Figure 4.4 Comparison of FSM, EFSM, Hertz Load and Numerical Analysis for the Study of Inertial Effect

5 Further Discussion on Enhanced Flexural Stiffness Method

5.1 Effect of Coefficient of Restitution (COR)

A sensitivity study was carried out using the impact case as shown in Figure 4.1,

involving a 1.5 m dia. boulder travelling at a translational velocity of 10 m/s which hits the crest of the barrier. As the input of COR varied from the typical range of 0.2 to 0.3 (see Section 3.1), the predicted flexural deflection of the barrier and the boulder impact force increased from 33 mm to 36 mm, and from 2690 kN to 2914 kN respectively. The results calculated using EFSM are not very sensitive to changes within the typical range of COR.

5.2 Young's Modulus of Rigid Barrier

The input of the Young's modulus of the rigid barrier is required for both FSM, EFSM and simplified Hertz Equation. UoM (2018) showed that the duration of a rigid barrier to achieve its maximum strain was 10 ms to 20 ms and that corresponds to a strain rate for concrete and steel reinforcement of approx. from 0.07 s^{-1} to 0.3 s^{-1}. For this range of strain rate, based on Rostasy et al (1984), Schmidt-Hertienne (2001), Berner (1981) and Levings & Sritharan (2012) (see Section 4 Appendix C), the dynamic Young's modulus of concrete and steel reinforcement is comparable to their corresponding static values. As such, adopting the static Young's modulus of the rigid barrier in EFSM is considered adequate.

5.3 Effect of Rotational Velocity of Boulder

EFSM considers only the translational velocity, rather than the rotational velocity, of the boulder. Rotational velocity is generally not considered in overseas design guidelines and literatures (VanDine, 1996; SWCB, 2005; NILIM, 2007; CAGHP, 2018; CGS, 2004; Hungr et al, 1984; Zhang et al, 1996) when estimating the boulder impact force. Rotational component of a boulder, if in contact with a barrier, might give rise to a tangential (i.e. not normal) reaction force component on the barrier. Glover (2015) suggested that the rotational energy of the boulder might lead to laceration (i.e. surface damage) of a netting structure upon boulder impact.

A preliminary study was carried out in order to study the effect of the angular velocity of the boulder on the flexural response of the rigid barrier using program LS-DYNA. It was found that the rotation of the boulder may not be a critical factor in controlling the flexural response of the barrier, as shown in the Table 5.1 below:-

Table 5.1 Sensitivity Study on the Rotational Velocity of the Boulder

	Input Rotational Velocity of a Boulder (revolution/s)	Deflection at the Crest of the Barrier (mm)	Estimated Boulder Impact Force (kN)
Case 5.3.1	0	36.2	2921
Case 5.3.2	2.1 (Forward spin)	34.3	2768

Note: The impact scenarios for Case 5.3.1 and 5.3.2 above involve a boulder of 1.5 m dia. both travelling at a translational velocity of 10 m/s which hits a 5.2 m high, 10 long and 0.8 m thick reinforced concrete wall with a fixed base (details are shown in Figure 4.1 and Table 4.1).

5.4 Effect of Young's Modulus of Boulder

EFSM is primarily based on conservation of energy and momentum, and thus does not require the input of Young's Modulus of the boulder. A preliminary study has also been carried out in order to investigate the effect of Young's modulus of the boulder on the flexural response of the rigid barrier using LS-DYNA. Typical values of Young's moduli of granitic and volcanic rocks were considered. It was found that the Young's modulus of boulder had no significant effect on the flexural response of the barrier (see Table 5.2 below).

Table 5.2 Results of Sensitivity Study on the Young's Modulus of the Boulder

	Input Young's Modulus of the Boulder (GPa)	Deflection at the Crest of the Barrier (mm)	Estimated Boulder Impact Force (kN)
Case 5.4.1	50	36.2	2921
Case 5.4.2	150	36.9	2977

Note: The impact scenarios for Case 5.4.1 and 5.4.2 above involve a boulder of 1.5 m dia. travelling at a translational velocity of 10 m/s which hits a 5.2 m high, 10 long and 0.8 m thick reinforced concrete wall with a fixed base (details are shown in Figure 4.1 and Table 4.1).

5.5 Effect of Shape of Boulder

A preliminary study using LS-DYNA was conducted to investigate effect of shape of a boulder to the flexural response of a rigid barrier. Three numerical simulations were constructed using LS-DYNA with an impactor of different shapes, i.e. cylinder, cone and sphere (see Figure 5.1 below). It was found that the spherical boulder would give rise to a slightly larger barrier deflection (i.e. about 10%) than the other two impactors.

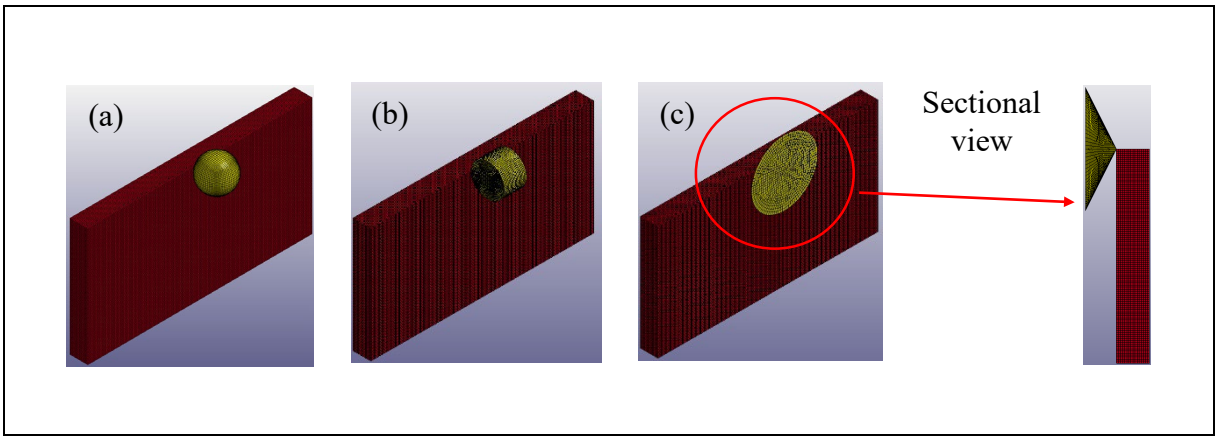

Figure 5.1 Numerical Simulations with Impact Objects in Different Shapes: (a) Sphere, (b) Cylinder and (c) Cone

Table 5.3 Results of Sensitivity Study on the Shape of the Boulder

Shape of Impactor	Mass of Impactor (kg)	Deflection at the Crest of the Barrier (mm)	Boulder Impact Force (kN)
Sphere	4683	36.2	2921
Cylinder (linear contact)		32.3	2606
Cone (point contact)		33.2	2679

Note: The impact scenarios for the three cases above involve a boulder of 1.5 m dia. travelling at a translational velocity of 10 m/s which hits a 5.2 m high, 10 long and 0.8 m thick reinforced concrete wall with a fixed base (details are shown in Figure 4.1 and Table 4.1).

5.6 Effect of Location of Boulder Impact

A preliminary study has also been conducted using program LS-DYNA to investigate the effect of the location of the point of contact on the flexural response of the rigid barrier. Three different model barriers were constructed (Case Nos. 5.6.1, 5.6.2 & 5.6.3 as shown in Figure 5.2 below). For each of these cases, three impact scenarios involving boulder impact close to the crest, at the mid height and near the base of the barrier were analysed (i.e. nine nos. of LS-DYNA models were analysed in total). It was found that the boulder impacting at the crest of the rigid barrier would give rise to the highest tensile strain on the flexural reinforcement at the base of the barrier (where bending moment is the highest), as compared to the other two impact locations (see Table 5.4 below).

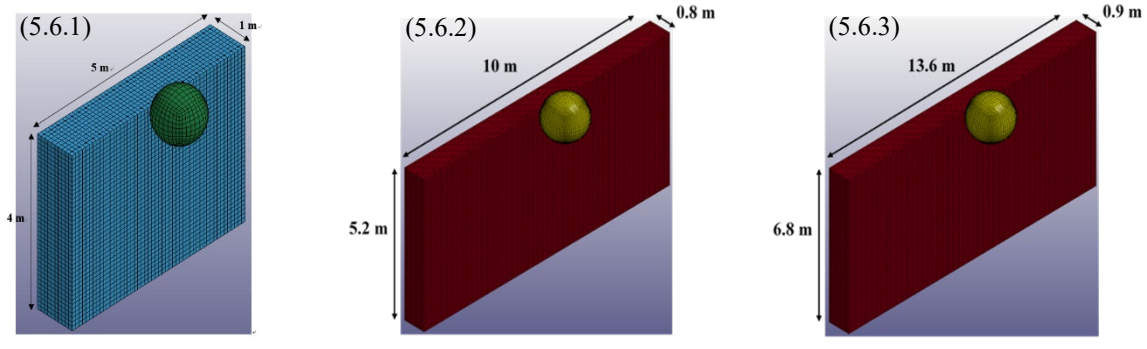

	Case 5.6.1	Case 5.6.2	Case 5.6.3
Boulder Diameter (m)	1.15	1.5	2.0
Translational Boulder Impact Velocity (m/s)	5	5	10

Figure 5.2 Numerical Simulations (i.e. Case Nos. 5.6.1, 5.6.2 & 5.6.3) with Boulder Impact on Three Different Model Rigid Barriers

Table 5.4 Results of Sensitivity Study on the Location of Boulder Impact

	Tensile Strain of Flexural Reinforcement (10^{-3}) at the Base of the Barrier		
	Case 5.6.1	Case 5.6.2	Case 5.6.3
Impact at the Crest of the Barrier	1.27	0.88	1.95
Impact at the Mid Height of the Barrier	0.8 (63%)	0.73 (83%)	1.25 (64%)
Impact near the Base of the Barrier	0.4 (31%)	0.43 (49%)	0.86 (44%)

Note: Figures in the bracket represent the percentage of tensile strain of flexural reinforcement compared to that for the impact at the crest of the barrier.

6 Further Work

As discussed in Sections 3 and 4, EFSM has been verified by means of small-scale impact tests along with results from numerical simulations employing an experimentally validated computer simulation. Large-scale physical impact tests have been carried out in order to further strengthen the validation of EFSM, which will be reported separately.

Furthermore, for rigid barriers subject to boulder impact, the risk of localised structural damage, such as perforation or punching failure, scabbing, etc. need to be studied. Another area that deserves further study is the flexural response of those rigid barriers provided with cushioning materials.

The discussion on the effects of the dynamic properties of rigid barrier, rotational velocity of boulder, angularity and shape of the boulder, Young's modulus of boulder and the location of boulder impact as given in Section 5 are established based on numerical simulations and deserve more in-depth study should more field data become available.

7 Conclusion

Positive results regarding the use of Enhanced Flexural Stiffness Method (EFSM) were obtained. The predicted flexural response of rigid barrier in various impact scenarios based on EFSM closely matched with the small-scale impact test and the validated numerical analyses. In addition, a more realistic boulder impact load could be predicted using EFSM, as compared with simplified Hertz equation or FSM. Notwithstanding, further development work, such as large-scale physical impact tests to further verify the reliability of EFSM, study of localised structural damage and study of the cushioning effect, needs to be undertaken in order to better improve the current design guidelines.

8 References

Ali, M., Sun, J., Lam, N., Zhang, L. & Gad, E. (2014). Simple hand calculation method for estimating deflection generated by the low velocity impact of a solid object. *Australian Journal of Structural Engineering*, 2014, 15(3): pp 243-259.

Berner, K. (1981). *Der Einfluss der Dehngeschwindigkeit auf das mechanische Verhalten von Betonstählen, 12. Forschungskolloquium des Deutschen Ausschusses für Stahlbeton, BAM, Berlin.*

CAGHP (2018). *Specification of Design for Debris Flow Prevention* (T/CAGHP *021-2018)*. China Association of Geological Hazard Prevention, 55p (in Chinese)

CGS (2004). *DZ/T0239-2004 - 泥石流災害防治工程設計規範.* 2004, 中國地質調查局 (in Chinese).

Chau, K.T., Wong, R.H.C. & Lee, C.F. (1998). Rockfall problems in Hong Kong and some new experimental results for coefficients of restitution. *International Journal of Rock Mechanics and Mining Sciences*, 1998, vol. 35, no. 4-5, pp 662-663.

Fujikake, K., Li, B. & Soeun, S. (2009). Impact response of reinforced concrete beam and its analytical evaluation. *Journal of Structural Engineering*, 2009, 135(8): pp 938-950.

Glover, J.M.H. (2015). *Rock-shape and its role in rockfall dynamics, Durham theses.* Durham University, 266 p. Available at Durham E-Theses Online: http://etheses.dur.ac.uk/10968/

Hungr, O., Morgan, G.C. & Kellerhals, R. (1984). Quantitative analysis of debris torrent hazards for design of remedial measures. *Canadian Geotechnical Journal*, vol. 21, pp 663-677.

Kishi, N. & Bhatti, A.Q. (2010). An equivalent fracture energy concept for nonlinear dynamic response analysis of prototype RC girders subjected to falling-weight impact loading. *International Journal of Impact Engineering*, 2010, 37(1): pp 103-113.

Kwan, J.S.H. (2012). *Supplementary Technical Guidance on Design of Rigid Debris-resisting Barriers (GEO Report No. 270)*. Geotechnical Engineering Office, Hong Kong, 88 p.

Kwan, J.S.H., Lam, H.W.K., Ng, C.W.W., Lam, N.T.K., Chan, S.L., Yiu, J. & Cheuk, J.C.Y. (2018). Recent technical advancement in natural terrain landslide risk mitigation measures in Hong Kong. *HKIE Transactions: Special Issue on Landslides and Debris Flow - Theory and Design, Mitigation, Stabilisation and Monitoring.* In Press.

Lam, C. (2016). *A Pilot Study of the Use of Cushioning Materials for Reducing Dynamic Impact Loads on Rigid Debris-resisting Barriers (Technical Note No. TN 5/2016).* Geotechnical Engineering Office, Hong Kong, 70 p.

Lam, C. & Kwan, J.S.H. (2016). *Displacement-based Assessment of Boulder Impacts on Rigid Debris-resisting Barriers - A Pilot Study (Technical Note No. TN 9/2016).* Geotechnical Engineering Office, Hong Kong, 66 p.

Lam, N. & Gad, E. (2016). The estimation of impact forces based on first principles. In *Australasian Structural Engineering Conference: ASEC 2016*, Engineers Australia.

Lam, N.T.K., Yong, A.C.Y., Lam, C., Kwan, J.S.H., Perera, J.S., Disfani, M.M. & Gad, E.

(2017). Displacement-based approach for the assessment of overturning stability of rectangular rigid barriers subject to point impact. *Journal of Engineering Mechanics*, in press.

Levings, J. & Sritharan, S. (2012). Effects of Cold Temperature and Strain Rate on the Stress-Strain Behavior of ASTM A706 Grade 420 (60) Steel Reinforcement, *ASCE Journal of Materials in Civil Engineering, Volume 24 Issue 12, December 2012*

Lo, D.O.K. (2000). *Review of Natural Terrain Landslide Debris-resisting Barrier Design* (*GEO Report No. 104)*. Geotechnical Engineering Office, Hong Kong, 91 p.

Masuya, H., Ihara, T., Onda, S., & Kamijo, A. (2001). Experimental study on some parameters for simulation of rock fall on slope. *Proc. 4th Asia-Pacific Conf. on Shock and Impact Loads on Structures*, pp. 63 - 69

Ng, C.W.W., Song, D., Choi, C.E., Liu, L.H.D., Kwan, J.S.H., Koo, R.C.H., Pun, W.K. (2016). Impact mechanisms of granular and viscous flows on rigid and flexible barriers. *Canadian Geotechnical Journal*, 54(2):188–206.

NILIM (2007). *Manual of Technical Standard for Designing Sabo Facilities against Debris Flow and Driftwood*. Technical Note of NILIM No. 365, Natural Institute for Land and Infrastructure Management, Ministry of Land, Infrastructure and Transport, Japan, pp 73 (in Japanese).

Rostary, F. S, Scheuermann, J., Sprenger, K. H. (1984). *Mechanical behaviour of some construction materials subjected to rapid loading and low temperature", Betonwerk+Fertigteil-Technik (Concrete Precasting Plant and Technology), Volume 50, Number 6, June, pp. 393-401*

Schmidt-Hurtienne, B. (2001). Ein dreiaxiales Schädigungsmodell für Beton unter Einschluss des Dehnrateneffektes bei Hochgeschwindigkeitsbelastung, Massivbau Baustofftechnologie Karlsruhe, Heft 42, 259 pp

Song, D., Ng, C.W.W., Choi, C.E., Zhou, G.G.D., Kwan, J.S.H., Koo, R.C.H. (2017). Influence of debris flow solid fraction on rigid barrier impact. *Canadian Geotechnical Journal*, 54(10):1421–1434.

SWCB (2005). *Manual of Soil and Water Conservation*. Soil and Water Conservation Bureau, Taiwan, 692 p (in Chinese).

Timoshenko, S.P., & Goodier, J.N. (1970). *Theory A Elasticity*, McGraw - Hill Book Company, New York.

VanDine, D.F. (1996). *Debris Flow Control Structures for Forest Engineering.* Ministry of Forests, British Columbia, Canada, 68 p.

UoM (2017). *Computer Services of Numerical Investigation of the Structural Performance of Rigid Debris-resisting Barriers Subjected to Boulder Impact*, Final Report No. 2 prepared for the Geotechnical Engineering Office, Civil Engineering and Development Department, Hong Kong, 50 p.

UoM (2018). *Large Scale Impact Test and Computer Services for Investigation of the Structural Response of Rigid Barrier subjected to Boulder Impact, Report No. 1 (Draft)* prepared for the Geotechnical Engineering Office, Civil Engineering and Development Department, Hong Kong, 51 p.

Wu, J., Tian, L., Kang, Z., Zhang, Y. & Liu, J. (1993). *Debris Flow and Its Comprehensive Control. Science Press, 332 p (in Chinese).*

Yang, Y., Lam, N.T.K. & Zhang, L. (2012). Evaluation of simplified methods of estimating beam responses to impact. *International Journal of Structural Stability and Dynamics*, 2012, 12(3): pp 1250016-1-1250016-24.

Zhang, S., Hungr, O. & Slaymaker, O. (1996). The calculation of impact force of boulders in debris flow. *Debris Flow Observation and Research*, edited by R. Du, Science Press, pp 67-72 (in Chinese).

Section 4
Appendix A

Derivation of Enhanced Flexural Stiffness Method (EFSM)

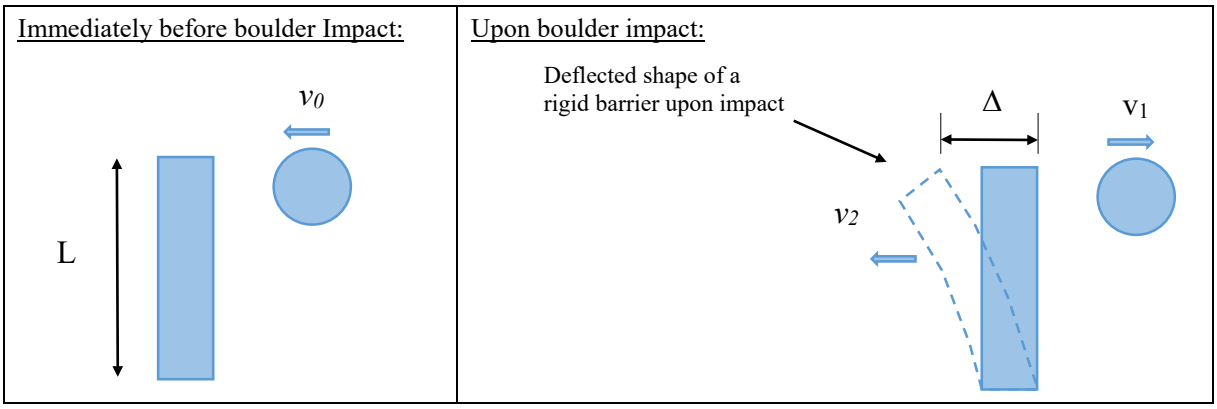

The above impact scenario, with an impactor of mass m and velocity v_0, is being considered. Immediately prior to contact, kinetic energy of the impactor, KE_0 is:

$$KE_0 = \frac{1}{2}mv_0^2 \quad \text{..... (A.1)}$$

Upon the boulder impact, the boulder rebounds in an opposite direction with a velocity of v_1 whereas the barrier deflects with a velocity of v_2. Assuming λ is the ratio between the participating mass of the barrier (see also Section 4 Appendix B) and the mass of the boulder, λ can be represented in Equation A.3, using conservation of momentum as given in Equation A.2:

$$mv_0 = -mv_1 + \lambda mv_2 \quad \text{..... (A.2)}$$

$$\lambda = \frac{v_1 + v_0}{v_2} \quad \text{..... (A.3)}$$

Coefficient of restitution (COR) in Newtonian mechanics is introduced, i.e.,

$$COR = \frac{v_1 + v_2}{v_0} \quad \text{..... (A.4)}$$

$$\frac{v_2}{v_0} = \frac{1 + COR}{1 + \lambda} \quad \text{..... (A.5)}$$

Based on the above, the ratio of the energy transferred to the barrier after the impact (i.e. KE_2) to the kinetic energy of the impactor before the impact is:

$$\frac{KE_2}{KE_0} = \frac{\frac{1}{2}\lambda mv_2^2}{\frac{1}{2}mv_0^2} \quad \text{..... (A.6)}$$

$$\frac{KE_2}{KE_0} = \lambda\left(\frac{1 + COR}{1+\lambda}\right)^2 = \beta^2 \quad \text{..... (A.7)}$$

Meanwhile, based on a linear force-displacement (i.e. F-Δ) relationship of the barrier, with a flexural stiffness k, the strain energy of the barrier, SE, is given by:-

$$F = k\Delta \quad \text{..... (A.8)}$$

$$SE = \frac{1}{2}k\Delta^2 \quad \text{..... (A.9)}$$

For Flexural Stiffness Method, which assumes no energy reduction, the kinetic energy of the boulder before impact (i.e. KE_0) simply equals the strain energy of the barrier (i.e. SE):

$$\frac{1}{2}mv_0^2 = \frac{1}{2}k\Delta^2 \quad \text{..... (A.10)}$$

$$\Delta = \sqrt{\frac{1}{k}mv_0^2} \quad \text{..... (A.11)}$$

$$F = \sqrt{mv_0^2 k} \quad \text{..... (A.12)}$$

For EFSM, based on conservation of momentum, only part of the kinetic energy of the boulder before impact (i.e. KE_0) converts to the kinetic energy of the barrier (i.e. KE_2), which then becomes the strain energy of the barrier (i.e. SE). The term generalised stiffness (k^*) is introduced (see Section 4 Appendix B) for the determination of flexural deflection of the barrier under dynamic motion (UoM, 2017):

$$\beta^2 \frac{1}{2}mv_0^2 = \frac{1}{2}k^*\Delta^2 \quad \text{..... (A.13)}$$

$$\Delta = \beta v_0 \sqrt{\frac{m}{k^*}} \quad \text{..... (A.14)}$$

The concept of equivalent static force (i.e. a static loading condition which gives rise to the same amount of flexural deflection as that of a dynamic impact) is applied to the flexural deflection. This time, flexural stiffness (k) is used as a problem of static is to be dealt with:

$$F = k\Delta \quad \text{..... (A.15)}$$

For an impact on the crest of the barrier where $k^* = k$,

$$F = \beta v_0 \sqrt{mk} \quad \text{..... (A.16)}$$

Section 4
Appendix B

Derivation of Flexural Stiffness of Wall (k) and Mass Ratio (λ)

Contents

	Page No.
Contents	209
List of Figures	210
References	216

List of Figures

Figure No.		Page No.
B1	Beam Segment under Bending (1)	211
B2	Beam Segment under Bending (2)	213
B3	A Cantilever Beam under a Point Load	215

Upon a boulder impact, a barrier wall would oscillate where there is an interchange between the kinetic energy and the strain energy of the wall. Based on findings of various impact tests and numerical analyses carried out by the University of Melbourne, oscillation of the wall can be described as a simple harmonic motion. The mode of oscillation of the barrier is characterised by its natural frequency, which is a function of its participating mass and its generalised stiffness. These two parameters represent the mass and the stiffness of the barrier associating with this mode of oscillation. As such, the participating mass contributes to the momentum gained by the barrier. Using the equations of simple harmonic motion, UoM (2017) derived the solution of the participating mass and the generalised stiffness as given below.

Derivation of k^* and λ – Generalised Expression

A beam segment under oscillation, which deflects in the x-direction as shown in Figure B1, is being considered.

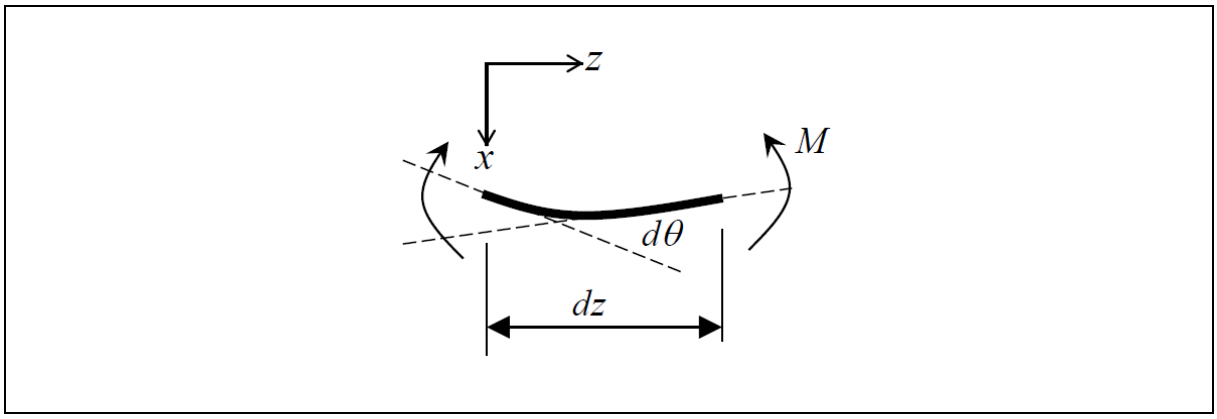

Figure B1 Beam Segment under Bending (1)

For a small interval of the beam (length = dz), the segmental kinetic energy dKE equals:-

$$dKE = \frac{1}{2}(mdz)(\dot{x})^2 \quad \text{..... (B.1)}$$

where m = mass per metre
$\dot{x}$ = velocity of beam segment in x-direction.

Assuming that the beam oscillates in a simple harmonic motion, the displacement response of the beam along the beam length z is given by:-

$$x = \psi(z)A\sin\omega t \quad \text{..... (B.2)}$$

By differentiating Equation B.2 with respect to time, the velocity of the beam segment $\dot{x}$ is obtained:

$$\dot{x} = \omega\, \psi(z)\, A \cos \omega t \quad \text{..... (B.3)}$$

where x = displacement-time response
$\psi(z)$ = dimensionless shape function
A = amplitude
ω = natural angular frequency
t = time.

Substituting Equation B.3 into Equation B.1, the segmental kinetic energy of the beam of length dz is:-

$$dKE = \frac{1}{2}(\, mdz\,)(\, \omega\, \psi(\mathrm{z}) A \cos \omega t\,)^2 \quad \text{..... (B.4)}$$

Integrating Equation B.4 with respect to z, the total kinetic energy of the whole beam KE is determined:

$$KE = \frac{A^2 \cos^2 \omega t}{2} \omega^2 \int m\,(\,\psi\,(\,z\,)\,)^2 dz \quad \text{..... (B.5)}$$

Substitute $\cos \omega t = 1$ into Equation B.5, the maximum kinetic energy KE_{max} of the beam is:

$$KE_{max} = \frac{A^2}{2} \omega^2 \int m \left(\psi(z)\right)^2 dz \quad \text{..... (B.6)}$$

On the other hand, there would be bending moment M in the beam when the angle of bending is $d\theta$. The corresponding segmental strain energy can be written in the form of Equation B.7.

$$dU = \frac{1}{2}(M)d\theta \quad \text{..... (B.7)}$$

Meanwhile, using simple beam theory, the bending moment M is simply given by (Gere, 2001):-

$$M = EI \times \phi \quad \text{..... (B.8)}$$

where E = Young's modulus
ϕ = Beam curvature
I = second moment of area.

Figure B2 shows a sketch of the beam segment under bending.

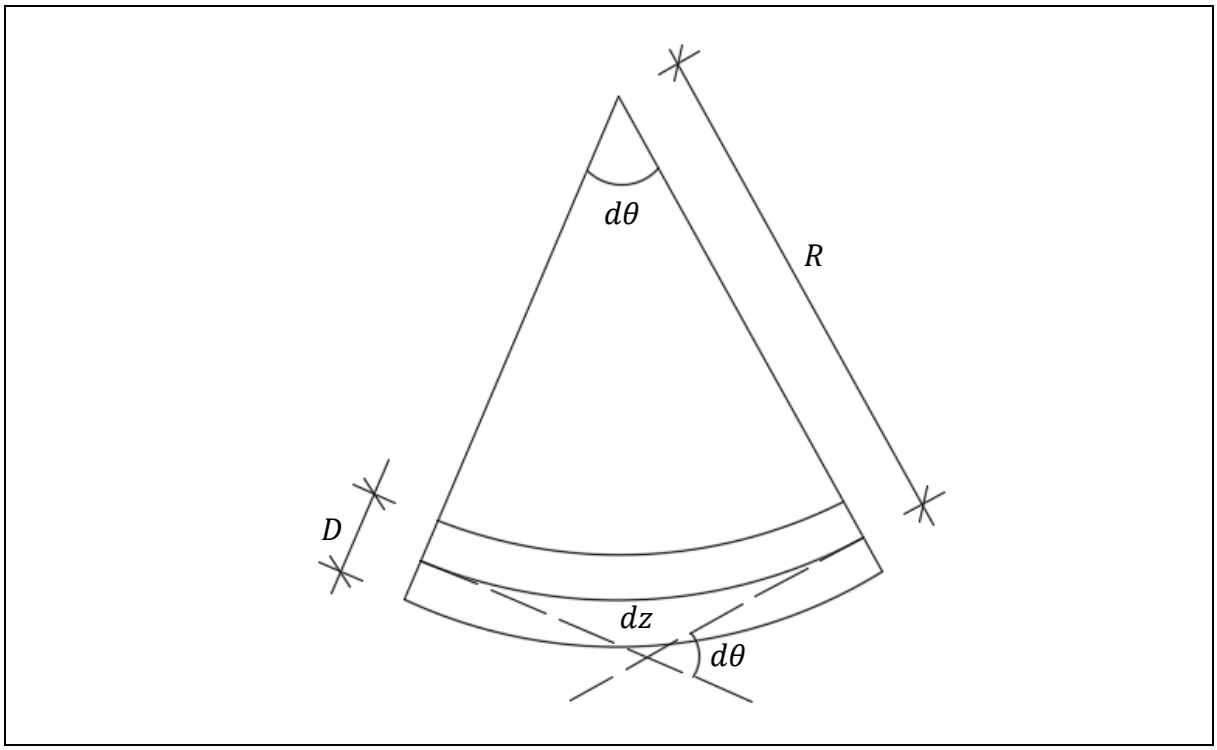

Figure B2 Beam Segment under Bending (2)

D is the depth of the beam segment. From Figure B2,

$$d\theta = \frac{1}{R} dz \quad \text{..... (B.9)}$$

since $\frac{1}{R} = \phi$,

$$d\theta = \phi \, dz \quad \text{..... (B.10)}$$

On the other hand, the curvature of the beam, ϕ, is obtained by differentiating the beam displacement, x, which is given by Equation B.2, twice with respect to z (Gere, 2001).

$$\phi = \frac{\partial^2 x}{\partial z^2} = A \sin \omega t \, \frac{\partial^2 \psi(z)}{\partial z^2} \quad \text{..... (B.11)}$$

Substituting Equation B.11 into Equation B.8,

$$M = EI \times A \sin \omega t \, \frac{\partial^2 \psi(z)}{\partial z^2} \quad \text{..... (B.12)}$$

Substituting Equation B.11 into Equation B.10,

$$d\theta = A \sin \omega t \, \frac{\partial^2 \psi(z)}{\partial z^2} \, dz \quad \text{..... (B.13)}$$

Substituting Equations B.12 and B.13 into Equation B.7,

$$dU = \frac{A^2 \sin^2 \omega t}{2} EI \left(\frac{\partial^2 \psi(z)}{\partial z^2}\right)^2 \quad \text{..... (B.14)}$$

Integrating Equation B.14 with respect to z, the total strain energy of the beam U is,

$$U = \frac{A^2 \sin^2 \omega t}{2} \int EI \left(\frac{\partial^2 \psi(z)}{\partial z^2}\right)^2 dz \quad \text{..... (B.15)}$$

Substitute $\sin \omega t = 1$ into Equation B.15, the maximum strain energy U_{max} is determined by:

$$U_{max} = \frac{A^2}{2} \int EI \left(\frac{\partial^2 \psi(z)}{\partial z^2}\right)^2 dz \quad \text{..... (B.16)}$$

Considering conservation of energy of the beam,

$$KE_{max} = U_{max} \quad \text{..... (B.17)}$$

Substituting Equations B.16 and B.6 into Equation B.17.

$$\frac{A^2}{2} \omega^2 \int m \left(\psi(z)\right)^2 dz = \frac{A^2}{2} \int EI \left(\frac{\partial^2 \psi(z)}{\partial z^2}\right)^2 dz \quad \text{..... (B.18)}$$

Rearranging Equation B.18, the expression for the natural angular frequency of the beam subject to the impact is obtained:

$$\omega = \sqrt{\frac{\int \mathrm{EI} \left(\frac{\partial^2 \psi(z)}{\partial z^2}\right)^2 dz}{\int m \left(\psi(z)\right)^2 dz}} \quad \text{..... (B.19)}$$

Since

$$\omega = \sqrt{\frac{k^*}{m^*}} \quad \text{..... (B.20)}$$

where k^* = generalised stiffness
m^* = participating mass.

The participating mass and the flexural stiffness are determined by Equation B.21 and B.22 respectively.

$$m^* = \int m \left(\psi(z)\right)^2 dz \quad \text{..... (B.21)}$$

$$k^* = \int EI \left(\frac{\partial^2 \psi(z)}{\partial z^2}\right)^2 dz \quad \text{..... (B.22)}$$

Derivation of k and λ for a Boulder Hitting the Tip of a Cantilever

Consider a cantilever beam under a point load at the free end, as shown in Figure B3.

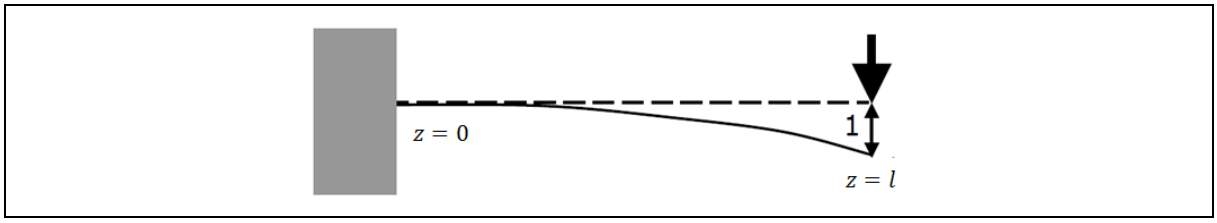

Figure B3 A Cantilever Beam under a Point Load

The deflection profile of the beam can be determined by Equation B.23.

$$\Delta = \frac{Fl^3}{6EI}\left(3\left(\frac{z}{l}\right)^2 - \left(\frac{z}{l}\right)^3\right) \quad \text{..... (B.23)}$$

The deflection profile can then be normalised into a unitless shape function in order that $\psi(z = l) = 1$:

$$\psi(z)=\frac{1}{2}\left(3\left(\frac{z}{l}\right)^2 - \left(\frac{z}{l}\right)^3\right) \quad \text{..... (B.24)}$$

Substituting Equation B.24 into Equation B.21 gives:-

$$m^* = \int_0^l m\left(\frac{1}{2}\left(3\left(\frac{z}{l}\right)^2 - \left(\frac{z}{l}\right)^3\right)\right)^2 dz \quad \text{..... (B.25)}$$

Putting $z = l$, the participating mass of the cantilever beam under a tip impact is given by:-

$$m^* = 0.24ml \quad \text{..... (B.26)}$$

Differentiating Equation B.24 twice with respect to z,

$$\frac{\partial^2\psi(z)}{\partial z^2} = \frac{3}{l^2}\left(1-\frac{z}{l}\right) \quad \text{..... (B.27)}$$

Substituting Equation B.27 into Equation B.22:-

$$k^* = \int_0^l EI\left(\frac{3}{l^2}\left(1-\frac{z}{l}\right)\right)^2 dz \quad \text{..... (B.28)}$$

Putting $z = l$, the generalised flexural stiffness of the cantilever beam under a tip impact is given by:-

$$k^* = \frac{3EI}{l^3} \quad \text{..... (B.29)}$$

References

Gere, J.M. (2001). *Mechanics of Materials (Fifth Edition).* Brooks/Cole Thomson Learning, 926 p.

UoM (2017). *Computer Services of Numerical Investigation of the Structural Performance of Rigid Debris-resisting Barriers* Subjected *to Boulder Impact, Final Report No. 2* prepared for the Geotechnical Engineering Office, Civil Engineering and Development Department, Hong Kong, 50 p.

Section 4
Appendix C

Dynamic Effect on the Young's Modulus of Rigid Barrier

Contents

	Page No.
Contents	218
List of Figure	219
References	221

List of Figure

Figure No.		Page No.
C1	Stress Strain Relationship of Concrete and Steel Reinforcement under Low Strain Rate	220

The input of the Young's modulus of the rigid barrier is required for both FSM, EFSM and simplified Hertz equation. No design guidelines explicitly recommend the use of a dynamic Young's modulus for the barrier. Notwithstanding this, adopting the dynamic properties of the rigid barrier under the correct strain rate is theoretically a better representation of the behaviour of the rigid barrier. The effects of strain rate on the Young's modulus are thus examined and are discussed below.

Recent large-scale impact tests conducted by the University of Melbourne (UoM, 2018) showed that the maximum strain of the barrier is developed at 10 ms to 20 ms upon impact which the strain rate for concrete and steel reinforcement corresponds approx. from 0.07 s^{-1} to 0.3 s^{-1}.

Figure C1 below shows the stress-strain relationship of concrete and steel reinforcements obtained by laboratory tests conducted by different researchers under various strain rates, $\dot{\varepsilon}$. The Young's modulus of concrete under compression at a low strain rate (0.1 s^{-1}) was found to be close to its quasi-static value (Rostasy et al, 1984). Similar finding was reported in Schmidt-Hertienne (2001). The Young's modulus of steel reinforcement was demonstrated largely unaffected by its strain rate (Berner, 1981; Levings & Sritharan, 2012). Therefore, the dynamic elastic modulus of the rigid barrier corresponding to the strain rate during a boulder impact is close to it static value.

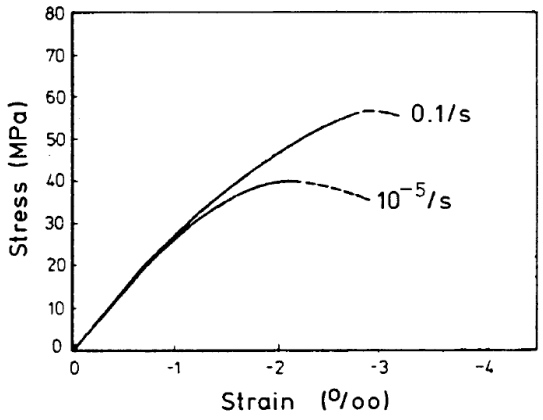

Stress strain relationship of concrete under compression in low strain rate (Rostasy et al, 1984)

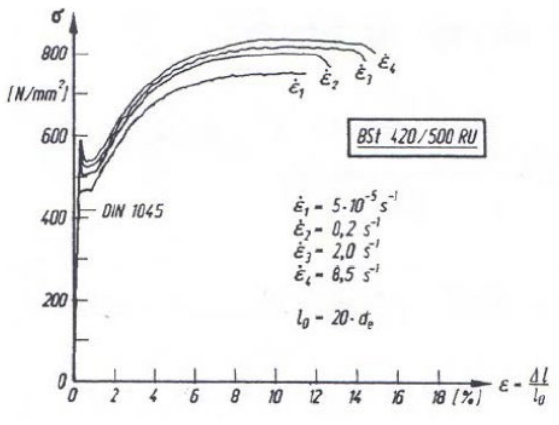

Stress strain relationship of steel reinforcements under various strain rates (Berner, 1981)

Figure C1 Stress Strain Relationship of Concrete and Steel Reinforcement under Low Strain Rate

In the large-scale impact tests recently conducted by the University of Melbourne (UoM, 2018), it was found that the use of EFSM with the input of static Young's Modulus could give a very close and slightly conservative prediction of the boulder impact force as compared with the actual flexural response of the rigid barrier. Also, in view that there is a lack of design guideline which sheds light on this aspect, adopting the static Young's modulus of the rigid barrier is considered adequate for routine design.

References

Schmidt-Hurtienne, B. (2001). Ein dreiaxiales Schädigungsmodell für Beton unter Einschluss des Dehnrateneffektes bei Hochgeschwindigkeitsbelastung, Massivbau Baustofftechnologie Karlsruhe, Heft 42, 259 pp

Rostary, F. S., Scheuermann, J. & Sprenger, K. H. (1984). *Mechanical behaviour of some construction materials subjected to rapid loading and low temperature", Betonwerk+Fertigteil-Technik (*Concrete *Precasting Plant and Technology),* Volume 50, Number 6, June, pp. 393-401

Berner, K. (1981). *Der Einfluss der Dehngeschwindigkeit auf das mechanische Verhalten von Betonstählen, 12.* Forschungskolloquium *des Deutschen Ausschusses für Stahlbeton, BAM, Berlin.*

Levings, J. & Sritharan, S. (2012). Effects of Cold Temperature and Strain Rate on the Stress-Strain Behavior of ASTM A706 Grade 420(60) Steel Reinforcement, *ASCE Journal of Materials in Civil Engineering,* Volume 24 Issue 12, December 2012

UoM (2018). *Service Contract for* Large *Scale Impact Test and Computer Services for Investigation of the Structural Performance of Rigid Barriers Subjected to Boulder Impact, Report No. 1 (Draft)* prepared for the Geotechnical Engineering Office, Civil Engineering and Development Department, Hong Kong, 51 p.

Section 4
Appendix D

Prediction of Impact Force and Flexural Displacement for Small-scale Impact Test Using EFSM

Contents

	Page No.
Contents	223
List of Table	224
List of Figure	225

List of Table

Table No.		Page No.
D1	Information of Small-scale Impact Test	226

List of Figure

Figure No.		Page No.
D1	Snapshots of Impact Test (a) Immediately before the Impact; (b) at the Instant of the Impact; and (c) Immediately after the Impact	226

Table D1 Information of Small-scale Impact Test

Parameters	Values
Steel Pole Height	1 m
Steel Pole Width	0.15 m
Steel Pole Thickness	0.02 m
Young's Modulus of Steel	200 GPa
Mass of Steel Pole	23.4 kg
Dummy Mass	38 kg
Impactor Mass	5 kg

By analysing velocity data obtained in the impact test:

Figure D1 Snapshots of Impact Test (a) Immediately before the Impact; (b) at the Instant of the Impact; and (c) Immediately after the Impact

$$\text{COR} = \frac{v_1 + v_2}{v_0} = 0.34$$

The Participating Mass of the Steel Pole

$\lambda m = 0.25 \times 23.4 + 38 = 43.85$ kg

$$\lambda m = \frac{\lambda m}{m} = \frac{43.85}{5} = 8.8$$

The Flexural Stiffness of the Steel Pole

$$I = \frac{bd^3}{12} = 1 \text{ x } 10^{-7} \text{ m}^4$$

$$k^* = k = \frac{3EI}{L^3} = 60000 \text{ N/m}$$

β factor

$$\beta = \sqrt{\lambda \left(\frac{1 + \text{COR}}{1 + \lambda}\right)^2} = \sqrt{8.8 \left(\frac{1 + 0.34}{1 + 8.8}\right)^2} = 0.406$$

The Predicted Impact Force and the Predicted Flexural Displacement at the tip of the Steel Pole using EFSM

$$F = \beta v \sqrt{mk} = 0.406 \text{ x } 4.43 \text{ x } \sqrt{5 \text{ x } 60000} = 984 \text{ N}$$

$$\Delta = \frac{F}{k} = \frac{984}{60000} = 0.0164 \text{ m} = 16.4 \text{ mm}$$

This displacement is comparable to the measured displacement in the impact experiment, i.e. 16.9 mm.

Section 4
Appendix E

Numerical Analyses - Model Validation

Contents

	Page No.
Contents	229
List of Tables	230
List of Figures	231
E.1 Introduction	232
E.2 Validation of LS-DYNA Model	232
References	235

List of Tables

Table No.		Page No.
E1	Key Parameters for Model Validation for Steel Reinforcement (Impact Tests by Kishi & Bhatti (2010))	234
E2	Key Parameters for Model Validation for Concrete (Impact Tests by Kishi & Bhatti (2010))	234

List of Figures

Figure No.		Page No.
E1	Impact Tests by Kishi & Bhatti (2010) for Model Validation	232
E2	Reinforcement Layout of the Reinforced Concrete Girder in the Impact Test Carried Out by Kishi & Bhatti (2010)	233
E3	Printout of LS-DYNA Input Replicating the Test Setup in Kishi & Bhatti (2010)	233
E4	Comparison of Impact Force and Beam Deflection for Model Validation (Impact Test by Kishi & Bhatti (2010))	234
E5	Comparison of Impact Force and Beam Deflection for Model Validation (Impact Test by Fujikake et al (2009))	235

E.1 Introduction

Parametric study on EFSM is carried out through a series of numerical analyses with the following steps:

(a) validating LS-DYNA models using two large-scale impact tests, and

(b) carrying out validated numerical simulations pertaining to various scenarios of boulder impacts on rigid barriers.

For part (a), the validatiom exercise against two documented dynamic impact tests on reinforced concrete structures reported by Fujikake et al (2009) and Kishi & Bhatti (2010) was conducted. Details of part (a) are elaborated in this Appendix. Part (b) above has been discussed in Section 4.

E.2 Validation of LS-DYNA Model

The validation was first carried out against two documented dynamic impact tests on reinforced concrete structures reported by Fujikake et al (2009) and Kishi & Bhatti (2010). Details of one of the tests for the validation using Kishi & Bhatti (2010) are shown in Figure E1.

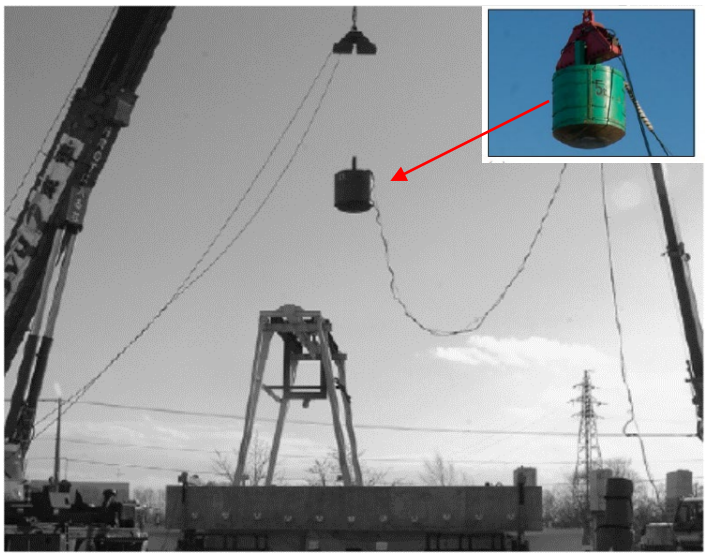

Note: A drop weight of 2,000 kg (which was made of a steel casing of 1 m in diameter, 97 cm in height and with a spherical base of 80 cm in radius) was released from a height of 10 m to achieve an impact velocity of 14 m/s onto the mid-portion of a 8 m spanned simply-supported rectangular reinforced concrete girder.

Figure E1 Impact Tests by Kishi & Bhatti (2010) for Model Validation

The above field test was carried out on a reinforced concrete girder with a cross-section of 1 m wide, 0.85 m deep and 8 m clear span. The compressive strength of concrete was 31.2 MPa, whereas the yield strengths of longitudinal rebar and stirrup were 401 MPa and 390 MPa respectively. The reinforcement layout of the girder is depicted in Figure E2.

Load cells were installed in the supports of the girders. Each load cell had a capacity of 1,500 kN and was operated at a measuring frequency of at least 1 kHz. The contact force was estimated by measuring the deceleration of the heavy weight, which was captured by the strain gauge typed accelerometer installed at the impacting mass. The accelerometer had a frequency ranged up to 7 kHz. To determine the flexural response of the girder, displacements were measured by laser type variable displacement transducers (LVDTs), with a maximum stroke of 200 mm and a measuring frequency of 915 Hz.

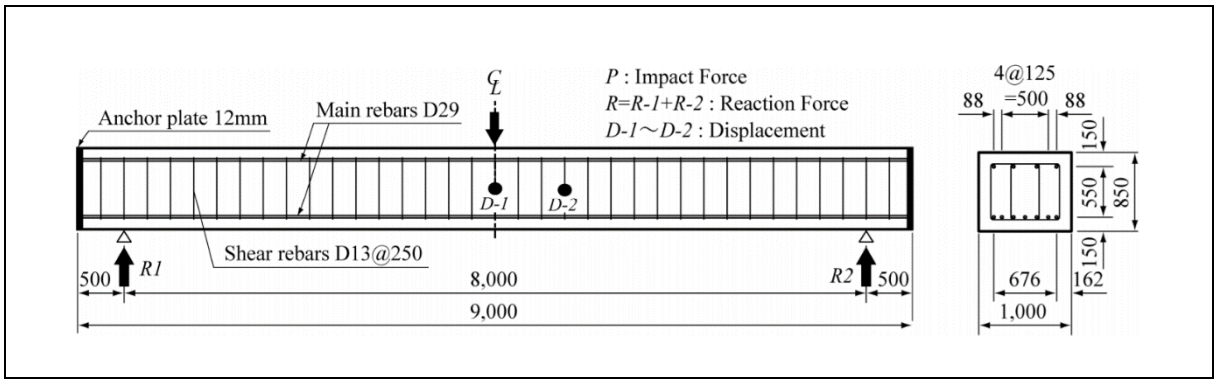

Figure E2 Reinforcement Layout of the Reinforced Concrete Girder in the Impact Test Carried Out by Kishi & Bhatti (2010)

In the validation exercise, material properties of the impactor, concrete and reinforcements were input in accordance with their actual values given in the literature. A summary of the inputs is given in Table E1 and Table E2 below. These properties include the elastic modulus, Poisson's ratio and the dimensions of each member, the density, the uniaxial compressive strength of concrete, etc. A snapshot of the model is shown in Figure E3 below.

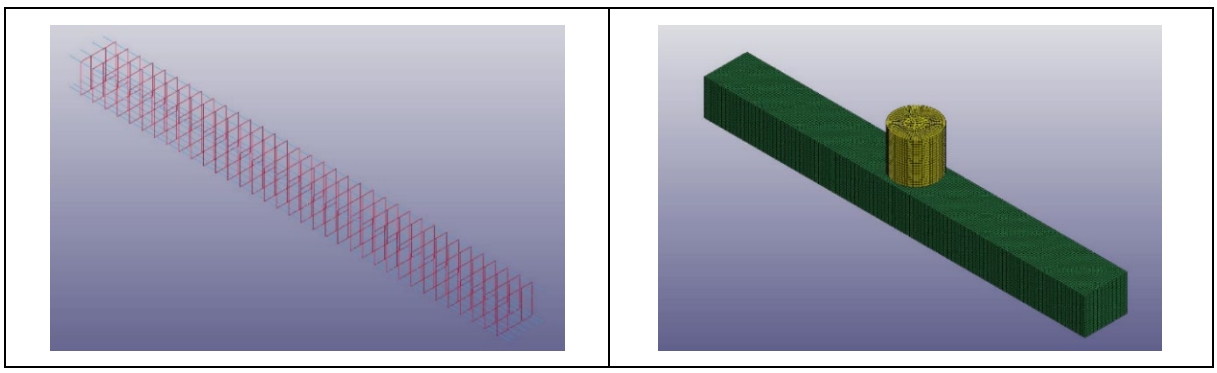

Figure E3 Printout of LS-DYNA Input Replicating the Test Setup in Kishi & Bhatti (2010)

Table E1 Key Parameters for Model Validation for Steel Reinforcement (Impact Tests by Kishi & Bhatti (2010))

Part Name	Reinforcement
Constitutive Model	Plastic Kinematic
Density	7,850 kg/m^3
Young's Modulus	200 GPa
Poisson's Ratio	0.3
Yield Stress	390 MPa (Stirrups) & 401 MPa (Flexural reinforcements)
Tangent Modulus	2 GPa

Table E2 Key Parameters for Model Validation for Concrete (Impact Tests by Kishi & Bhatti (2010))

Part Name	Concrete
Constitutive Model	Winfrith Concrete
Density	2,400 kg/m^3
Young's Modulus	30.1 GPa
Poisson's Ratio	0.2
Uniaxial Compressive Strength	31.2 MPa
Uniaxial Tensile Strength	1.5 MPa

The outputs of numerical analyses, including impact force-time history and deflection-time history of the R.C. girder, were examined. These data are then compared with the published experimental results, which are shown in Figure E4 and Figure E5.

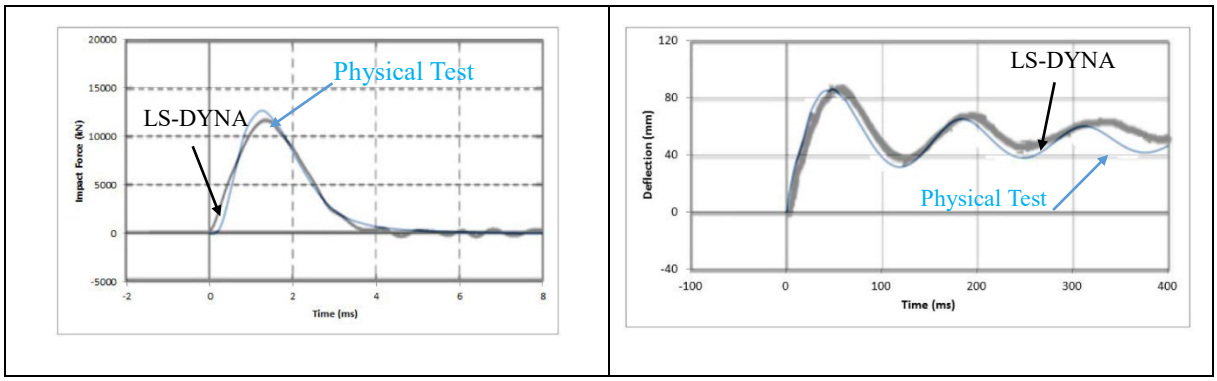

Figure E4 Comparison of Impact Force and Beam Deflection for Model Validation (Impact Test by Kishi & Bhatti (2010))

As shown in Figure E4 above, the contact force and the flexural response of the R.C. girder predicted using LS-DYNA closely match with the published results of the impact experiment. Meanwhile, similar positive results have also been found from results of impact test published by Fujikake et al (2009) in Figure E5 below.

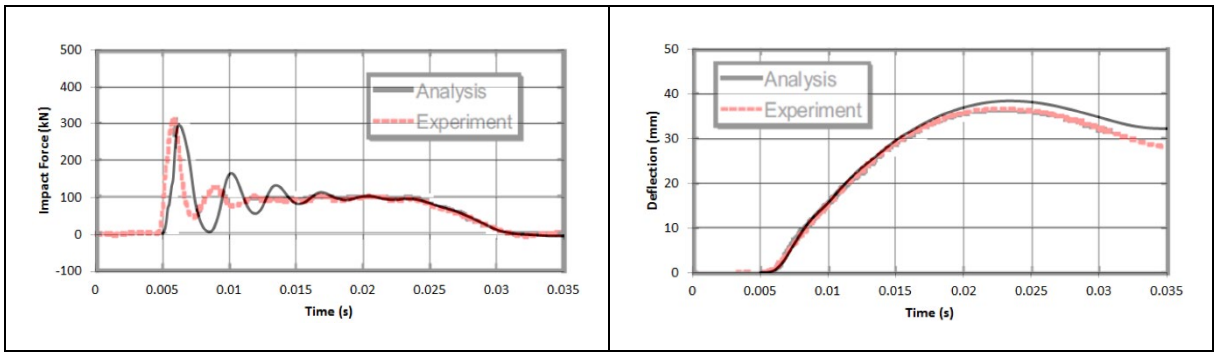

Figure E5 Comparison of Impact Force and Beam Deflection for Model Validation (Impact Test by Fujikake et al (2009))

Based on the above, the ability to simulate impact scenarios on reinforced concrete member using LS-DYNA is demonstrated in this validation exercise. Taking advantage of this, the computer program LS-DYNA is adopted in the next step of investigation, i.e. parametric study of various boulder impact scenarios on reinforced concrete rigid barriers. The details of the parametric study have been presented in Section 4.

References

Fujikake, K., Li, B. & Soeun, S. (2009). Impact response of reinforced concrete beam and its analytical evaluation. *Journal of Structural Engineering*, 2009, 135(8): pp 938-950.

Kishi, N. & Bhatti, A.Q. (2010). An equivalent fracture energy concept for nonlinear dynamic response analysis of prototype RC girders subjected to falling-weight impact loading. *International Journal of Impact Engineering*, 2010, 37(1): pp 103-113.

[Blank Page]

Section 5:
Large-scale Experimental Study of Structural Response of Rigid Barriers Subject to Hard Impacts

L.A. Wong & H.W.K. Lam

This section is largely based on GEO Technical Note No. TN 7/2018 produced in December 2018

Foreword

This Technical Note summarises findings of a series of large-scale impact tests with a view to investigate the structural response of a rigid barrier subject to impacts by a solid steel impactor. This study was carried out by Mr L.A. Wong under the supervision of Mr H.W.K. Lam in collaboration with Professor N.T.K. Lam from the University of Melbourne and his research assistant, Mr A.C.Y. Yong. The Drafting Unit of the Standards and Testing Division assisted in formatting this Note.

Draft version of the report was reviewed by Professor N.T.K. Lam. Many colleagues in the GEO provided constructive comments on the Note. All contributions are gratefully acknowledged.

J.S.H. Kwan
Chief Geotechnical Engineer/Standards and Testing
December 2018

Abstract

This study comprises a series of large-scale impact tests with a view to investigate the structural response of a rigid barrier subject to impacts by a solid steel impactor. It aims to validate the Enhanced Flexural Stiffness Method for simulating the flexural response of rigid barriers subject to boulder impact. This study also investigates the localised damage of rigid barriers and the cushioning effect of rockfill gabions through the impact tests. It provides quality experimental data to facilitate formulation of more rational design methodologies for rigid debris-resisting barriers.

Contents

			Page No.
Title Page			237
Foreword			238
Abstract			239
Contents			240
List of Tables			242
List of Figures			243
1	Background		244
2	Large-scale Impact Tests		244
	2.1	Model Barrier and Impactors	244
	2.2	Instrumentation	244
	2.3	Test Plan and Results	246
		2.3.1 Test Plan for Objective 1 - Verification of EFSM	247
		2.3.2 Results for Test Objective 1	247
		2.3.3 Test Plan for Objective 2 - Study of Structural Response of Rigid Barrier with Cushioning Materials	249
		2.3.4 Results for Objective 2	251
		2.3.5 Test Plan for Objective 3 - Study of Localised Damage	252
		2.3.6 Results for Objective 3	252
3	Summary		255
4	Concluding Remark		256
5	References		256
Section 5 Appendix A:	Estimation of Cracked Flexural Stiffness		258
Section 5 Appendix B:	Calculations of Flexural Deflection of Model Barrier		264

		Page No.
Section 5 Appendix C:	Video of Impact Test No. D1	271

List of Tables

Table No.		Page No.
2.1	Specifications of Instruments	245
2.2	Test Plan for Objective 1	247
2.3	Comparison of Observed Deflection and Predicted Deflection Using EFSM	249
2.4	Test Plan for Objective 2	250
2.5	Test Results for Objective 2	252
2.6	Test Plan for Objective 3	253
2.7	Test Results for Objective 3	254

List of Figures

Figure No.		Page No.
2.1	Photographs Showing the Model Barrier and the Impactors	245
2.2	Details of Instrumentation of the Impact Tests	246
2.3	Comparison of the Deflection Measured at the Crest of Wall Stem from Experiment and the Estimations by EFSM for Test No. A6 (Time = 0 ms Denotes the Moment When the Impact Started)	248
2.4	Overview of Rigid Barrier with Granite Gabions	250
2.5	Snapshot of Test Series C3 (Top: Side View of Impact Test; Bottom: Condition of Gabion (Rockfill) after Each of the Four Consecutive Strikes)	251
a2.6	Location of Impacts for Tests under Objective 3	253
2.7	Photographs Showing Localised Damages under Test Nos. ND1 to ND4	254
2.8	Destructive Impact Test No. D1 (Top: Snapshot of Destructive Impact Test; Bottom: Localised Structural Damage)	255

1 Background

Reinforced concrete rigid barriers are commonly adopted in Hong Kong as structural counter-measures to mitigate natural terrain landslide hazards. In recent years, GEO has initiated a series of research and development work on rigid barriers, covering debris-barrier interaction using centrifuge tests, performance in geotechnical stability as well as structural response of barrier subject to boulder impacts (Ng et al, 2016; Song et al, 2017; Lam & Kwan, 2016; Lam et al, 2018; Wong & Lam, 2018).

A recent study conducted by Wong & Lam (2018) has indicated the potential of the Enhanced Flexural Stiffness Method (EFSM) (Ali et al, 2014; UoM, 2017; Yang et al, 2012) in producing reasonable prediction of flexural response of rigid barriers subject to boulder impact. In their study, the predictions of EFSM matched closely with the results of a small-scale pendulum test and the output of a series of rigorously calibrated numerical models. This method was modified from the conventional Flexural Stiffness Method (Hungr et al, 1984; CAGHP, 2018), taking into account the inertia of rigid barrier and energy loss during the impact process.

In April 2018, GEO collaborated with the University of Melbourne (UoM) who carried out a series of impact tests, with an aim to further validating the reliability of EFSM under large-scale impact conditions (UoM, 2018). This study also investigates localised damage of rigid barriers and the cushioning effect of rockfill gabions. This Technical Note (TN) summarises the findings of this large-scale experimental study.

2 Large-scale Impact Tests

2.1 Model Barrier and Impactors

An inverted T-shaped model rigid barrier was constructed for the study. The model barrier was 3 m wide and 0.23 m thick, with a wall stem of 1.5 m high (see Figure 2.1). The barrier was made of C40 concrete with steel reinforcement. The wall was reinforced both vertically and horizontally by 20 mm diameter steel reinforcement at a 200 mm spacing. The steel reinforcement has a characteristic strength of 500 MPa. The base slab of the model barrier measured 1.23 m in length and 0.5 m in thickness, and was fixed to the ground by means of 12 nos. of post-tensioned steel anchors. The fixity of the barrier eliminated the effects of energy loss due to overturning and sliding movements of the model barrier, and that, in turn would yield the largest flexural response of the model barrier when subject to impact.

Three different steel impactors were used in this study, weighing 280 kg, 435 kg and 1,020 kg. The impactors are all torpedo shaped (Figure 2.1). For each impact test, a steel impactor was used to produce a strike to the wall stem of the model barrier using a pendulum setup.

2.2 Instrumentation

The instrumentation used in this study are summarised in Table 2.1 below. A high-speed camera and laser sensors were adopted to capture the impact velocity of the impactor and the deflection profile of the wall stem of the model barrier. A total of 18 nos. of Linear

Variable Differential Transformers (LVDTs) were installed on the surface of the wall stem for the measurement of the concrete strain at different levels. Besides, 30 nos. of strain gauges were installed on the vertical reinforcement bars at both sides of the model wall to capture the strain of the steel reinforcement. An accelerometer was secured onto the flat side of each impactor. Figure 2.2 below shows the instrumentation adopted in this study.

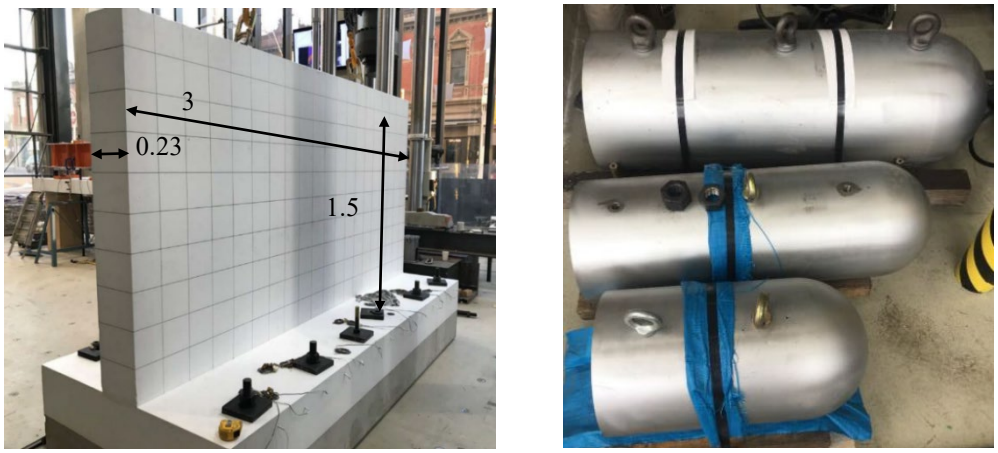

Figure 2.1 Photographs Showing the Model Barrier and the Impactors

Table 2.1 Specifications of Instruments

Instruments	Resolution	Frequency	Quantity
LVDT	0.01 mm	0.5 kHz	18
Laser sensor	0.1 mm	0.75 kHz	12
Strain gauge	1×10^{-5}	> 2 kHz	30
Accelerometer	-	10 kHz	1 (for each impactor)
High speed camera	-	3000 fps	1

The following measurements were taken during the impact tests:-

(a) time-histories of the contact force as derived from the measurements of the accelerometer attached on the impactor;

(b) time-histories of the deflection of the wall stem based on the measurements of the laser sensors;

(c) strains of the longitudinal reinforcements of the wall stem based on the readings from the strain gauges attached onto the reinforcements at the base of the barrier;

(d) strains of the concrete surface based on the measurements from the LVDTs that were stacked vertically up the height of the barrier at its centreline and along the base of the barrier;

(e) velocity of the impactor prior to the impact, and on re-bounce, as inferred from images captured by the high-speed camera;

(f) photographs of the damaged pattern of gabions, and the damaged pattern of the barrier, following each strike; and

(g) crack pattern developed on the surface of the wall stem following each strike.

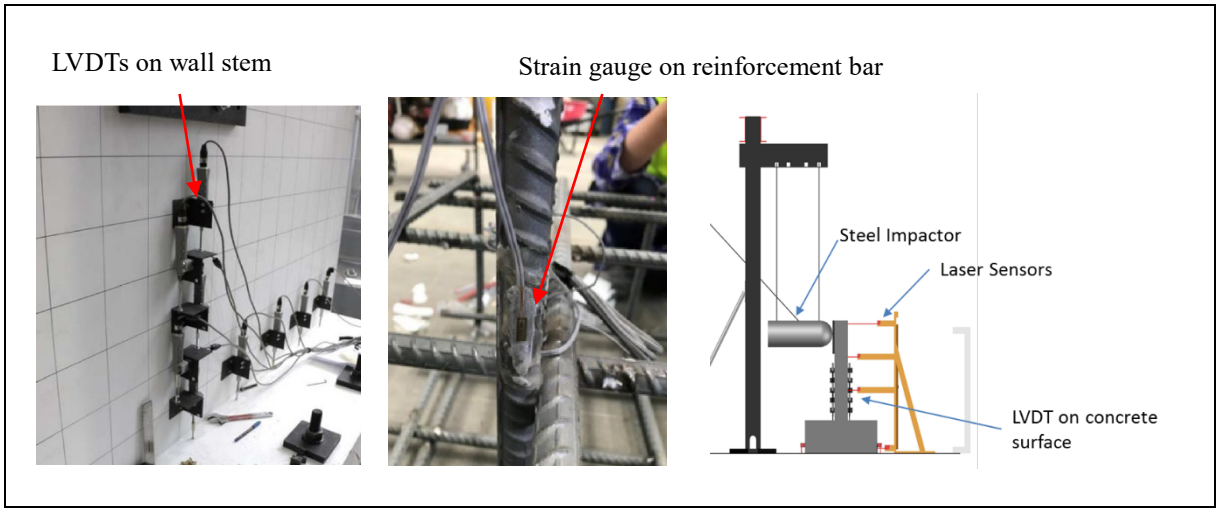

Figure 2.2 Details of Instrumentation of the Impact Tests

2.3 Test Plan and Results

This study covers the following three major objectives:-

(1) verification of EFSM;

(2) investigation of the cushioning effect offered by Rockfill gabions with respect to the flexural and localised damage of a rigid barrier; and

(3) study of the localised damage of a bare model barrier (i.e. without any cushion) when it is subject to impacts by a hard object.

The test plans and the results for each of these objectives are discussed in the following sections.

2.3.1 Test Plan for Objective 1 - Verification of EFSM

For Objective 1, eleven impact tests were conducted, which involved the use of two impactors with a mass of 280 kg and 435 kg (see Table 2.2). The release height of the impactors varied from 0.129 m to 1.4 m, which corresponds to an impact velocity of about 1.59 m/s to 5.24 m/s (i.e. kinetic energy of up to 3.85 kJ). This test plan allows a systematic verification of the EFSM under various energy levels of impacts, and mass ratios between the barrier and the impactor. In all 11 nos. of impact tests (i.e. Test Nos. A1 to A7 & Test Nos. B1 to B4), the impactor was positioned to strike the barrier at its centreline and 250 mm below the crest of the wall stem. To prevent energy loss due to localised or surface damage of the wall stem, in Test Nos. A1 to A7, a thin protective steel plate with dimensions of 500 mm × 500 mm × 32 mm was attached onto the barrier at the impact location. In Test Nos. B1 to B4, the protective steel plate was removed.

Table 2.2 Test Plan for Objective 1

Test No.	Impactor Mass (kg)	Release Height (m)	Impact Energy (kJ)	Protective Steel Plate
A1	280	0.2	0.55	Yes
A2	280	0.5	1.37	Yes
A3	280	0.9	2.47	Yes
A4	280	1.4	3.85	Yes
A5	435	0.129	0.55	Yes
A6	435	0.322	1.37	Yes
A7	435	0.579	2.47	Yes
B1	280	0.2	0.55	No
B2	280	0.5	1.37	No
B3	280	0.9	2.47	No
B4	280	1.4	3.85	No

2.3.2 Results for Test Objective 1

Figure 2.3 shows a typical deflection time-history of the crest of the model barrier due to the impact (i.e. for Test No. A6). The deflection time-history shows a simple harmonic motion, which is consistent with the assumption made in the EFSM. The deflection was highly transient. In this test, the maximum deflection occurred within 20 ms after initial contact was made.

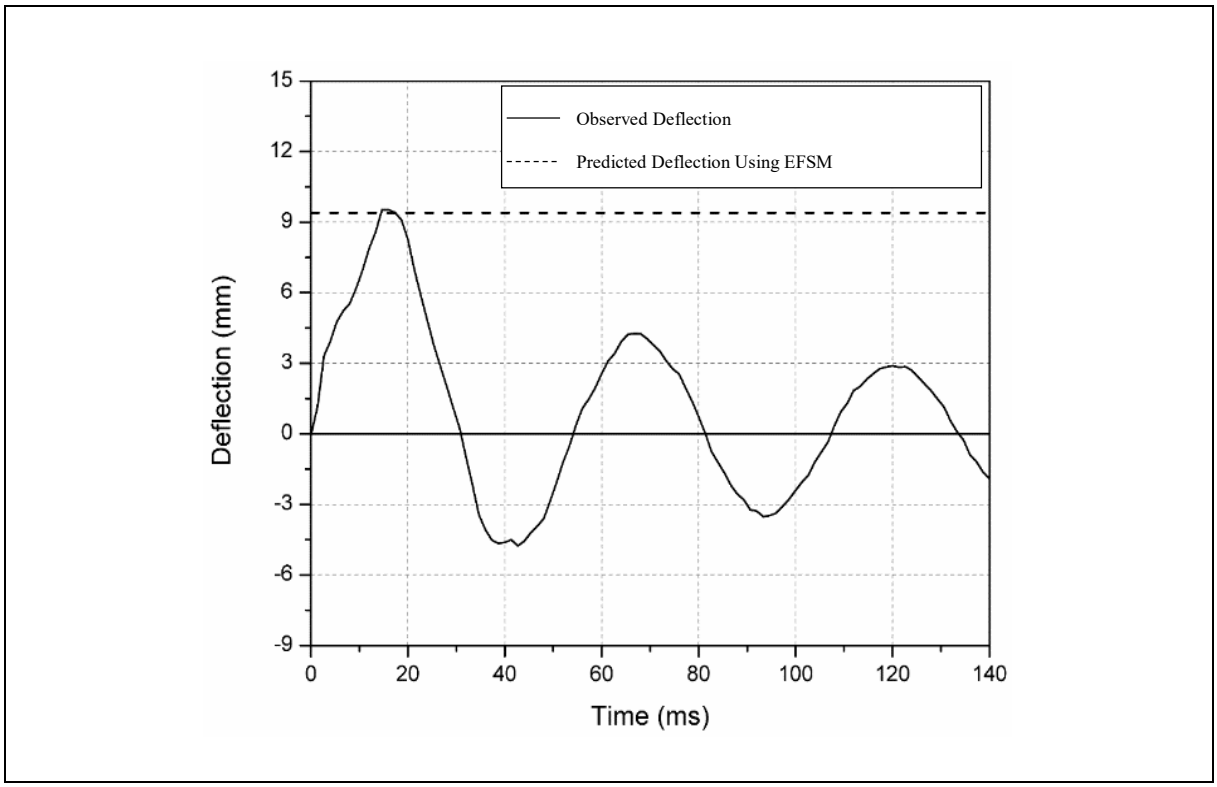

Figure 2.3 Comparison of the Deflection Measured at the Crest of Wall Stem from Experiment and the Estimations by EFSM for Test No. A6 (Time = 0 ms Denotes the Moment When the Impact Started)

Table 2.3 shows the comparison of the observed maximum deflections at the crest of the barrier in each test and those predicted based on the EFSM. The prediction based on EFSM requires the input of impactor mass, mass of model barrier, impact velocity, coefficient of restitution and cracked flexural stiffness of the barrier. All of these input parameters are measured from the experiments, except for (1) coefficient of restitution which is derived from observed velocities of the impactor before and after the impact, and based on the assumption of conservation of momentum, and (2) cracked flexural stiffness of the barrier, of which detailed calculation is given in Section 5 Appendix A. The prediction of the barrier deflection for Test No. A6 is presented in Section 5 Appendix B as an example.

As shown in Table 2.3, the predicted deflections of the barrier given by EFSM are generally in a good agreement with the experimental results, for both series, i.e. Test Nos. A1 to A7, and Test Nos. B1 to B4.

The strain levels of the steel reinforcements have been examined. For these impact tests, i.e. Test Nos. A1 to A7, and Test Nos. B1 to B4, the maximum strain levels of each vertical reinforcement at the tension side at the base of the wall stem (i.e. at the location of maximum flexural strain) are found well below the yield limit of 0.0028, which suggests that the steel bars are within its elastic range as assumed in the EFSM.

Table 2.3 Comparison of Observed Deflection and Predicted Deflection Using EFSM

Test No.	Observed Maximum Deflection at the Crest of the Barrier (mm)	Predicted Deflection at the Crest of the Barrier Using EFSM (mm)
A1	4.0	5.5
A2	5.7	8.0
A3	8.9	10.2
A4	11.9	11.9
A5	5.9	6.1
A6	9.5	9.4 (see Section 5 Appendix B for Derivation of Predicted Deflection)
A7	13.0	13.0
B1	5.2	5.2
B2	8.2	8.1
B3	11.5	11.6
B4	14.4	13.3

2.3.3 Test Plan for Objective 2 - Study of Structural Response of Rigid Barrier with Cushioning Materials

The second objective of this study is to investigate the flexural response of a rigid barrier protected with a layer of cushioning materials. In local design practice, rockfill gabions are used as a cushioning layer. The design of gabions is prescriptive and the protection offered by the gabions is not quantified. As one of the objectives of this study, the cushioning effect offered by rockfill gabions is examined.

Four series of impact tests were conducted (i.e. Test Nos. C1 to C4), two of which involved 500 mm thick gabions infilled with 70 to 100 mm diameter crushed granite cobbles. The remaining two series of tests involved 500 mm thick gabions infilled with 50 to 100 mm diameter river pebbles (see Figure 2.4). Table 2.4 shows the details of the test plan under this objective.

For this part of the study, the cushioning materials were placed in front of the model barrier. For all of these impact tests (i.e. Test Nos. C1 to C4), the impactor was positioned to strike directly onto the cushioning materials at the centerline and 250 mm below the crest of the wall stem of the cushioned barrier. The deflection of the model barrier was measured. In each series of test, three to four consecutive strikes were made on the cushioning materials at the same location and no maintenance of the gabions was allowed between the consecutive strikes. In the last test (i.e. Test No. C4), only three consecutive strikes were made because the gabions involved were severely damaged after the first three strikes.

Figure 2.4 Overview of Rigid Barrier with Granite Gabions

Table 2.4 Test Plan for Objective 2

Series No.	Impactor Mass (kg)	Release Height (m)	Impact Energy (kJ)	Protective Layer	Strike Number
C1	280	1.4	3.85	Gabions (Granite)	1
	280	1.4	3.85	Gabions (Granite)	2
	280	1.4	3.85	Gabions (Granite)	3
	280	0.5	1.37	Gabions (Granite)	4
C2	435	0.579	2.47	Gabions (Granite)	1
	435	0.579	2.47	Gabions (Granite)	2
	435	0.579	2.47	Gabions (Granite)	3
	435	0.322	1.37	Gabions (Granite)	4
C3	280	1.4	3.85	Gabions (River Pebbles)	1
	280	1.4	3.85	Gabions (River Pebbles)	2
	280	1.4	3.85	Gabions (River Pebbles)	3
	280	0.5	1.37	Gabions (River Pebbles)	4
C4	435	0.579	2.47	Gabions (River Pebbles)	1
	435	0.579	2.47	Gabions (River Pebbles)	2
	435	0.579	2.47	Gabions (River Pebbles)	3

The impactors used and the impact energy levels of the first three strikes in these four series of tests were identical to two of those tests (i.e. Test Nos. A4 and A7) conducted under Objective 1 where no gabion cushion was provided. Comparisons between the experimental results of these two sets of tests reveal the cushioning effect of the gabions.

2.3.4 Results for Objective 2

Figure 2.5 shows the conditions of the gabion cushion following each strike for Test No. C3. Table 2.5 shows the comparison of the flexural response of the model barrier with and without gabion cushion. It is found that the provision of 500 mm thick gabions can substantially reduce the flexural deflection at the crest of the model barrier by about 67% to 90%. This finding provides useful data which could facilitate a more rational design of cushioning materials.

The four impact tests under Objective 2 were conducted at the same model barrier after the impacts under Objective 1. The severity of cracking before and after the four impact tests (i.e. Test No. C1 to C4) was examined. It was observed that only one hairline crack was newly formed due to the four impact tests. Similarly, no observable localised damage was found in the large-scale impact tests reported in Lam (2016), which involved the use of a 1.12 m diameter boulder travelling at a speed up to about 8 m/s hitting a model barrier protected with various cushioning materials including 1 m thick gabions. It suggests that gabions are effective in preventing localised damage, such as surface cracking, on a reinforced concrete barrier when it is subject to impact by a hard object.

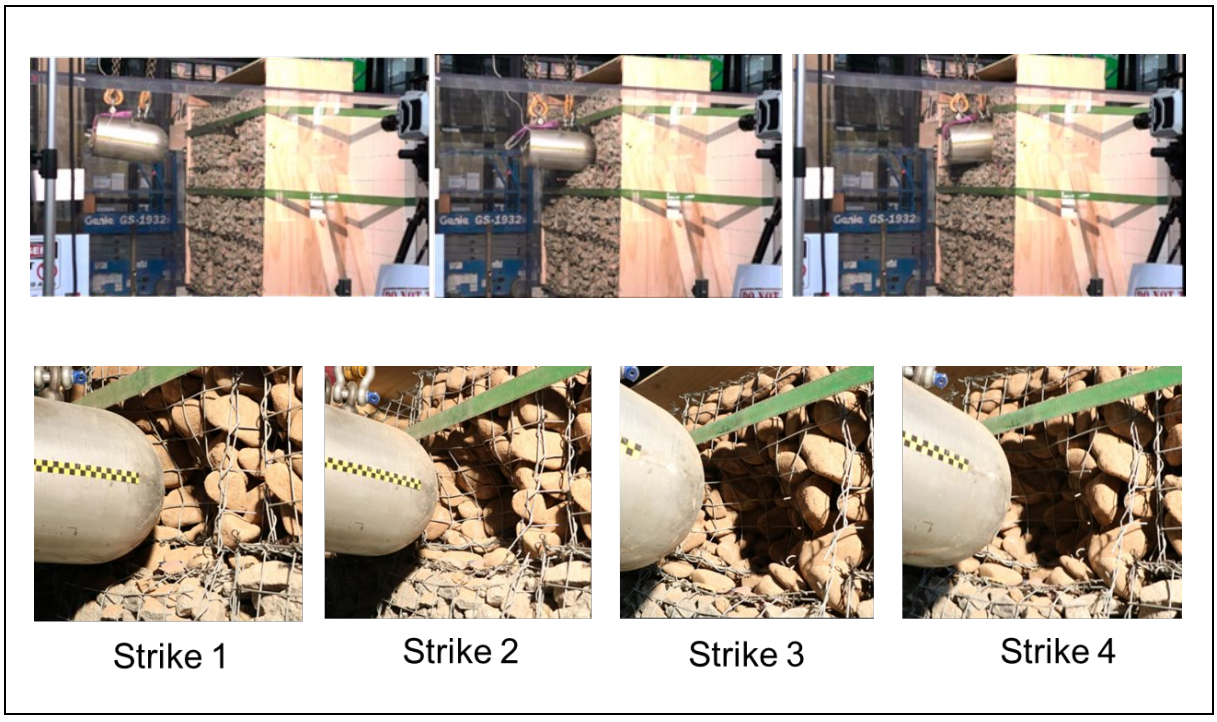

Figure 2.5 Snapshot of Test Series C3 (Top: Side View of Impact Test; Bottom: Condition of Gabion (Rockfill) after Each of the Four Consecutive Strikes)

Table 2.5 Test Results for Objective 2

Test No.	Maximum Tip Deflection ***with Cushion*** (for the First 3 Strikes) (mm)	Maximum Tip Deflection ***without Cushion*** (mm) (i.e. Test Results for Test A4 and A7)	Reduction in Tip Deflection Due to Cushioning Effect (%)
C1	1.8 - 3.9	11.9	67 - 85%
C2	1.3 - 3.2	13.0	75 - 90 %
C3	2.5 - 3.5	11.9	71 - 79 %
C4	1.3 - 2.1	13.0	84 - 90 %

Note: The maximum reductions in the crest deflection of the model barrier are recorded in the first impact (out of the three successive impacts) under these four tests.

The duration of the impact process was examined. The durations of contact observed from the impact tests with cushion materials were in the order of 70 ms to 100 ms, which were much longer than those impact tests that did not involve the use of any gabions (about 1 ms to 3 ms) as discussed in Section 2.3.1.

2.3.5 Test Plan for Objective 3 - Study of Localised Damage

Literatures (Algaard et al, 2005; Chen & May, 2009; Fujikake et al, 2009) reported that impact on bare reinforced concrete slabs by a hard object could probably induce localized damages, in the form of penetration, perforation, scabbing, etc., depending on various factors (e.g. the mass and velocity of the impactor, the thickness and the concrete strength of the slab, etc.). Table 2.6 lists the test plan for the study of localised damage of bare rigid barrier (i.e. without cushion).

The tests were divided into two stages. Stage 1 involved 4 nos. of non-destructive impacts while Stage 2 involved a destructive impact. An impactor was set to strike the model barrier without any form of surface protection. The locations of impacts for each test in this part of the study are shown in Figure 2.6. Details of the test plan are given in Table 2.6.

2.3.6 Results for Test Objective 3

Figure 2.7 shows the severity of localised damages observed under Test Nos. ND1 to ND4. Table 2.7 summarises the observed localised damage for the tests under Objective 3. For the Non-destructive Impact Test Nos. ND1 to ND4, the strain responses of steel and concrete remained elastic.

Table 2.6 Test Plan for Objective 3

Test No.	Weight of Impactor (kg)	Impact Velocity (m/s)
ND1	280	2.0
ND2		3.1
ND3		4.2
ND4		5.2
D1	1,020	6.0

Note: One impact was conducted for each test, except Test No. ND 3 where 5nos. of successive impacts were conducted.

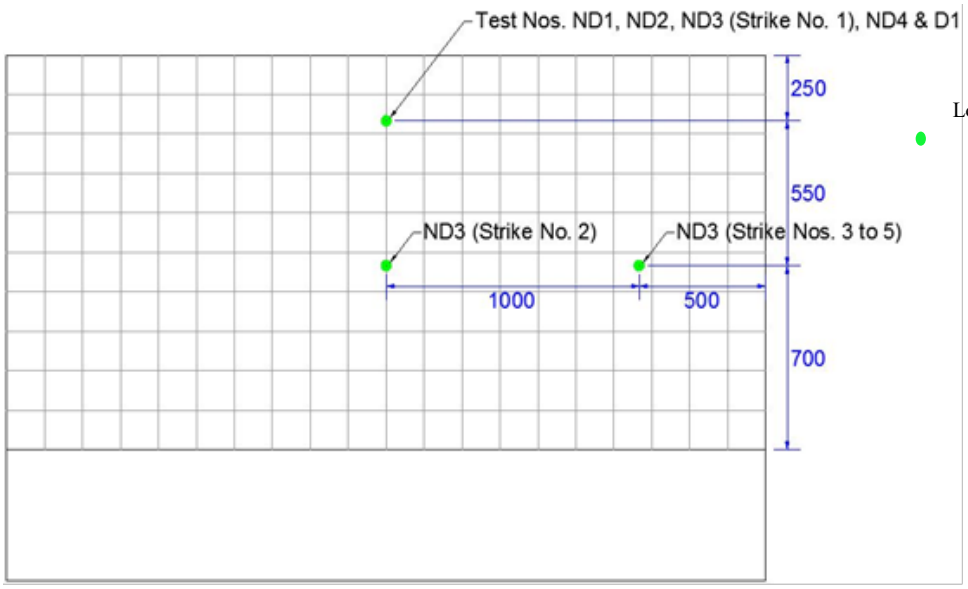

Elevation

Figure 2.6 Location of Impacts for Tests under Objective 3

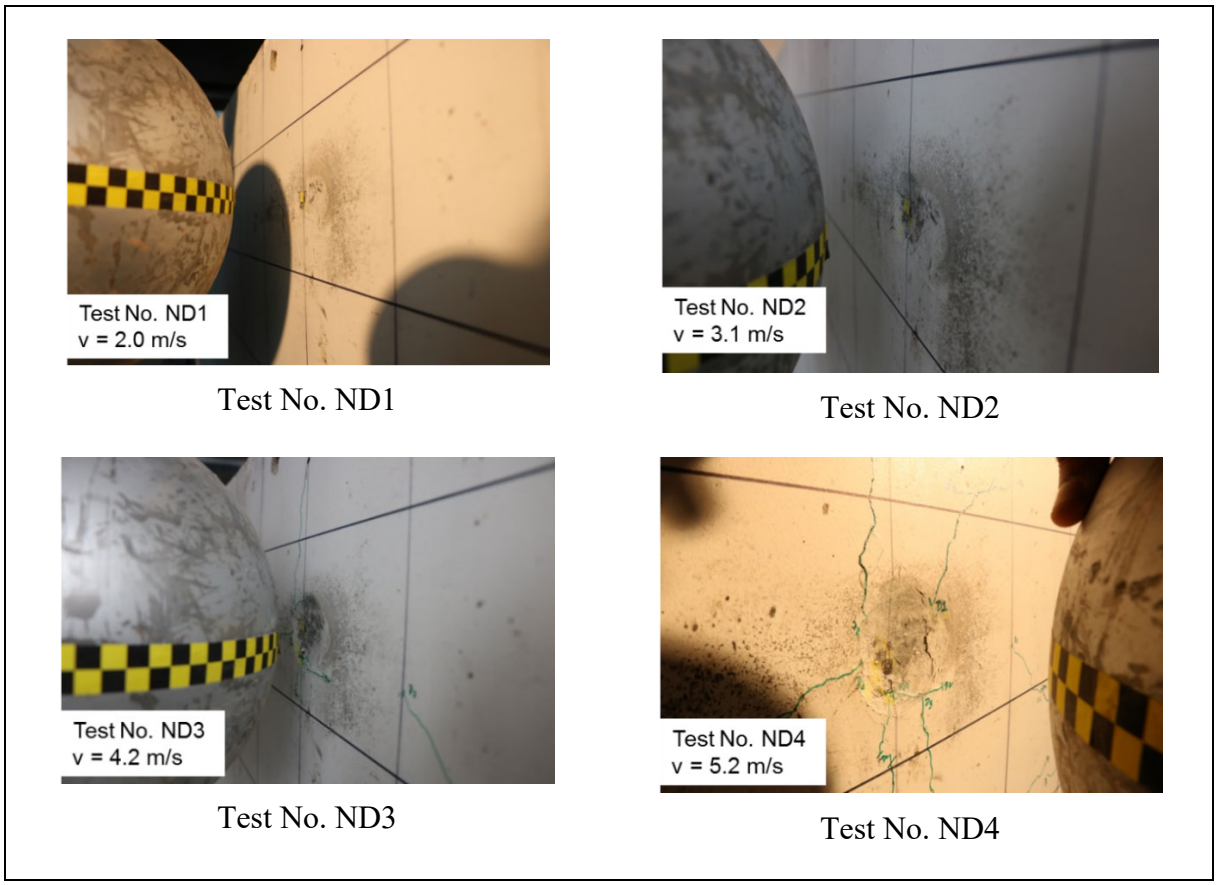

Figure 2.7 Photographs Showing Localised Damages under Test Nos. ND1 to ND4

Table 2.7 Test Results for Objective 3

Test No.	Weight of Impactor (kg)	Impact Velocity (m/s)	Observed Localised Structural Damage
ND1	280	2.0	Some hairline cracks were formed. Local indentation of about 0.35 mm was observed.
ND2		3.1	Some hairline cracks were formed. Local indentation of about 0.60 mm was observed.
ND3		4.2	More hairline cracks were formed after successive impacts. Local indentation of about 2.72 mm was observed.
ND4		5.2	Some hairline cracks were formed. Local indentation of about 3.43 mm was observed.
D1	1,020	6.0	The barrier was severely damaged (Figure 2.8). In particular, the concrete material at the back side of the wall stem was severely cracked and partially detached. This mode of structural damage is known as scabbing in the literatures (Bangash, 2001).

For Destructive Impact Test No. D1, the mode of localised structural damage of the model barrier after the impact is shown in Figure 2.8 below. The video of the test is given in Section 5 Appendix C.

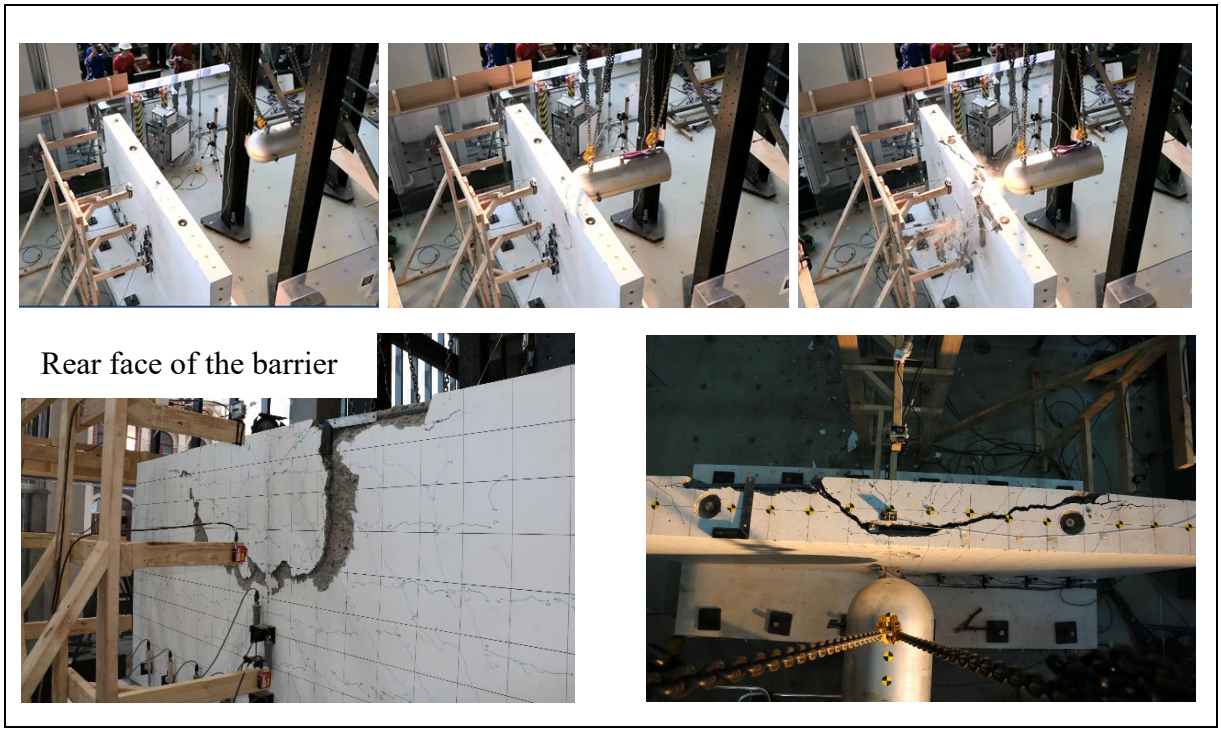

Figure 2.8 Destructive Impact Test No. D1 (Top: Snapshot of Destructive Impact Test; Bottom: Localised Structural Damage)

3 Summary

GEO has initiated a series of large-scale impact tests to investigate the structural response of a rigid barrier subject to impacts by a steel impactor. These impact tests demonstrate the reliability of the EFSM in predicting the flexural response of rigid barriers subject to hard impacts at the barrier crest.

This experimental study also provides quality data that could quantify the cushioning effect offered by rockfill gabions with respect to the flexural response of a rigid barrier when subject to impacts by a hard object. The test results show that the flexural response of the barrier was significantly reduced by 67% to 90% due to the cushioning effect of the rockfill gabions. These experimental results provide useful data which could facilitate further study of a more rational design approach for cushioned rigid barriers.

For rigid barriers without cushioning materials, localised damages in form of scabbing, indentation and cracking are probable when the barriers are subject to impacts by boulders. Having considered that impacts of debris-resisting barriers by landslide debris are rare events in Hong Kong, it is more cost effective to adopt a performance-based approach in the design of rigid debris-resisting barriers. In line with this, localised or minor damages that can be

repaired after a landslide event are generally tolerable as long as the rigid barrier would not collapse or fail to satisfy the performance criteria in retaining the design volume of landslide debris.

4 Concluding Remarks

This study validates the reliability of the EFSM in predicting the flexural response of rigid barriers subject to hard impacts at the barrier crest. It also provides quality experimental data to facilitate formulation of more rational design methodologies for rigid debris-resisting barriers. In particular, analytical solutions for the prediction of flexural response of rigid barriers are being investigated with consideration given to protection effects of rockfill gabions.

5 References

Algaard, W., Lyle, J. & Izatt, C. (2005). Perforation of composite floors. *5th European LS-DYNA Users Conference*. Ove Arup & Partners Ltd.

Ali, M., Sun, J., Lam, N., Zhang, L. & Gad, E. (2014). Simple hand calculation method for estimating deflection generated by the low velocity impact of a solid object. *Australian Journal of Structural Engineering*, 2014, 15(3): pp 243-259.

Bangash, M.Y.H. (2001). *Manual of Numerical Methods in Concrete: Modelling and Applications Validated by Experimental and Site-monitoring Data*, 918 p.

CAGHP (2018). *Specification of Design for Debris Flow Prevention* (T/CAGHP *021-2018)*. China Association of Geological Hazard Prevention, 55p (in Chinese).

Chen, Y. & May, I.M. (2009). Reinforced concrete members under drop-weight impacts. *Proceedings of the ICE - Structures and Buildings, 2009,* 162(1): pp 45-56.

Fujikake, K., Li, B. & Soeun, S. (2009). Impact response of reinforced concrete beam and its analytical evaluation. *Journal of Structural Engineering*, 2009, 135(8): pp 938-950.

Hungr, O., Morgan, G.C. & Kellerhals, R. (1984). Quantitative analysis of debris torrent hazards for design of remedial measures. *Canadian Geotechnical Journal*, vol. 21, pp 663-677.

Lam, C. (2016). *A Pilot Study of the Use of Cushioning Materials for Reducing Dynamic Impact Loads on Rigid Debris-resisting Barriers (Technical Note No. TN 5/2016).* Geotechnical Engineering Office, Hong Kong, 70 p.

Lam, C. & Kwan, J.S.H. (2016). *Displacement-based Assessment of Boulder Impacts on Rigid Debris-resisting Barriers - A Pilot Study (TN 9/2016).* Geotechnical Engineering Office, Hong Kong, 66 p.

Lam, N.T.K., Yong, A.C.Y., Lam, C., Kwan, J.S.H., Perera, J.S., Disfani, M.M. & Gad, E. (2018). Displacement-based approach for the assessment of overturning stability of rectangular rigid barriers subject to point impact. *Journal of Engineering Mechanics*. https://doi.org/10.1061/(ASCE)EM.1943-7889.0001383,04017161

Ng, C.W.W., Song, D., Choi, C.E., Liu, L.H.D., Kwan, J.S.H., Koo, R.C.H. & Pun, W.K. (2016). Impact mechanisms of granular and viscous flows on rigid and flexible barriers. *Canadian Geotechnical Journal*, 54(2):188-206.

Song, D., Ng, C.W.W., Choi, C.E., Zhou, G.G.D., Kwan, J.S.H. & Koo, R.C.H. (2017). Influence of debris flow solid fraction on rigid barrier impact. *Canadian Geotechnical Journal*, 54(10):1421-1434.

UoM (2017). *Computer Services of Numerical Investigation of the Structural Performance of Rigid Debris-resisting Barriers Subjected to Boulder Impact*, Final Report No. 2 prepared for the Geotechnical Engineering Office, Civil Engineering and Development Department, Hong Kong, 50 p.

UoM (2018). *Large Scale Impact Test and Computer Services for Investigation of the Structural Response of Rigid Barrier subjected to Boulder Impact, Final Report No. 1* prepared for the Geotechnical Engineering Office, Civil Engineering and Development Department, Hong Kong, 51 p.

Wong, L.A. & Lam, H.W.K. (2018). *Study of Flexural Response of Rigid Barriers Subject to Boulder Impact (Technical Note No. TN 3/2018).* Geotechnical Engineering Office, Hong Kong, 40 p.

Yang, Y., Lam, N.T.K. & Zhang, L. (2012). Evaluation of simplified methods of estimating beam responses to impact. *International Journal of Structural Stability and Dynamics*, 2012, 12(3): pp 1250016-1-1250016-24.

Section 5
Appendix A

Estimation of Cracked Flexural Stiffness

Contents

	Page No.
Contents	259
List of Figures	260
References	262

List of Figures

Figure No.		Page No.
A1	Crack Patterns Observed in Test Nos. A1 to A7: (a) Front View (b) Rear View	261
A2	Simplification of Moment-Curvature Relationship with Bi-linear Line of Best Fit	262

The governing equation to predict the cracked flexural stiffness of a reinforced concrete barrier is shown in Equation A.1. Cracked flexural stiffness is adopted for a more accurate prediction of the actual flexural response of the rigid barrier (UoM, 2018), in view that cracking of the barrier was developed after the initial impacts for Test Objective 1 (see Figure A1).

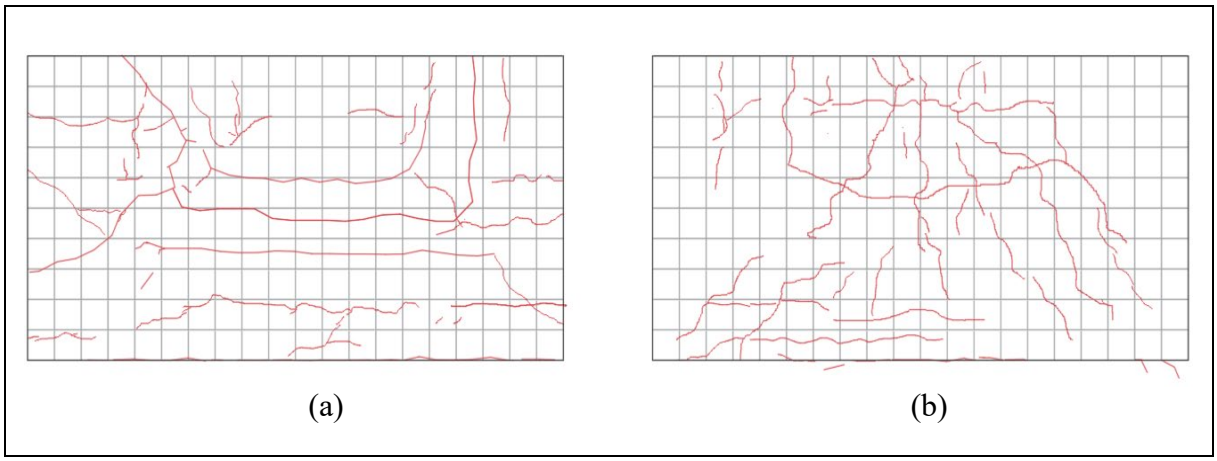

Figure A1 Crack Patterns Observed in Test Nos. A1 to A7: (a) Front View (b) Rear View

$$k_{cr} = \frac{3EI_{cr}}{h^3} \quad \text{..... (A.1)}$$

where k_{cr} = cracked flexural stiffness of the barrier (in N/m)
EI_{cr} = cracked flexural rigidity of the barrier (in N m^2)
h = the height of the barrier (in m).

Given that the height of the barrier (h) is readily known, the only remaining input parameter to Equation A.1 is the flexural rigidity of the barrier (EI_{cr}). Note that subscript *cr* denotes cracked concrete. Moment-curvature analysis which is executable using program *Response 2000* (Bentz, 2000) was used for calculating the value of EI_{cr}. Results of this program have been checked and found consistent with those assessed by other methods (e.g. fibre-element analyses by Lam et al (2011), and the empirical expression derived by Priestley et al (2007)). The moment-curvature relationships derived from program *Response 2000* are shown in Figure A2, where the initial portion (i.e. moment up to about 100 kNm) generally represents the uncracked condition, followed by cracked conditions (i.e. moment between 100 kNm to 370 kNm). A simplified bi-linear model, with an initial portion of the curve representing the cracked conditions, is also shown in Figure A2. The slope of the initial portion of the bi-linear curve is taken as EI_{cr}.

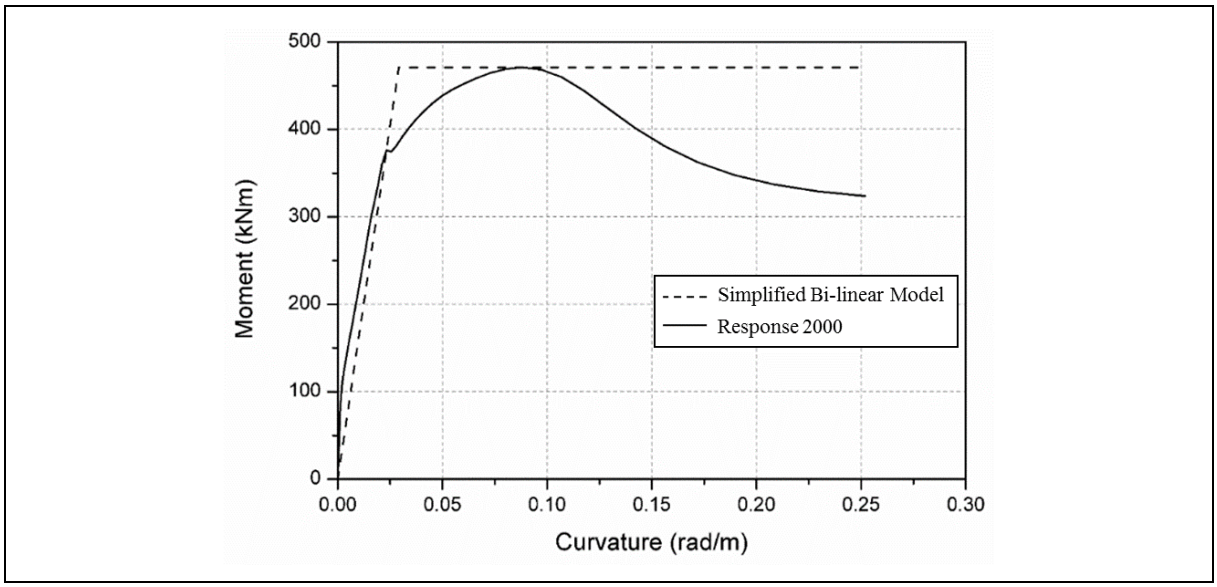

Figure A2 Simplification of Moment-Curvature Relationship with Bi-linear Line of Best Fit

From Figure A2, cracked flexural rigidity equals:

$$EI_{cr}=16{,}176 \text{ kNm}^2$$

The model barrier is 1.5 m high (i.e. h =1.5 m). The value of k_{cr} can then be calculated using Equation A.1:

$$k_{cr}=\frac{3EI_{cr}}{h^3}=\frac{3(16176)}{1.5^3}=14{,}379 \text{ kN/m}$$

The above cracked flexural stiffness will be adopted in the prediction of flexural deflection of the model barrier based on EFSM for the tests under Section 2.3.1 (i.e. Test Nos. A1 to A7 and B1 to B4).

References

Bentz, E.C. (2000). *Sectional Analysis of Reinforced Concrete Members*. 2000: University of Toronto, Toronto.

Lam, N., Wilson, J. & Lumantarna, E. (2011). *Force-deformation Behaviour Modelling of Cracked Reinforced Concrete by EXCEL Spreadsheets.* Computers and Concrete, 8(1): p. 43-57.

Priestley, M.J.N., Calvi, G.M. & Kowalsky, M.J. (2007). *Displacement-Based Seismic Design of Structures*. Pavia, Italy: IUSS Press.

UoM (2018). *Large Scale Impact Test and Computer Services for Investigation of the Structural Response of Rigid Barrier subjected to Boulder Impact, Draft Report No. 2* prepared for the Geotechnical Engineering Office, Civil Engineering and Development Department, Hong Kong, 121 p.

Section 5
Appendix B

Calculations of Flexural Deflection of Model Barrier

Contents

	Page No.
Contents	265
List of Table	266
List of Figure	267
Reference	270

List of Table

Table No.		Page No.
B1	Information of Large-scale Impact Test No. A6	268

List of Figure

Figure No.		Page No.
B1	Snapshots of Impact Test Immediately (a) before the Impact; and (b) after the Impact	269

Test No. A6 is taken as an example for demonstrating the calculation procedures for the interpretation of test results under Objective 1.

The flexural response of the model barrier is predicted based on EFSM using the following expressions:-

$$\Delta = \beta v_0 \sqrt{\frac{m}{k_{cr}}} \quad \text{(B1)}$$

$$F = k_{cr}\Delta \quad \text{(B2)}$$

where Δ = the flexural deflection of the model barrier (in m)
F = boulder impact force given by EFSM (in N)
β = $\sqrt{\lambda\left(\frac{1+\text{COR}}{1+\lambda}\right)^2}$
COR = Coefficient of Restitution between the impactor and the model barrier
λ = the mass ratio between the participating mass of the model barrier and the mass of the impactor
v_0 = the impact velocity of the impactor (in m/s)
m = the mass of the impactor (in kg)
k_{cr} = the cracked flexural stiffness of the model barrier (in N/m, see Section 5 Appendix A for details of estimation).

Some of the parameters above are readily known and are listed in Table B1 below:

Table B1 Information of Large-scale Impact Test No. A6

Parameters	Values
Mass of the impactor, m	435 kg
Impact velocity of the impactor, v_0	2.48 m/s
Cracked Flexural Stiffness of Model Barrier, k_{cr}	14,379 kN/m (See Section 5 Appendix A)
Mass of Model Barrier	2,484 kg
Mass of Protective Steel Plate	62.8 kg

In order to determine the β factor, the mass ratio between the participating mass of the model barrier and the mass of the impactor (λ) and Coefficient of Restitution between the impactor and the model barrier (COR) have to be estimated.

For an impact at the crest of the barrier, participating mass (λm) refers to the mass of the top quarter of the height of the model barrier. The mass of the protective steel plate is part of this participating mass since it is located at the top quarter portion as well:-

$$\lambda m = 0.25 \times 2484 + 62.8 = 683.8 \text{ kg}$$

Therefore, the mass ratio (λ) is given by:-

$$\lambda = \frac{\lambda m}{m} = \frac{683.8}{435} = 1.57$$

Coefficient of Restitution between the impactor and the model barrier (COR) is given by:

$$\text{COR} = \frac{v_1 + v_2}{v_0}$$

where v_1 = the velocity of the impactor after impact (in m/s)
v_2 = the velocity of the model barrier after impact (in m/s).

By analysing the velocity data obtained in the impact test:

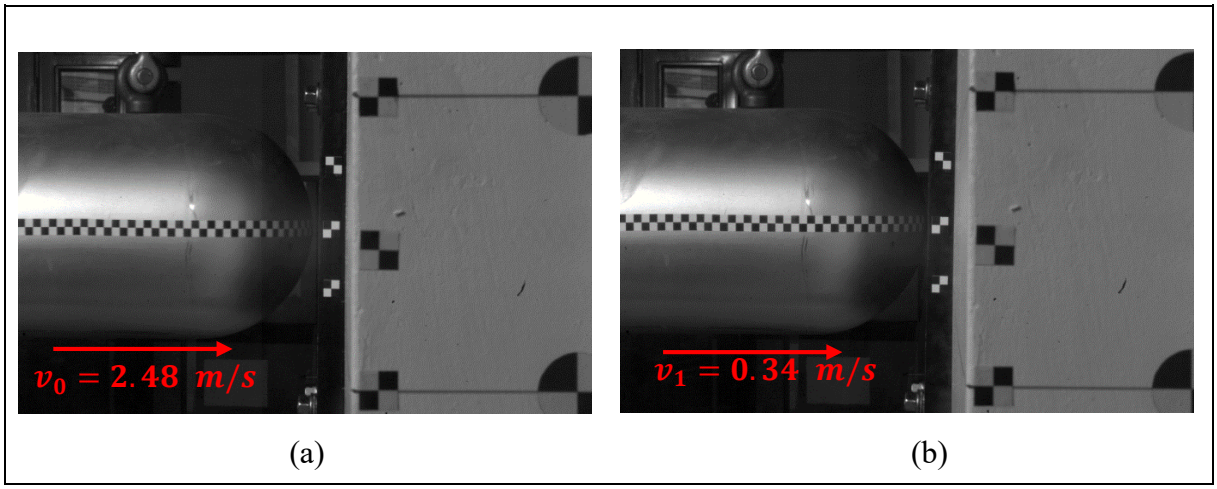

Figure B1 Snapshots of Impact Test Immediately (a) before the Impact; and (b) after the Impact

Direct measurement of v_2 is not practical because v_2 refers to the aggregate velocity of the lumped participating mass of the model barrier. The value of v_2 can be calculated using the following equation, which is based on conservation of momentum:

$$v_2 = \frac{v_0 + v_1}{\lambda} = \frac{2.48\text{-}0.34}{1.57} = 1.36 \text{ m/s}$$

$$\text{COR} = \frac{v_1 + v_2}{v_0} = \frac{-0.34 + 1.36}{2.48} = 0.41$$

(Note: v_1 is taken as a negative value as the impactor travels in the same direction as the wall immediately following the impact.)

Using COR and λ, β factor can be readily determined:-

$$\beta = \sqrt{\lambda\left(\frac{1+\mathrm{COR}}{1+\lambda}\right)^2} = \sqrt{1.57\left(\frac{1+0.41}{1+1.57}\right)^2} = 0.687$$

The predicted flexural deflection at the Crest of Model Barrier is given by:-

$$F = \beta v_0\sqrt{mk} = 0.687\times 2.48\times\sqrt{435\times 14379} = 134.8 \text{ kN}$$

$$\Delta = \frac{F}{k} = \frac{134.8}{14379} = 9.4 \text{ mm}$$

Reference

UoM (2018). *Large Scale Impact Test and Computer Services for Investigation of the Structural Response of Rigid Barrier subjected to Boulder Impact, Draft Report No. 2* prepared for the Geotechnical Engineering Office, Civil Engineering and Development Department, Hong Kong, 121 p.

Section 5
Appendix C

Video of Impact Test No. D1

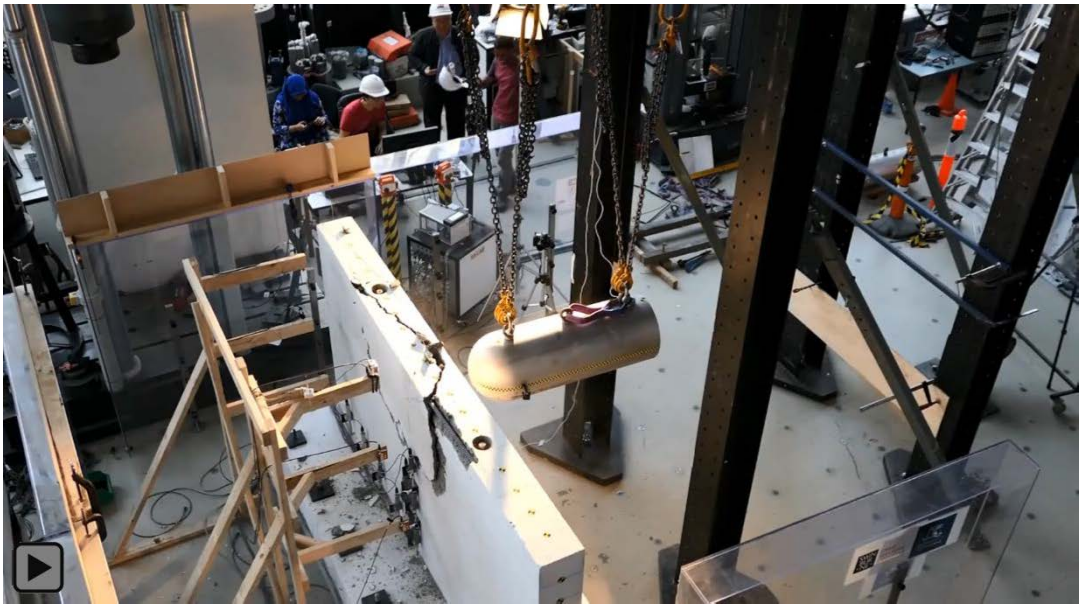

Video of Destructive Impact Test No. D1

Section 6: Supplementary Experimental Study of Structural Response of Rigid Barriers Subject to Hard Impacts

L.A. Wong & H.W.K. Lam

This section is largely based on GEO Technical Note No. TN 3/2019 produced in December 2019

Foreword

This Technical Note summarises findings of a series of large-scale impact tests and numerical analyses with a view to investigating the flexural response of rigid barriers subject to hard impacts. The experimental study involved the use of natural boulders of different shapes as impactors. Along with the numerical analyses, it aims to provide a comprehensive validation of the Enhanced Flexural Stiffness Method and examine the effect of different critical parameters, including Coefficient of Restitution and location of impact, on flexural response of rigid barriers. This study was carried out by Mr L.A. Wong under the supervision of Mr H.W.K. Lam in collaboration with Professor N.T.K. Lam from the University of Melbourne and his research team. The Drafting Unit of the Standards and Testing Division assisted in formatting this Note.

Many colleagues in the GEO provided constructive comments on the Note. All contributions are gratefully acknowledged.

T.K.C. Wong
Chief Geotechnical Engineer/Standards and Testing
December 2019

Abstract

This study comprises a series of large-scale impact tests using natural boulders of different shapes as an impactor. It aims to further validate the Enhanced Flexural Stiffness Method and to examine the effect of different parameters, including Coefficient of Restitution and location of impact, on flexural response of rigid barriers. The findings of this study supplement the previous studies documented in GEO Technical Note Nos. TN 3/2018 – Flexural Response of Rigid Barriers subject to Boulder Impact and TN 7/2018 – Large-scale Experimental Study of Structural Response of Rigid Barriers subject to Hard Impacts.

Contents

			Page No.
Title Page			273
Foreword			274
Abstract			275
Contents			276
List of Tables			277
List of Figures			278
1	Background		279
2	Large-scale Impact Tests		279
	2.1	Model Barrier and Impactors	279
	2.2	Instrumentations	280
	2.3	Test Plan and Results	282
		2.3.1 Test Objectives	282
		2.3.2 Test Programme	282
		2.3.3 Test Results for Objective 1 - Study of Coefficient of Restitution	283
		2.3.4 Test Results for Objective 2 - Verification of Enhanced Flexural Stiffness Method	285
		2.3.5 Test Results for Objective 3 - Effect of Locations of Impacts	286
3	Numerical Analyses for Further Study of Locations of Impacts		287
4	Considerations in Structural Design		289
5	Conclusion		290
6	References		290

List of Tables

Table No.		Page No.
2.1	Specifications of Instruments	281
2.2	Test Programme	283
2.3	Findings of Study of Coefficient of Restitution	284
2.4	Comparison of Observed Deflection and Predicted Deflection Using EFSM	286
2.5	Experimental Study of Effect of Locations of Impacts	287

List of Figures

Figure No.		Page No.
2.1	Photographs Showing the Model Barrier and the Impactors	280
2.2	Layout of Strain Gauges and Laser Sensors	281
3.1	Validated Numerical Analyses Series 1 & 2 for the Study on the Effect of Locations of Impacts	288
3.2	Results of Validated Numerical Analyses Series 1 (Left) & Series 2 (Right)	288

1 Background

GEO in collaboration with the University of Melbourne (UoM) has developed an analytical approach, namely Enhanced Flexural Stiffness Method (EFSM), to predict flexural response of rigid barriers subject to hard impacts. This method was modified from the conventional Flexural Stiffness Method (Hungr et al, 1984; CAGHP, 2018), taking into account cracked flexural stiffness and inertia of rigid barriers, as well as energy loss during the impact process. The derivation of the EFSM is documented in Wong & Lam (2018a).

To validate the EFSM, in 2018, GEO had conducted eleven large-scale impact tests which involved a 1.5 m high cantilever reinforced concrete wall under a series of impacts by solid steel impactors (Wong & Lam, 2018b). The impact velocity ranged from 1.59 m/s to 5.24 m/s (i.e. kinetic energy of up to 3.85 kJ). These tests allowed a systematic verification of the EFSM under various energy levels and a range of mass ratios between barrier and impactor relevant to design practice. The experimental results indicated that the predicted flexural response based on the EFSM reasonably matched with that observed in the tests. Details of the tests and the key technical findings are documented in Wong & Lam (2018b). This series of tests were conducted using impactors which were made of solid steel.

To simulate more realistic boulder impacts, in early 2019, GEO has arranged another series of impact tests, where natural boulders of different shapes were used as the impactors. These tests aim to further validate the EFSM and shed light on the probable range of Coefficient of Restitution of boulder impacts, which is a critical input parameter for the EFSM. This study also examines the effect of different impact locations on flexural response of rigid barriers, with the aid of physical tests and numerical analyses. This Technical Note summarises the findings of this series of experimental tests and numerical analyses.

2 Large-scale Impact Tests

2.1 Model Barrier and Impactors

An inverted T-shaped model rigid barrier was constructed for the experimental study. The model barrier was 1.5 m high, 3 m wide and 0.23 m thick (see Figure 2.1). The barrier was made of Grade 40 concrete with 20 mm diameter. steel reinforcements spaced at 200 mm vertically and horizontally. The steel reinforcement has a characteristic strength of 500 MPa. The base slab of the model barrier measured 1.23 m in length and 0.5 m in thickness, and was fixed to the ground slab by means of 12 nos. of post-tensioned steel anchors. The fixity of the barrier aims to eliminate the energy loss due to global overturning and sliding movements of the model barrier, in order to obtain the critical flexural response of the model barrier.

In this series of experimental study, four different natural boulders (either granitic or volcanic) of different shapes (i.e. Impactor G-B, VB, G-1 and G-2) were used as impactors, with a weight ranging from 155 kg to 315 kg. Impactors VB, G-1 and G-2 are natural materials that are flat to elongated and subangular to angular, whereas Impactor G-B is equidimensional and rounded (see Figure 2.1). In each impact test, an impactor was used to produce a strike to the wall stem of the model barrier using a pendulum setup.

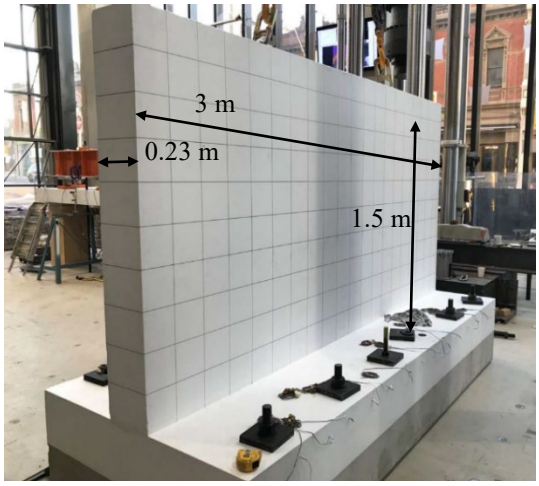

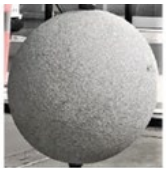

Impactor G-B

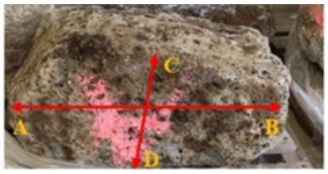

Impactor VB

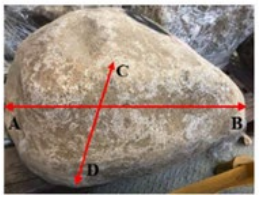

Impactor G-1

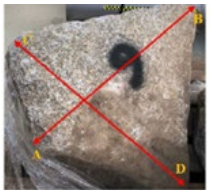

Impactor G-2

Impactor	Rock Type	Mass (kg)	Young's Modulus (GPa)	Uniaxial Compressive Strength (MPa)	Longest Dimensions (mm)
G-B	Granite	315	49.1	113	612 (Diameter)
VB	Volcanic	155	5.5	26	670 (Side AB)
G-1	Granite	220	19.1	59	800 (Side AB)
G-2	Granite	200	94.4	101	650 (Side CD)

Note: The Young's modulus and uniaxial compressive strength were obtained from laboratory tests on the rock core retrieved from each boulder after the impact tests.

Figure 2.1 Photographs Showing the Model Barrier and the Impactors

2.2 Instrumentations

The instrumentations used in this study are summarised in Table 2.1 below. A high-speed camera and laser sensors were adopted to capture the impact velocity of the impactor and the deflection profile of the wall stem of the model barrier. A total of 24 nos. of strain gauges were installed on the concrete surface (in both impact face and rear face) of the wall stem for the measurement of the concrete strains at different levels. Besides, 30 nos. of strain gauges were installed on the vertical reinforcement bars at both sides of the model wall to capture the strains of the steel reinforcements. Figure 2.2 below shows the instrumentations adopted in this study.

Table 2.1 Specifications of Instruments

Instruments	Resolution	Frequency	Quantity
Laser sensor	0.1 mm	0.75 kHz	11
Strain gauge	1 x 10^{-5}	2 kHz	24 (on concrete surface); & 30 (on steel reinforcements)
High speed camera	-	3000 fps	1

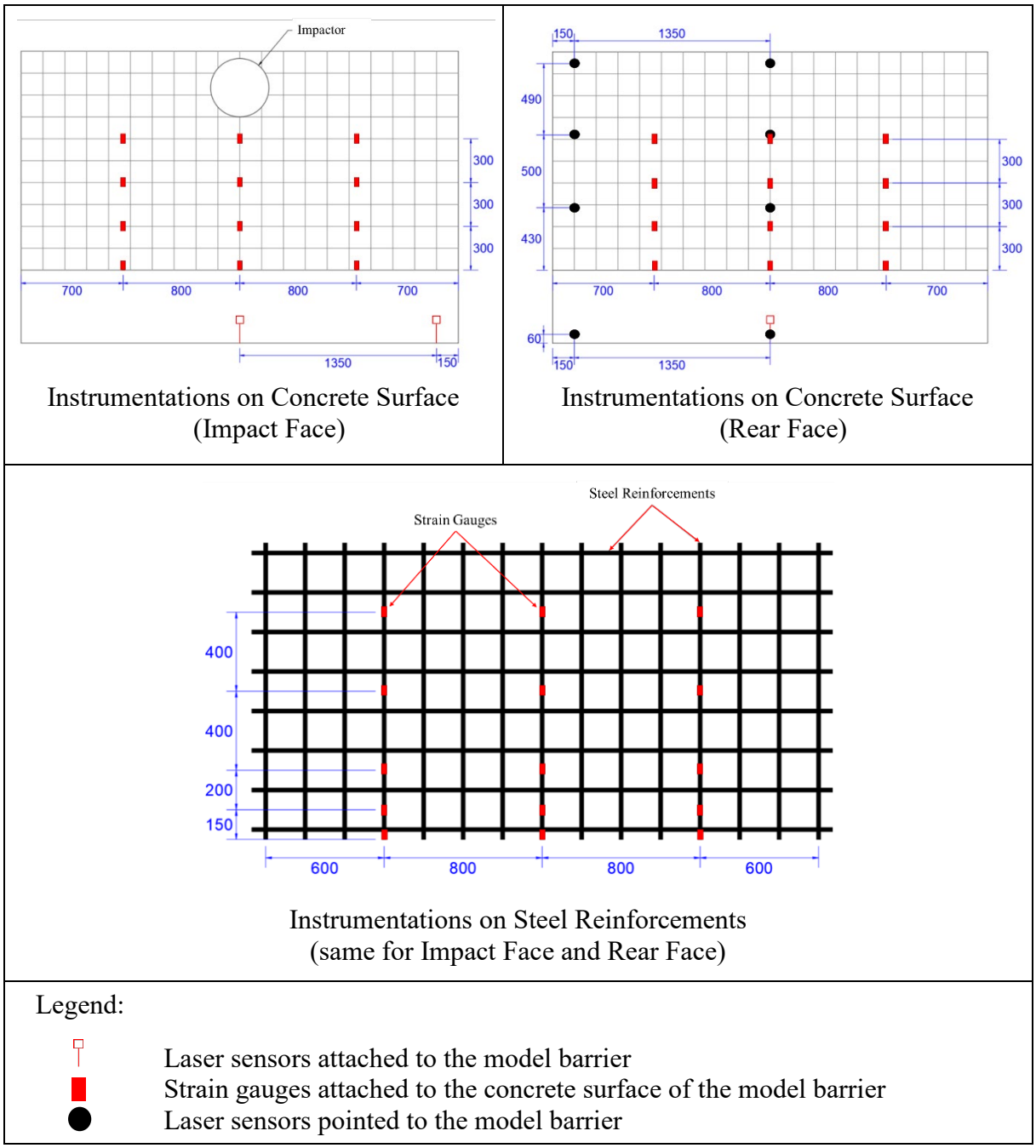

Figure 2.2 Layout of Strain Gauges and Laser Sensors

The following measurements were taken during the impact tests:-

(a) time-histories of the deflection of the wall stem based on the measurements of the laser sensors;

(b) strains of the vertical reinforcements of the wall stem based on the readings from the strain gauges attached onto the reinforcements at the base of the barrier (see Figure 2.2);

(c) strains of the concrete surface based on the measurements from the strain gauges that were stacked vertically up the height of the barrier at its centreline and along the base of the barrier (see Figure 2.2); and

(d) velocity of the impactor prior to the impact, and on re-bounce, as inferred from images captured by the high-speed camera.

2.3 Test Plan and Results

2.3.1 Test Objectives

This study covers the following major objectives:-

(1) study of Coefficient of Restitution;

(2) verification of EFSM for impacts involving natural rocks ; and

(3) study of the effect of impact locations on flexural response of rigid barriers.

The test programme and the results pertaining to each of these objectives are discussed in the following sections.

2.3.2 Test Programme

17 nos. of impact tests were conducted in total, which involved the use of four different rock specimens as the impactors (see Table 2.2). The release height of the impactors varied from 0.2 m to 1.85 m, which corresponds to an impact velocity of about 1.73 m/s to 6.00 m/s (i.e. kinetic energy of up to 4 kJ). This test plan allows a systematic study of Coefficient of Restitution (COR) under various energy levels of impacts, mass ratios between the barrier and the impactor, rock type and positions of impact. COR is defined as the ratio of relative speeds after and before an impact (Lam & Kwan, 2016). In 15 out of 17 nos. of impact tests, the impactor was positioned to strike the barrier at its centreline and 250 mm below the crest of the wall stem, except that for Test Nos. C3M and C4M in which the point of impact was at the mid-height, i.e. 750 mm below the crest, of the wall stem.

Table 2.2 Test Programme

Test No.	Impactor	Rock Type of Impactor	Impactor Mass (kg)	Release Height (m)	Impact Energy (kJ)
A1	G-B	Granite	315	0.2	0.62
A2				0.5	1.55
A3				0.7	2.16
A4				0.9	2.78
B1	V-B	Volcanic	155	0.2	0.30
B2				0.4	0.61
B3				1.4	2.13
C1	G-1	Granite	220	0.29	0.62
C2				1.00	2.16
C3				1.29	2.78
C4				1.85	4.00
C3M				1.29	2.78
C4M				1.85	4.00
D1	G-2	Granite	200	0.31	0.60
D2				0.77	1.51
D3				1.08	2.11
D4				1.79	3.50

2.3.3 Test Results for Objective 1 - Study of Coefficient of Restitution

In the last series of impact tests conducted in 2018, solid steel impactors were adopted. In this series of impact tests, as mentioned before, natural boulders of different shapes were used instead, which provided useful data on the probable range of COR for impacts involving natural boulders onto reinforced concrete structures. The COR for all 17 nos. of tests are summarised in Table 2.3. In general, a range of values of COR was observed, probably due to the fact that natural angular boulders were adopted in these tests where different degrees of energy dissipation could be resulted from local crushing at contact point or localised fracturing of boulder during the impact process. On average, a COR of about 0.2 was observed, which is comparable to that reported in literature (i.e. typically around 0.2 to 0.3) where vertical drop tests using natural boulders or rocks were carried out (Chau et al, 1998; Masuya et al, 2001).

Table 2.3 Findings of Study of Coefficient of Restitution

Test No.	Impactor Mass (kg)	Release Height of Boulder (m)	Boulder Velocity before Impact [1] (m/s)	Boulder Velocity after Impact [1][2] (m/s)	Barrier Velocity after Impact [3] (m/s)	COR
A1	315	0.2	2.02	0.2	0.92	0.36
A2		0.5	3.1	0.41	1.36	0.31
A3		0.7	3.54	0.53	1.52	0.28
A4		0.9	4.31	0.82	1.77	0.22
B1	155	0.2	1.73	0	0.43	0.25
B2		0.4	2.73	0.23	0.62	0.14
B3		1.4	5.29	0.75	1.13	0.07
C1	220	0.3	2.12	0	0.75	0.35
C2		1.0	4.28	0.57	1.31	0.17
C3		1.3	4.98	1	1.41	0.08
C4		1.9	6.00	1.39	1.63	0.04
C3M		1.3	4.93	1.02	1.38	0.07
C4M		1.9	5.99	1.36	1.64	0.05
D1	200	0.3	2.33	0.4	0.62	0.09
D2		0.8	3.66	0.75	0.94	0.05
D3		1.1	4.42	1	1.10	0.02
D4		1.8	5.88	1.39	1.44	0.01

Notes:
(1) The boulder impact velocity and boulder rebound velocity were interpreted from footages taken by high speed camera.
(2) Except for Test B1 and C1, the direction of boulder velocity after impact was all towards the barrier wall.
(3) The barrier velocity was estimated based on conservation of momentum before and after the impact, following the approach given in Wong & Lam (2018b).

It is worth-noting that, from the above test results (e.g. comparing results of Tests A1, A2, A3 and A4), impacts of a higher impact velocity often showed a lower COR value. Such trend is generally consistent with that reported in the literatures (e.g. Yong et al, 2019). In view of the test results above, it may be appropriate to adopt a COR value of 0.3 in routine designs. A sensitivity study based on this range of COR indicates the change in predicted flexural response is not sensitive (less than 10% difference). Details of the sensitivity study have been documented in Wong & Lam (2018a).

2.3.4 Test Results for Objective 2 - Verification of Enhanced Flexural Stiffness Method

Table 2.4 shows a comparison of the observed maximum deflections at the crest of the barrier in each test and those predicted based on the EFSM. The predictions based on EFSM require the input of impactor mass, mass of model barrier, impact velocity, COR and cracked flexural stiffness of the barrier (see Equation 2.1). Estimation of COR has been reported in Section 2.3.3. Method of estimation of cracked flexural stiffness of the barrier is given in Wong & Lam (2018b). Other input parameters, i.e. impactor mass, mass of model barrier, and impact velocity, were directly measured from the experiments.

$$\Delta = \beta v_0 \sqrt{\frac{m}{k_{cr}}} \quad \text{..... (2.1)}$$

where Δ = Flexural deflection of the model barrier (in m)

$\beta = \sqrt{\lambda \left(\frac{1 + \text{COR}}{1 + \lambda}\right)^2}$

COR = Coefficient of Restitution

λ = Ratio between participating mass of model barrier and mass of impactor

v_0 = Impact velocity of the impactor (in m/s)

m = Mass of impactor (in kg)

k_{cr} = Cracked flexural stiffness of model barrier (in N/m)

As shown in Table 2.4, the predicted deflections of the barrier based on EFSM are generally in a good agreement with the experimental results.

The strain levels of the steel reinforcements are examined. The maximum strain levels of each vertical reinforcement at the tension side at the base of the wall stem (i.e. at the location of maximum flexural strain) are found well below the yield limit of 0.0028, which suggests that the steel bars are still within the elastic range as assumed in the EFSM.

In theory, the boulder could deform (i.e. by compression) and/or be fractured when hitting a rigid barrier. Such deformation or fracturing could involve energy dissipation, which is not considered in the EFSM. That could explain why the observed deflection in the tests is generally smaller than the predictions by EFSM.

Table 2.4 Comparison of Observed Deflection and Predicted Deflection Using EFSM

Test No.	Impactor	Impactor Mass (kg)	Impact Velocity (m/s)	Observed Peak Deflection at the Crest of the Barrier (mm)	Predicted Deflection at the Crest of the Barrier Using EFSM (mm)
A1	G-B	315	2.02	4.86	6.08
A2		315	3.1	8.13	8.98
A3		315	3.54	10.04	10.02
A4		315	4.31	10.50	11.63
B1	V-B	155	1.73	2.43	3.35
B2		155	2.73	3.69	4.83
B3		155	5.29	6.94	8.78
C1	G-1	220	2.12	4.09	5.29
C2		220	4.28	8.55	9.26
C3		220	4.98	9.55	9.94
C4		220	6	11.27	11.53
D1	G-2	200	2.33	2.93	4.48
D2		200	3.66	5.35	6.77
D3		200	4.42	6.60	7.95
D4		200	5.88	8.76	10.47

Note: The values of COR adopted in the prediction of deflection are shown in Table 2.3.

2.3.5 Test Results for Objective 3 - Effect of Locations of Impacts

The EFSM is developed based on an impact location at the crest of a barrier wall, which is often the most critical impact location which will give rise to the largest bending of the barrier. Wong & Lam (2018a) has conducted a preliminary parametric study and found that the boulder impacting at the crest of the rigid barrier would give rise to the most critical tensile strain on the flexural reinforcement (where bending moment is the highest) than those impacting at the lower part of the wall (i.e. mid-height and near the base of the wall).

In this regard, one of the objectives of this study is to further examine the effect of impact locations. Tests were carried out involving pairs of impact scenarios where the impactor was set to hit the barrier at different locations of impacts (i.e. mid-height and crest). The measured tensile strains from the three strain gauges installed at the vertical reinforcement (on the Impact face, which is the tension side) at the base of the wall stem was examined (see Figure 2.2). The peak tensile strains on these three locations were similar and the average values are shown in Table 2.5. This tensile strain of the vertical steel reinforcements is a measure of flexural response of the barrier.

Table 2.5 Experimental Study of Effect of Locations of Impacts

Test No.	Impactor Mass (kg)	Release Height (m)	Impact Velocity (m/s)	Measured Average Peak Tensile Strain of Flexural Reinforcement
C3 (Impact at crest)	220	1.3	4.98	0.00154
C3M (Impact at mid-height)			4.93	0.00105 (68% of that in Test No. C3)
C4 (Impact at crest)		1.9	6.00	0.00184
C4M (Impact at mid-height)			5.99	0.00124 (67% of that in Test No. C4)

As shown above, the strain levels of flexural steel bars (and the bending moment as well) at the base under an impact at the mid-height of the model barrier (i.e. Test Nos. C3M and C4M) is lowered by about 30%, as compared to those at the crest of the model barrier (i.e. Test Nos. C3 and C4).

3 Numerical Analyses for Further Study of Locations of Impacts

In this study, a series of systematic numerical analyses were carried out to examine the effect of impact locations. The analyses involved a 10 m long, 5.2 m high and 0.8 m thick reinforced concrete model barrier being impacted by two different model boulders. The model boulders were spherical and were 1.5 m and 0.5 m in diameter for numerical analyses Series nos. 1 and 2 respectively. The model barrier was restrained in rotational and translational movement at the base, and thus behaved as a cantilevered wall. In each series of analyses, seven boulder impact tests were modelled numerically, and the boulder impact velocity (translational) varied from 5 m/s to 11 m/s. Impact scenarios involving both impacts at the crest (for Series 1a & 2a) and the mid-height (for Series 1b & 2b) of the model barrier were analysed (see Figure 3.1).

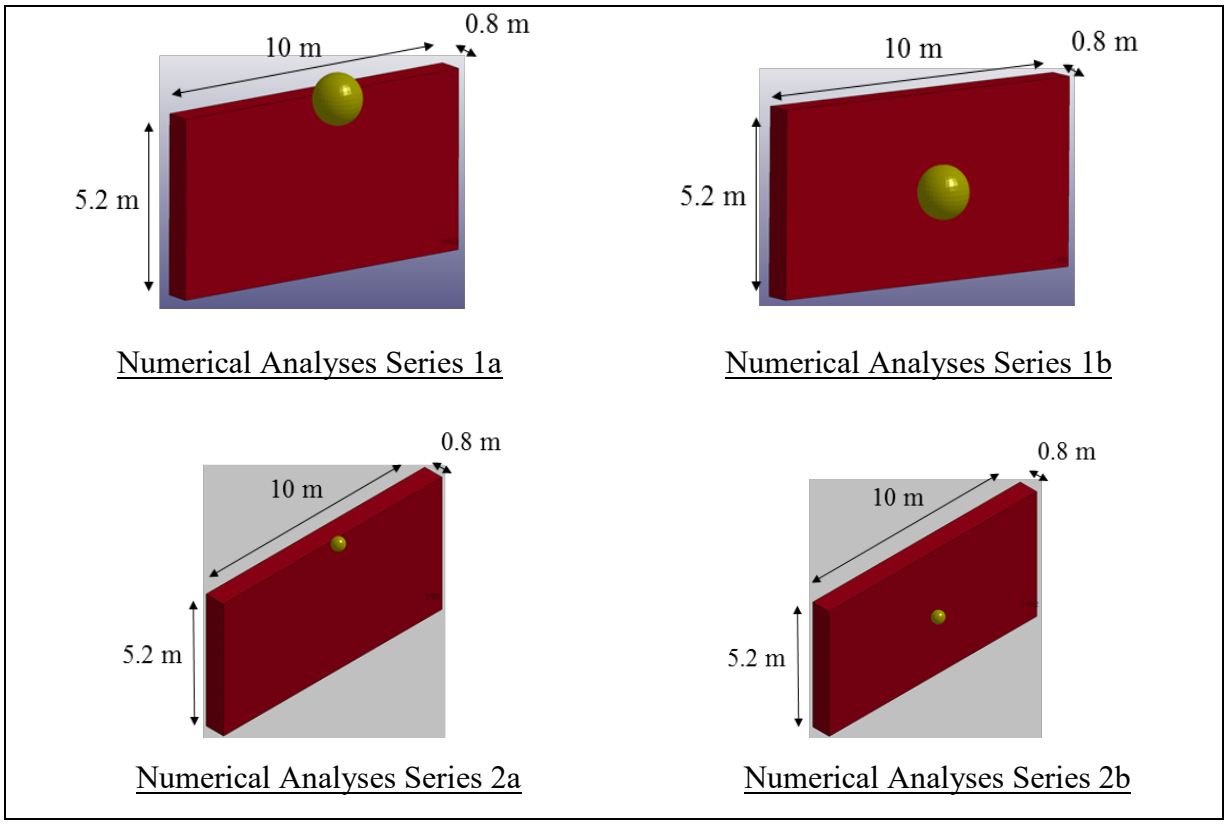

Figure 3.1 Validated Numerical Analyses Series 1 & 2 for the Study on the Effect of Locations of Impacts

Comparisons of the numerical outputs of series 1a against 1b, and series 2a against 2b were conducted. Average peak tensile strain at the vertical steel bars along the base of wall were shown in Figure 3.2. It was found that tensile strains of steel reinforcements under mid-height impact scenarios are generally reduced by about 50% on average of those under crest impacts scenarios.

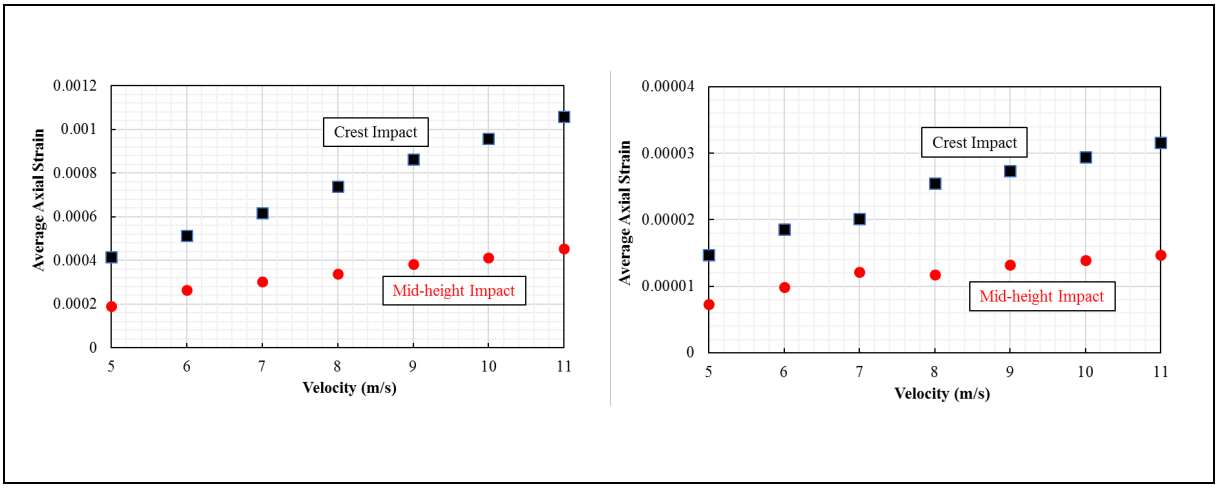

Figure 3.2 Results of Validated Numerical Analyses Series 1 (Left) & Series 2 (Right)

4 Considerations in Structural Design

Flexural response of rigid barriers subject to boulder impact is transient and occurrence of a debris flow event is relatively infrequent. GEO (2014) recommends that debris and boulder impact loads should be considered as an accidental action, and loading scenarios involving debris and boulder impacts should be assessed as the ultimate limit state under Accidental Design Situation in BSI (2002) and BSI (2004). In Hong Kong, for different projects (e.g. public works projects, private developments, etc.), different structural design codes may be adopted. In general, for accidental load or exception load, a partial load factor of 1.0 to 1.05 is recommended in these codes (BD, 2013; BSI, 2006; GEO, 2014).

According to the structural design codes that are commonly used in Hong Kong, limit state design approach is often adopted. Under the ultimate limit state, the common practice adopts an elastic analysis to estimate flexural response of reinforced concrete members. However, these structural codes have provisions to allow plastic design approaches such as yield line analysis (BD, 2013), or other similar approaches that consider plastic response of structural member (BSI, 2006). These approaches may yield a more economical solution, and, advice from structural engineers may be sought if such approach is adopted in the structural design.

For design events involving both soil debris and boulders, the multiple-surge load model in Figure 2.1 of GEO Report No. 270 (Kwan, 2012) should be followed for structural integrity check for rigid barrier. Meanwhile, the assessment of impact load arising from boulders of 1 m diameter or below is generally not required in the structural design of a rigid barrier. This approach is based on consideration of the transient and localised nature of boulder impact, the probable benefits of 3-dimensional effects of typical barriers with wing walls, built-in conservatism in the dynamic soil debris impact model, as well as the low probability of simultaneous occurrence of the peak dynamic soil debris and boulder impact loads.

Under special circumstances if boulder impact loads are required to be considered in the structural design, the flexural response of barriers due to boulder impact can be assessed based on Enhanced Flexural Stiffness Method.

Alternatively, designers may consider adopting measures such as baffles, boulder straining structures, cushioning materials, etc. to deal with the boulder impact, taking into account cost-effectiveness, constructability and maintenance requirement, etc.

5 Conclusion

GEO has conducted a series of large-scale impact tests to further validate the flexural response of a rigid barriers subject to impacts by natural rock of different shapes. These impact tests further validate EFSM in predicting the flexural response of rigid barriers subject to hard impacts and the EFSM can be used in structural design for rigid barriers.

Based on the test results, a COR value of 0.3 is recommended in routine designs. Based on the experiments and the numerical analyses, it was found that the flexural response of the barrier subject to impact at its mid-height is lower, by around 30% to 50%, as compared to those impacts at the crest of barrier. Various considerations of structural design of rigid barriers have also been discussed.

6 References

BD (2013). *Code of Practice for Structural Use of Concrete 2013*. Buildings Department, 187 p.

BSI (2002). *Eurocode. Basis of Structural Design (BS EN 1990:2002+A1:2005)*. British Standards Institution, London, 120 p.

BSI (2004). *UK National Annex for Eurocode. Basis of Structural Design (NA to BS EN 1990:2002+A1:2005)*. British Standards Institution, London, 18 p.

BSI (2006). *Eurocode 1: Actions on Structures – Part 1-7: General Actions – Accidental Actions (BS EN 1991-1-7:2006)*. British Standards Institution, London, 72 p.

CAGHP (2018). *Specification of Design for Debris Flow Prevention* (T/CAGHP *021-2018)*. China Association of Geological Hazard Prevention, 55 p. (in Chinese)

Chau, K.T., Wong, R.H.C. & Lee, C.F. (1998). Rockfall problems in Hong Kong and some new experimental results for coefficients of restitution. *International Journal of Rock Mechanics and Mining Sciences*, 1998, vol. 35, no. 4-5, pp 662-663.

GEO (2014). *Supplementary Guidelines on the Use of Eurocodes and UK National Annexes for Structural Design of Slope Works under the Landslip Prevention and Mitigation Programme (GEO TGN 42)*, 7 p.

Hungr, O., Morgan, G.C. & Kellerhals, R. (1984). Quantitative analysis of debris torrent hazards for design of remedial measures. *Canadian Geotechnical Journal*, vol. 21, pp 663-677.

Lam, C. & Kwan, J.S.H. (2016). *Displacement-based Assessment of Boulder Impacts on Rigid Debris-resisting Barriers - A Pilot Study (Technical Note No. TN 9/2016).* Geotechnical Engineering Office, Hong Kong, 66 p.

Masuya, H., Ihara, T., Onda, S. & Kamijo, A. (2001). Experimental study on some parameters for simulation of rock fall on slope. *Proc. 4th Asia-Pacific Conf. on Shock and Impact Loads on Structures*, pp. 63 – 69.

Wong, L.A. & Lam, H.W.K. (2018a). *Study of Flexural Response of Rigid Barriers Subject to Boulder Impact (Technical Note No. TN 3/2018).* Geotechnical Engineering Office, Hong Kong, 40 p.

Wong, L.A. & Lam, H.W.K. (2018b). *Large-scale Experimental Study of Structural Response of Rigid Barriers Subject to Hard Impact (Technical Note No. TN 7/2018).* Geotechnical Engineering Office, Hong Kong, 30 p.

Yong, A.C.Y., Lam, C., Lam, N.T.K. & Perera, J.S. (2019). Analytical solution for estimating sliding displacement of rigid barriers subjected to boulder impact. *Journal of Engineering Mechanics, 2019,* 145(3): 04019006.

[Blank Page]

Section 7: Analytical Study of Cushioning Effect Provided by Rockfill Gabions in Reducing Flexural Response of Rigid Barriers Subject to Boulder Impacts

L.A. Wong & H.W.K. Lam

This section was originally produced in December 2019 as GEO Technical Note No. TN 6/2019

Foreword

This Technical Note summarises findings of a study of cushioning effect provided by rockfill gabions on the flexural response of rigid barriers subject to boulder impact. This study was carried out by Mr L.A. Wong under the supervision of Mr H.W.K. Lam in collaboration with Professor N.T.K. Lam from the University of Melbourne and his assistants, Mr A.C.Y. Yong and Mr J. Perera. The Drafting Unit of the Standards and Testing Division assisted in formatting this Note.

The contents in the report were reviewed by Prof N.T.K. Lam. Many colleagues in the GEO provided constructive comments on the Note. All contributions are gratefully acknowledged.

T.K.C. Wong
Chief Geotechnical Engineer/Standards and Testing
December 2019

Abstract

Previous experimental studies indicate that flexural response of a rigid barrier subject to boulder impacts could be effectively reduced by the provision of rockfill gabion cushions. This study aims to quantify such cushioning effect for rockfill gabions. It comprises literature review and analytical studies using a spring-connected two degree-of-freedom lumped mass model. The analytical model has been calibrated against large-scale pendulum impact tests. Sensitivity analyses using this analytical model are presented to study the cushioning effect under various boulder impact scenarios.

Contents

		Page No.
Title Page		293
Foreword		294
Abstract		295
Contents		296
List of Tables		298
List of Figures		299
1	Introduction	300
2	Literature Review	300
3	Analytical Model to Predict Cushioning Effect based on Two Degree-of-Freedom Lumped Mass Model	301
	3.1 General	301
	3.2 Validation of Analytical Model	304
4	Parametric Study Using Two Degree-of-Freedom Lumped Mass Model	305
	4.1 General	305
	4.2 Effect of Impact Velocity of Boulder	305
	4.3 Effect of Diameter of Boulder	306
	4.4 Effect of Reinforcement Contents of Rigid Barrier	306
	4.5 Effect of Thickness of Rockfill Gabion Cushion	307
	4.6 Effect of Height of Rigid Barrier	307
	4.7 Discussion on Parametric Study	308
5	Summary	308
6	References	308
Section 7 Appendix A:	Analytical Expression for Damping Coefficient and Contact Spring Stiffness for Hunt & Crossley Contact Force Model	310
Section 7 Appendix B:	Identification of Contact Force Model for the Prediction of Contact Spring Stiffness in Hunt & Crossley Model	314

		Page No.
Section 7 Appendix C:	Details of Computation of Two Degree-of-Freedom Lumped Mass Model	322
Section 7 Appendix D:	Verification of Two Degree-of-Freedom Lumped Mass Model	326
Section 7 Appendix E:	Worked Example	334

List of Tables

Table No.		Page No.
3.1	Summary of Validation of 2DOF Analyses	304
4.1	Study on the Effect of Boulder Impact Velocity	306
4.2	Study on the Effect of Diameter of Boulder	306
4.3	Study on the Effect of Reinforcement Contents	307
4.4	Study on the Effect of Thickness of Rockfill Gabion Cushion	307
4.5	Study on the Effect of Height of Rigid Barrier	308

List of Figures

Figure No.		Page No.
3.1	2DOF Spring Mass System Utilising Hunt and Crossley Model	303
3.2	Comparison of Measured Deflection-time History and Predicted Deflection-time History based on 2DOF Analysis for Strike Number 4 in Test Series C2	304

1 Introduction

Cushioning materials are prescriptively used in Hong Kong to protect reinforced concrete rigid barriers against boulder impacts. In 2015, GEO engaged the Hong Kong University of Science and Technology (HKUST) to carry out pendulum impact tests to study the effectiveness of various cushioning materials in reducing boulder load on rigid barriers (HKUST, 2015; Lam, 2016). Four different types of cushioning materials were studied, including rockfill gabions, ethylene-vinyl acetate foam, recycled glass cullet and cellular glass aggregates. The test results indicate that rockfill gabions are effective in attenuating the boulder impact load.

In 2018, GEO engaged the University of Melbourne (UoM) to conduct physical impact tests with a view to quantifying the cushioning effect of rockfill gabions in reducing flexural response of a rigid barrier subject to boulder impacts. The impact test results (based on impact energy level up to 10 kJ) were promising and clearly indicate that the cushioning effect of rockfill gabions could be substantial. Technical findings have been documented in Wong & Lam (2018).

With a view to rationalising the use of cushion in routine designs, a study is initiated which comprised literature review, development of a new analytical approach and associated validation. The analytical approach adopts a newly-developed model, namely Two Degree-of-Freedom Lumped Mass Model (2DOF Model). This Note documents the key findings of the study.

Cushioning effect of rockfill gabions to prevent localised damage of a rigid barrier subject to boulder impact is being studied and would be separately covered.

2 Literature Review

Literature review on overseas design guidelines on cushioning materials to reduce flexural response of a rigid structure has been carried out.

The Swiss design guideline for rockfall galleries recommended the use of Equation 2.1 to establish the contact force of boulder acting on the cushioning material of a rockfall gallery (ASTRA, 2008). It was derived from experimental studies and numerical analyses. The experimental studies involved impact tests of up to 100 kJ. In these tests, boulders of 100 kg, 500 kg and 1,000 kg were dropped onto a 3.4 m x 3.4 m x 0.2 m reinforced concrete slab covered by 0.35 m, 0.5 m and 1 m thick cushioning materials, e.g. crushed gravel. The deceleration of boulder was captured by an accelerometer that was pre-installed on the boulder. The contact force was taken as the multiple of the measured deceleration and the mass of boulder. Verification of Equation 2.1 was extended to numerical analyses on rockfall events of a larger scale with an impact energy up to 20 MJ (Khasraghy, 2011). The equation is given below:

$$F_c = 2.8\, t^{-0.5}\, r^{0.7}\, E^{0.4}\, \tan\phi \left(\frac{m v_0^{\,2}}{2000}\right)^{0.6} \quad \text{..... (2.1)}$$

where F_c = Contact force between boulder and cushioning material of a rockfall gallery (in kN)
t = Thickness of cushioning material (in m)
r = Radius of boulder (in m)
E = Stiffness of cushioning material (in kPa)
ϕ = Internal friction angle of cushioning material (in deg)
m = Mass of boulder (in kg)
v_0 = Impact velocity of boulder (in m/s)

In Japan, JRA (2000) proposed Equation 2.2 for the estimation of boulder impact force acting on sand cushioned rockfall gallery. This expression is valid when the roof slab of the gallery remains elastic. The equation is given below:

$$F = 2.108 \left(\frac{mg}{1000}\right)^{\frac{2}{3}} E^{\frac{2}{5}} H^{\frac{3}{5}} \left(\frac{t}{2r}\right)^{-0.5} \quad \text{..... (2.2)}$$

where F = Boulder impact force (in kN)
m = Mass of boulder (in kg)
g = Acceleration due to gravity, i.e. 9.81 m/s^2
E = Stiffness of sand cushion (in kPa, and is recommended to be 1000 kPa for loosely packed sand cushion)
H = Drop height of boulder (in m)
t = Thickness of sand cushion (in m)
r = Radius of boulder (in m)

Equations 2.2 is an empirical equation, largely based on impact scenarios involving vertical drop of boulder. The physical meaning of the force calculated was not well defined in the JRA (2000) (e.g. whether it is a contact force or an equivalent static force for estimating flexural response). All these factors limit the application of Equation 2.2 in routine designs.

3 Analytical Model to Predict Cushioning Effect based on Two Degree-of-Freedom Lumped Mass Model

3.1 General

Mass-spring-damper models are known to be suitable for modelling object with complex material properties such as non-linearity and viscoelasticity. As observed in the impact experiments (Wong & Lam, 2018), impacts on cushioned rigid barriers can cause (1) localised and permanent indentation of the cushioned layer in the vicinity of the point of contact and (2) global flexural deflection of the rigid barrier.

With reference to the experimental observations as well as other similar researches on impact mechanics, the University of Melbourne recently established an analytical model to predict the cushioning effect of rockfill gabions for reduction of flexural response of a rigid

barrier subject to boulder impacts. This model adopts a spring-connected two degree-of-freedom lumped mass (2DOF) system (see Figure 3.1) that could capture the time histories of contact force of an impactor, indentation as well as the global flexural response of a barrier in an integrated manner (UoM, 2019). Similar 2DOF analyses were widely researched in overseas practices for dynamic impact mechanisms (Chikatamarla, 2006; Delhomme et al, 2007; Fujikake, 2007).

The analytical model involves the first degree of freedom representing contact process of an impactor to a cushioned layer, as presented in Equation 3.1. The contact process is assumed to be simulated by a damper and a spring based on the visco-elastic contact model developed by Hunt & Crossley (1975)[1]. The damper allows for energy dissipation in the cushioned layer in the vicinity of the contact area during the impact process, which includes plastic deformation of cushion, work done on re-arrangement of rockfill particles, energy loss due to sound and heat, etc. The damping force shown in Equation 3.1 will increase with the deformation, i.e. indentation of the cushion, which is commonly observed in impact experiments (Flores et al, 2011; Gilardi et al, 2002). The spring in Equation 3.1 is assumed linear and is used to allow for elastic energy absorption associated with the indentation process.

Equation 3.1 defines the contact force-time history at the cushioned layer subject to an impact. It involves two modelling parameters, i.e. k_1 and D_1, which can be analytically derived (see Section 7 Appendix A). These two parameters would vary under different impact conditions, e.g. different cushion thickness, size and impact velocity of impactor, etc., and are proven to be dependent on the peak contact force during the contact process (see Section 7 Appendix A). In this study, the peak contact force is estimated based on Equation 2.1 (ASTRA, 2008), and that estimation was found to be reasonable as demonstrated in Section 7 Appendix B.

The second degree of freedom of the analytical model is simulated by a simple linear spring system representing the flexural stiffness of the rigid barrier. This reflects the global response of the rigid barrier during the impact process. The ultimate goal of the analytical model is to identify the deflection of the crest of the rigid barrier (i.e. x_2), which represents flexural response of a rigid barrier under boulder impacts.

Equation 3.2 represents the relationship of the time histories of contact force (F_c), acceleration of the lump mass of the cushioned barrier (a_2) and flexural deflection of rigid barrier (x_2), based on force equilibrium at different time interval during the impact process. The lump mass of the cushioned barrier (m_2) includes participating masses of the cushioned layer and the rigid barrier.

$$F_c(t) = k_1\delta(t) + D_1\delta(t)\,\dot{\delta}(t) \quad \text{..... (3.1)}$$

$$F_c(t) = m_2\,a_2(t) + k_2\,x_2(t) \quad \text{..... (3.2)}$$

[1] Other contact model such as Hertz Law has been considered but not adopted because the Hertz Law is typically for impact between two elastic bodies, and thus not applicable to hard impact on rockfill cushion where plastic deformation is commonly observed.

where $F_c(t)$ = Contact force-time history between boulder and lumped mass of cushion-barrier, i.e. force at contact spring in Figure 3.1 (in N)
k_1 = Contact spring stiffness (in N/m)
$\delta(t)$ = Shortening of contact spring (i.e. the movement of the centre of the boulder resulted from both compression of the boulder and indentation into the surface of the barrier) (in m)
D_1 = Damping coefficient (in kg/s m)
$\dot{\delta}(t)$ = Rate of shortening of contact spring (in m/s)
m_2 = Lumped mass of cushioned barrier (in kg)
$a_2(t)$ = Acceleration of cushion-barrier lumped mass (in m/s^2)
k_2 = Rear spring stiffness, i.e. cracked flexural stiffness of rigid barrier (in N/m)
$x_2(t)$ = Flexural deflection of the crest of rigid barrier (in m)

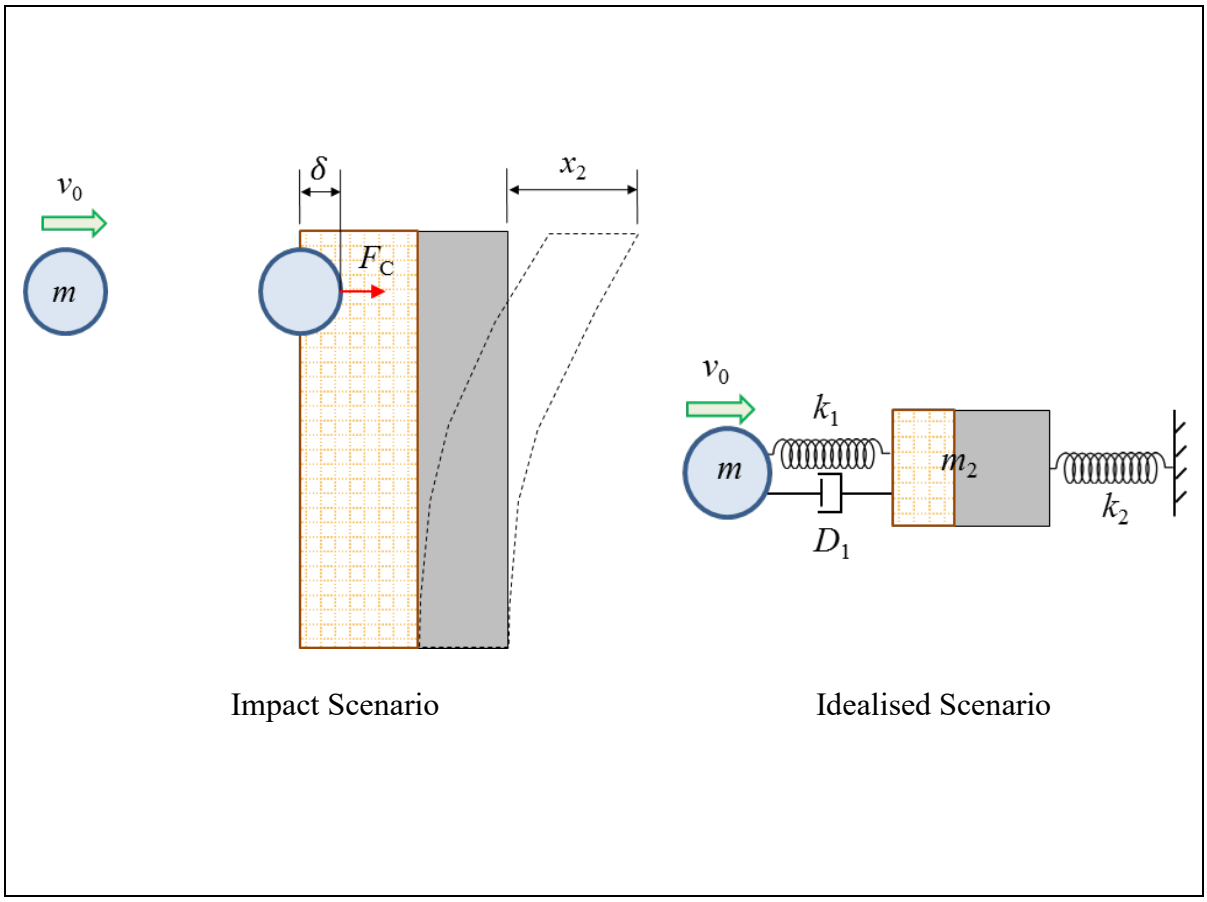

Figure 3.1 2DOF Spring Mass System Utilising Hunt and Crossley Model

Equations 3.1 and 3.2 are the two governing equations in the analytical model. This analytical method can model the contact force-time history with the consideration of the cushioning effect, and the flexural response of a rigid barrier in an integrated manner. The arithmetic of the analytical model is simple and can be operated using computer spreadsheets. Through time-step analyses (as detailed in Section 7 Appendix C), the deflection-time history of a rigid barrier, x_2, can be obtained.

3.2 Validation of Analytical Model

The reliability of the analytical model as described in Section 3.1 has been assessed by means of comparing the predicted flexural deflection of cushioned rigid barriers based on the analytical model and those measured during the large-scale impact tests (Wong & Lam, 2018) as shown in Table 3.1. The deflection-time histories of the barrier were also examined. A comparison of such deflection-time history for Strike No. 4 in Test Series C2 is extracted in Figure 3.2 below as an example.

Table 3.1 Summary of Validation of 2DOF Analyses

Test Series	Strike Number	Impactor Mass (kg)	Impact Velocity (m/s)	Measured Peak Deflection (by laser sensor) at the Crest of the Barrier (mm)	Predicted Peak Deflection at the Crest of the Barrier based on 2DOF Analyses (mm)
C1	1 to 3	280	5.24	1.8 - 3.6	4.9
C1	4	280	3.13	1.3	2.7
C2	1 to 3	435	3.37	1.3 - 3.3	3.9
C2	4	435	2.51	2.2 (See Figure 3.2 for the measured deflection-time history)	2.7 (See Figure 3.2 for the predicted deflection-time history)

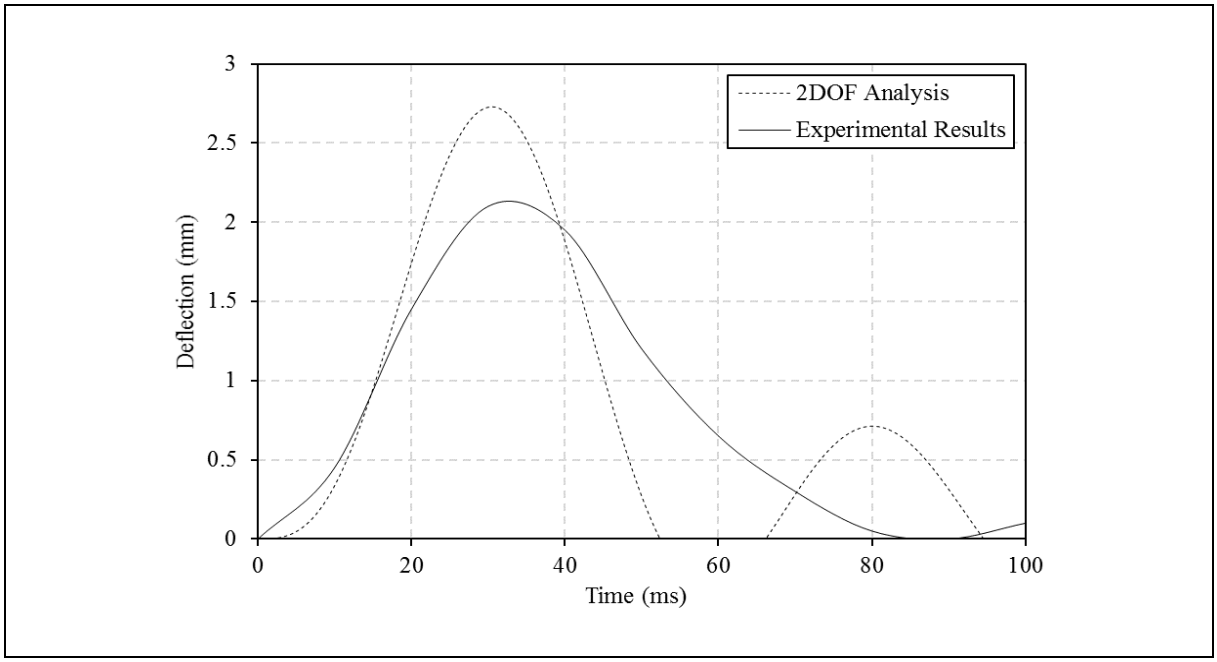

Figure 3.2 Comparison of Measured Deflection-time History and Predicted Deflection-time History based on 2DOF Analysis for Strike Number 4 in Test Series C2

As shown in Table 3.1 and Figure 3.2 above, the predicted peak flexural deflections based on 2DOF analyses were generally comparable to the experimental results. Details of the above validation are given in Section 7 Appendix D. It should be noted that the 2DOF model assumes that friction between the impactor and the cushioning materials is negligible and lump mass of rigid barrier is fully fixed. These assumptions could lead to a conservative prediction of flexural response as shown in Table 3.1 above.

4 Parametric Study Using Two Degree-of-Freedom Lumped Mass Model

4.1 General

A series of parametric studies of the cushioning effect was conducted using the validated 2DOF model. The boulder impact scenarios adopted are generally those commonly encountered in routine designs in local practice. The sensitivity of the following parameters are analysed:

(a) impact velocity of the boulder;

(b) diameter of the boulder;

(c) reinforcement contents of rigid barrier;

(d) thickness of rockfill gabion cushion; and

(e) height of rigid barrier.

In each analysis, the boulder impact force is estimated based on 2DOF Model, i.e. F_{2DOF} representing flexural response of a cushioned barrier, and is then compared with the boulder impact force estimated based on Enhanced Flexural Stiffness Method, i.e. F_{EFSM}, which represents flexural response of barrier without cushion. The comparison of these two forces allows for the study of the cushioning effect provided by rockfill gabions.

4.2 Effect of Impact Velocity of Boulder

The first parameter under the study was the boulder impact velocity. The impact scenario adopted involves a 1 m diameter boulder impacting onto a 5.5 m high, 10 m long, 0.8 m thick reinforced concrete model barrier (concrete grade of C30), with reinforcement of T40 - 200 (yield strength of 500 MPa) for both vertical and horizontal reinforcement on tension and compression sides. The barrier was cushioned by a 1 m thick rockfill gabion. Several boulder impact scenarios with different boulder impact velocities, ranging from 6 m/s to 12 m/s, were analysed. Table 4.1 shows the results.

Table 4.1 Study on the Effect of Boulder Impact Velocity

Boulder Impact Velocity (m/s)	Boulder Impact Force for Flexural Response for Barrier without Cushion (kN) (i.e. EFSM)	Boulder Impact Force for Flexural Response for Barrier with Cushion (kN) (i.e. 2DOF Model)	Reduction in Flexural Response
6	523	280	46% (See Section 7 Appendix E for the analyses)
8	697	384	45%
10	871	490	44%
12	1045	597	43%

4.3 Effect of Diameter of Boulder

The second parameter under study was the boulder size. The impact scenarios adopted were the same as those in Section 4.2, except that the boulder impact velocity was fixed at 10 m/s and the boulder diameter varied from 0.5 to 1.5 m. Table 4.2 shows the results.

Table 4.2 Study on the Effect of Diameter of Boulder

Boulder Diameter (m)	Boulder Impact Force for Flexural Response for Barrier without Cushion (kN) (i.e. EFSM)	Boulder Impact Force for Flexural Response for Barrier with Cushion (kN) (i.e. 2DOF Model)	Reduction in Flexural Response
0.5	114	72	37%
1.0	871	490	44%
1.5	2628	1449	45%

4.4 Effect of Reinforcement Contents of Rigid Barrier

The third parameter under study was the effect of reinforcement content of the rigid barrier. Reinforcement contents would affect the cracked flexural stiffness of a rigid barrier (i.e. k_2). The impact scenarios adopted were the same as those in Section 4.2, except that the boulder impact velocity was fixed at 10 m/s, and different reinforcement contents were adopted, i.e. (a) from 2T40 - 100 (i.e. reinforced with 2 layers of high yield tensile reinforcements of 40 mm diameter at 100 mm centre-to-centre spacing on both tension and compression sides), (b) T40 - 200 (i.e. reinforced with high yield tensile reinforcements of 40 mm diameter at 200 mm centre-to-centre spacing on both tension and compression sides)

and (c) T32 - 200 (i.e. reinforced with high yield tensile reinforcements of 32 mm diameter at 200 mm centre-to-centre spacing on both tension and compression sides). Table 4.3 shows the results.

Table 4.3 Study on the Effect of Reinforcement Contents

Reinforcement Contents	Cracked Flexural Stiffness of Rigid Barrier (kN/m)	Boulder Impact Force for Flexural Response for Barrier without Cushion (kN) (i.e. EFSM)	Boulder Impact Force for Flexural Response for Barrier with Cushion (kN) (i.e. 2DOF Model)	Reduction in Flexural Response
2T40 - 100	193600	1468	604	61%
T40 - 200	68192	871	490	44%
T32 - 200	56648	794	464	42%

4.5 Effect of Thickness of Rockfill Gabion Cushion

The fourth parameter under study was the effect of the thickness of gabion cushion. The impact scenarios adopted were the same as those in Section 4.2, except that the boulder impact velocity was fixed at 10 m/s, and the thickness of gabions varied from 0.5 m to 1.0 m. Table 4.4 shows the results.

Table 4.4 Study on the Effect of Thickness of Rockfill Gabion Cushion

Thickness of Gabion Cushion (m)	Boulder Impact Force for Flexural Response for Barrier without Cushion (kN) (i.e. EFSM)	Boulder Impact Force for Flexural Response for Barrier with Cushion (kN) (i.e. 2DOF Model)	Reduction of Flexural Response
0.5	871	565	35%
1.0	871	490	44%

4.6 Effect of Height of Rigid Barrier

The effect of the height of rigid barrier was studied. The impact scenarios adopted were the same as those in Section 4.2, except that the boulder impact velocity was fixed at 10 m/s, and the height of rigid barrier varied from 4 m to 7 m. Table 4.5 shows the results.

Table 4.5 Study on the Effect of Height of Rigid Barrier

Height of Rigid Barrier (m)	Boulder Impact Force for Flexural Response for Barrier without Cushion (kN) (i.e. EFSM)	Boulder Impact Force for Flexural Response for Barrier with Cushion (kN) (i.e. 2DOF Model)	Reduction of Flexural Response
4.0	1777	629	65%
5.5	871	490	44%
7.0	544	359	34%

4.7 Discussion on Parametric Study

Based on the impact scenarios considered in the above parametric study, the reduction of flexural response offered by rockfill gabions generally ranges from 35% to 65%. It was observed that the extent of reduction in flexural response of a rigid barrier would generally increase with the thickness of the gabions. Nevertheless, such increment is not prominent for the impact scenarios considered in Section 4.5. It was also observed that the size of the boulder and the boulder impact velocity may not have a significant effect on the flexural response of a cushioned barrier (see results in Section 4.2 and 4.3). As shown in Table Nos. 4.3 and 4.5, in general, gabion cushion would result in a more significant reduction of flexural response for a stiffer barrier wall, e.g. shorter wall or wall with heavier reinforcement contents.

5 Summary

An analytical model based on a two degree-of-freedom lumped mass system was developed to predict the cushioning effect of rockfill gabions on a rigid barrier under a boulder impact. This model has been validated using large-scale impact tests on rockill cushioned rigid barriers.

Parametric study has been conducted. Based on the impact scenarios considered in the above parametric study, the reduction of flexural response offered by rockfill gabions generally ranges from 35% to 65%.

6 References

ASTRA (2008). *Einwirkungen infolge Steinschlags auf Schutzgalerien, Richtlinie (Effects of Rockfall on Protection Galleries, Guideline)*. Bundesamt für Strassen ASTRA (Federal Roads Office), Switzerland, 21 p.

Chikatamarla, R. (2006). *Optimisation of Cushion Materials for Rockfall Protection Galleries*, Dissertation, Diss. Number 16315, ETH Zurich, Switzerland.

Delhomme, F., Mommessin, M., Mougin, J.P. & Perrotin, P. (2007). Simulation of a block impacting a reinforced concrete slab with a finite element model and a mass-spring system. *Engineering Structures*, 29: p. 2844-2852.

Flores, P., Machado, M., Silva, M.T. & Martins, J.M. (2011). On the continuous contact force models for soft materials in multibody dynamics. *Multibody System Dynamics, 2011.* 25(3): p. 357-375.

Fujikake, K. (2007). Response analysis of RC beams subjected to impact loads, *Proceeding of 1st Int. Workshop on Performance, Protection and Strengthening of Structures under Extreme Loading (CD-ROM),* University of British Columbia, Vancouver.

Gilardi, G. & Sharf, I. (2002). Literature survey of contact dynamics modelling. *Mechanism and Machine Theory, 2002*. 37(10): p. 1213-1239.

HKUST (2015). *Service Contact for Carrying Out a Pilot Study of the Cushioning Effects of Gabions and other Impact Absorption Materials Subject to Dynamic Impact Load,* Final Report prepared for the Geotechnical Engineering Office, Civil Engineering and Development Department, Hong Kong.

Hunt, K.H. & Crossley, F.R.E. (1975). Coefficient of restitution interpreted as damping in vibroimpact. *Journal of Applied Mechanics*, 1975, 42(2): p. 440.

JRA (2000). *Manual for Anti-impact Structures against Falling Rock (in Japanese).* Japan Road Association, Japan.

Khasraghy, S.G. (2011). *Numerical Simulation of Rockfall Protection Galleries*, Dissertation, Diss. Number 19931, ETH Zurich, Switzerland.

Lam, C. (2016). *A Pilot Study of the Use of Cushioning Materials for Reducing Dynamic Impact Loads on Rigid Debris-resisting Barriers (Technical Note No. TN 5/2016).* Geotechnical Engineering Office, Hong Kong, 70 p.

UoM (2019). *Large Scale Impact Test and Computer Services for Investigation of the Structural Response of Rigid Barrier Subjected to Boulder Impact,* Compilation of all submitted Reports prepared for the Geotechnical Engineering Office, Civil Engineering and Development Department, Hong Kong.

Wong, L.A. & Lam, H.W.K. (2018). *Large-scale Experimental Study of Structural Response of Rigid Barriers Subject to Hard Impacts (Technical Note No. TN 7/2018).* Geotechnical Engineering Office, Hong Kong, 30 p.

Section 7
Appendix A

Analytical Expression for Damping Coefficient and Contact Spring Stiffness for Hunt & Crossley Contact Force Model

Contents

	Page No.
Contents	311
References	313

Sun et al (2014) and Sun (2015) derived the expression of damping coefficient D_1 in A.1. This expression is valid for classical model of viscous damping. The derivation was based on an assumed elliptical relationship between *δ (t) and $\dot{\delta}(t)$* during the course of impact.

$$D_1 = 1.5\left(\frac{1\text{ - COR}}{\text{COR}}\right)\frac{k_1}{v_0} \quad \ldots\ldots\ldots\ldots\ldots\ldots\ldots\ldots\ldots\ldots\ldots \quad \text{(A.1)}$$

where D_1 = Damping coefficient of contact spring (in kg/s m)
COR = Coefficient of restitution between boulder and cushion-barrier lump mass (dimensionless)
k_1 = Contact spring stiffness (in N/m)
v_0 = Impact velocity of boulder (in m/s)

In the cushioned impact tests reported in Wong & Lam (2018), i.e. Test Series C1 and C2, the impactor was observed to embed into the gabion cushion and a COR close to zero was observed. Thus, a very small COR was assumed in the analyses. A sensitivity analysis of COR was conducted (UoM, 2019), where the predicted peak contact force is not sensitive to the assumed COR value. Thus, Equation A.1 can be simplified as:

$$D_1 = 148.5\frac{k_1}{v_0} \quad \ldots\ldots\ldots\ldots\ldots\ldots\ldots\ldots\ldots\ldots\ldots\ldots \quad \text{(A.2)}$$

Perera et al (2016) derived an analytical expression for contact spring stiffness k_1, by considering conservation of energy and momentum of impactor and the target:

$$k_1 = \frac{{F_{\text{c,peak}}}^2}{50 m {v_0}^2}\left(\frac{1+\lambda_2}{\lambda_2}\right) \ldots\ldots\ldots\ldots\ldots\ldots\ldots\ldots\ldots\ldots\ldots \quad \text{(A.3)}$$

where k_1 = Contact spring stiffness (in N/m)
$F_{\text{c,peak}}$ = Peak contact force (in N)
m = Mass of boulder (in kg)
v_0 = Impact velocity of boulder (in m/s)
λ_2 = Mass ratio between cushion-barrier lump mass (m_2) and boulder (m) (dimensionless)

Based on Equation A.3 above, contact spring stiffness k_1 is a function of peak contact force. Thus, in order to obtain an appropriate value of k_1 for the 2DOF analyses in Section 3, the peak contact force shall be estimated.

Prediction of peak contact force for an impactor hitting a cushioned rigid barriers generally follows Equation 2.1 (ASTRA, 2008) and the details are given in Section 7 Appendix B.

References

ASTRA (2008). *Einwirkungen Infolge Steinschlags Auf Schutzgalerien, Richtlinie (Effects of Rockfall on Protection Galleries, Guideline)*. Bundesamt für Strassen ASTRA (Federal Roads Office), Switzerland, 21 p.

Perera, S., Lam, N., Pathirana, M., Zhang, L., Ruan, D. & Gad, E. (2016). Deterministic solutions for contact force generated by impact of windborne debris. *Int. J. Impact Eng*, 91: p. 126-141.

Sun, J., Lam, N., Zhang, L., Gad, E. & Ruan, D. (2014). Contact forces generated by fallen debris. *Structural Engineering and Mechanics*, 2014, 50(5): p. 589-603.

Sun, J. (2015). *Measuring and Modelling Impact Forces of Fallen and Flying Object.* PhD Thesis, Department of Infrastructure Engineering, The University of Melbourne, 248 p.

UoM (2019). *Large Scale Impact Test and Computer Services for Investigation of the Structural Response of Rigid Barrier Subjected to Boulder Impact,* Compilation of all submitted Reports prepared for the Geotechnical Engineering Office, Civil Engineering and Development Department, Hong Kong.

Wong, L.A. & Lam, H.W.K. (2018). *Large-scale Experimental Study of Structural Response of Rigid Barriers Subject to Hard Impacts (Technical Note No. TN 7/2018).* Geotechnical Engineering Office, Hong Kong, 30 p.

Section 7
Appendix B

Identification of Contact Force Model for the Prediction of Contact Spring Stiffness in Hunt & Crossley Model

Contents

	Page No.
Contents	315
List of Tables	316
List of Figures	317
References	321

List of Tables

Table No.		Page No.
B1	Back-analyses of Contact Force for Impact Tests Reported in Wong & Lam (2018)	319
B2	Back-analyses of Contact Force for Impact Tests Reported in Lam (2016)	320

List of Figures

Figure No.		Page No.
B1	Impact Tests on Rigid Barrier with Rockfill Gabion Cushion (Wong & Lam, 2018)	318
B2	Impact Tests on Rigid Barrier with Rockfill Gabion Cushion (Lam, 2016)	319
B3	Uniaxial Compression Test on Specimen of Rockfill Gabion Cushion	321

As shown in Section 7 Appendix A, contact spring stiffness k_1 in Hunt & Crossley Model is dependent on the peak contact force. An appropriate model for the prediction of peak contact force is thus required.

Two common empirical formulae, which include ASTRA (2008) and JRA (2000), have been discussed in Section 2. JRA (2000) cannot be applied to horizontal impact scenarios. On the other hand, Equation 2.1 in ASTRA (2008) was derived from experimental studies and numerical analyses of various impact scenarios on reinforced concrete structure cushioned by crushed gravel. The impact energies of the experimental studies and the numerical analyses were up to 100 kJ and 20 MJ respectively. Thus, ASTRA (2008) was being studied based on the previous large-scale impact tests conducted in the University of Melbourne and the Hong Kong University of Science and Technology. These boulder impact tests involve impacts on cushioned rigid barrier at different energy levels with successive boulder impacts. The investigation is briefly discussed below.

(1) Large-scale Impact Tests conducted by University of Melbourne

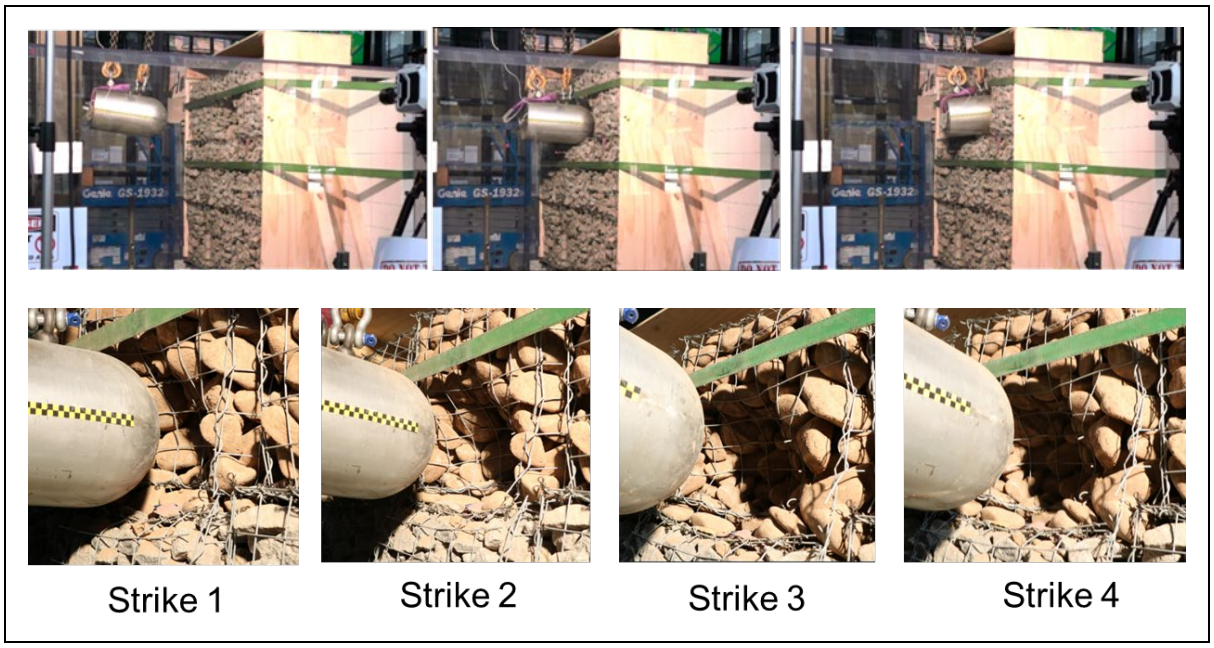

Figure B1 Impact Tests on Rigid Barrier with Rockfill Gabion Cushion (Wong & Lam, 2018)

The setup, instrumentation and test program of the large-scale impact tests conducted in Melbourne in April 2018 have been reported in Wong & Lam (2018). Two series of impact tests on rockfill gabions cushioned rigid barrier were conducted (i.e. Test Nos. C1 to C2). Both 280 kg and 435 kg impactor, with a radius of the head of 150 mm, was positioned to strike directly onto the 525 mm thick cushioning materials at the centerline of the cushioned barrier (see Figure B1). The contact force was measured using the accelerometer attached to the impactor. Peak contact force of the boulder, i.e. a multiple of the peak deceleration and the mass of the impactor, is compared with that predicted using ASTRA (2008) as follows:

Table B1 Back-analyses of Contact Force for Impact Tests Reported in Wong & Lam (2018)

Test Series	Strike Number	Impactor Mass (kg)	Impact Velocity (m/s)	Measured Peak Contact Force (kN)	Predicted Peak Contact Force Using ASTRA (2008) (kN)
C1	1 to 3	280	5.24	23 - 41	38 (See Sample Calculation at the end of this Appendix)
C1	4	280	3.13	17	21
C2	1 to 3	435	3.37	19 - 31	29
C2	4	435	2.51	23	21

(2) Large-scale Impact Tests conducted by Hong Kong University of Science & Technology

The impact tests conducted in Melbourne had an energy level of < 5 kJ, which was relatively lower than those impact scenarios typically encountered in routine design. The Hong Kong University of Science and Technology conducted a series of impact tests on gabions cushioned rigid barrier (Lam, 2016) which were of higher impact energy (i.e. 20 kJ and 70 kJ). These impact tests utilised a reinforced concrete wall of 3 m wide × 1.5 m high × 1.5 m thick with 1 m thick rockfill gabion cushion (see Figure B2). The cushion barrier received strikes from a 1.2 m diameter boulder at impact velocities of 4.5 m/s and 8.4 m/s. Contact force of the first five boulder impacts measured by the accelerometer is compared with that predicted contact force using ASTRA (2008) as follows:

Figure B2 Impact Tests on Rigid Barrier with Rockfill Gabion Cushion (Lam, 2016)

Table B2 Back-analyses of Contact Force for Impact Tests Reported in Lam (2016)

Test Series	Strike Number	Impactor Mass (kg)	Impact Velocity (m/s)	Measured Contact Force (kN)	Predicted Contact Force Using ASTRA (2008) (kN)
G-4	1 to 5	1961	4.5	87 - 180	191
G-8	1 to 5	1961	8.4	213 - 341	403

Based on the above investigation, the prediction of contact force based on ASTRA (2008) is found to be consistent with the experimental results reported in Wong & Lam (2018) and Lam (2016). As such, ASTRA (2008) is adopted for the back-calculation of k_1 in further analyses.

(3) Sample calculation for Prediction of Contact Force based on ASTRA (2008)

The prediction of contact force based on ASTRA (2008) Strike Number 1 to 3 in Test Series C1 is demonstrated below based on the following data:

Test Series	C1
Strike Number	1 to 3
Impactor Mass (kg)	280
Radius of Impactor (m)	0.15
Impact velocity, v_0 (m/s)	5.24
Cushioning Material	Gabions (Granite)
Internal Friction Angle of Rockfill, ϕ (degree)	40° (assumed)
Thickness of Cushion (m)	0.525
Young's Modulus for Gabions Cushion, E (kPa)	1740 [(1)]

Note: [(1)] Two quasi-static uniaxial compression tests were conducted on a single cell of rockfill gabions before the impact test. The gabion cell was loaded at a deformation rate of 1 mm/s up to a compressive displacement of 100 mm. The force was exerted by a load actuator on the gabion cell through a 32 mm thick steel plate which allows an even load distribution (see Figure B1 below). According to the test results, stress-strain behaviour of single gabion cell exhibits bi-linear strain hardening characteristics, with a higher stiffness at high strain level because of the increased degree of compactness. The secant Young's modulus of the gabion cells ranges from 290 kPa to 600 kPa at low strain level, and from 800 kPa to 870 kPa at high strain level. Lin et al (2010) demonstrated that the stiffness of gabions with lateral confinement, which is the case during impact test, can be doubled as compared with the stiffness of gabions which is uniaxially loaded. As such, the Young's modulus for gabion cushion, E has been taken as 1740 kPa in the analyses.

Figure B3 Uniaxial Compression Test on Specimen of Rockfill Gabion Cushion

Estimated peak Contact force based on ASTRA (2008):

$$F_{c,peak} = 2.8t^{-0.5}r^{0.7}E^{0.4}\tan\phi\left(\frac{mv_0^2}{2}\right)^{0.6}$$

$$= 2.8 \times 0.525^{-0.5} \times 0.15^{0.7} \times (1740)^{0.4} \times \tan 40 \times \left(\frac{280 \times 5.24^2}{2000}\right)^{0.6}$$

$$= 38 \text{ kN}$$

References

ASTRA (2008). *Einwirkungen Infolge Steinschlags Auf Schutzgalerien, Richtlinie (Effects of Rockfall on Protection Galleries, Guideline)*. Bundesamt für Strassen ASTRA (Federal Roads Office), Switzerland, 21 p.

JRA (2000). *Manual for Anti-impact Structures against Falling Rock (in Japanese).* Japan Road Association, Japan.

Lam, C. (2016). *A Pilot Study of the Use of Cushioning Materials for Reducing Dynamic Impact Loads on Rigid Debris-resisting Barriers (Technical Note No. TN 5/2016).* Geotechnical Engineering Office, Hong Kong, 70 p.

Lin, Y.L., Yang, G.L., Li, Y. & Zhao, L.H. (2010). Engineering Behaviors of Reinforced Gabion Retaining Wall Based on Laboratory Test. *J. Cent. South Univ. Technol.* 17, 1351-1356

Wong, L.A. & Lam, H.W.K. (2018). *Large-scale Experimental Study of Structural Response of Rigid Barriers Subject to Hard Impacts (Technical Note No. TN 7/2018).* Geotechnical Engineering Office, Hong Kong, 30 p.

Section 7
Appendix C

Details of Computation of Two Degree-of-Freedom Lumped Mass Model

Time step analysis can be used to solve the governing equations of 2DOF model, which has been outlined in Section 3. It can be implemented on computer spreadsheets to predict time histories of contact force and flexural response of barrier. Details of the time step analysis are given below:

Initial Condition (at time $t = 0$)

Immediately prior to boulder impact (at time $t = 0$), the initial condition of the 2DOF system is as follows:

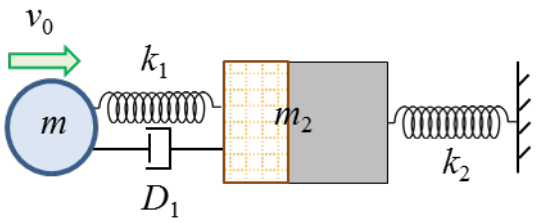

Immediately prior to the impact, the velocity of lump mass m, i.e. the boulder, equals to the boulder impact velocity, i.e.:

$$v_1(0) = v_0$$

There is no initial displacement of lump mass, m at time step $t = 0$, thus:

$$x_1(0) = 0$$

At this stage, there is no indentation. Thus, the shortening of contact spring is:

$$\delta(0) = 0$$

Similarly, the rate of shortening of contact spring is:

$$\dot{\delta}(0) = 0$$

Putting the shortening and the rate of shortening into Hunt & Crossley contact force model (i.e. Equation 3.1), the contact force can be estimated as follows (the expression of k_1 and D_1 is given in Section 7 Appendix A.):

$$F_c(0) = k_1\delta(0) + D_1\delta(0)\dot{\delta}(0) = 0$$

The acceleration of lump mass m can be estimated based on the contact force above:

$$a_1(0) = \frac{-F_c(0)}{\mathrm{m}} = 0$$

On the other hand, there is no flexural deflection of the barrier at this stage. Thus, the displacement of lump mass m_2 is:

$$x_2(0) = 0$$

Immediately prior to the impact, the velocity of lump mass m_2 is zero:

$$v_2(0) = 0$$

Furthermore, there is no boulder impact force on lump mass m_2 (i.e. for estimation of flexural response of the cushioned barrier), i.e.:

$$F_{2DOF}(0) = k_2 x_2(0) = 0 :$$

Hence, the acceleration of lump mass m_2 can be estimated based on dynamic force equilibrium equation (i.e. Equation 3.2), which is also zero:

$$a_2(0) = \frac{F_c(0) - F_{2DOF}(0)}{m_2} = 0$$

Subsequent Time Steps (at time $t = \Delta t$)

The outputs of the previous time step (i.e. $t = 0$) including the displacement, velocity and acceleration of lump mass m and m_2, i.e. $x_1(0)$, $x_2(0)$, $v_1(0)$, $v_2(0)$, $a_1(0)$ and $a_2(0)$, would be used in order to estimate the responses of the boulder, cushion, and the barrier at the next time step (e.g. $t = \Delta t$). Details of calculation for the time step $t = \Delta t$ are given below:

The updated displacement of lump mass, m at time step $t = \Delta t$ is given by:

$$x_1(\Delta t) = x_1(0) + v_1(0)\Delta t$$

Similarly, the updated flexural deflection of the barrier (i.e. displacement of lump mass, m_2) at time step $t = \Delta t$ is given by:

$$x_2(\Delta t) = x_2(0) + v_2(0)\Delta t$$

Using the updated displacement of lump masses m and m_2, the shortening of contact spring can also be updated:

$$\delta(\Delta t) = x_1(\Delta t) - x_2(\Delta t)$$

Meanwhile, the updated velocity of lump mass, m at time step $t = \Delta t$ is given by:

$$v_1(\Delta t) = v_1(0) + a_1(0)\Delta t$$

Similarly, the updated velocity of lump mass, m_2 at time step $t = \Delta t$ is given by:

$$v_2(\Delta t) = v_2(0) + a_2(0)\Delta t$$

Using the updated velocity of lump masses m and m_2, rate of shortening of contact spring can be updated:

$$\dot{\delta}(\Delta t) = v_1(\Delta t) - v_2(\Delta t)$$

Putting the updated shortening and the rate of shortening into Hunt & Crossley contact force model (i.e. Equation 3.1), the contact force can be estimated:

$$F_c(\Delta t) = k_1\delta(\Delta t) + D_1\delta(\Delta t)\dot{\delta}(\Delta t)$$

Then, the acceleration of lump mass m can be updated based on the contact force above:

$$a_1(\Delta t) = \frac{-F_c(\Delta t)}{\mathrm{m}}$$

Meanwhile, the boulder impact force on lump mass m_2 (i.e. for estimation of flexural response of the cushioned barrier) can be updated based on the new flexural deflection of the barrier using Equation 3.3, i.e.:

$$F_{2DOF}(\Delta t) = k_2 x_2(\Delta t)$$

The acceleration of lump mass m_2 can be updated based on dynamic force equilibrium equation (i.e. Equation 3.2):

$$a_2(\Delta t) = \frac{F_c(\Delta t) - F_{2DOF}(\Delta t)}{m_2}$$

The above steps are repeated such that the shortening of the contact spring $\delta(t)$ in a time step is less than zero (i.e. no contact force). The F_{2DOF} (i.e. force contributes to the flexural response of the cushioned barrier) in each time step can then be extracted to produce a force time history, and that the peak F_{2DOF} can be obtained.

Section 7
Appendix D

Verification of Two Degree-of-Freedom Lumped Mass Model

Contents

	Page No.
Contents	327
List of Table	328
List of Figure	329
D.1 Background	330
D.2 Sample calculation for Strike Number 4 in Test Series C2	330
D.3 References	332

List of Table

Table No.		Page No.
D1	Back-Analysis of Test Series C1 & C2 (Strike Nos. 1 to 4) Using 2DOF Model	330

List of Figure

Figure No.		Page No.
D1	Comparison of Deflection-time History of the Crest of the Barrier for Strike No. 4 in Test Series C1	332

D.1 Background

The verification of the 2DOF Model based on the large-scale impact tests conducted by the University of Melbourne is reported in this Appendix. The setup, instrumentation and results of these test were reported in Wong & Lam (2018b) and is briefly described in Section 7 Appendix B. 2DOF model involving time step analyses as discussed in Section 7 Appendix C was used to predict the flexural response of the barrier for each strike under Test Series C1 and C2. The predicted deflection based on the 2DOF model was then compared with the peak flexural deflection measured by laser sensor during the impact test as follows:

Table D1 Back-Analysis of Test Series C1 & C2 (Strike Nos. 1 to 4) Using 2DOF Model

Test Series	Strike Number	Measured Peak Deflection at the Crest of the Barrier (mm)	Predicted Peak Deflection at the Crest of the Barrier (mm)
C1	1 to 3	1.8 - 3.6	4.9
C1	4	1.3	2.7
C2	1 to 3	1.3 - 3.3	3.9
C2	4	2.2	2.7 (See sample calculation in Section D.2 below)

Based on the above comparison, it is demonstrated that the 2DOF model provides conservative predictions of flexural response of rigid barrier protected by rockfill gabions as compared with the experimental results. A sample calculation of the predicted barrier deflection for Strike No. 4 in Test Series C2 is presented below.

D.2 Sample calculation for Strike Number 4 in Test Series C2

A sample calculation of prediction of flexural response of cushioned barrier is demonstrated below, based on the following input data:

Impactor Mass (kg)	435
Radius of Impactor (m)	0.15
Impact velocity, v_0 (m/s)	2.51
Mass of Barrier (kg)	2,484
Thickness of Cushion (m)	0.525
Bulk density of Cushion (kg/m^3)	1450
Cracked Stiffness of the Wall k_2 (kN/m)	14379 Based on moment-curvature analysis. See Wong & Lam (2018b)

Mass ratio, λ_2

The participating mass of barrier, m_B is given by (see Section 7 Appendix B in Wong & Lam (2018a) for detailed derivation of participating mass of barrier):

$$m_B = 0.25 \times 2484 = 621 \text{ kg}$$

Assuming that the boulder impact load could spread behind the gabion cushion at a 20° loading cone as shown below.

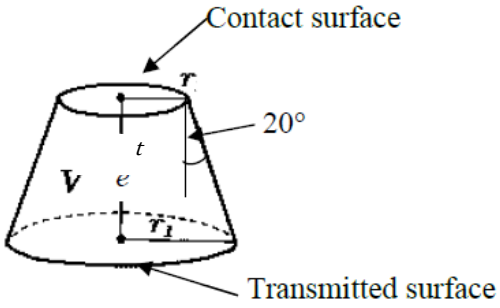

Thus, the radius of area for transmitted surface of impact force, r_1 equals:

$$r_1 = r + t \tan 20° = 0.15 + 0.525 \tan 20° = 0.34 \text{ m}$$

The mass of gabions in the 20° cylinder, m_G is given by:

$$m_G = \frac{1}{3}\pi (r_1^2 + r_1 r + r^2)\, t\rho_G$$

$$m_G = \frac{1}{3}\pi(0.34^2 + 0.34 \times 0.15 + 0.15^2)\,(0.525)(1450) = 151 \text{ kg}$$

Hence, lump mass of gabions and barrier behind the contact spring, m_2, equals:

$$m_2 = m_G + m_B = 151 + 621 = 772 \text{ kg}$$

Mass ratio between cushioned barrier lump mass (m_2) and boulder (m), λ_2 is given by:

$$\lambda_2 = \frac{m_2}{m} = \frac{772}{435} = 1.77$$

Contact Parameters k_1 and D_1

The validity of Equation 2.1 to predict the peak contact force, $F_{c,peak}$, has been studied in Section 7 Appendix B, which provides reasonable estimates of peak contact force in large-scale impact tests of various scales. According to Section 7 Appendix B, the predicted peak contact force is given by:

$$F_{c,peak} = 21 \text{ kN}$$

The stiffness of contact spring, k_1 (for Strike No. 4) is estimated using Equation A.3:

$$k_1 = \frac{F_{c,peak}{}^2}{50 m v_0{}^2}\left(\frac{1+\lambda_2}{\lambda_2}\right) = \frac{(21 \times 1000)^2}{50 \times 435 \times 2.51^2}\left(\frac{1+1.77}{1.77}\right) = 4813 \text{ N/m}$$

The damping coefficient, D_1 (for Strike No. 1) is estimated using Equation A.2:

$$D_1 = 148.5\frac{k_1}{v_0} = 148.5\left(\frac{4813}{2.51}\right) = 284753 \ \frac{\text{kg}}{\text{m s}}$$

Time step analyses using the same steps as discussed in Section 7 Appendix C were conducted. The predicted peak flexural deflection based on 2DOF analysis was found to be 2.7 mm. The predicted time history of flexural deflection was compared with the experimental results as given below.

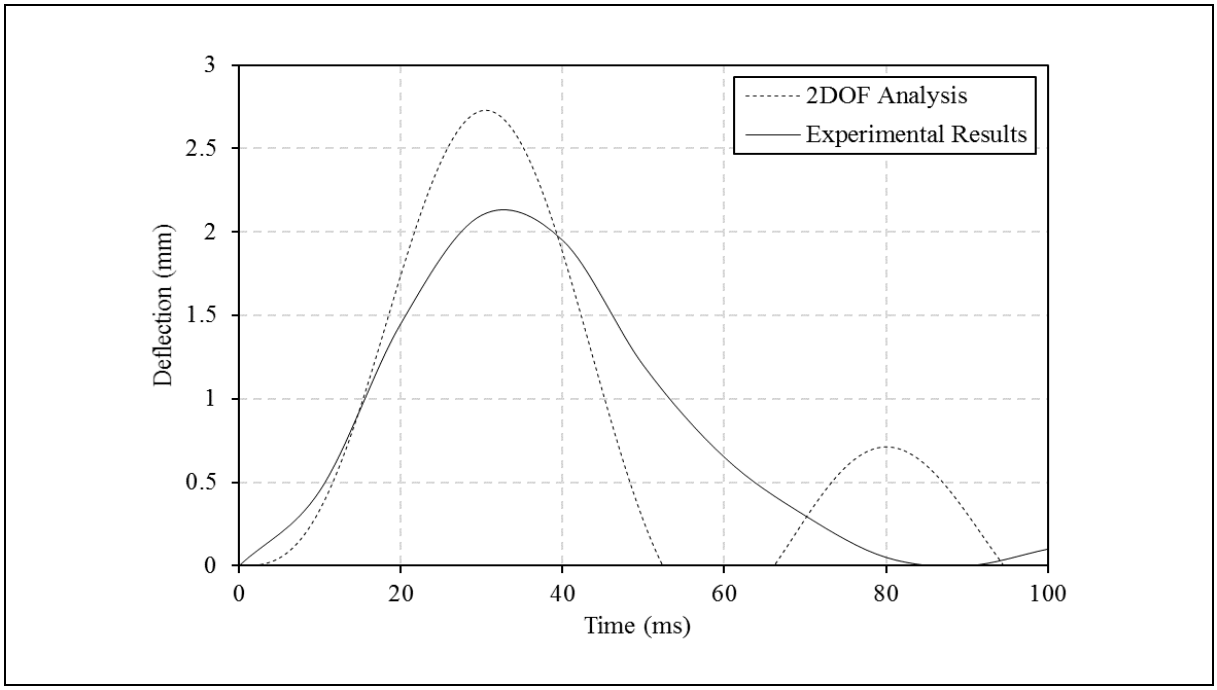

Figure D1 Comparison of Deflection-time History of the Crest of the Barrier for Strike No. 4 in Test Series C1

D.3 References

Wong, L.A. & Lam, H.W.K. (2018a). *Study of Flexural Response of Rigid Barriers subject to Boulder Impact (Technical Note No. TN 3/2018).* Geotechnical Engineering Office, Hong Kong, 40 p.

Wong, L.A. & Lam, H.W.K. (2018b). *Large-scale Experimental Study of Structural Response of Rigid Barriers Subject to Hard Impacts (Technical Note No. TN 7/2018).* Geotechnical Engineering Office, Hong Kong, 30 p.

Section 7
Appendix E

Worked Example

Contents

	Page No.
Contents	334
E.1 Background	335
E.2 Parameters for 2DOF Analysis	335
E.3 2DOF Analysis	337
E.4 Reference	340

E.1 Background

One of the sensitivity studies in Section 4.1 is taken as an example for demonstrating the calculation procedures for the estimation of reduction in flexural response offered by rockfill gabions. Some of the parameters are listed in table below.

Impactor Mass (kg)	1388
Radius of Impactor (m)	0.5
Impact velocity, v_0 (m/s)	6
Barrier length (m)	10
Barrier height (m)	5.5
Barrier thickness (m)	0.8
Mass of Barrier (kg)	105600
Cushioning Material	Rockfill Gabions
Thickness of Cushion (m)	1
Bulk density of Cushion (kg/m^3)	1450
Cracked Stiffness of the Wall k_2 (kN/m)	68192 Based on moment-curvature analysis. See Wong & Lam (2018)
Young's modulus of Cushion (kPa)	1740 (See Section 7 Appendix B)
Friction angle of Rockfill (deg)	40

E.2 Parameters for 2DOF Analysis

The participating mass of barrier, m_B is given by (see Section 7 Appendix B in Wong & Lam (2018) for detailed derivation of participating mass of barrier):

$$m_B = 0.25 \times 105600 = 26400 \text{ kg}$$

Assuming that the boulder impact load could spread behind the gabion cushion at a 20° loading cone as shown below.

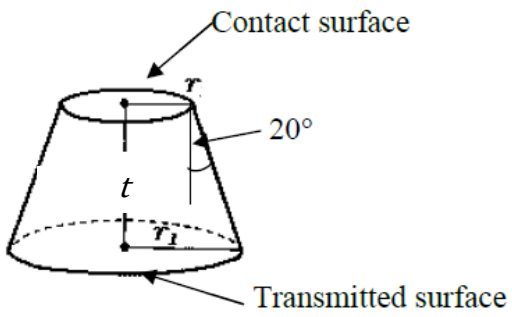

Thus, the radius of area for transmitted surface of impact force, r_1 equals:

$$r_1 = r + t\tan 20° = 0.5 + 1 \times \tan 20° = 0.864 \text{ m}$$

The mass of gabions in the 20° cylinder, m_G is given by:

$$m_G = \frac{1}{3}\pi({r_1}^2 + r_1 r + r^2)t\rho_G$$
$$= \frac{1}{3}\pi(0.864^2 + 0.864 \times 0.5 + 0.5^2)(1)(1450) = 2169 \text{ kg}$$

Hence, lump mass of gabions and barrier behind the contact spring, m_2 equals:

$$m_2 = m_G + m_B = 2169 + 26400 = 28569 \text{ kg}$$

Mass ratio between cushioned barrier lump mass and boulder, λ_2 is given by:

$$\lambda_2 = \frac{m_2}{m} = \frac{28569}{1388} = 21$$

The peak contact force, $F_{\text{c,peak}}$, is estimated using Equation 2.1, which was validated in Section 7 Appendix B:

$$F_{\text{c,peak}} = 2.8(1)^{-0.5}(0.5)^{0.7}(1740)^{0.4}(\tan 40)\left(\frac{1388 \times 6^2}{2000}\right)^{0.6} = 197 \text{ kN}$$

The stiffness of contact spring, k_1, is estimated using the above peak contact force and Equation A.3 as follows:

$$k_1 = \frac{{F_{\text{c,peak}}}^2}{50m{v_0}^2}\left(\frac{1+\lambda_2}{\lambda_2}\right) = \frac{(197 \times 1000)^2}{50 \times 1388 \times 6^2}\left(\frac{1+21}{21}\right) = 16333 \text{ N/m}$$

The damping coefficient, D_1, is estimated using the above k_1 and Equation A.2 as follows:

$$D_1 = 148.5\frac{k_1}{v_0} = 148.5\frac{16333}{6} = 404242 \text{ kg/m s}$$

E.3 2DOF Analysis

The basic inputs of time step analysis are summarised as follows:

m (kg)	1,388
m_2 (kg)	28,569
v_0 (m/s)	6
k_1 (N/m)	16,333
D_1 (kg/m s)	404,242
k_2 (kN/m)	68,192

Using the above data, time step analysis following the steps given in Section 7 Appendix C is performed:

Initial Condition (at time $t = 0$)

Immediately prior to boulder impact (at time $t = 0$), the initial condition of the 2DOF system is as follows:

Immediately prior to the impact, the velocity of lump mass m, i.e. the boulder, equals to the boulder impact velocity, i.e.:

$$v_1(0) = v_0 = 6 \text{ m/s}$$

There is no initial displacement of lump mass, m at time step $t = 0$, thus:

$$x_1(0) = 0$$

At this stage, there is no indentation. Thus, the shortening of contact spring is:

$$\delta(0) = 0$$

Similarly, the rate of shortening of contact spring is:

$$\dot{\delta}(0) = 0$$

Putting the shortening and the rate of shortening into Hunt & Crossley contact force model (i.e. Equation 3.1), the contact force can be estimated as follows (the expression of k_1 and D_1 is given in Section 7 Appendix A.):

$$F_c(0) = k_1\delta(0) + D_1\delta(0)\dot{\delta}(0) = 0$$

The acceleration of lump mass m can be estimated based on the contact force above:

$$a_1(0) = \frac{-F_c(0)}{\text{m}} = 0$$

On the other hand, there is no flexural deflection of the barrier at this stage. Thus, the displacement of lump mass m_2 is:

$$x_2(0) = 0$$

Immediately prior to the impact, the velocity of lump mass m_2 is zero:

$$v_2(0) = 0$$

Furthermore, there is no boulder impact force on lump mass m_2 (i.e. for estimation of flexural response of the cushioned barrier), i.e.:

$$F_{2DOF}(0) = k_2 x_2(0) = 0 :$$

Hence, the acceleration of lump mass m_2 can be estimated based on dynamic force equilibrium equation (i.e. Equation 3.2), which is also zero:

$$a_2(0) = \frac{F_c(0) - F_{2DOF}(0)}{m_2} = 0$$

Subsequent Time Steps (at time $t = \Delta t = 0.00001$)

The updated displacement of lump mass, m at time step $t = 0.00001$ is given by:

$$x_1(0.00001) = x_1(0) + v_1(0) \text{ x } 0.00001 = 0 + 6 \text{ x } 0.00001 = 0.00006 \text{ m}$$

Similarly, the updated flexural deflection of the barrier (i.e. displacement of lump mass, m_2) at time step $t = \Delta t$ is given by:

$$x_2(0.00001) = x_2(0) + v_2(0) \text{ x } 0.00001 = 0$$

Using the updated displacement of lump masses m and m_2, the shortening of contact spring can also be updated:

$$\delta(0.00001) = x_1(0.00001) - x_2(0.00001) = 0.00006 - 0 = 0.00006 \text{ m}$$

Meanwhile, the updated velocity of lump mass, m at time step $t = \Delta t$ is given by:

$$v_1(0.00001) = v_1(0) + a_1(0) \text{ x } 0.00001 = 6 + 0 = 6 \text{ m/s}$$

Similarly, the updated velocity of lump mass, m_2 at time step $t = \Delta t$ is given by:

$$v_2(0.00001) = v_2(0) + a_2(0) \text{ x } 0.00001 = 0 \text{ m/s}$$

Using the updated velocity of lump masses m and m_2, rate of shortening of contact spring can be updated:

$$\dot{\delta}(0.00001) = v_1(0.00001) - v_2(0.00001) = 6 - 0 = 6 \text{ m/s}$$

Putting the updated shortening and the rate of shortening into Hunt & Crossley contact force model (i.e. Equation 3.1), the contact force can be estimated:

$$F_c(0.00001) = k_1\delta(0.00001) + D_1\delta(0.00001)\dot{\delta}(0.00001)$$
$$= 16333 \text{ x } 0.00006 + 404242 \text{ x } 0.00006 \text{ x } 6 = 147 \text{ N}$$

Then, the acceleration of lump mass m can be updated based on the contact force above:

$$a_1(0.00001) = \frac{-F_c(0.00001)}{\text{m}} = \frac{-147}{1388} = -0.106\frac{\text{m}}{s^2}$$

Meanwhile, the boulder impact force on lump mass m_2 (i.e. for estimation of flexural response of the cushioned barrier) can be updated based on the new flexural deflection of the barrier using Equation 3.3, i.e.:

$$F_{2DOF}(0.00001) = k_2 x_2(0.00001) = 0$$

The acceleration of lump mass m_2 can be updated based on dynamic force equilibrium equation (i.e. Equation 3.2):

$$a_2(0.00001) = \frac{F_c(0.00001) - F_{2DOF}(0.00001)}{m_2}$$

$$a_2(0.00001) = \frac{147 - 0}{28569} = 0.0051\frac{m}{s^2}$$

The above analysis has been repeated for each time step (time interval taken as 0.00001 s) using a computer spreadsheet. The result, in terms of the time history of flexural deflection of the barrier (x_2) during the first 200 ms, is plotted below.

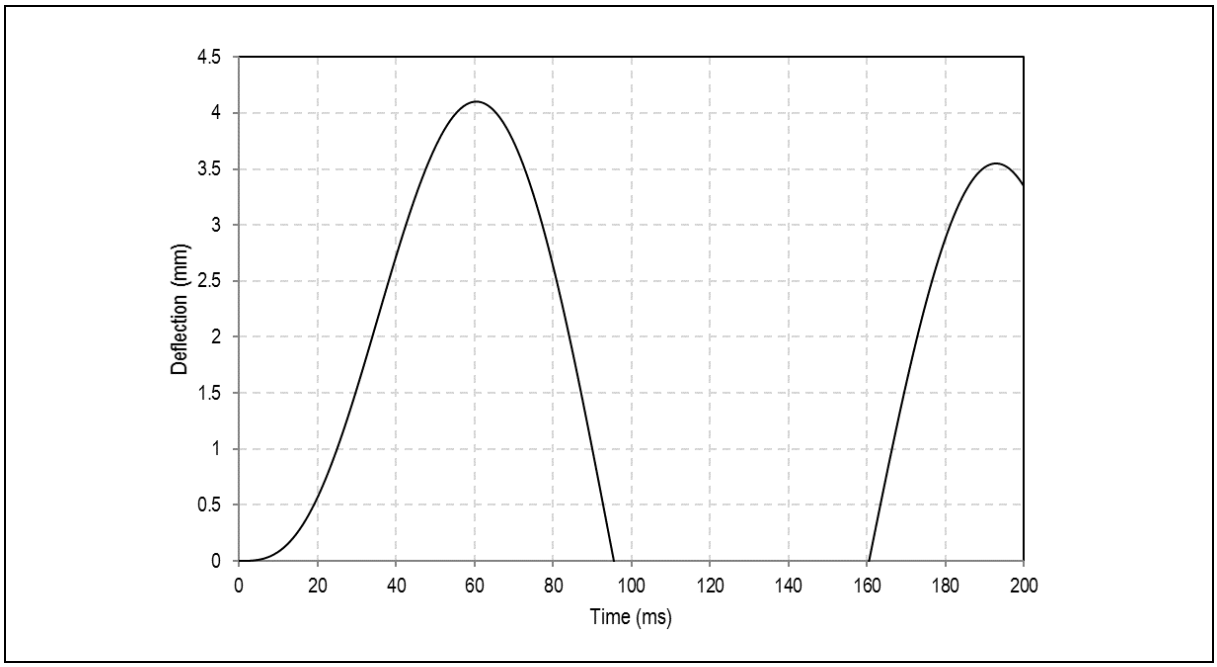

The peak deflection is 4.1 mm (i.e. at 60 ms after the contact process). The predicted boulder impact force based on 2DOF analysis, F_{2DOF}, is the multiple of the peak deflection and the flexural stiffness of the barrier which equals 280 kN.

The flexural response of the same rigid barrier (without cushion) under the same impact scenario is estimated using the Enhanced Flexural Stiffness Method (Wong & Lam, 2018) and equals 7.7 mm. The corresponding predicted boulder impact force, F_{EFSM}, equals 523 kN.

The reduction of flexural response based on 2DOF Model is thus about 46%.

E.4 Reference

Wong, L.A. & Lam, H.W.K. (2018). *Study of Flexural Response of Rigid Barriers Subject to Boulder Impact (Technical Note No. TN 3/2018).* Geotechnical Engineering Office, Hong Kong, 40 p.

Part 3

Detailing for Deflector

[Blank Page]

Section 8:
Spillage Mechanism of Landslide Debris Intercepted by Rigid Barriers and Deflectors to Prevent Spillage

L.A. Wong & H.W.K. Lam

This section is largely based on GEO Technical Note No. TN 5/2018 produced in November 2018

Foreword

This Technical Note summarises findings of a study on the spillage mechanism of landslide debris intercepted by rigid barriers. Potential refinements of existing design guidance for deflector at barrier crest to prevent spillage have been discussed. This study was carried out by Mr L.A. Wong under the supervision of Mr H.W.K. Lam in collaboration with Dr C.E. Choi from the Hong Kong University of Science and Technology (HKUST). The Drafting Unit of the Standards and Testing Division assisted in formatting this Note.

Professor C.W.W. Ng and Dr C.E. Choi of the HKUST and various colleagues in the GEO provided constructive comments. All contributions are gratefully acknowledged.

J.S.H. Kwan
Chief Geotechnical Engineer/Standards and Testing
November 2018

Abstract

This study aims to improve understanding on the spillage mechanism for landslide debris impacting onto rigid barriers, to evaluate the effectiveness of the use of deflectors to prevent spillage of landslide debris and to optimize the geometrical requirements of the deflector. The study comprises a literature review, a series of laboratory flume tests and a large-scale flume test. The laboratory flume tests and the large-scale flume test were carried out by the Hong Kong University of Science and Technology. Potential refinements of existing design guidance for deflectors to prevent spillage have been discussed.

Contents

		Page No.
Title Page		343
Foreword		344
Abstract		345
Contents		346
List of Tables		348
List of Figures		349
1	Background	350
2	Current Design Practice to Prevent Spillage of Landslide Debris in Rigid Barriers	350
3	Laboratory Flume Tests	352
3.1	General	352
3.2	Laboratory Test Setup	352
3.3	Instrumentation	354
3.4	Test Program	354
4	Laboratory Flume Tests to Study Spillage Mechanism	354
4.1	General Observations	354
4.2	Model Barrier with Gabion	357
4.3	Dry Sand Flow	358
5	Geometrical Requirements of Deflectors	358
6	Landslide Debris Run-up Height	359
6.1	Laboratory Flume Tests	359
6.2	Large-scale Flume Test	360
7	Potential Refinements of Technical Guidance for Deflector Design	362
8	Conclusion	363
9	References	363

		Page No.
Section 8 Appendix A:	Video of a Debris Flow Occurred in Susten, Switzerland in 2018	365
Section 8 Appendix B:	Videos of Laboratory Flume Tests and Large-scale Flume Test	367

List of Tables

Table No.		Page No.
3.1	Summary of the Instrumentations of the Laboratory Flume Tests	354
4.1	Summary of 13 Nos. of Laboratory Flume Tests (i.e. Series A) to Study Spillage Mechanism	355
5.1	Summary of 9 Nos. of Laboratory Flume Tests (i.e. Series B) to Study Geometrical Requirement of a Deflector	358
6.1	Summary of the Run-up Heights in Laboratory Flume Test Nos. S1 to S13	360
6.2	Summary of the Run-up Heights in Large-scale Flume Test No. L1	361

List of Figures

Figure No.		Page No.
1.1	Example of a Deflector Constructed in Bowen Road	350
2.1	Details of Deflector Recommended by Kwan (2012)	351
2.2	Photographs Showing the Construction of a Deflector	351
3.1	Example of a Seawall Recurve and the Associated Laboratory-scale Experiment (Schoonees, 2014)	352
3.2	Overview, Section and Plan View of the Setup of Laboratory Flume Test Facility in the HKUST (HKUST, 2018)	353
4.1	Observed Spillage Mechanism for Water Flow Test (Test No. S1)	356
4.2	PIV Analysis of Spillage Mechanism for Water Flow Test (Test No. S1)	356
4.3	Observed Spillage of Hard Inclusion (Test No. S7)	357
4.4	Observed Spillage Mechanism of Water Flow with a Model Gabion (Test No. S2)	357
4.5	Observed Deposition Mechanism of Dry Sand Flow (Test No. S4)	358
5.1	Deflector (L/H_{Max} = 0.5) Effectively Prevented Spillage of Water (with hard inclusion) to Downstream Area (Test No. D9)	359
5.2	PIV Analysis Showing a Deflector (L/H_{Max} = 0.5) Effectively Prevented Spillage of Water to Downstream Area (Test No. D6)	359
6.1	Snapshots Showing (a) the Test Setup, (b) the Model Barrier and (c) & (d) the Run-up of Debris in Large-scale Flume Test (Test No. L1)	361
7.1	Potential Refinement of Design Guidance - Details of Deflectors	362

1 Background

A debris flow impacting onto a rigid barrier can lead to run-up of debris mass along the stem of the barrier wall. A video footage in Youtube (see Section 8 Appendix A) captured a debris flow occurred in Susten, Switzerland in 2018, where the run-up height of the landslide debris was significant, and the run-up debris could affect facilities adjacent to the obstruction which intercepts the debris flow. Lo (2000) and CAGHP (2018) stated that the height of a rigid barrier should be designed to account for the possibility of run-up of the debris. Kwan (2012) suggested the use of a deflector installed at the crest of a rigid barrier to prevent possible spillage of landslide debris. An example of a deflector constructed at the crest of a rigid barrier in Hong Kong is shown in Figure 1.1 below.

Figure 1.1 Example of a Deflector Constructed in Bowen Road

The Geotechnical Engineering Office (GEO) has initiated a study on the use of deflectors to prevent spillage of debris materials. This Technical Note summarises the findings of this study, which aims (1) to investigate the spillage mechanism for landslide debris when it impacts onto a rigid barrier, (2) evaluate the effectiveness of the use of a deflector to prevent spillage of landslide debris and (3) optimize the geometrical requirements of the deflector. The study comprises a review of local and overseas literature and design guidelines, a series of laboratory flume tests and a large-scale flume test. Potential refinements of existing design guidance for deflectors are discussed.

2 Current Design Practice to Prevent Spillage of Landslide Debris in Rigid Barriers

Overseas design guidance documents of landslide debris-resisting rigid barriers, including VanDine (1996), SWCB (2005), NILIM (2007), CAGHP (2018), ASI (2011; 2013) and MLR (2006), do not provide much details on the use of deflectors, probably due to the fact that the barriers concerned are normally located far from settlements in other regions.

Local design guidance (Kwan, 2012) suggests that the height of a rigid barrier should be checked against the debris run-up height. If the predicted run-up height is greater than the height of the rigid barrier, a deflector should be provided at the crest of the rigid barrier, so as to help deflecting the run-up debris backwards to the retention basin, and to avoid spillage of landslide debris to the downstream areas. The inclination of a deflector is recommended to be less than 45° whereas its horizontal projected length (denoted as L in Figure 2.1) should be at least equal to the maximum debris flow depth (denoted as H_{Max} in Figure 2.1).

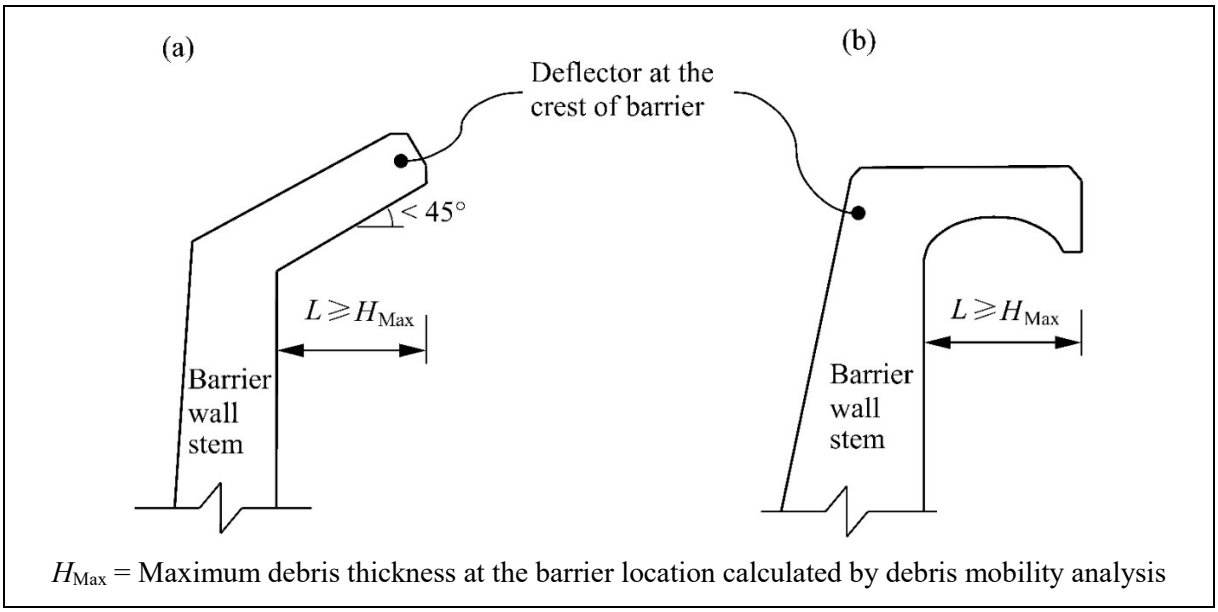

Figure 2.1 Details of Deflector Recommended by Kwan (2012)

Local experiences show that construction of a deflector could be difficult and involves substantial temporary works as shown in Figure 2.2. There is a need to better understand the spillage mechanism and to explore the possibility of optimising the geometrical requirements of a deflector.

Figure 2.2 Photographs Showing the Construction of a Deflector

3 Laboratory Flume Tests

3.1 General

Literatures which study the spillage mechanism of landslide debris intercepted by rigid barriers and the effectiveness of deflector are limited. The Hong Kong University of Science and Technology (HKUST) was commissioned by the GEO to carry out a series of laboratory flume tests as well as a large-scale flume test for this study. The latter was carried out at the Kadoorie Centre. This Study aims to collect quality test data to better understand the spillage mechanism, and evaluate the effectiveness of deflectors in different geometries (i.e. required length and inclination). The use of laboratory flume tests is a common research approach adopted in port works engineering for the design of a seawall recurve, as shown in Figure 3.1, which is similar in nature as compared with a deflector on a rigid barrier (Cornett et al, 1999; Van Doorslaer & De Rouck, 2010; Schoonees, 2014; Ng et al, 2017; Choi et al, 2015; Choi et al, 2016).

Figure 3.1 Example of a Seawall Recurve and the Associated Laboratory-scale Experiment (Schoonees, 2014)

3.2 Laboratory Test Setup

The laboratory test setup involved a 5 m long flume at a gradient of 26°. Such channel gradient could produce a flow with a Froude number (Hübl et al, 2009) of about 5, which is similar to debris flows scenarios in Hong Kong. The flume was formed with transparent acrylic boards. It had an uniform rectangular cross-section, which was 0.2 m wide and 0.5 m deep. The inclined flume transited into a 250 mm long deposition platform via a curvilinear transition in order to avoid energy dissipation caused by an abrupt change of channel gradient. A 225 mm high model barrier (see Figure 3.2) was installed at the deposition platform to receive strike from the debris flows. The height of the model barrier would yield a ratio between the barrier height and the debris flow depth of about 10, which is comparable to those commonly encountered in routine design. A storage container was provided at the top of the flume with a maximum storage capacity of 0.08 m^3, where the source material was retained by an air-pressurised gate which was controlled by a hydraulic actuator. Details of the flume are shown in Figure 3.2.

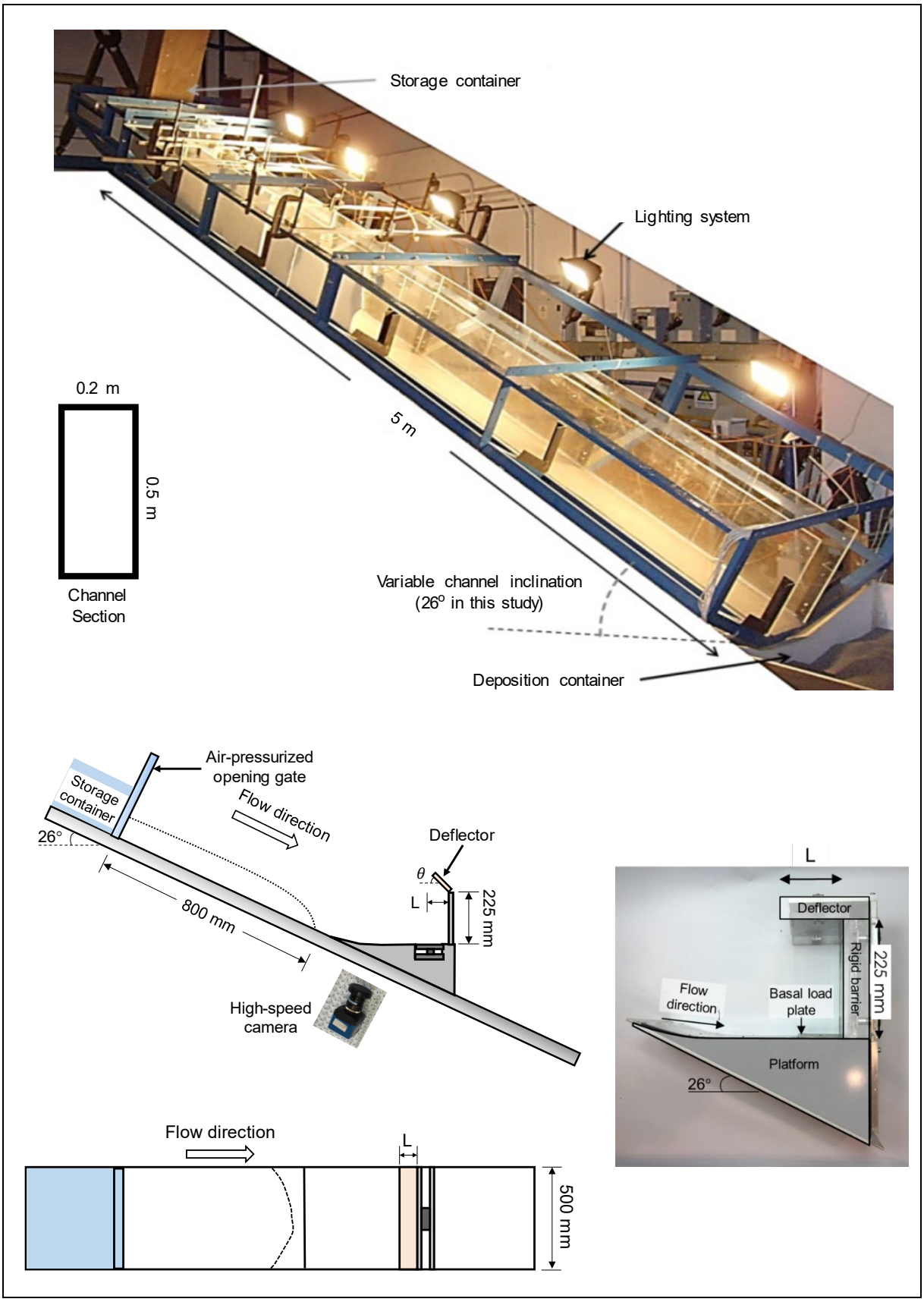

Figure 3.2 Overview, Section and Plan View of the Setup of Laboratory Flume Test Facility in the HKUST (HKUST, 2018)

3.3 Instrumentation

The instrumentation for the laboratory tests comprised a laser sensor and a high speed camera (see Table 3.1). The dynamics of the debris was interpreted using Particle Image Velocimetry (PIV) analysis (White et al, 2003; Ng et al, 2017), from which the flow kinematics including the velocity field could be obtained.

Table 3.1 Summary of the Instrumentations of the Laboratory Flume Tests

Instruments (Location of the Instrument)	Specification	Measurement
Laser Sensor (Above the centerline of the flume, and approx. 80 mm upstream of the model barrier)	Range: 300 - 600 mm	Flow depth (for test of dry sand only)
High-speed camera (At the side of the flume)	1696 × 1710 pixels (Operating at 200 frames per second)	Flow kinematics; Flow depth of debris other than dry sand; Flow velocity & Run-up height

Note: Laser sensor for the measurement of flow depth is of a better accuracy than that measured by high-speed camera. Nevertheless, laser could penetrate water which renders the use of laser sensor to measure the flow depth of water unsuitable. Therefore, high-speed camera was adopted to measure the flow depth of water flow.

3.4 Test Program

Twenty two nos. of laboratory flume tests were carried out. 13 nos. of these tests were carried out using a model barrier without any deflector (i.e. Series A). These tests served to study the spillage mechanism of different debris materials. The remaining 9 nos. of tests were carried out using a model barrier with a deflector, where different combinations of length and inclination of the deflector were used in the tests (i.e. Series B). The latter series of tests aims to evaluate the effectiveness of the deflectors in preventing spillage of debris.

All 22 nos. of tests were conducted using the same debris source volume of 0.011 m^3.

4 Laboratory Flume Tests to Study Spillage Mechanism

4.1 General Observations

For the 13 nos. of tests in Series A (i.e. model barriers without a deflector), different types of materials were adopted to simulate debris, including pure water, water mixed with glass beads, water mixed with aggregates, water mixed with 40% to 60% Toyoura Sand (by volume) of particle size ranging from 0.1 mm to 0.4 mm, water mixed with 40% to 60% completely decomposed granite, and dry Leighton Buzzard Fraction C sand (denoted as LBC sand) of particle size ranging from 0.3 mm to 0.6 mm. The flow characteristics, including the flow depth and the flow velocity, obtained in each test are summarised in Table 4.1 below.

Table 4.1 Summary of 13 Nos. of Laboratory Flume Tests (i.e. Series A) to Study Spillage Mechanism

Test No.	Debris Material		Maximum Flow Depth [(1)] (mm)	Observed Frontal Velocity [(2)] (m/s)	Remarks
S1	100% Water		21.5 - 24.5	2.3 - 3.1	-
S2			22.5 - 25.5	1.8 - 2.6	With 15 mm thick model Gabion infilled with 5 - 10 mm diameter aggregates
S3	90% Water	Glass beads (23 mm)	41.5 - 44.5	2.2 - 3.0	
S4	100% LBC Sand	-	22.6 - 23.4	1.7 - 2.5	-
S5	90% Water	10% Glass beads (39 mm)	38.5 - 41.5	2.1 - 2.9	
S6	90% Water	10% Glass beads (23 mm)	40.5 - 43.5	2.2 - 3.0	
S7	90% Water	10% Aggregate (39 mm)	40.5 - 43.5	2.3 - 3.1	
S8	40% Water	60% CDG	24.5 - 27.5	2.4 - 3.2	
S9	50% Water	50% CDG	21.5 - 24.5	1.8 - 2.4	
S10	60% Water	40% CDG	29.5 - 32.5	2.1 - 2.9	
S11	40% Water	60% Toyoura Sand	23.5 - 26.5	2.3 - 3.1	
S12	50% Water	50% Toyoura Sand	29.5 - 32.5	2.0 - 2.8	
S13	60% Water	40% Toyoura Sand	17.5 - 20.5	2.3 - 3.1	

Notes: [(1)] Accuracy: ± 0.4 mm (for Test S4) & ± 1.5 mm (for the other tests).
[(2)] Accuracy: ± 0.4 m/s.

Figures 4.1 and 4.2 show the debris run-up and the corresponding PIV analysis in the water flow test (i.e. Test No. S1). It was found that upon impacting the model barrier, the frontal debris materials were deflected upwards along the vertical stem of the model barrier. The frontal debris materials continued to travel upwards until it attained its maximum run-up height. The debris materials then descended vertically downwards under gravity and interacted with the upward jet of the subsequent flow. This interaction resulted in a lateral spreading of the debris, causing some debris overtopped the model barrier (see Figure 4.2).

Similar spillage mechanism was observed for the other debris materials used in Test Nos. S2 to S13, except Test No. S4. Test No. S4 involved a dry sand flow where no materials ran-up beyond the crest of the model barrier. Further details of the deposition mechanism for this test are given in Section 4.3.

It is worth-mentioning that, for debris flow tests with hard inclusions (i.e. Test Nos. S3, S5 to S7), some hard inclusions were displaced up and overtopped the model barrier (Figure 4.3).

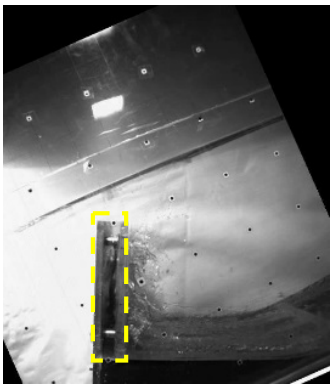

(1) Run-up of water against the barrier (t = 0.375 s)

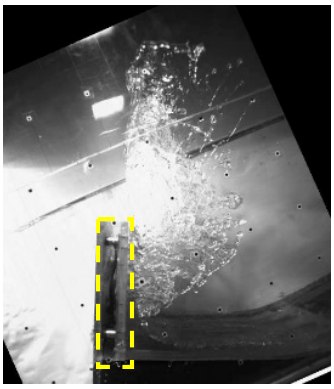

(2) Water ran-up beyond the barrier crest (t = 0.630 s)

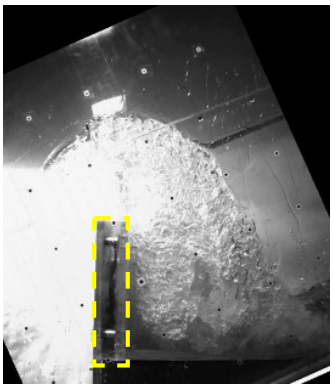

(3) Lateral splashing and water overtopped the barrier (t = 1.150 s)

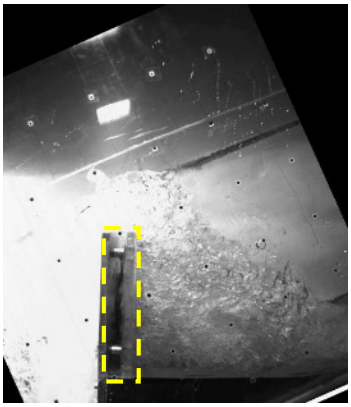

(4) Spillage continued (t = 1.330 s)

Note: See Section 8 Appendix B for video of Test No. S1.

Figure 4.1 Observed Spillage Mechanism for Water Flow Test (Test No. S1)

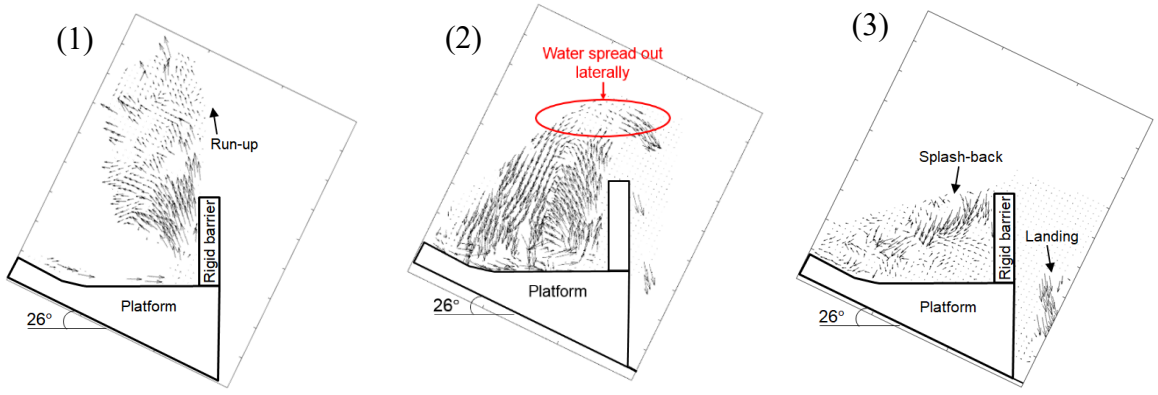

Figure 4.2 PIV Analysis of Spillage Mechanism for Water Flow Test (Test No. S1)

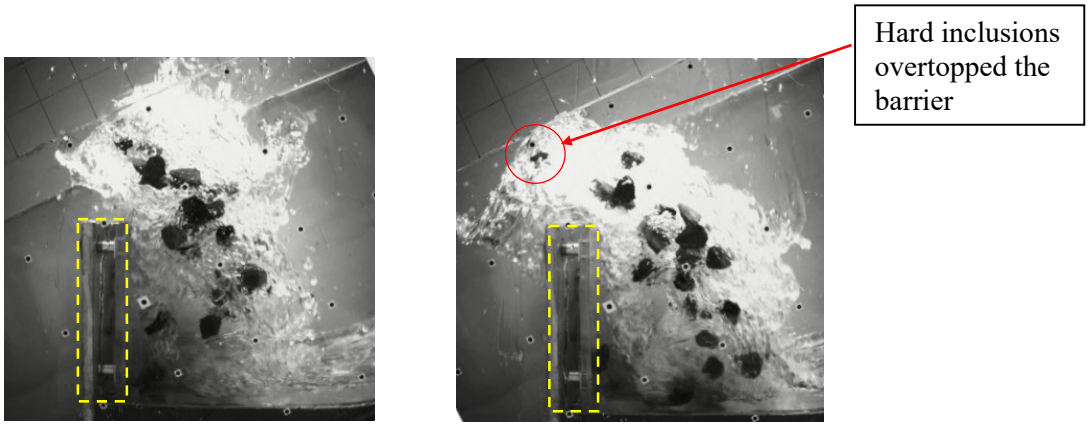

Note: See Section 8 Appendix B for video of Test No. S7.

Figure 4.3 Observed Spillage of Hard Inclusion (Test No. S7)

4.2 Model Barrier with Gabion

In Hong Kong, rockfill gabion is commonly used to protect the wall stem of rigid barriers. In order to better simulate the actual field condition, the effect of gabion on the spillage mechanism was also studied. Two tests (i.e. Test Nos. S2 and S3) involved a barrier wall with a model gabion (see Figure 4.4). For these two tests, similar spillage mechanism as that observed for flows onto a bare model barrier was observed (see Section 4.1). However, the observed run-up height of the debris was found slightly lower (approx. 20%) as compared to those tests without gabion. The reduced run-up height was probably caused by the surface roughness of the gabion which could have retarded the run-up velocity of the debris flows.

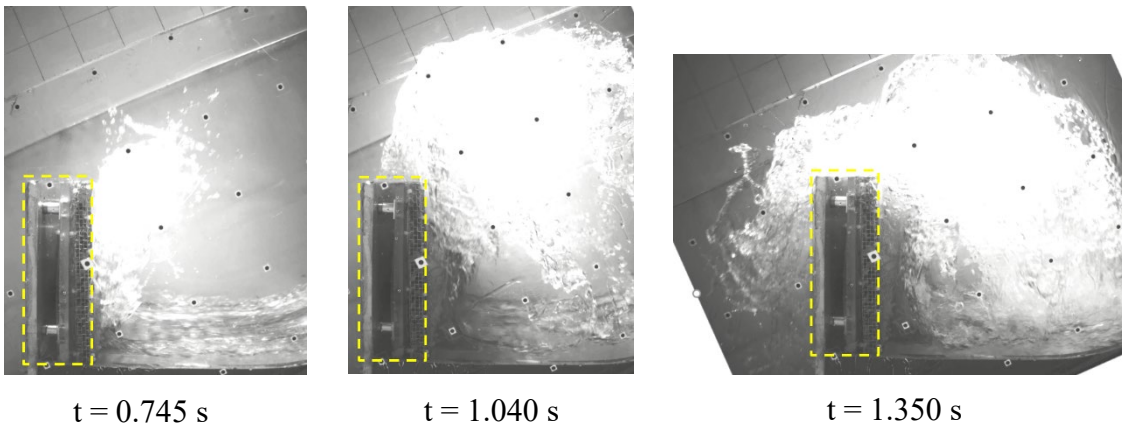

Figure 4.4 Observed Spillage Mechanism of Water Flow with a Model Gabion (Test No. S2)

4.3 Dry Sand Flow

No spillage was observed for dry sand flow because it exhibited a different deposition mechanism. Instead of the rapid run-up mechanism as observed in the other tests, the dry sand was deposited gradually behind the barrier without reaching the crest of the model barrier (see Figure 4.5).

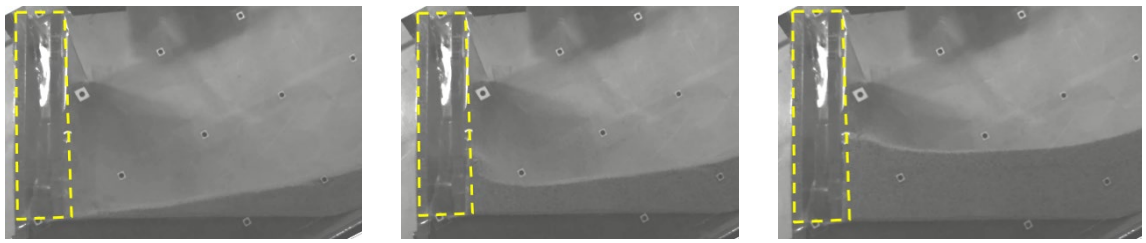

t = 0.295 s t = 0.380 s t = 0.515 s

Note: See Section 8 Appendix B for video of Test No. S4.

Figure 4.5 Observed Deposition Mechanism of Dry Sand Flow (Test No. S4)

5 Geometrical Requirements of Deflectors

Nine nos. of debris impact tests (i.e. Test No. D1 to D9 under Series B) were carried out using the same model barrier as given in Section 3 with a deflector of different geometries as shown in Table 5.1. Water was used to simulate debris flows in order to produce a higher flow mobility. A summary of the test results is shown in Table 5.1 below.

Table 5.1 Summary of 9 Nos. of Laboratory Flume Tests (i.e. Series B) to Study Geometrical Requirement of a Deflector

Test No.	Inclination to the Horizontal	Ratio of Horizontal Projected Length to Debris Flow Depth, L/H_{Max}	Flow Material	Video
D1	0°	4	Water	-
D2	45°	4	Water	-
D3	0°	2	Water	-
D4	45°	2	Water	-
D5	0°	1	Water	See Section 8 Appendix B
D6	0°	0.5	Water	
D7	45°	0.5	Water	
D8	0°	0.25	Water	
D9	0°	0.5	Water with 39 mm Glass beads	

The results showed that a deflector with a ratio between horizontal projected length (L) and maximum flow depth (H_{Max}) of 0.5 could adequately prevent spillage of the debris materials from the barriers (see Figures 5.1 and 5.2). In the case of a deflector with L/H_{Max} of 0.25, some limited spillage was observed (see the video capturing Test No. D8).

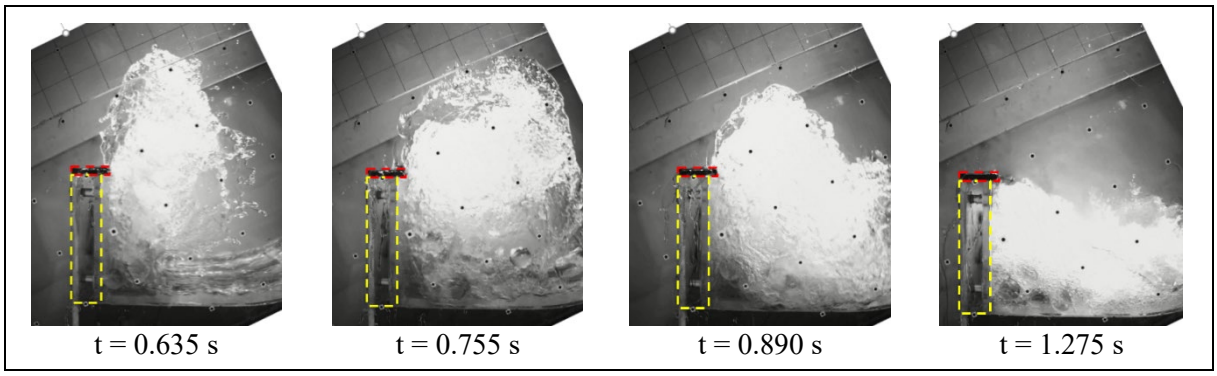

Figure 5.1 Deflector (L/H_{Max} = 0.5) Effectively Prevented Spillage of Water (with hard inclusion) to Downstream Area (Test No. D9)

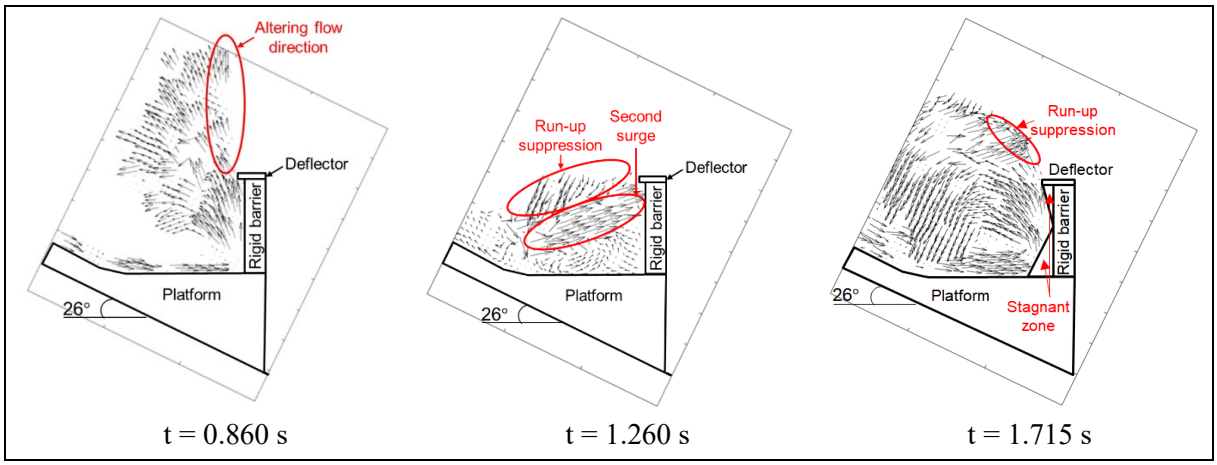

Figure 5.2 PIV Analysis Showing a Deflector (L/H_{Max} = 0.5) Effectively Prevented Spillage of Water to Downstream Area (Test No. D6)

6 Landslide Debris Run-up Height

6.1 Laboratory Flume Tests

An attempt was made to study the prediction model for run-up heights of a debris flow. Details of the laboratory flume tests, including test setup, instrumentation and test plan, are given in Section 3. The observed run-up height from the laboratory flume tests, which is defined as the maximum level of splashing, for these tests are given in Table 6.1.

Based on the current design guideline (Kwan, 2012), it is recommended that (1) the Energy Model, and (2) the Momentum Jump Model (Hákonardóttir, 2003; Jóhannesson et al, 2009) shall be used to predict the run-up height of the debris when hitting a barrier.

Literature review indicated that the run-up mechanism of a debris flow is complex and is sensitive to many factors such as debris composition, flow kinematics (e.g. flow depth and velocity), degree of lateral confinement along the run-up path (Ng et al, 2017; Iverson et al, 2016; Song et al, 2017). Based on the current laboratory flume tests, the predicted run-up heights based on the Energy Model with the incorporation of maximum debris flow depth provide a reasonable upper bound of the observed experimental results.

The Momentum Jump Model appears to under-predict the run-up heights measured in the tests of this study (see Table 6.1). This model calculates run-up height with consideration given to material compressibility may not describe the observed run-up process in the tests.

Table 6.1 Summary of the Run-up Heights in Laboratory Flume Test Nos. S1 to S13

Test No.	Observed Run-up (i.e. Max. level of splashing) (mm)	Maximum Flow Depth, i.e. H_{Max} (mm)	Observed Frontal Velocity, i.e. v (m/s)	Predicted Run-up based on Energy Model (mm)	Predicted Run-up based on Momentum Jump Model (mm)
S1	544	21.5 - 24.5	2.3 - 3.1	291 - 514	173 - 223
S2	427	22.5 - 25.5	1.8 - 2.6	188 - 370	141 - 195
S3	362	41.5 - 44.5	2.2 - 3.0	288 - 503	237 - 303
S4	(dry sand flow with no run-up observed, see Section 4.3)	22.6 - 23.4	1.7 - 2.5	170 - 342	136 - 179
S5	450	38.5 - 41.5	2.1 - 2.9	263 - 470	219 - 282
S6	466	40.5 - 43.5	2.2 - 3.0	287 - 502	231 - 296
S7	523	40.5 - 43.5	2.3 - 3.1	310 - 533	243 - 272
S8	338	24.5 - 27.5	2.4 - 3.2	318 - 549	194 - 249
S9	-	21.5 - 24.5	1.8 - 2.4	187 - 369	138 - 194
S10	383	29.5 - 32.5	2.1 - 2.9	254 - 461	189 - 249
S11	249	23.5 - 26.5	2.3 - 3.1	293 - 516	180 - 236
S12	405	29.5 - 32.5	2.0 - 2.8	233 - 432	181 - 239
S13	393	17.5 - 20.5	2.3 - 3.1	287 - 510	155 - 206

Notes: (1) Predicted Run-up height is calculated by combining the results of analytical models (i.e. Energy Model or Momentum Jump Model) and the maximum debris flow depth.
(2) The run-up height for Test No. S9 could not be measured due to the misplacement of the high speed camera.

6.2 Large-scale Flume Test

A large-scale flume test was recently conducted by the HKUST at Kadoorie Centre in Hong Kong. The test involved the use of a two-phased debris mix (water content of 40%, and

particle size ranging from 0.001 mm to 30 mm). A volume of 3.5 m^3 of debris was released from a storage tank. The debris then travelled along a 15 m long by 2 m wide flume at a gradient of 20° and impacted on a 1.55 m high reinforced concrete L-shaped barrier. The test setup and the model barrier are shown in Figure 6.1. The frontal velocity and the run-up height of the debris were captured by high speed cameras while the debris flow depth was measured by laser sensors. The result of this test (denoted as Test No. L1) is presented in Table 6.2. The frontal velocity and the debris flow depth were approx. 6.1 m/s and 55 mm respectively. The predicted run-up height based on the Energy Model generally matches with the experimental results. No spillage of debris out of the model barrier was observed in this test. Video of Test No. L1 is given in Section 8 Appendix B.

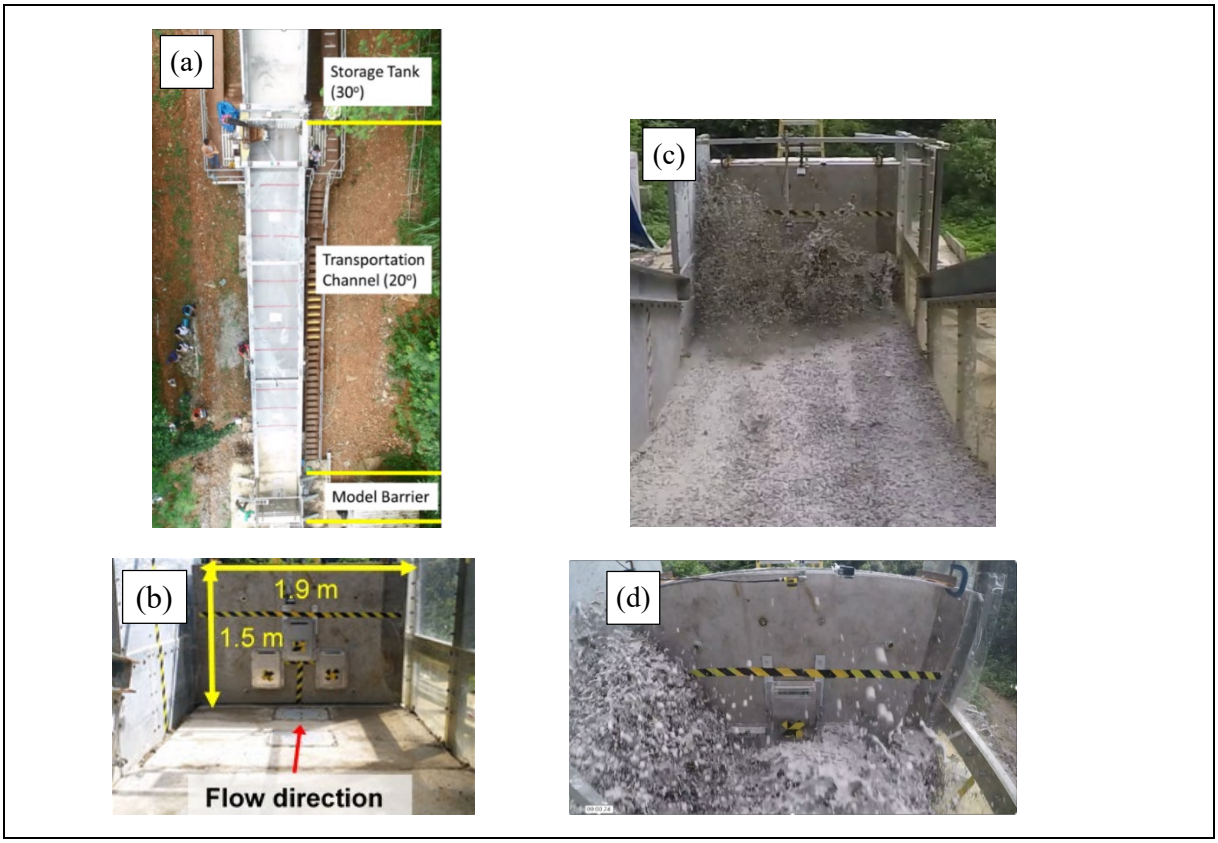

Figure 6.1 Snapshots Showing (a) the Test Setup, (b) the Model Barrier and (c) & (d) the Run-up of Debris in Large-scale Flume Test (Test No. L1)

Table 6.2 Summary of the Run-up Heights in Large-scale Flume Test No. L1

Test No.	Observed "Run-up" (i.e. Max. level of splashing) (mm)	Maximum Flow Depth, i.e. H_{Max} (mm)	Observed Frontal Velocity, i.e. v (m/s)	Predicted Run-up based on Energy Model (mm)	Predicted Run-up based on Momentum Jump Model (Kwan, 2012) (mm)
L1	1500 - 1600	47 - 55	6.1	1944 - 1952	578 - 730

7 Potential Refinements of Technical Guidance for Deflector Design

Results of this study indicate that a deflector is effective in preventing spillage of debris materials from a rigid barrier and the prediction of debris run-up heights based on the Energy Model generally matches with the experimental results. On this basis, potential refinements of the existing design guidance for deflectors could include:

(1) The prediction of run-up height can be based on Energy Model (see Section 6 for details) with the incorporation of the maximum debris flow depth. If the height of a barrier is less than the predicted debris run-up height, a deflector at the crest of the barrier would be needed, so as to prevent possible spillage of debris materials to downstream areas.

(2) The deflector can be horizontal or inclined up to 45° to the horizontal. In general, the required horizontal projected length of the deflector (L) could be, at least, half of H_{Max} (see Figure 7.1).

(3) In case that cushioning materials are provided, the horizontal projected length of the deflector refers to the length measured from the outer face of the cushion.

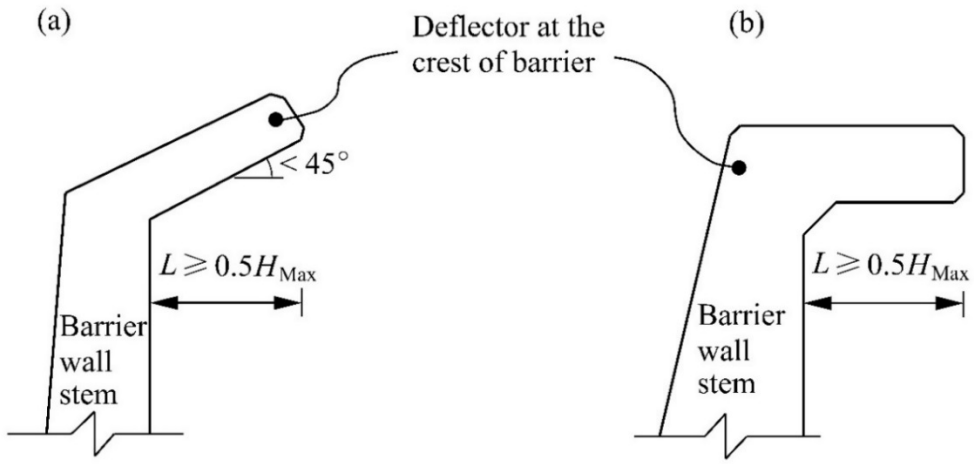

H_{Max} = Maximum debris flow depth at the barrier location calculated by debris mobility analysis

Notes:
(1) In selecting a suitable shape and form for a deflector (e.g. reinforced concrete or steel), due regard should be given to various factors including the construction cost and the constructability (including temporary works required), the maintenance requirement, and the landscaping requirement of the barriers, etc.
(2) If reinforced concrete deflector is adopted, for improving its buildability in respect of steel fixing, formwork placement and concreting, the geometry of the deflector can be of a corbel shape.

Figure 7.1 Potential Refinement of Design Guidance - Details of Deflectors

8 Conclusion

Literature reviews, a series of laboratory flume tests and a large-scale flume test were carried out to investigate spillage mechanism of landslide debris intercepted by rigid barriers and deflectors at the crest of the barriers for prevention of spillage of landslide debris. Potential refinements of existing design guidance for deflectors have been discussed, with a view to improving the current design practice.

Notwithstanding the above, if the predicted run-up height does not exceed the height of the wall stem, spillage of landslide debris is generally not a concern.

The provision of a crest deflector to prevent spillage of landslide debris is generally not necessary and should be considered as a last resort if the barrier is situated in close proximity to downstream facilities where there is a safety concern when spillage of landslide debris occurs. As an alternative, other precautionary measures such as provision of freeboard may also be considered to prevent spillage of debris.

9 References

ASI (2011). *ONR 24802 Protection Works for Torrent Control - Design of Structures*. Austrian Standard Institute, Austria, 96 p.

ASI (2013). *ONR 24801 Protection Works for Torrent Control - Static and Dynamic Actions on Structures*. Austrian Standard Institute, Austria.

CAGHP (2018). *Specification of Design for Debris Flow Prevention* (T/CAGHP *021-2018)*. China Association of Geological Hazard Prevention, 55 p. (in Chinese)

Choi, C.E., Au-Yeung, S.C.H. & Ng, C.W.W. (2015). Flume investigation of landslide granular debris and water runup mechanisms. *Géotechnique Letters 5*(1): 28-32.

Choi, C.E., Ng, C.W.W., Goodwin, G.R., Liu, H. & Kwan, J.S.H. (2016). Flume investigation of the influence of rigid barrier deflector angle on dry granular overflow mechanisms. *Canadian Geotechnical Journal 53*(10): 1751-1759.

Cornett, A., Li, Y. & Budvietas, A. (1999). Wave overtopping at chamfered and overhanging vertical structures. *In Proceedings International Workshop on Natural Disasters by Storm Waves and their Reproduction in Experimental Basins*. November 1999. Kyoto, Japan.

Hákonardóttir, K.M. (2003). *The Interaction between Snow Avalanches and Dams*. PhD Thesis, School of Mathematics, The University of Bristol, United Kingdom.

HKUST (2018). *Investigation of the Interaction between Debris Flows and Deflectors Installed on Rigid-resisting Barriers*. Final Report prepared for the Geotechnical Engineering Office, Civil Engineering and Development Department, Hong Kong, 28 p.

Hübl, J., Suda, J., Proske, D., Kaitna, R. & Scheidl, C. (2009). Debris flow impact estimation. *In Proceedings of the 11th International Symposium on Water Management and Hydraulic Engineering, Ohrid, Macedonia*, 1 - 5 September 2009, 1-5.

Iverson, R.M., George, D.L. & Logan, M. (2016). Debris flow runup on vertical barriers and adverse slopes. *Journal of Geophysical Research Earth Surface 121*, pp 2333-2357.

Jóhannesson, T., Gauer, P., Issler, P. & Lied, K. (2009). *The Design of Avalanche Protection Dams - Recent Practical and Theoretical Developments*. Directorate-General for Research, Environment Directorate, European Commission, EUR2339, 205 p.

Kwan, J.S.H. (2012). *Supplementary Technical Guidance on Design of Rigid Debris-resisting Barriers (GEO Report No. 270)*. Geotechnical Engineering Office, Hong Kong, 88 p.

Lo, D.O.K. (2000). *Review of Natural Terrain Landslide Debris-resisting Barrier Design (GEO Report No. 104)*. Geotechnical Engineering Office, Hong Kong, 91 p.

MLR (2006). *Specification of Geological Investigation for Debris Flow Stabilization*. DZ/T 0220-2006, National Land Resources Department, China, 32 p. (in Chinese).

Ng, C.W.W., Choi, C.E., Liu, L.H.D., Wang, Y., Song, D. & Yang, N. (2017). Influence of particle size on the mechanism of dry granular run-up on a rigid barrier. *Géotechnique Letters, Vol. 7, No. 1*, pp 79-89.

NILIM (2007). *Manual of Technical Standard for Designing Sabo Facilities against Debris Flow and Driftwood*. Technical Note of NILIM No. 365, Natural Institute for Land and Infrastructure Management, Ministry of Land, Infrastructure and Transport, Japan, 73 p. (in Japanese).

Schoonees, T. (2014). *Impermeable Recurve Seawalls to Reduce Wave Overtopping*. MEng Thesis, Stollenbosch University, South Africa, 89 p.

Song, D., Ng, C.W.W., Choi, C.E., Kwan, J.S.H. & Koo, R.C.H. (2017). Influence of debris flow solid fraction on rigid barrier impact. *Canadian Geotechnical Journal* 54(10): 1421-1434.

SWCB (2005). *Manual of Soil and Water Conservation.* Soil and Water Conservation Bureau, Taiwan, 692 p. (in Chinese).

VanDine, D.F. (1996). *Debris Flow Control Structures for Forest Engineering*. Ministry of Forests, British Columbia, Canada, 68 p.

Van Doorslaer, K. & De Rouck, J. (2010). Reduction on wave overtopping on a smooth dike by means of a parapet. *Coastal Engineering Proceedings*, 1(32), pp 1-6.

White, D.J., Take, W.A. & Bolton, M.D. (2003). Soil deformation measurement using particle image velocimetry (PIV) and photogrammetry. *Géotechnique 53*, No. 7, pp 619-632.

Section 8
Appendix A

Video of a Debris Flow Occurred in Susten, Switzerland in 2018

Video for a Debris Flow Occurred in Susten, Switzerland in 2018

Source: https://www.youtube.com/watch?v=YZTZ4VTXKlE

Section 8
Appendix B

Videos of Laboratory Flume Tests and Large-scale Flume Test

Video for Test No. S1

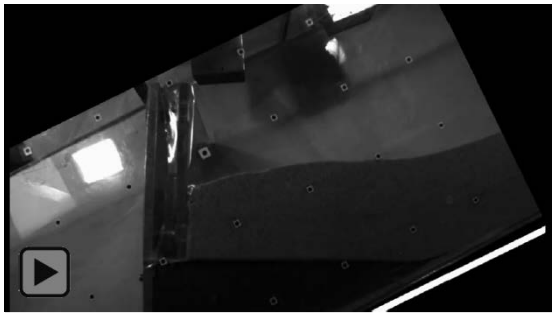

Video for Test No. S4

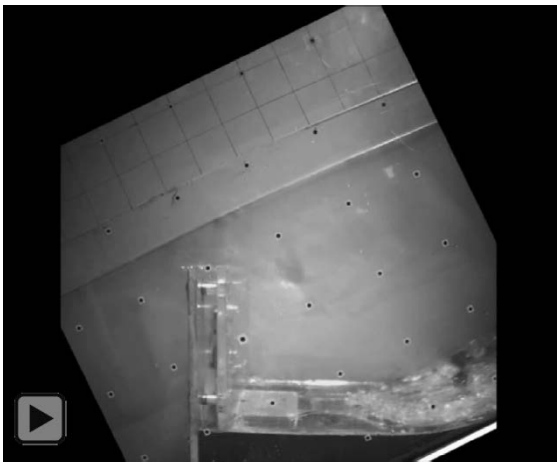

Video for Test No. S7

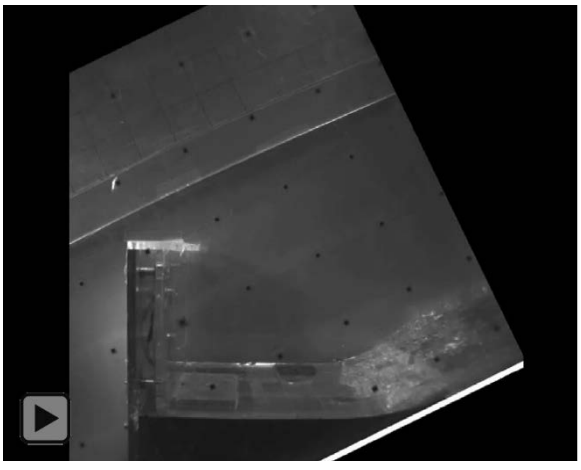

Video for Test No. D5

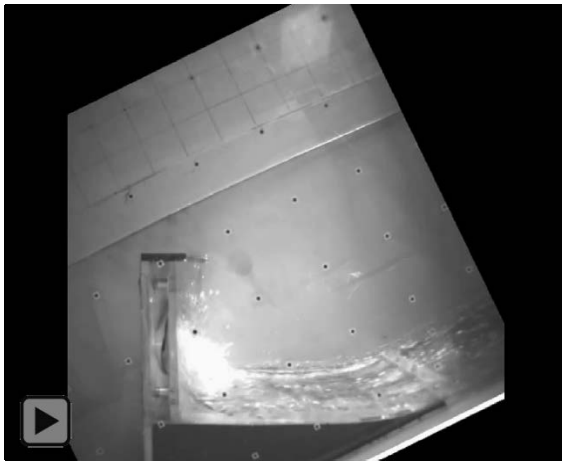

Video for Test No. D6

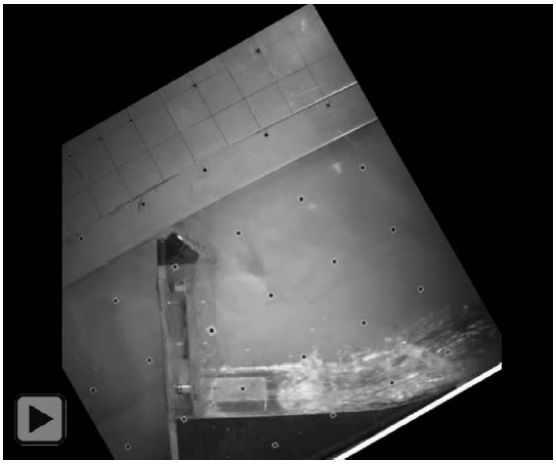

Video for Test No. D7

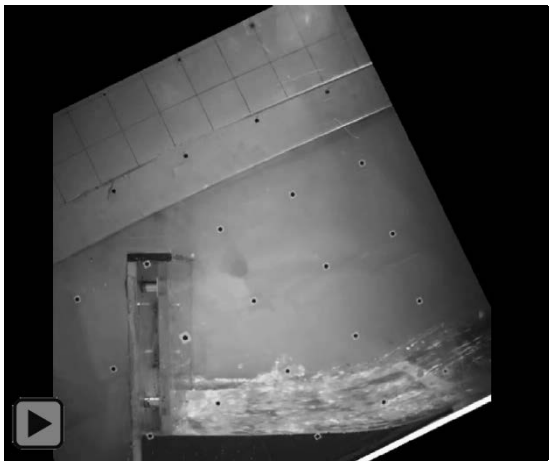

Video for Test No. D8

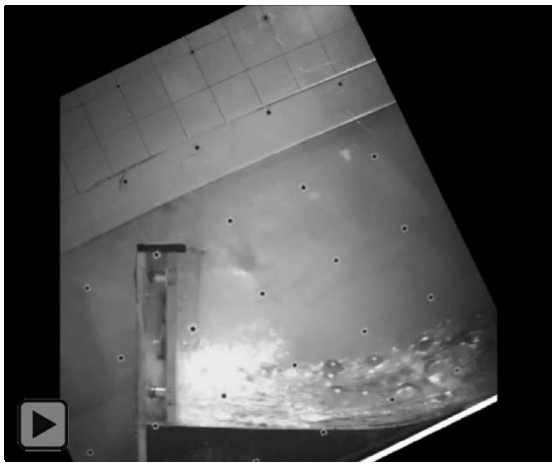

Video for Test No. D9

Video for Test No. L1

Section 9: Supplementary Study of Spillage Mechanism of Landslide Debris Intercepted by Rigid Barriers and Deflectors to Prevent Spillage

L.A. Wong & H.W.K. Lam

This section was originally produced in December 2019 as GEO Technical Note No. TN 7/2019

Foreword

This Technical Note summarises findings of a study on the spillage mechanism of landslide debris intercepted by rigid barriers based on large-scale flume tests and numerical analyses. It supplements the previous studies documented in GEO Technical Note No. TN 5/2018 - Spillage Mechanism of Landslide Debris Intercepted by Rigid Barriers and Deflectors to Prevent Spillage. This study was carried out by Mr L.A. Wong under the supervision of Mr H.W.K. Lam in collaboration with Dr C.E. Choi from the Hong Kong University of Science and Technology (HKUST). The numerical analyses using computational fluid dynamics - discrete element method were carried out by the Hong Kong University of Science and Technology. The Drafting Unit of the Standards and Testing Division assisted in formatting this Note.

Many colleagues in the GEO provided constructive comments on the Note. All contributions are gratefully acknowledged.

T.K.C. Wong
Chief Geotechnical Engineer/Standards and Testing
December 2019

Abstract

This study provides supplementary technical information on the spillage mechanism for landslide debris impacting onto rigid barriers, with a view to optimising the geometrical requirements of a deflector. The study comprises large-scale flume tests and numerical analyses. The key finding is that a deflector with a protruding length of half of frontal debris flow depth could effectively prevent spillage of debris. This finding is consistent with the previous study based on laboratory tests as documented in GEO Technical Note No. TN 5/2018 - Spillage Mechanism of Landslide Debris Intercepted by Rigid Barriers and Deflectors to Prevent Spillage.

Contents

			Page No.
Title Page			371
Foreword			372
Abstract			373
Contents			374
List of Tables			376
List of Figures			377
List of Videos			378
1	Background		379
2	Large-scale Experimental Study		379
	2.1	General	379
	2.2	Flume Facilities	380
	2.3	Model Barrier	381
	2.4	Instrumentations	381
	2.5	Test Program	382
3	Results of Large-scale Flume Tests		383
	3.1	General Observations	383
	3.2	Flow Tests on Barrier with a Deflector	384
		3.2.1 Pure Water Flow	384
		3.2.2 Water Flow with Hard Inclusions	385
4	Numerical Analyses		387
	4.1	General	387
	4.2	Numerical Study of the Effectiveness of Deflector Installed on a Rigid Barrier	387
5	Conclusion		389
6	References		389

		Page No.
Section 9 Appendix A:	Computational Fluid Dynamics - Discrete Element Method (CFD-DEM) Analyses	390

List of Tables

Table No.		Page No.
2.1	Summary of the Instrumentations of the Flume Tests	382
2.2	Test Program	383
3.1	Summary of 5 Nos. of Large-scale Flume Tests	383

List of Figures

Figure No.		Page No.
1.1	Snapshot of a Laboratory-scale Flume Test Conducted in 2018 (Wong & Lam, 2018)	379
2.1	Photograph of the Flume Facility	380
2.2	Side View of Model Barrier and Close-up View of Model Deflector	381
2.3	Photograph of Granite Spheres and Lightweight Plastic Balls with Pure Water	382
3.1	Observed Spillage of Pure Water (Test No. W) on Barrier without Deflector	384
3.2	Observed Spillage Suppression of Pure Water (Test No. D1)	384
3.3	Observed Spillage Suppression of Water Mixed with Granitic Spheres (Test No. D2)	385
3.4	Observed Spillage Suppression of Water Mixed with Light-weight Beach Balls (Test No. D3)	385
3.5	Observed Spillage Suppression of Water Mixed with Aggregates (Test No. D4)	386
3.6	Observed Spillage Suppression of Water Mixed with Aggregates (Test No. D4 (Control))	386
4.1	Snapshot of Simulation No. S1 (without Deflector)	388

List of Videos

Video No.		Page No.
4.1	Results of Simulation No. S1 (without Deflector)	388
4.2	Results of Simulation No. S2 (with a 0.25 m long Deflector, i.e. L/H = 0.5)	389

1 Background

A debris flow impacting onto a rigid barrier can lead to run-up of debris mass along the stem of the barrier wall, resulting in possible spillage of landslide debris which may affect facilities in downstream areas (Ng et al, 2018). Local design guidance (Kwan, 2012) suggests that if the predicted run-up is higher than the wall stem of a rigid barrier, a deflector should be provided at the crest of the barrier to prevent spillage of landslide debris to downstream areas.

Local construction experiences show that a long deflector could be practically difficult for construction due to the substantial temporary works involved. In 2018, Geotechnical Engineering Office in collaboration with the Hong Kong University of Science and Technology (HKUST), conducted an experimental study to explore the possibility of optimising the geometrical requirements of a deflector. Based on the results of laboratory-scale flume tests (conducted in a 0.2 m wide and 5 m long flume at a gradient of 26°), it was found that model deflector with a protruding length (L) of half of the frontal debris flow depth (H, i.e. $L/H = 0.5$) is adequate to prevent spillage of model debris and hard inclusions (see Figure 1.1), while the current design guidance (Kwan, 2012) suggests such protruding length to frontal flow depth ratio of 1.0. More details of the laboratory-scale flume tests, including the setup, instrumentations, debris mix, and test results, have been documented in Wong & Lam (2018).

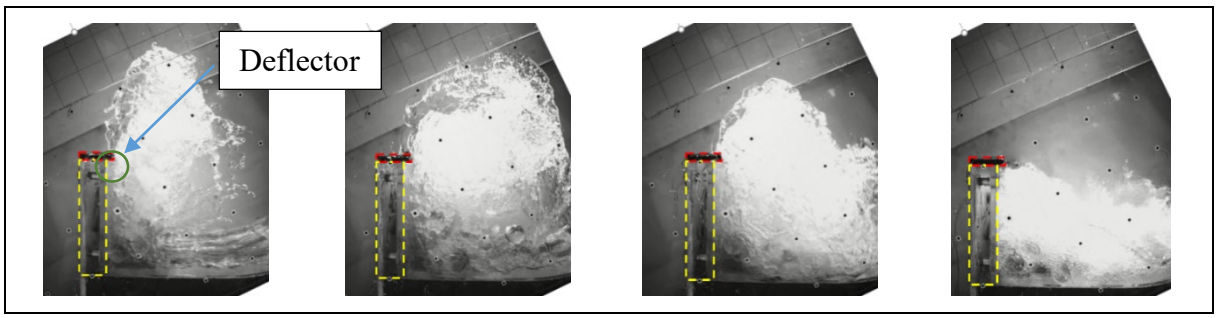

Figure 1.1 Snapshot of a Laboratory-scale Flume Test Conducted in 2018 (Wong & Lam, 2018)

To further validate the effectiveness of deflector with a protruding length of 0.5H for preventing spillage of debris, a series of large-scale physical tests and numerical analyses were constructed in 2019. The physical tests were conducted in a 20 m long flume facility developed by the HKUST in the Kadoorie Centre in Hong Kong. Numerical analyses were also conducted to simulate debris impact scenarios that are typically encountered in routine design. This Technical Note summarises the findings of this series of experimental tests and numerical analyses.

2 Large-scale Experimental Study

2.1 General

This experimental study utilises the newly established flume facilities in the Kadoorie Centre in Hong Kong. The flume facilities, test setup, instrumentation and test program are discussed in this section.

2.2 Flume Facilities

The flume established in the Kadoorie Centre is about 28 m long, 2 m wide and 1 m deep (see Figure 2.1). It comprises three key components, including a storage tank at the upstream, a transportation channel, and a deposition zone.

The storage tank has a capacity of about 10 m^3, with a gradient of 30° at the base to facilitate initiation of debris flows. There is a mechanical opening gate at the outlet of the storage tank which has been designed to simulate landslide initiation in a repeatable manner.

There is a 2 m wide transportation channel inclining at 20° below the storage tank, which is formed by a steel frame structure with two sides of 1 m high side-walls. The side-walls are propped to each other with cross beams at the top at a spacing of about 5 m.

The deposition zone of 2 m wide and 8 m long, where two side-walls along this zone are supported by external raking struts, is located at the outlet of the transportation channel. It is founded on a 5 m wide and 8 m long levelled concrete pad.

The transition between the transportation channel and the deposition zone is made of mass concrete, which is smoothened to minimise energy loss of the debris flow during testing.

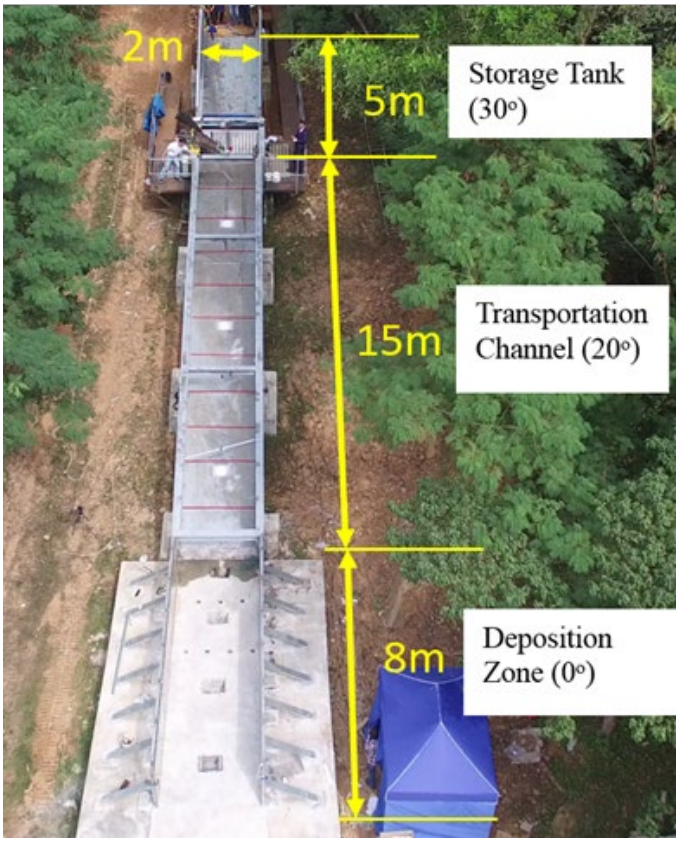

Figure 2.1 Photograph of the Flume Facility

2.3 Model Barrier

To simulate a realistic debris-barrier interaction, a model barrier was constructed at the deposition zone to receive strikes from debris flow materials. The model barrier is an L-shaped reinforced concrete barrier (see Figure 2.2) where the wall stem is 1.8 m high (including thickness of base slab), 1.9 m wide and 0.3 m thick, and the base slab is 1.5 m long (excluding thickness of wall stem), 1.9 m wide and 0.3 m thick. The characteristic strength of concrete used is 30 MPa. The reinforcement of the barrier involves two layers of A393 wire mesh (characteristic strength of 500 MPa) at the front side (i.e. tension side) of the wall stem, and one layer of such wire mesh at the other side of the stem and wall base. There was a steel plate installed in front of the reinforced concrete barrier wall.

An acrylic plate of 1.9 m wide, 0.04 m long and 0.01 m thick was installed at the top of steel plate in front of the barrier (see Figure 2.2), forming a deflector structure with a protruding length of 40 mm. Based on a trial flow test involving 1.5 m^3 pure water where the flow depth (H) was observed to be approx. 80 mm from the laser sensor depth measurement taken at 900 mm upstream of the wall face, such a protruding length (L) of 40 mm would correspond to an L/H ratio of 0.5, which is the target ratio for testing.

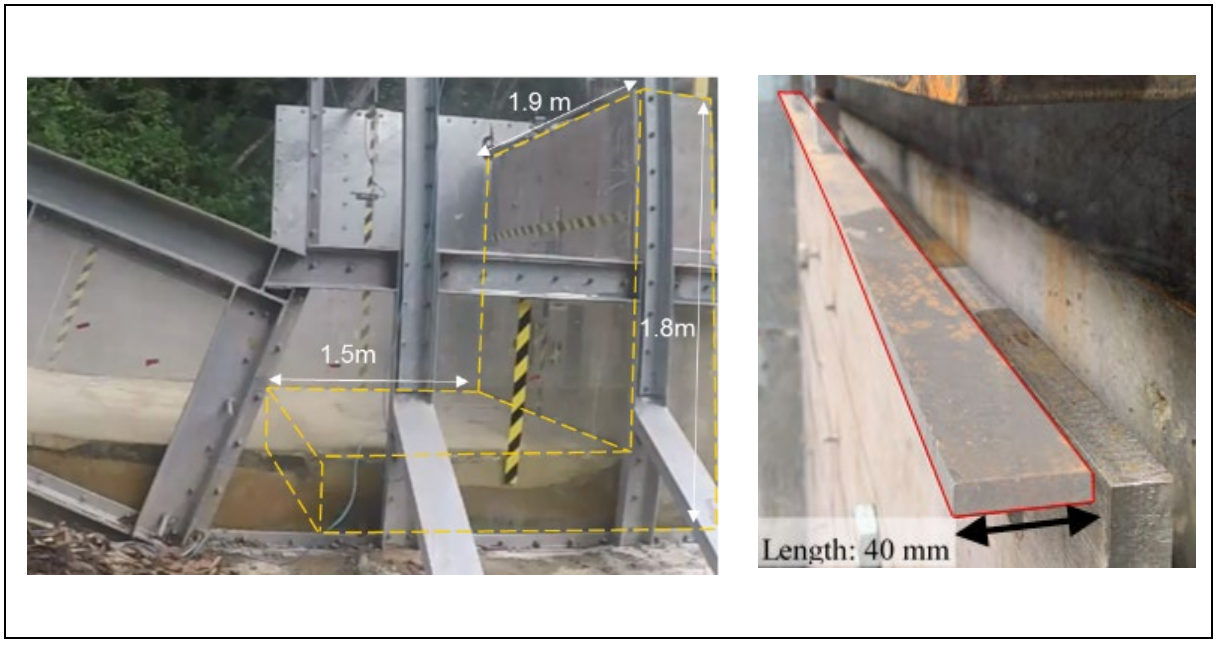

Figure 2.2 Side View of Model Barrier and Close-up View of Model Deflector

2.4 Instrumentations

The instrumentations used in this study are summarised in Table 2.1 below. A high-speed camera was installed at the side of deposition zone to capture the impact process and the flow velocity of the debris flow. A laser sensor was installed at 0.9 m upstream of the wall stem of the model barrier to measure debris flow depth.

Table 2.1 Summary of the Instrumentations of the Flume Tests

Instruments	Measurable Range	Frequency	Accuracy	Measurement (Location of the Instrument)
Laser Sensor	< 1 m	2 kHz	+/- 0.5%	Flow depth (Above the centerline of the flume, and approx. 900 mm upstream of the model barrier)
High-speed camera (2336 × 1728 pixels)	-	Operating at 560 frames per second	-	Flow kinematics & Flow velocity (At the side of the flume)

2.5 Test Program

Five numbers of large-scale flume tests were carried out. As discussed in Section 2.3, one of these tests were carried out using a model barrier without any deflector (i.e. Test No. W), which aimed to capture the flow depth of debris so as to determine the length of deflector to be tested. Four numbers of tests (i.e. Test Nos. D1 to D4) were carried out using a model barrier with a deflector with a 40 mm protruding length. Also, a control test (i.e. Test No. D4 (Control)) was conducted for Test No. D4 where no deflector was installed.

Pure water with a source volume of about 1.5 m^3 was adopted as the fluid portion of debris in order to maximise the mobility of flow, hence resulting in a greater extent of spillage. To allow easy observation of spillage mechanism, blue dye was added to water. In Test Nos. W and D1, pure water was used. In Test Nos. D2 to D4 and Test No. D4 (Control), hard inclusions including 80 mm diameter granite spheres, 300 mm diameter lightweight plastic balls and 40 mm diameter aggregates were added (see Figure 2.3). Table 2.2 summarises the test program.

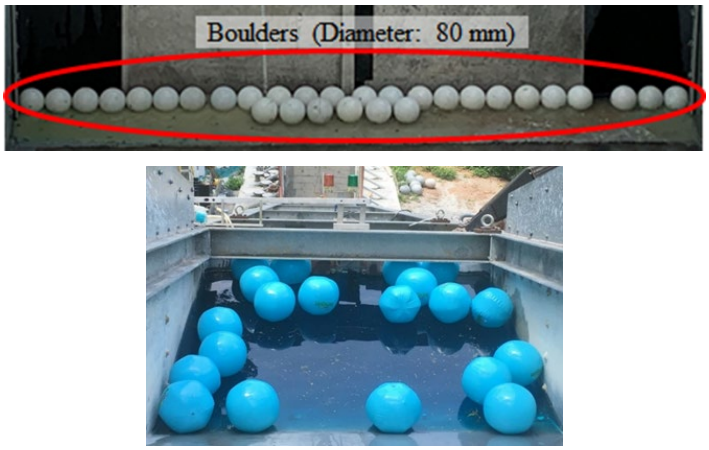

Figure 2.3 Photograph of Granitic Spheres and Lightweight Plastic Balls with Pure Water

Table 2.2 Test Program

<table>
<tr><th>Test No.</th><th colspan="2">Debris Material</th><th>Length of Model Deflector</th></tr>
<tr><td>W</td><td rowspan="6">1.5 m^3 of Pure Water</td><td>-</td><td>No deflector</td></tr>
<tr><td>D1</td><td>-</td><td rowspan="3">40 mm
(i.e. L/H = 0.5)</td></tr>
<tr><td>D2</td><td>20 nos. of 80 mm diameter granite sphere (each weighing 0.7 kg)</td></tr>
<tr><td>D3</td><td>20 nos. of 300 mm diameter plastic ball (each weighing 0.15 kg)</td></tr>
<tr><td>D4</td><td rowspan="2">40 mm diameter aggregates (total weight of 40 kg)</td><td rowspan="2">No deflector</td></tr>
<tr><td>D4 (Control)</td></tr>
<tr><td>Note:</td><td colspan="3">L and H represent protruding length of model deflector and frontal flow depth of debris before impacting onto model barrier respectively.</td></tr>
</table>

3 Results of Large-scale Flume Tests

3.1 General Observations

The flow characteristics, including the flow depth and the flow velocity, obtained in each test are summarised in Table 3.1 below.

Table 3.1 Summary of 5 Nos. of Large-scale Flume Tests

Test No.	Frontal Flow Depth (mm)	Observed Frontal Velocity (m/s)
W	80	7.5
D1	80	7.5
D2	80	7.4
D3	78	7.5
D4	76	7.3

Figure 3.1 shows the run-up observed in the water flow test (i.e. Test No. W). Water run-up behaviour was deduced from this test involving pure water flow, which should have a higher mobility as compared with landslide debris. In this test where the model barrier was not equipped with any deflector structure, it was observed that upon impacting the model barrier, the frontal water ran up along the stem of the model barrier. The frontal water continued to travel upwards until it attained its maximum run-up height, and then descended vertically downwards under gravity and interacted with the upward jet of the subsequent flow. This interaction resulted in a lateral spreading of the water, causing some water overtopping the model barrier.

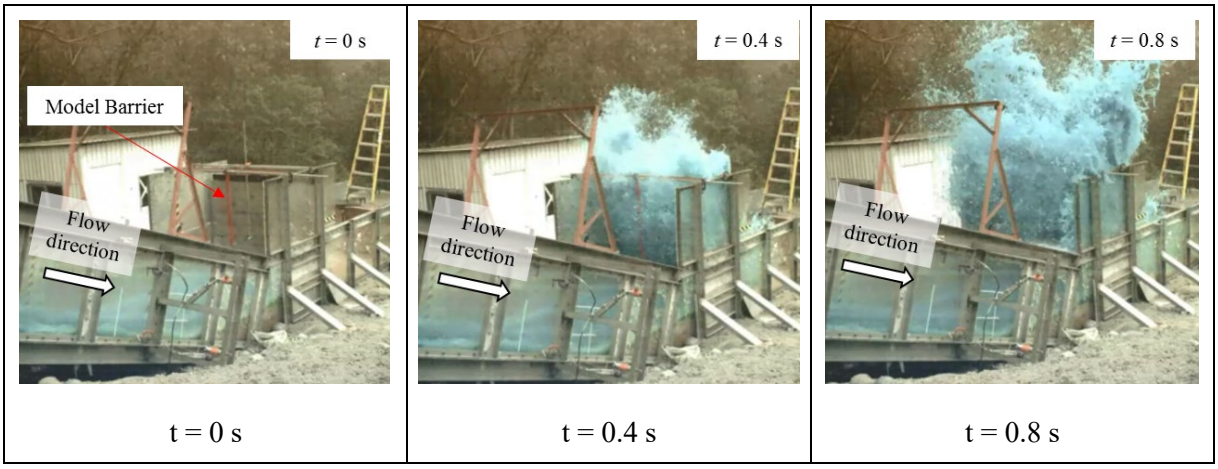

Figure 3.1 Observed Spillage of Pure Water (Test No. W) on Barrier without Deflector

3.2 Flow Tests on Barrier with a Deflector

3.2.1 Pure Water Flow

To verify the performance of a deflector at a target L/H ratio of 0.5, Test No. D1 was conducted. In this test, protruding length of deflector was 40 mm, i.e. half of the debris flow depth of approx. 80 mm. It can be seen that with the presence of the model deflector, negligible water spillage was observed (see Figure 3.2).

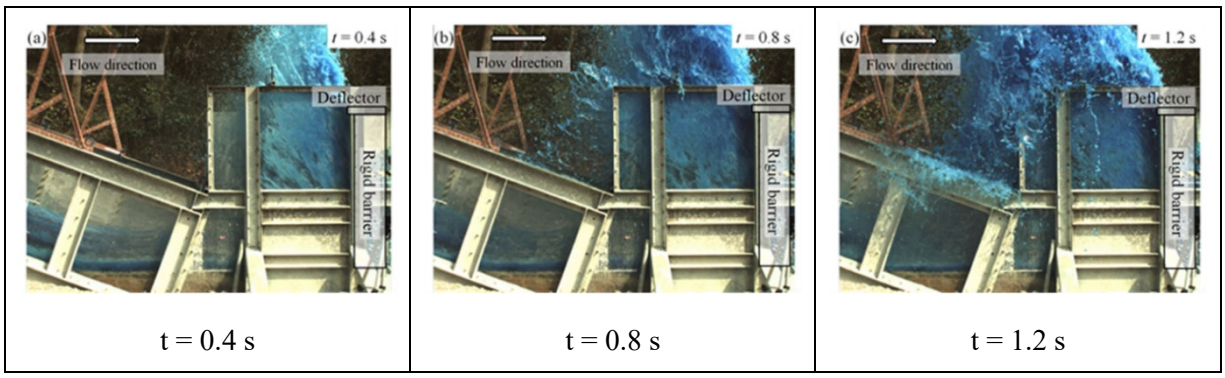

Figure 3.2 Observed Spillage Suppression of Pure Water (Test No. D1)

3.2.2 Water Flow with Hard Inclusions

In addition to pure water used in Test Nos. W and D1, different types of hard inclusions were added in the water for Test Nos. D2 to D4. The results of these tests are that spillage of water was effectively prevented by the model deflector. In Test No. D2, granite spheres of 80 mm diameter with a density of 2650 kg/m^3, each weighing 0.7 kg were added to simulate boulder front in a debris flow. The diameter of these granite spheres approximately equals the frontal flow depth of debris. Yet, only minor uplift of granite spheres was observed and none of the spheres reached or overtopped the barrier (see Figure 3.3).

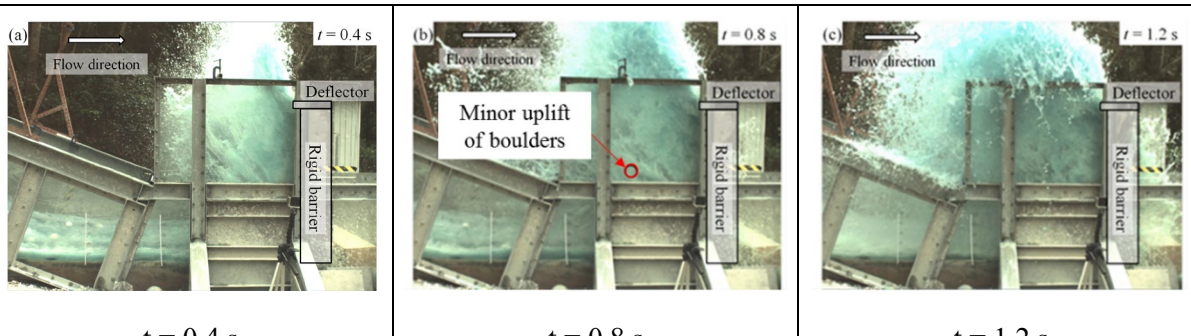

t = 0.4 s | t = 0.8 s | t = 1.2 s

Figure 3.3 Observed Spillage Suppression of Water Mixed with Granitic Spheres (Test No. D2)

Test No. D3 was conducted using hard inclusions of lighter weight. In this test, twenty plastic balls of 300 mm diameter, each weighing 0.15 kg, were added to the water. Because these balls have a density lower than water, they floated on the water flow. None of these balls overtopped the barrier (see Figure 3.4).

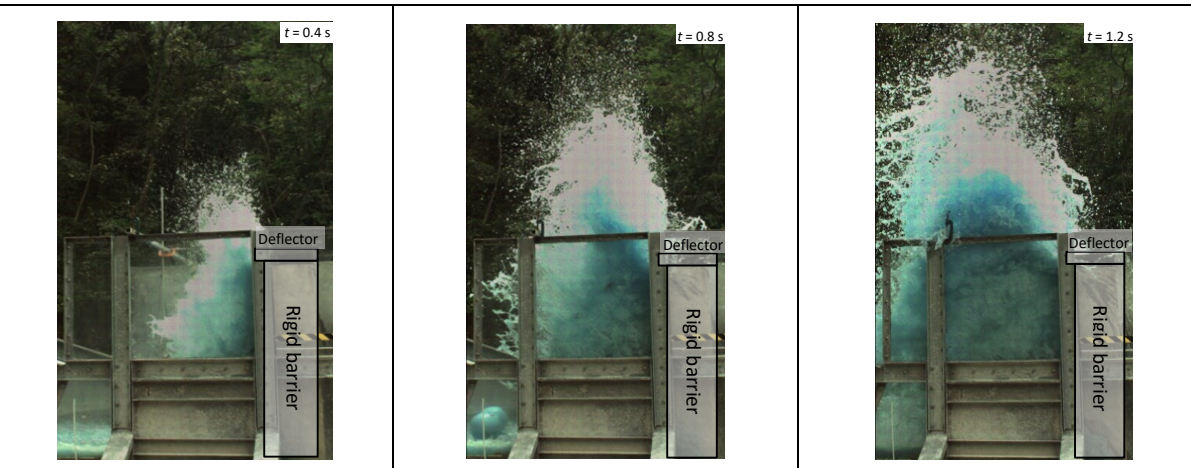

t = 0.4 s | t = 0.8 s | t = 1.2 s

Figure 3.4 Observed Spillage Suppression of Water Mixed with Light-weight Beach Balls (Test No. D3)

Test No. D4 was conducted where aggregates of 40 mm diameter weighing 40 kg in total were added in the water. These aggregates were intended to resemble the small size hard inclusions in the debris flow. In this test, the aggregates were carried along by water flow. When the flow reaching the top of the barrier, the flow was largely deflected by the deflector. Some minor spillage of flow was observed. About 0.02 kg (i.e. 1.5 %) of aggregates, together with fluid portion of the flow, overtopped the barrier, and deposited at the downstream of the barrier (see Figure 3.5).

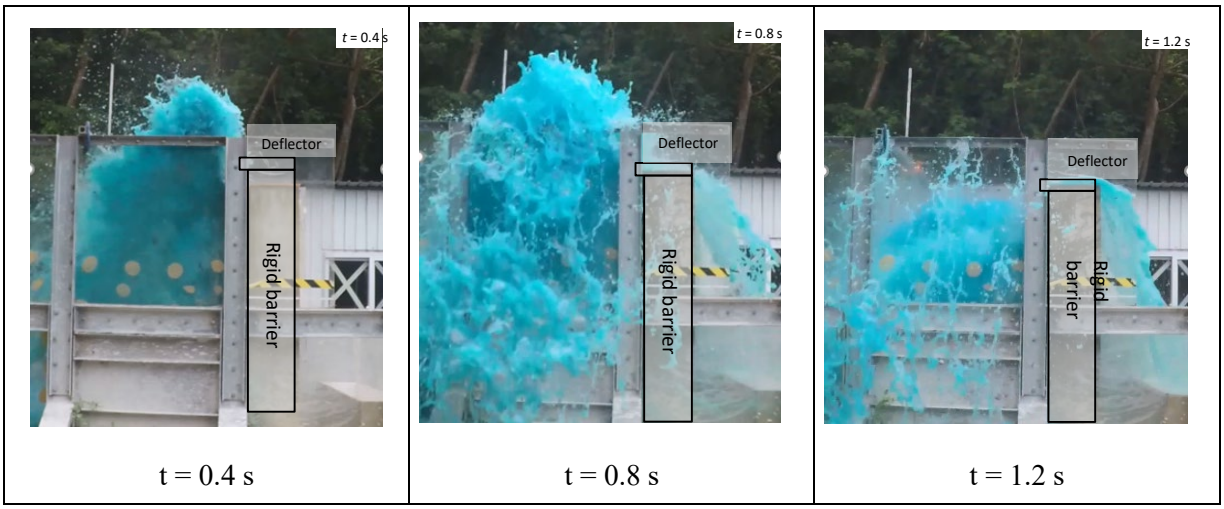

Figure 3.5 Observed Spillage Suppression of Water Mixed with Aggregates (Test No. D4)

A control test, i.e. Test No. D4 (Control), was conducted where no deflector was provided for the barrier. In this control test, spillage mechanism of water in Test No. D4 (control) was found similar to that observed in Test No. W (see Figure 3.6). 4 % by mass of aggregates was found overtopping the barrier under the same flow conditions as Test No. D4. As such, the presence of a deflector has significantly (> 60%) reduced the chance of spillage of small hard inclusions.

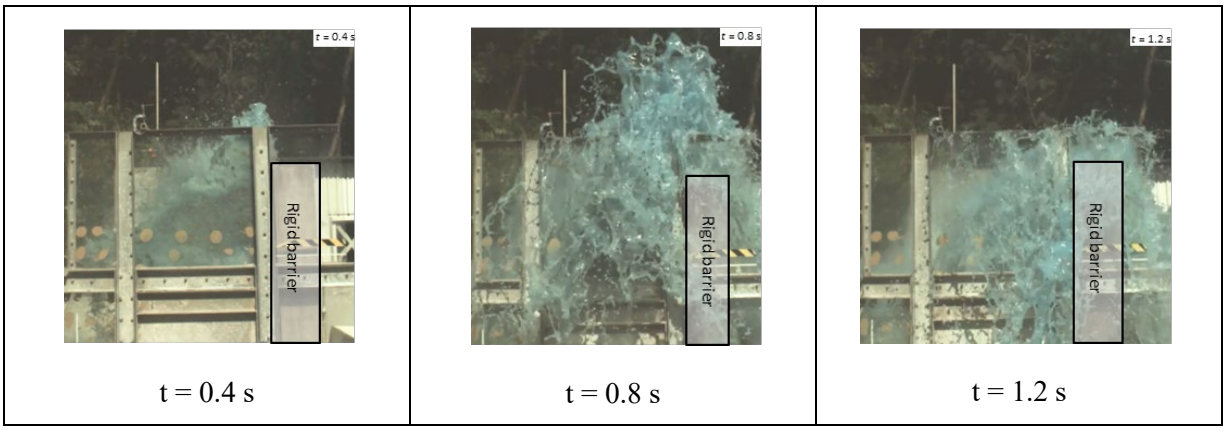

Figure 3.6 Observed Spillage Suppression of Water Mixed with Aggregates (Test No. D4 (Control))

In summary, results of large-scale flume tests indicate that spillage of debris could be effectively prevented with the use of a deflector with a protruding length of half of frontal flow depth. According to the test results, extent of uplifting of hard inclusions contained in a water flow depends on the size of such hard inclusions. Based on Test No. D2, run-up of hard inclusions with a diameter similar to flow depth is not significant. From Test No. D4, minor spillage of small hard inclusions was observed.

4 Numerical Analyses

4.1 General

Numerical analyses were conducted in this study to simulate debris impact event of a larger scale. Coupled analyses based on computational fluid dynamics - discrete element method (CFD-DEM analyses) were adopted. The capability of CFD-DEM modelling can effectively model the interaction between fluid and particle, as well as their interaction with structures.

The numerical analyses based on CFD-DEM approach were conducted by Dr. Jidong Zhao of the Hong Kong University of Science and Technology. In the CFD-DEM method, the motion of particle phase is calculated by DEM using Newton's laws of motion, while the flow of continuum fluid is described by the local averaged Navier–Stokes equations that can be solved using the traditional Computational Fluid Dynamics (CFD) approach. As for the interaction between particle and fluid, it can be modelled using Newton's third law of motion (Zhao & Shan, 2013). More details of CFD-DEM modelling are presented in Section 9 Appendix A.

4.2 Numerical Study of the Effectiveness of Deflector Installed on a Rigid Barrier

Validation of the CFD-DEM model (i.e. Simulation No. S0) was first conducted against Test No. D4 described in Section 3. Details of the back-analysis including input parameters, modelling setup and results are presented in Section 9 Appendix A. The flow kinematics of debris obtained from numerical analyses were more mobile as compared with those observed in the flume test conducted in Kadoorie Centre. The flow when reaching the deflector generally deflected backwards in a similar manner as that observed in physical tests described in Section 3. As such, this CFD-DEM modelling technique would be used for further analyses of effectiveness of deflector under large-scale debris flow events.

After the validation exercise, two large-scale debris impact scenarios (Simulation Nos. S1 & S2) with a source volume of about 200 m^3 were simulated in CFD-DEM model (Figure 4.1). Simulation No. S1 involved a model barrier without deflector while Simulation No. S2 involved a model deflector, with a protruding length of half of the frontal debris flow depth, installed at the crest of the model barrier.

In both two simulations, the width of the flume and rigid barrier were 10 m. The barrier height was 5 m, which is typical in a routine design. The length of the storage tank is 10 m for a large volume of water. 300 nos. of boulders of 0.4 m diameter were used and the volume of water was increased to 200 m^3. Other parameters were kept consistent with Simulation No. S0. A snapshot of the graphical input of Simulation No. S1 is as shown below:

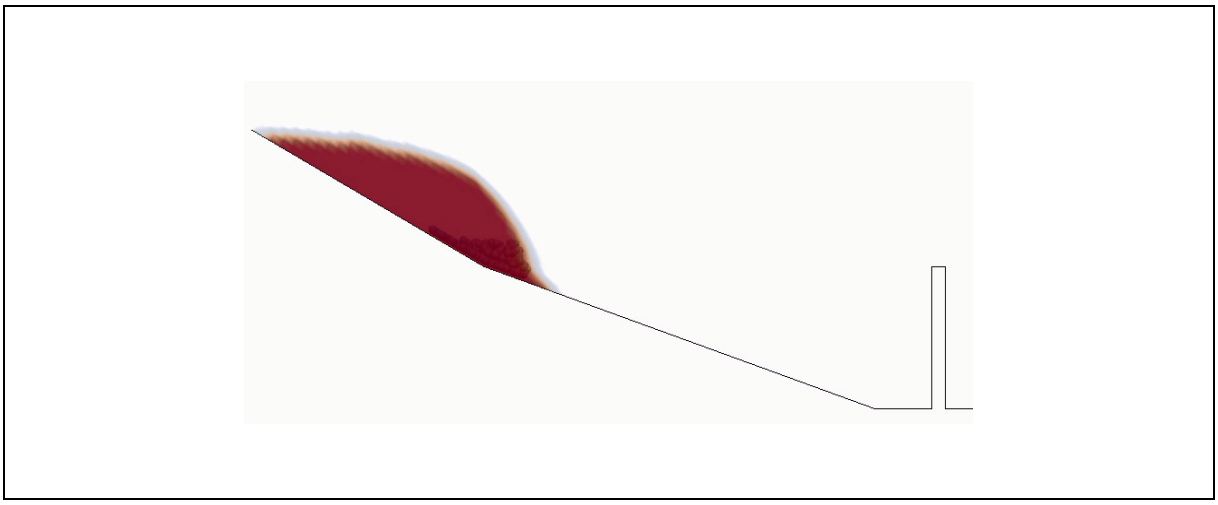

Figure 4.1 Snapshot of Simulation No. S1 (without Deflector)

The results of Simulation No. S1 are shown in the animation below:-

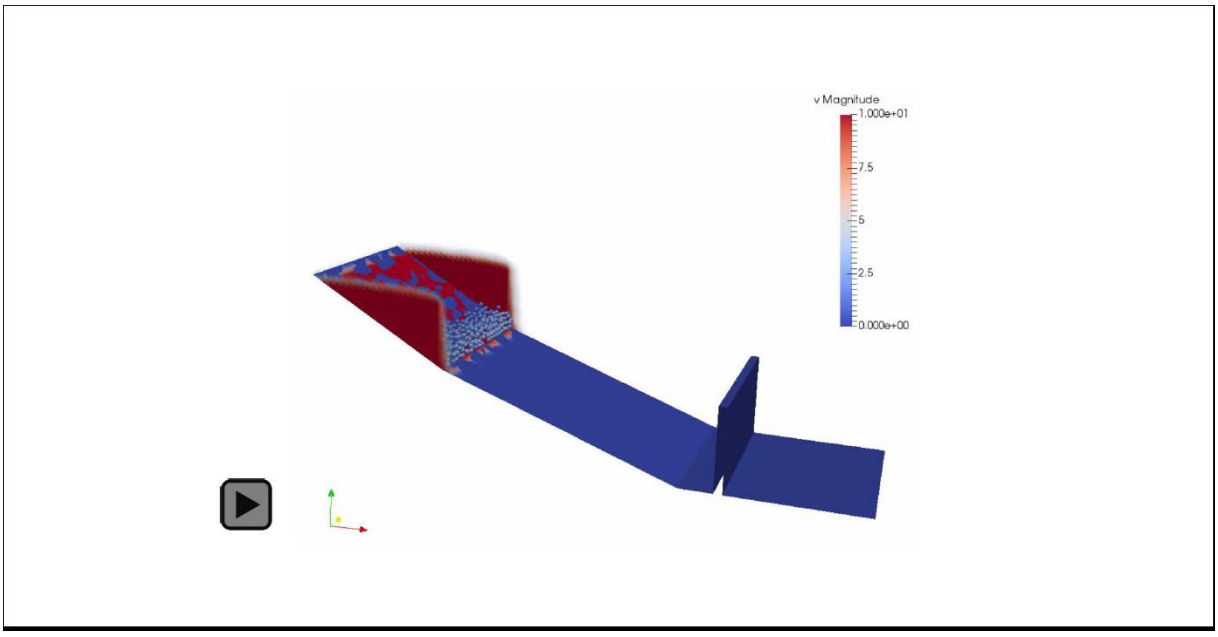

Video 4.1 Results of Simulation No. S1 (without Deflector)

The frontal velocity and flow depth of debris immediately before impacting the model barrier were 10 m/s and 0.5 m respectively. It was found that the fluid of the debris material slightly overtopped the barrier. Hard inclusions were not lifted up high (lower than the wall height) and did not overtop the barrier.

Simulation No. S2 was conducted with a model barrier having a deflector of 0.25 m long (i.e. L/H = 0.5) installed at the crest of the wall stem. The debris impact scenario and other details of the wall are the same as those adopted in Simulation No. S1.

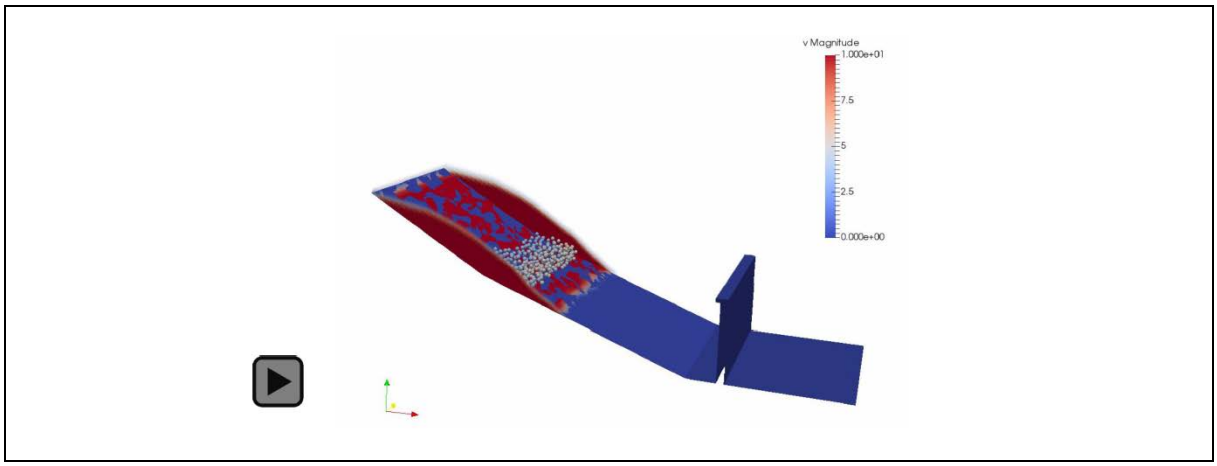

Video 4.2 Results of Simulation No. S2 (with a 0.25 m long Deflector, i.e. L/H = 0.5)

The result of Simulation No. S2 showed that, with the deflector provided, no signs of spillage of debris (both fluid part and hard inclusions) was observed. The debris predominately deflected backward when interacting with the deflector. The flow deflection behaviour closely assembled that observed in the flume tests in Kadoorie Centre described in Section 3. In addition, hard inclusions did not spill out from the model barrier and quickly settled in the fluid mix upon run-up.

5 Conclusion

Based on the results of both large-scale flume tests and CFD-DEM modelling of debris impact scenario that is typically encountered in routine design, a deflector with a protruding length of half of the frontal debris flow depth (i.e. L/H = 0.5) at the crest of a rigid barrier could effectively prevent spillage of debris. The finding is consistent with that from the previous laboratory-scale flume tests reported in Wong & Lam (2018).

6 References

Kwan, J.S.H. (2012). *Supplementary Technical Guidance on Design of Rigid Debris-resisting Barriers (GEO Report No. 270)*. Geotechnical Engineering Office, Hong Kong, 88 p.

Ng, C.W.W., Choi, C.E., Koo, R.C.H., Goodwin, G.R., Song, D. & Kwan, J.S.H. (2018). Dry Granular Flow Interaction with Dual-barrier Systems. *Géotechnique v68(5)*, May 2018, pp. 386-399

Wong, L.A. & Lam, H.W.K. (2018). *Spillage Mechanism of Landslide Debris Intercepted by Rigid Barriers and Deflectors to Prevent Spillage (Technical Note No. 5/2018).* Geotechnical Engineering Office, Hong Kong, 28 p.

Zhao, J.D. & Shan, T. (2013). Coupled CFD-DEM Simulation of Fluid-particle Interaction in Geomechanics. *Powder Technology*. 239, 248-258.

Section 9
Appendix A

Computational Fluid Dynamics - Discrete Element Method (CFD-DEM) Analyses

Contents

		Page No.
Contents		391
List of Tables		392
List of Figures		393
A.1	General Principles of CFD-DEM Analyses	394
	A.1.1 General	394
	A.1.2 Modelling of Granular System	394
	A.1.3 Modelling of Fluid System	394
	A.1.4 Modelling of Fluid-particle Interaction	394
	A.1.5 Modelling of Fluid-structure Interaction	394
A.2	Numerical Back-analyses of Large-scale Flume Test No. D4 (Simulation No. S0)	395
References		397

List of Tables

Table No.		Page No.
A1	Summary of Input of Numerical Back-analyses	396
A2	Summary of Flow Kinematics in Numerical Back-analyses	396

List of Figures

Figure No.		Page No.
A1	Modelling of Granular Flow into a Water Tank (after Shan and Zhao, 2014)	395
A2	Geometry setup for Simulating the Flume Facility in Kadoorie Centre	395
A3	Animation showing Result of Simulation No. S0	397

A.1 General Principles of CFD-DEM Analyses

A.1.1 General

Since the interaction between fluid and particle could influence the mechanism of fluid particle interaction, coupled analyses based on computational fluid dynamics - discrete element method (CFD-DEM) analyses were conducted by Hong Kong University of Science and Technology. Principles of the CFD-DEM modelling are briefly described in this Appendix.

A.1.2 Modelling of Granular System

A particle in a granular system may experience translational and rotational motions and may interact with its adjacent particles, structure or fluid which causes interchange of energy and momentum. The motion of a particle in a granular system is influenced by the mass, forces and torques created from these interactions. Discrete Element Method (DEM) is a popular tool to simulate the behaviour of granular system. For a particle in a DEM model, the governing equations of its motion are based on Newton's second law of motion.

A.1.3 Modelling of Fluid System

Fluid phase can be treated as a continuum fluid by a Computational Fluid Dynamics (CFD). Continuous fluid domain is discretised into cells in the CFD method which will solve the governing equations for fluid at each cell. Solving these equations could yield locally averaged state variables such as fluid velocity, pressure and density. The governing equations for fluid are based on momentum in terms of local-average quantities and conservation of mass (Anderson & Jackson, 1967).

A.1.4 Modelling of Fluid-particle Interaction

Proper consideration of fluid-particle interaction forces is required for coupling the CFD and DEM. In general, drag force and buoyancy force are modelled in common fluid-particle interaction for geomechanics problems (Shan & Zhao, 2014), which are based on Di Felice (2007) and Kafui et al (2002) respectively.

When a particle accelerates in a fluid, it must deflect the surrounding fluid to move through and hence generates some additional inertia to the system. Shan (2015) considered this inertia force in fluid-particle coupling and is based on the virtual mass force in Odar & Hamilton (1964).

A.1.5 Modelling of Fluid-structure Interaction

Shan & Zhao (2014) used the coupled CFD-DEM numerical tool to study the impact of a gravity-driven granular flow falling into a water tank. The side view of the impacting process is shown in Figure A1. Such impact mechanism was found highly comparable to that observed in physical experiments.

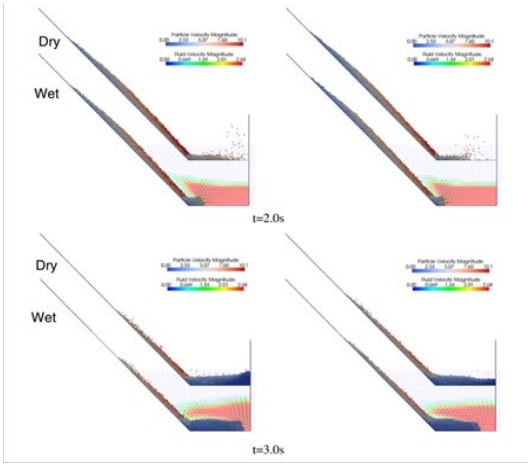

Figure A1 Modelling of Granular Flow into a Water Tank (after Shan and Zhao, 2014)

A.2 Numerical Back-analyses of Large-scale Flume Test No. D4 (Simulation No. S0)

In order to study the effectiveness of deflectors to suppress spillage of debris and boulders by numerical mean, the field data obtained from physical test No. D4 (see Section 3) were used to validate the numerical CFD-DEM program.

The model setup for the numerical back-analysis is shown in Figure A2. Rigid walls are generated as boundaries of the storage tank and flume. The dimensions and geometry of the flume are identical to those used in large-scale flume test. The width of the storage tank and flume is 2 m, whilst infinitely high side walls are assumed. The inclination of the storage tank (length 5 m) is 30° and the slope of the transportation zone (length 15 m) is 20°. The zone connecting the 20° section with the flat outflow section (length 1.5 m) has a slight degree of curvature to allow the water grains to pass smoothly downstream. The barrier at the end of the flume is 1.5 m in height and 2 m in width. On the top of the barrier, a deflector (length of 0.04 m) perpendicular to the barrier is modelled as a rigid plate.

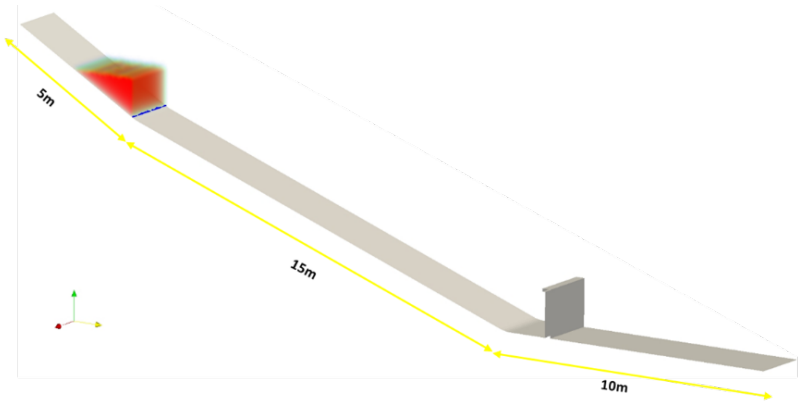

Figure A2 Geometry setup for Simulating the Flume Facility in Kadoorie Centre

The parameters for the CFD-DEM model are shown in Table A1 below. Due to the high computation demand for a large amount of discrete particles, only 9 kg (i.e. 100 nos.) of 40 mm diameter aggregates instead of 40 kg of aggregates have been modelled.

Table A1 Summary of Input of Numerical Back-analyses

Particle	General	100 nos. of Particles; Diameter = 40 mm
	Density (kg/m^3)	2650
	Young's modulus (GPa)	70
	Poisson's ratio	0.3
	Rolling friction coefficient	0.15
	Coefficient of restitution	0.4
	Friction coefficient	0.57
	Volume fraction	0.4
Liquid	Density (kg/m^3)	1000
	Volume (m^3)	approx. 1.5 m^3
	Viscosity (Pa-s)	0.001
Air	Density (kg/m^3)	1
	Viscosity (Pa-s)	1.48 x 10^{-5}

The results of numerical back-anaylses, including the frontal flow depth, frontal flow velocity and run-up height of fluid are summarised as follows:-

Table A2 Summary of Flow Kinematics in Numerical Back-analyses

	Flume Test in Kadoorie Centre	Simulation No. S0
Frontal flow depth (mm)	80	105
Frontal flow velocity (m/s)	7.3	9.3

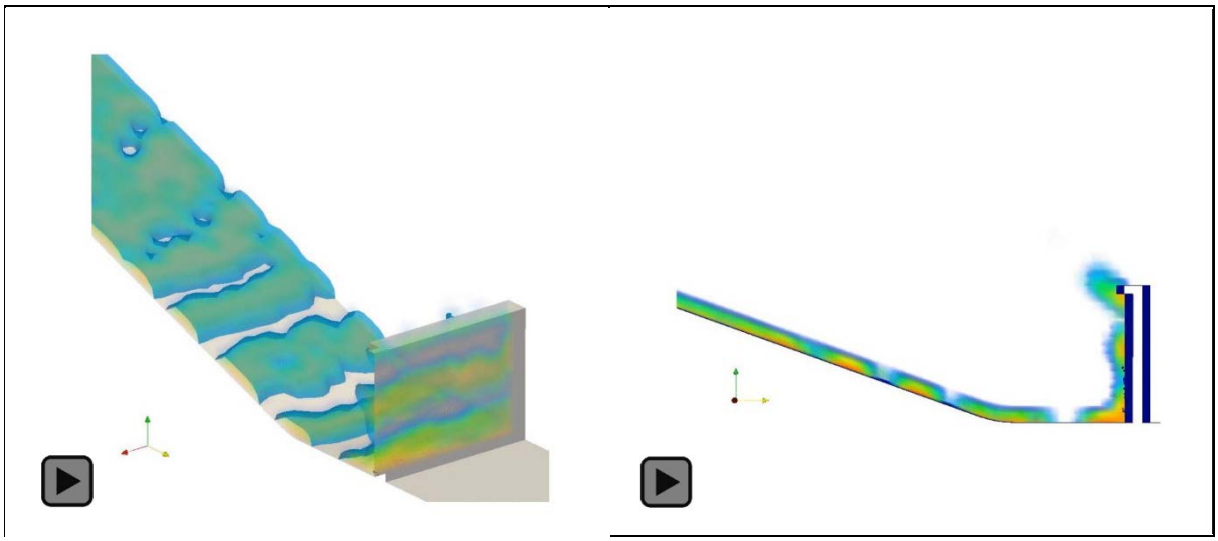

Figure A3 Animation showing Result of Simulation No. S0

The flow kinematics of debris obtained from numerical analyses are more mobile as compared with those observed in the flume test conducted in Kadoorie. In particular, the numerical model predicted that debris does not spill off from the barrier if a deflector (of L/H = 0.5) is provided, which is consistent with that observed in the physical tests. As such, CFD-DEM modelling would be used for further analyses of effectiveness of deflector under large-scale debris flow events (see Section 4).

References

Anderson, T.B. & Jackson, R. (1967). A fluid mechanical description of fluidized beds. *Ind. Engng Chem. Fundam*, 6, pp.527–539.

Di Felice, R. (2007). Liquid suspensions of single and binary component solid particles - An overview. *China Particuology*, 10.1016/j.cpart.2007.06.001, 5, 5, pp.312-320.

Kafui, K. D., Thornton, C. & Adams, M.J. (2002). Discrete particle-continuum fluid modelling for gas–solid fluidised beds. *Chemical Engineering Science*, 57(13), pp.2395-2410.

Odar, F. & Hamilton, W.S. (1964). Forces on a sphere accelerating in a viscous fluid. *Journal of Fluid Mechanics*, 18(2), pp.302-314.

Shan, T. (2015). *Coupled CFD-DEM Modeling of Fluid-particle Interaction in Geomechanics* (Doctoral dissertation, Hong Kong University of Science and Technology).

Shan, T. & Zhao, J. (2014). A coupled CFD-DEM analysis of granular flow impacting on a water reservoir. *Acta Mechanica*, 225(8), pp.2449-2470.

GEO PUBLICATIONS AND ORDERING INFORMATION
土力工程處刊物及訂購資料

An up-to-date full list of GEO publications can be found at the CEDD Website http://www.cedd.gov.hk on the Internet under "Publications". The following GEO publications can also be downloaded from the CEDD Website:

i. Manuals, Guides and Specifications
ii. GEO technical guidance notes
iii. GEO reports
iv. Geotechnical area studies programme
v. Geological survey memoirs
vi. Geological survey sheet reports

詳盡及最新的土力工程處刊物目錄，已登載於土木工程拓展署的互聯網網頁http://www.cedd.gov.hk 的"刊物"版面之內。以下的土力工程處刊物亦可於該網頁下載：

i. 指南、指引及規格
ii. 土力工程處技術指引
iii. 土力工程處報告
iv. 岩土工程地區研究計劃
v. 地質研究報告
vi. 地質調查圖表報告

Copies of some GEO publications (except geological maps and other publications which are free of charge) can be purchased either by:

Writing to
Publications Sales Unit,
Information Services Department,
Room 626, 6th Floor,
North Point Government Offices,
333 Java Road, North Point, Hong Kong.

or

- Calling the Publications Sales Section of Information Services Department (ISD) at (852) 2537 1910
- Visiting the online Government Bookstore at http:// www.bookstore.gov.hk
- Downloading the order form from the ISD website at http://www.isd.gov.hk and submitting the order online or by fax to (852) 2523 7195
- Placing order with ISD by e-mail at puborder@isd.gov.hk

讀者可採用以下方法購買部分土力工程處刊物(地質圖及免費刊物除外):

書面訂購
香港北角渣華道333號
北角政府合署6樓626室
政府新聞處
刊物銷售組

或

- 致電政府新聞處刊物銷售小組訂購 (電話：(852) 2537 1910)
- 進入網上「政府書店」選購，網址為 http://www.bookstore.gov.hk
- 透過政府新聞處的網站 (http://www.isd.gov.hk) 於網上遞交訂購表格，或將表格傳真至刊物銷售小組 (傳真：(852) 2523 7195)
- 以電郵方式訂購 (電郵地址：puborder@isd.gov.hk)

1:100 000, 1:20 000 and 1:5 000 geological maps can be purchased from:

Map Publications Centre/HK,
Survey & Mapping Office, Lands Department,
23th Floor, North Point Government Offices,
333 Java Road, North Point, Hong Kong.
Tel: (852) 2231 3187
Fax: (852) 2116 0774

讀者可於下列地點購買1:100 000、1:20 000及1:5 000地質圖：

香港北角渣華道333號
北角政府合署23樓
地政總署測繪處
電話: (852) 2231 3187
傳真: (852) 2116 0774

Any enquires on GEO publications should be directed to:

Chief Geotechnical Engineer/Standards and Testing,
Geotechnical Engineering Office,
Civil Engineering and Development Department,
Civil Engineering and Development Building,
101 Princess Margaret Road,
Homantin, Kowloon, Hong Kong.
Tel: (852) 2762 5351
Fax: (852) 2714 0275
E-mail: ivanli@cedd.gov.hk

如對本處刊物有任何查詢，請致函：

香港九龍何文田公主道101號
土木工程拓展署大樓
土木工程拓展署
土力工程處
標準及測試部總土力工程師
電話: (852) 2762 5351
傳真: (852) 2714 0275
電子郵件: ivanli@cedd.gov.hk